The Influence of Residual Stresses on Structural Integrity of Renewable Energy Marine Structures

A Thesis submitted for the Degree of Engineering Doctorate of Cranfield University

by

Anais Louise Melanie Jacob

July 2019

Renewable Energy Marine Structures Centre for Doctoral Training (REMS CDT)

Principal Supervisor: Dr Ali Mehmanparast

Associate Supervisor: Professor Feargal Brennan

Abstract

Offshore wind turbines operate in harsh environments and are subjected to severe cyclic loading conditions which result in corrosion and fatigue damage particularly in the support structures which are predominantly made of monopile type foundations. A reliable assessment for the fatigue life of offshore wind turbine monopile foundations is significantly dependent on the level of locked-in welding residual stresses at circumferential weld regions. In this work, fatigue crack growth tests have been conducted in air and seawater on S355 G10+M structural steel which is widely used in the fabrication of offshore wind turbine foundations. Fracture mechanics tests have been performed on compact tension specimens with the crack tip located in the heat affected zone. All tests were performed at room temperature and the obtained results are compared with the literature data available on a range of offshore structural steels and also the recommended trends in BS7910 using the 2-stage law and simplified law. Moreover, the specimen orientation, with respect to the weld geometry, has been examined and discussed in this work.

This study presents, for the first time, residual stress characterisation in compact tension specimens extracted from monopile weldments using three different methods; 1- Neutron diffraction, as a non-destructive technique which is widely used to measure lattice spacing from which residual strains and subsequently residual stresses can be calculated, 2 Neutron imaging, which is a relatively new non-destructive technique that enables residual stresses to be measured through strain mapping of the area of interest, 3- Contour method, as a destructive technique which can be used to measure residual stresses in engineering components and structures. Neutron diffraction and neutron imaging are two complementary techniques which have been employed in this work by performing measurements on the Engin-X and newly developed IMAT instruments, respectively, at the Rutherford Appleton Laboratory.

Neutron diffraction residual strain measurements were conducted along all three directions (i.e. transverse, longitudinal and normal with respect to the weld geometry) on compact tension specimens with the crack tip located in the heat affected zone whilst neutron imaging technique was used to measure residual strains in the longitudinal direction. A comparison of the obtained results from neutron diffraction and neutron imaging techniques has shown that neutron imaging can provide an acceptable measure of residual strains, and subsequently residual stresses, if an accurate value of strain-free lattice spacing, d_0, is employed in data

analysis. Moreover, it has been shown that the contour residual stress measurement results are in good agreement with the neutron diffraction results. The residual stress measurement results have been discussed in terms of the possible sources of error encountered in each technique and the accuracy of each method against the others. The residual stress measurement results showed notably significant remnant residual stresses in compact tension specimens that could have an impact on subsequent fracture and fatigue test results. In addition, the measured 2D map of transverse residual stresses, acting normal to the crack plane, exhibited variations in through thickness direction. This implies that the residual stresses in small laboratory samples extracted from large scale weldments should be carefully characterised and taken into account in interpretation of the structural integrity test results.

In order to examine the specimen size effects on welding residual stress profiles, the contour method has been applied to a compact tension specimen as well as a large welded mock-up, typical of the weldment used in fabrication of offshore wind monopiles. The measurement results on the welded mock-up showed that the level of damaging tensile residual stress in large-scale mock-ups, hence real size structural welded monopiles, is considerably larger than residual stresses in extracted laboratory samples. This means that the welding residual stresses play an even bigger role in structural integrity assessment of full scale offshore wind turbine monopiles.

Finally, a numerical model has been developed to implement the residual stress profile in ABAQUS finite element simulations and calculate the effective stress intensity factor range in the presence of residual stresses for accurate characterisation of fatigue crack growth behaviour, particularly in the near threshold region. The results have shown that when the transverse residual stresses ahead of the crack tip are predominantly compressive, the values of effective stress intensity factor range in compact tension specimens are less than the applied stress intensity factor range by around 10 MPa$\sqrt{m}$. This indicates that residual stresses play a key role in the fatigue life of welded structures, especially in the near threshold region.

Acknowledgements

The work presented herein would not have been possible without the help of many people who I would like to thank. First of all, I would like to express my deepest gratitude to my supervisor, Dr. Ali Mehmanparast, for his guidance and constant support during my MSc and EngD at Cranfield University. He was always there to support and encourage me to pursue a variety of research topics. I also would like to thank my second supervisor, Prof. Feargal Brennan, from the University of Strathclyde, for his expert comments and support. The main experimental aspects of this project would not have been possible without the help of Dr. Joe Kelleher and Dr. Genoveva Burca my industrial supervisors at the Rutherford Appleton Laboratory.

I am extremely grateful that I was part of the Centre for Doctoral Training in Renewable Energy Marine Structures (REMS CDT). It brought a wonderful, diverse and challenging environment for research and I would like to thank every stakeholder. I am also grateful to my office and lab colleagues: Maria Martinez Luengo, Ali Al-Turaihi, Victor Igwemezie, Anastasia Ioannou, Waseem Khodabux and Vera Mytilinou.

One of the main pleasures during this research project was to work with experts in the fracture mechanics domain and I would like to thank Dr. Amir Chahardehi and Dr. Mehdi Yasaee for their constructive comments throughout my research. I also greatly acknowledge the lab technicians at Cranfield, Mr. Jarryd Braithwaite and Mr. Steve Pope for their great assistance during the experiments.

Last but not least, I would like to thank my beloved husband, Yoan Delporte, who always pushes me to go beyond the limit, as well as my family and in-laws for their love and endless support.

This work was supported by grant EP/L016303/1 for Cranfield, Oxford and Strathclyde Universities, Centre for Doctoral Training in Renewable Energy Marine Structures - REMS (http://www.rems-cdt.ac.uk/) from the UK Engineering and Physical Sciences Research Council (EPSRC). Anais Jacob would like to acknowledge the ISIS-STFC financial support for the facility development studentship.

Declaration

I hereby declare that the work presented in this dissertation is original and has not been submitted for a degree or diploma at any other university or institution. Information derived from the published and unpublished work of others has been acknowledged in the text and references are given in the list of sources.

Contents

List of Tables

List of Figures

Nomenclature

a	Crack length
a_f	Crack length at the end of the fatigue test
a_i	Initial crack length
a_0	Crack length at the end of pre-fatigue cracking
a, b, c	Lattice parameters
A_p	Ramberg-Osgood power law coefficient
B	Thickness
C	Paris law coefficient
d	Grain diameter for a polycrystalline material
d_{err}	Error in the *d*-spacing measurements
d_{hkl}	Lattice interplanar spacing of the crystal measured, also known as *d*
$d_{0,err}$	Error in the *d*-spacing measurements of the strain-free sample
$d_{0,hkl}$	Lattice interplanar spacing of the strain-free sample, also known as *d0*
D	Length of the impression diagonal
da/dN	Fatigue Crack Growth rate
E	Modulus of elasticity or Young's modulus
E'	Modulus of elasticity or Young's modulus for plane strain conditions
E_{hkl}	Young's modulus of the *hkl* plane
f	Cyclic frequency
F	Applied load
$F_{y,d}$	Force in *y* direction applied on node *d*
G	Energy release rate
hkl	Miller indices
HV	Vickers Pyramid number
I(t)	Transmitted neutron beam intensity
I(0)	Incident neutron beam intensity
J	J-integral
K	Stress Intensity Factor
K_I	Stress Intensity Factor for mode I
K_{max}	Maximum stress intensity factor

K_{min}	Minimum stress intensity factor
K_{op}	Stress intensity at which the crack opens
m	Paris law exponent
N	Ramberg-Osgood power law plasticity stress exponent
P_{max}	Maximum applied load
P_{min}	Minimum applied load
r_p	Plastic zone size ahead of the crack tip
R	Stress ratio
S	Loading stress
t	Total path length through the material
T	Traction vector
$U_{y,b}$, $U_{y,c}$	Displacement along *y* direction on node *b* and *c* respectively
W	Width
W_d	Strain energy density
Y	Shape function
Γ	Curve surrounding the notch tip
Δa	Crack extension
ΔK	Stress Intensity Factor range
ΔK_{eff}	Effective stress intensity factor range
$\Delta K_{eff,th}$	Effective threshold stress intensity factor range
ΔK_{th}	Threshold stress intensity factor range
ΔP	Load range
ε	Strain
ε_1	Residual strain in the first direction (e.g. longitudinal)
ε_2	Residual strain in the second direction (e.g. transverse)
ε_3	Residual strain in the third direction (e.g. normal)
ε_e	Elastic strain
ε_{err}	Error in the residual strain measurements
ε_{err1}	Error in the strain measurement in the first direction (e.g. longitudinal)
ε_{err2}	Error in the strain measurement in the second direction (e.g. transverse)
ε_{err3}	Error in the strain measurement in the third direction (e.g. normal)
ε_{hkl}	Residual strain corresponding to the *hkl* plane
ε_p	Plastic strain

ε_{p0}	normalising strain for plasticity
θ_{hkl}	Scattering angle
λ	wavelength of the neutron radiation
ν	Poisson's ratio
ν_{hkl}	Poisson's ratio of the *hkl* plane
σ	Stress
σ_0	Shear stress required to ensure gliding dislocations
σ_{erri}	Error in the residual stress measurements
σ_i	Residual stress corresponding to ε_i residual strain
σ_{max}	Maximum stress levels applied in a fatigue cycle
σ_{min}	Minimum stress levels applied in a fatigue cycle
σ_{p0}	normalising stress for plasticity
σ_y	Yield stress of the material
Σ	Macroscopic cross section per unit volume
A(T)	Arc Shaped Tension
BCC	Body Centered Cubic
CCT	Centered Cracked Tension
CM	Contour Method
CTOD	Crack Tip Opening Displacement
C(T)	Compact Tension
DC(T)	Disk Shaped Tension
DIC	Digital Image Correlation
EBSD	Electron Backscatter Diffraction
EDX	Energy Dispersive X-ray
EFGM	Element Free Galerkin Method
EPFM	Elastic-Plastic Fracture Mechanics
FCG	Fatigue Crack Growth
FCC	Face Centered Cubic
FEA	Finite Element Analysis
GMAW	Gas Metal Arc Welding
HAZ	Heat Affected Zone
HCF	High Cycle Fatigue
HCP	Hexagonal Close Packed

LCF	Low Cycle Fatigue
LCoE	Levelized Cost of Electricity
LEFM	Linear Elastic Fracture Mechanics
MCP	Micro Channel Plate
M(T)	Middle Tension
ND	Neutron Diffraction
NI	Neutron Imaging
OWT	Offshore Wind Turbine
PWHT	Post Weld Heat Treatment
RITS	Rietveld Imaging of Transmission Spectra
RS	Residual Stress
SAW	Submerged Arc Welding
SE(B)	Single Edge Notched Bend
SEM	Scanning Electron Microscopy
SIF	Stress Intensity Factor
SLIC	Structural Lifecycle Industry Collaboration
TM	Thermomechanical
TOF	Time Of Flight
UTS	Ultimate Tensile Strength
XFEM	eXtended Finite Element Method
2D	2-Dimensional
3D	3-Dimensional

1 Introduction

With the continuous increase in the energy demand around the world, which has resulted in global warming, a challenge for the international community is to reduce greenhouse gas emissions. An efficient and reliable source of clean renewable energy, which can help in meeting this target, is offshore wind which can gradually replace a proportion of the energy supply from fossil fuels in the close future. Among different sources of renewable energy, offshore wind has become one of the most preferred solutions in recent years due to its large-scale deployment potential and significant reductions in its levelised cost, especially since 2016 [1][2][3][4][5]. The offshore wind farm installation, operation and in-service condition monitoring require consideration of a variety of issues associated with the design and assessment of these structures. Indeed, due to the offshore turbulence and cyclic loads from wave, wind and current, these offshore structures are subjected to fatigue damage [6]. Moreover, for the offshore wind turbine foundation, which is in direct contact with seawater, the additional environmental damage due to corrosion must also be considered and accounted for. In order to withstand the critical conditions in harsh environments, the structural integrity of offshore wind turbines needs to be carefully assessed to provide a reliable estimate for the remaining life of these structures.

Among the different types of existing offshore wind turbine support structures, monopile is the most popular foundation type which is widely used in shallow water offshore wind farms and has great design advantages as well as minimal footprint on the seabed [7] [8]. Typical dimensions for the offshore wind turbine monopile range from 50m to 70m in length, 3m to 10m in diameter and 40mm to 150mm in wall thickness [9][10][11]. Monopiles are installed by driving them into the seabed; hence the structure should withstand the hammering loads during installation which vary from site to site depending on the soil conditions. During operation in harsh offshore environment, monopiles are subjected to wind, wave and sea current cyclic loads; hence they have to be designed for a certain fatigue life with suitable safety margins against failure. Moreover, they have to be designed to withstand the horizontal and vertical loads acting on the entire assembly including the transition piece, tower and wind turbine blades. The manufacturing procedure for offshore wind monopile structures consists of rolling and bending large structural steel plates and subsequently welding them together in longitudinal and circumferential directions [12]. The design, fabrication and inspection of offshore wind turbine monopile foundations are costly. Therefore, an important challenge for

the offshore wind industry is to improve the current best practice for structural design and integrity assessment of monopiles that are operating in the harsh offshore environments with constant exertion of wind and wave loads inducing corrosion-fatigue damage, particularly at the weld regions and in the presence of residual stresses (RS). Materials used in offshore structures are mainly chosen from medium to high strength structural steel, due to their corrosion resistance [13]. The studies in the literature have shown that fatigue crack initiation and growth primarily occur at the weld toe, for the as-welded conditions, and at circumferential welds [5]. Depending on the welding procedure, the crack may propagate from the Heat Affected Zone (HAZ) into the Base Metal (BM) in the through thickness direction [5]. More information about the fatigue damage and loading analysis of the monopile foundations can be found in [14][15].

One of the important challenges in the offshore wind industry is the accurate characterisation of fatigue crack propagation in an offshore wind turbine, which is one of the largest engineering structures currently used in the energy sector. For this purpose, the influence of residual stresses around the weld toes must be examined to investigate their effect on the fatigue life predictions of offshore wind turbine foundations. It is known that residual stresses have a substantial influence on the structural integrity and fatigue life of engineering components and structures, as discussed by Nelson [16], Lawrence [17] and Baumgartner [18]. To measure residual stresses, various techniques can be employed which are generally categorised as destructive (such as contour or deep hole drilling), as discussed by Kandil et al. [19], and non-destructive (such as X-ray diffraction or neutron diffraction), as presented by Ruud [20]. In order to accurately characterise the service life of offshore wind monopile welded structures, residual stresses should be measured and accounted for in interpretation of the fatigue crack propagation behaviour of monopile weldments.

A significant effort has been made in the SLIC JIP (Structural Lifecycle Industry Collaboration Joint Industry Project) to characterise the fatigue crack growth (FCG) behaviour of these welded structures in air as well as in seawater in order to better estimate the remaining life of monopiles based on laboratory scale tests on base metal (BM) and weldments (i.e. weld metal (WM) and HAZ) [21][22]. The SLIC project has successfully developed FCG curves to investigate the fatigue behaviour of offshore wind welded steel foundations made of S355 G8+M steel. However, due to the lack of data available at the time, the effect of residual stress on the FCG behaviour particularly in the near threshold

region was not considered in the analysis and therefore was proposed as an important future work.

There is a significant research gap in reliable characterisation of the state of residual stress in monopile structures upon fabrication, after pile driving, during service operation and also the effect of welding sequence on residual stress distribution in monopiles [23][5][24][25]. In addition, the weld quality itself plays a significant role in fatigue life of welded components [26]. There is currently high level of uncertainty and conservatism in the existing codes and standards for the design process and structural integrity assessment of monopiles due to the lack of accurate information about residual stress profiles in these gigantic structures. This is particularly crucial due to the fact that unlike many other industries such as nuclear, no post weld heat treatment is performed on monopiles because of the size and cost issues. Moreover, it is quite well-known that residual stress measurement results from laboratory scale specimens are not easily transferable to components, due to the size effects and therefore different constraint levels, which subsequently result in different residual stress states.

Due to the reasons mentioned above, the industrial motivation of the current research is to remove the uncertainty and conservatism in the structural design and integrity assessment of monopiles by characterising the welding residual stresses in laboratory scale fracture mechanics specimens extracted from monopile weldments and accounting for these locked-in stresses in the analysis of the test data obtained from fatigue crack propagation experiments in air and seawater. Therefore, the industrial impact from this research is to investigate the significance of welding residual stress effects on the FCG behaviour of offshore wind monopiles particularly at circumferential weld regions where the cracks are expected to initiate.

1.1 Aims and objectives

The overall aim of this research is to determine the influence of welding residual stresses on subsequent fatigue crack growth behaviour of the material by performing experimental and numerical investigations. In order to achieve this goal, the following main objectives have been set for this project:

1. To experimentally investigate the FCG behaviour of S355 structural steel weldments in air and in simulated seawater.

2. To quantify the level of locked-in residual stresses in laboratory scale C(T) test specimens using neutron diffraction (ND), neutron imaging (NI) and contour measurements.
3. To develop a numerical framework which accounts for the measured residual stress profiles in interpretation of the FCG test results using the effective stress intensity factor (SIF) range approach.
4. To examine the influence of residual stresses on the fatigue life assessment of C(T) specimens extracted from offshore wind monopile weldments, as well as a large scale weld mock-up representative of real size monopile structures.

1.2 Structure of the thesis

The linear elastic and elastic-plastic fracture mechanics concepts are reviewed in Chapter 2and the theoretical background relevant to the fatigue damage in air and in seawater are presented. Furthermore, a summary of the residual stress measurement techniques are presented and the influence of welding residual stresses on the fatigue life assessment of steel structures available in the literature are reviewed and given in Chapter 2. Specimen design and C(T) specimen extraction details for FCG testing are explained in Chapter 3. Further included in this chapter are the material characterization test results performed on the selected material for this study. Residual stress characterisation using the contour method on a large welded mock-up, in the form of a plate, typical of offshore wind monopile weldment is presented in Chapter 4. Neutron diffraction and contour method measurements have also been conducted on C(T) specimens extracted from the large welded mock-up and the results are included in this chapter (published conference paper in Procedia Structural Integrity). In Chapter 5, the FCG test results on HAZ specimens in air are presented and compared with the data available in the literature as well as the recommended trends in BS7910 standard, "Guide to methods for assessing the acceptability of flaws in metallic structures" [27]. A numerical modelling framework which has been developed to predict the effective Stress Intensity Factor (SIF) range, by taking into account the measured residual stress profiles in C(T) specimens, is presented in Chapter 6 and the results from Chapter 5 are re-evaluated to correlate the fatigue crack growth rate with the effective SIF range predicted using finite element analysis (FEA) simulations. The fatigue crack growth data from HAZ specimens tested in seawater environment are shown in Chapter 7 and the results are compared with the recommended trends in BS7910 standard for free-corrosion condition. Post-mortem analysis

by performing fractography studies on samples tested in air and in seawater environments has been performed and the results are presented in both Chapter 5 and Chapter 7 respectively. Finally, a list of key conclusions from this research and suggested future work are stated in Chapter 8.

Chapter 4 is a published journal paper in Theoretical and Applied Fracture Mechanics

Chapter 5 and Chapter 6 are published papers in International Journal of Fatigue

Chapter 7 is a draft journal paper to be submitted to the Journal of Marine Structures

2 Theoretical background

2.1 Offshore wind turbine design requirements and material selection

The cumulative offshore wind capacity in Europe has reached 18,499 MW at the end of 2018. When sites with partial grid connection are included, there are currently 105 offshore wind farms installed in 11 European countries and 4,543 grid-connected wind turbines [28]. The United Kingdom represented 49% of Europe's gross capacity with 1,312 MW brought online by 2018. Out of 7 wind farms that were grid-connected by 2018, 6 were fully commissioned and one (Beatrice 2) began the connection process to the grid. The Walney 3 Extension wind farm was completed in October 2018, becoming the largest operational offshore wind farm worldwide with 87 turbines and a capacity of 657 MW [28].

The Levelized Cost of Electrcity (LCoE) is a measure of a power source that allows comparison of different methods of electricity generation on a consistent basis. It is an economic assessment of the average total cost to build and operate a power-generating asset over its lifetime divided by the total energy output of the asset over that lifetime. According to their studies, the British government has stated in their report [29] in 2018 that solar and onshore wind power energy were the cheapest energy sources. Offshore wind has seen significant innovations, such as larger turbines with longer blades, allowing it to capture more wind and the report presented in [29] shows that its LCoE will fall below onshore wind by 2028. Unless the government makes changes to planning regulations affecting turbines on land, offshore wind will overtake onshore wind as the least expensive source of renewable power in the UK. This will not only benefit consumers with cheaper cleaner energy but help the government towards its decarbonisation targets.

The main factors to consider in the design of support structures for offshore wind turbines (OWT) are the dynamic response of the structure, the constructability and the required logistics relevant to the selected site (e.g. water depth, distance from shore and soil conditions), manufacturing costs, availability of the selected material and the environmental impact [30]. The main types of support structures for OWTs are described below [31]. Gravity based support structures are made of concrete and are typically used where the commissioning of piles in the seabed is difficult [30]. Based on a simple design, monopile support structures are large plates welded together to form cans using a thermomechanical (TM) rolling process [32]. Offshore wind monopiles consist of large structural steel pipe

sections of up to 10m diameter and 150mm wall thickness [30]. The current generation of installed monopiles have the capacity to support 7.5 MW to 10 MW wind turbines. The installation of such massive engineering components is dependent on the subsurface conditions. Indeed, the monopile is typically hammered into the seabed using either large impact or vibratory techniques [30]. Guyed monopile towers are another type of support structure where the monopile is stabilised with tensioned guy wires [30]. This technique can be particularly useful in deeper water. Tripods are effective where the deflection of the wind turbine tower has to be restricted and where the seabed preparation is too challenging. The braced lattice frame is a modification of the tripod frame which consists of additional structural components. The stiffness of the jacket structure is provided by a 3 to 4-legged assembly made of steel pipes interconnected with bracing [30]. This version of the wind turbine foundation is of particular interest in deep water (>60 meters). Finally, floating structures that are partially submerged have the benefit of requiring simple installation, maintenance and repair as the structure can be floated to the site and consequently connected/disconnected to anchor piles [30]. Another advantage of the floating installation is that it helps reduce the motion of the system. An example of some of these above mentioned foundation types is given in Figure 2-1.

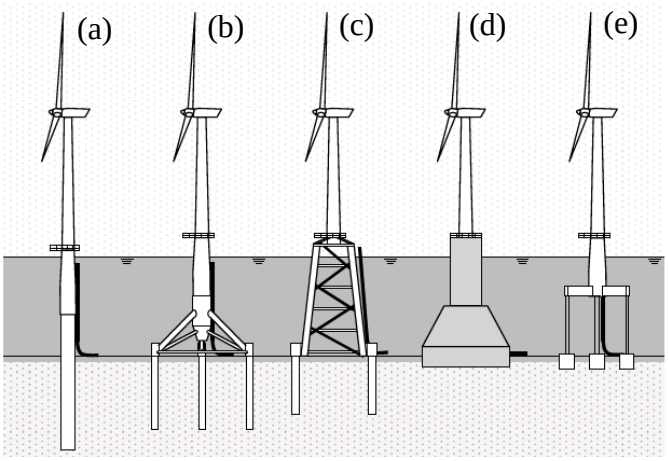

Figure 2-1: Offshore wind turbine foundation types (from left to right: (a) monopile, (b) tripod, (c) jacket, (d) gravity based and (e) floating) [31]

As mentioned in [33] the expected dominant failure mechanisms in offshore wind turbine steel structures are corrosion and fatigue. Therefore, in the offshore wind industry, material selection has a considerable impact on the project cost and performance of the structures. A considerable number of materials such as stainless steel, stainless cast steel, copper and copper alloys and aluminium alloys are being used in the fabrication of offshore wind energy

structures [33] [34]. All these metallic materials are regulated by the standard DNVGL-OS-B101 [35]. This standard provides guidance, technical requirements and production techniques for metallic materials used in the fabrication of offshore wind structures. With respect to the offshore wind turbine monopiles, these are mainly manufactured from steel. Structural steel is often chosen for its high strength to weight ratio as well as its excellent corrosion resistance. S355 structural steel is mostly used in the fabrication of the offshore wind turbine monopiles [36]. The focus of this study is on monopile support structure, hence the material of interest is S355 structural steel as the most commonly used material option in the fabrication of OWT monopile foundations.

An overview of the load analysis is an important consideration in the material selection for OWTs where the structure is subjected to harsh marine environment. The offshore wind turbine must be built to withstand loads originating from tides, waves and wind acting on the support structure as well as the turbine in operation and the interaction with the soil [31]. Indeed the basic function of the foundation is to support the whole structure and keep the wind turbine in operating condition. Indeed foundation dynamics is a key analysis in the design of an offshore wind turbine. The main requirement of an offshore wind turbine foundation is that the fundamental frequency of the structure should lie within a recommended range in order to avoid resonance [37]. While rotating, the blades of the offshore wind turbine travel past the tower creating sensitive vibrations for the foundation [38]. It has been shown in [37] that two significant rotational frequencies must be considered as a design requirement for OWTs. The first corresponds to a single rotation of the entire rotor and the second relates to each turbine blade passing the tower individually [37]. Assuming a three bladed rotor, these two frequencies are often referred to as 1P and 3P, where P is the blade passing frequency. These two frequencies vary with the rotational speed of the turbine which in turn depends on the wind speed. The key requirement in the design of the foundation of the offshore wind turbine is that the natural frequency of the monopile does not lie within the 1P and 3P frequency bands [37]. The blade passing frequency for a typical variable speed turbine is between 0.18 Hz and 0.26 Hz. Moreover, the rotation frequency is between 0.54 Hz and 0.78 Hz. Finally, the cyclic loading from the sea waves typically occurs at frequencies between 0.04 Hz and 0.34 Hz [38]. Therefore, to avoid resonance, the offshore wind turbine should be designed with a natural frequency that is different from the outlined above ranges. The typical range of the 1P and 3P frequency bands is presented in Figure 2-2.

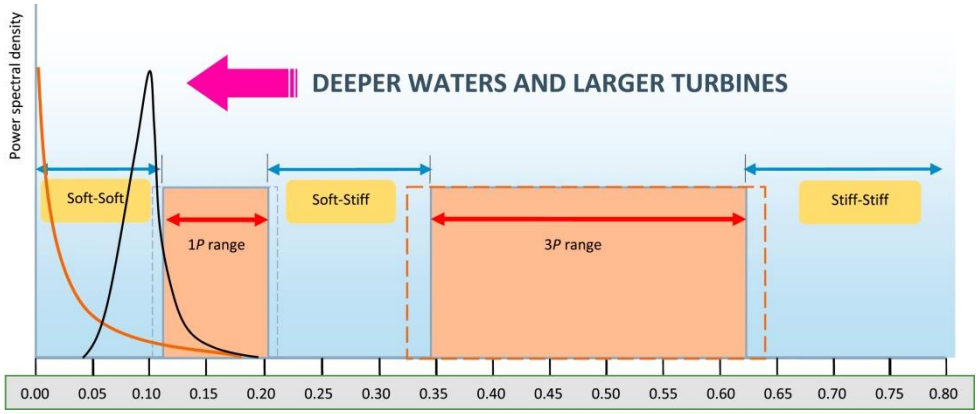

Figure 2-2: Power spectral density vs forcing frequency (Hz) for a three bladed wind turbine [39]

Another important point to consider for the design of an OWT is the dynamic soil-structure interaction as the offshore wind turbines are dynamically sensitive structures. As part of the design of the foundation, soil stiffness estimation is essential to draw an accurate design of the actual operational frequency. In conclusion, soft–stiff range, which is the interval in which the natural frequency lies between 1*P* and 3*P*, is the optimum range for the best possible design [39].

2.2 Material characterisation

In order to select a material for a certain application, the material must first be characterised to determine its mechanical properties. The key mechanical tests which need to be conducted on a new material are tensile tests, chemical composition analysis and hardness tests which are briefly explained below.

2.2.1 Tensile test

Tensile test is a method used to measure the resistance of a material to a force pulling the piece in one direction. The results of a tensile test can be used for material selection for specific applications. Tensile tests are often performed on round bars or dog-bone shape specimens and the tensile properties are measured during the development stage of new materials and processes for comparison purposes. The schematic geometry of a dog-bone shape tensile specimen is shown in Figure 2-3.

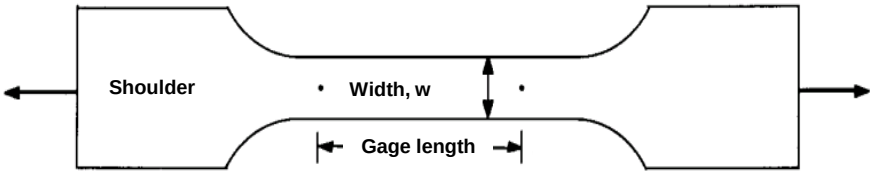

Figure 2-3: Dog-bone shape tensile test specimen [40]

As seen in Figure 2-3 the enlarged ends, or shoulders, are designed for gripping purposes and the deformation of the material is conducted in the gauge region. As the tensile specimen deforms, the cross-sectional area is reduced over the gauge length and failure eventually occurs in the gauge region which has a smaller cross sectional area compared to the gripping ends. Universal testing machines, either electromechanical or hydraulic, can be used to generate the stress-strain tensile curve for a given material. Once a tensile test is completed and the stress σ is plotted against strain ε, the elastic and plastic tensile properties can be identified. In the elastic region, the stress and strain are correlated by the Hooke's law [41][42]:

$$\varepsilon_e = \frac{\sigma}{E} \qquad \text{Equation 2-1}$$

where E is the modulus of elasticity or Young's modulus and ε_e is the elastic strain. In the plastic region, the plastic strain can be correlated with the applied stress using a power-law relationship where N is the power-law exponent and A_p is the power-law coefficient:

$$\varepsilon_p = A_p \sigma^N \qquad \text{Equation 2-2}$$

The key mechanical properties which are specified by performing a tensile tests are 1- the elastic Young's modulus, 2- 0.2% proof stress (which is often taken as the yield stress of the material), 3- the ultimate tensile strength (UTS) and 4- The strain at failure.

2.2.2 Ramberg-Osgood material model

The Ramberg-Osgood model is used to describe the non-linear relationship between stress and strain of materials close to their yield point. This model is based on the fact that the hardening behaviour of the material depends on the material constants. The exponential relationship suggested in [43] is used to describe the plastic strain in a material. The following equations are used to describe the Ramberg-Osgood material model [44]:

$$\varepsilon = \frac{\sigma}{E} + A_p \sigma^N$$ Equation 2-3

in uniaxial form and:

$$\frac{\varepsilon}{\varepsilon_{p0}} = \frac{\sigma}{\sigma_{p0}} + \alpha \left(\frac{\sigma}{\sigma_{p0}} \right)^N$$ Equation 2-4

in non-dimensional form. In the above equations, σ is the applied stress, ε is the corresponding strain, E is the elastic (Young's) modulus of the material, N is the power law plasticity stress exponent, ε_{p0} and σ_{p0} are the normalising strain and stress for plasticity, respectively, and α and A_p are constants which can be related by $A_p = \frac{\alpha \varepsilon_{p0}}{\sigma_{p0}^{\ N}}$. In each of these equations, the first term describes the linear elastic deformation and the second term defines the non-linear plastic deformation of the material [44]. In the Ramberg-Osgood model, the σ_{p0} stress is often taken as 0.2% proof stress, $\sigma_{0.2}$, of the material.

2.2.3 Chemical and microstructural analysis

Surface material characterisation techniques have been employed in this project in order to obtain adequate data to characterise the material used and draw accurate comparisons in the test results analysis. Scanning Electron Microscopy (SEM) with Energy Dispersive X-ray Spectroscopy (EDS or EDX) measurements has been chosen for chemical characterisation. SEM is a test that scans a specimen using an electron beam in order to produce a magnified image for analysis. The surface structure is observed and studied on a microscopic scale [45]. One of the requirements to perform SEM measurements is that the surface needs to be conductive, which can be achieved by spraying the surface with a thin layer of gold [45]. The result of a typical SEM analysis is a magnified image of the sample. Moreover, EDX is useful to identify the element composition of a material. The EDX technique uses the X-ray spectrum emitted by a solid sample illuminated by a focused electron beam, and provides a localised chemical analysis [45] and elemental analysis spectrum [46].

Electron Backscatter Diffraction (EBSD) is another useful technique in the material characterisation phase of the study. EBSD is an SEM based microstructural-crystallographic characterisation technique. This method is commonly used in the study of crystalline or polycrystalline materials. It allows for microstructural analysis in conjunction with the chemical analysis provided by the EDX measurements. Crystallographic orientations, texture

measurements, grain size and boundary type examination and phase analysis can be obtained from EBSD measurements [47]. Grain size is a key characteristic in the understanding of material failure with the mechanical properties of metallic materials linked to the grain size through the Hall-Petch equation as described below [48]

$$\sigma_y = \sigma_0 + Kd^{-1/2} \qquad \text{Equation 2-5}$$

where σ_y is the yield stress of the material, σ_0 is the shear stress required to ensure gliding dislocations, K is a constant dependant on the material, also known as the Hall-Petch parameter, and d is the grain diameter for a polycrystalline material. In a polycrystalline material, the Hall-Petch relationship gives a quantitative representation of a decrease in the yield stress as the grain size increases. This law is based on dislocation mechanisms, and it has been stated in [49] that grain boundaries delay dislocation movements.

2.2.4 Hardness test

Hardness tests are used to determine the resistance of a material to indentation. Hardness is a material characteristic and is determined by measuring the permanent depth of the indentation. This mechanical property depends on the combination of the yield strength, the tensile behaviour and the Young's modulus of the material [50]. The basic principle of any hardness test method is to apply an indenter onto the specimen surface and then measure the dimensions of the indentation. Depending on the force applied and the dimensions of the indenter, the hardness test can be macro, micro or nano [51]. The indentation hardness value is recorded in kilograms-force according to the corresponding hardness scale. Macro-hardness tests, such as Brinell, Rockwell, and Vickers, are the most widely used. Micro-hardness test methods, such as micro-Vickers and Knoop, are used for surface hardness quantification, for coatings or for a multi-phase material. Finally, nano-hardness tests apply small loads of approximately 1 nN.

In this study, micro-hardness or Vickers hardness has been used. This test method is outlined by the ASTM E384 [52]. A 136 degrees square-based diamond pyramid is applied onto the surface of the metal. As discussed in [53], this method is more accurate than the Brinell hardness test method as the indentation is clearer. The load is applied for a maximum of 30 seconds and varies from 1kgf to 120 kgf [53]. The Vickers Pyramid number, HV, is then calculated using the following formula [52][53]:

$$HV = 1.854\frac{F}{D^2}$$ Equation 2-6

where F is the applied load in kg and D is the length of the impression diagonal in mm measured using a microscope part of the Vickers tester.

2.3 Fracture mechanics theory

2.3.1 Historical perspective

The field of fracture mechanics has seen rapid expansion since the Second World War. Most structural failures are generally due to malpractice during design or production although can also occur unexpectedly even for carefully designed and manufactured products. A famous example is the World War II Liberty ship program which was a success before one of the vessels broke in two while sailing Siberia and Alaska as shown in Figure 2-4. This failure occurred as a result of a design change which saw riveted hulls being replaced with welded hulls.

Figure 2-4: The Liberty ship fracture [54]

A milestone marked in fracture mechanics was the establishment of the fundamentals of linear elastic fracture mechanics (LEFM). LEFM is restricted to limited plastic deformations [54]. Significant research work has been performed to account for yielding correction at the crack tip, with the most influential studies performed by Irwin [55], Wells [56] and Rice [57]. In its most basic form, fracture can be classified as ductile, with significant plastic deformation, or brittle, with little or no plastic deformation. Fracture mechanisms are also distinguished as shear fracture, cleavage fracture, fatigue fracture, crazing and de-adhesion [58]. Only fatigue fracture is described and is of interest in this study.

2.3.2 Standard fracture mechanics specimen geometries

Standard fracture mechanics specimen geometries have been well documented and are described in ASTM standards in order to characterise crack initiation and growth for engineering materials. Some of the key specimen designs currently in use include the compact tension (C(T)) specimen, the single-edge-notched bend (SE(B)) geometry, the arc-shaped tension (A(T)) specimen, the disk-shaped compact tension (DC(T)) specimen and the middle tension (M(T)) sample. These geometries are shown in Figure 2-5.

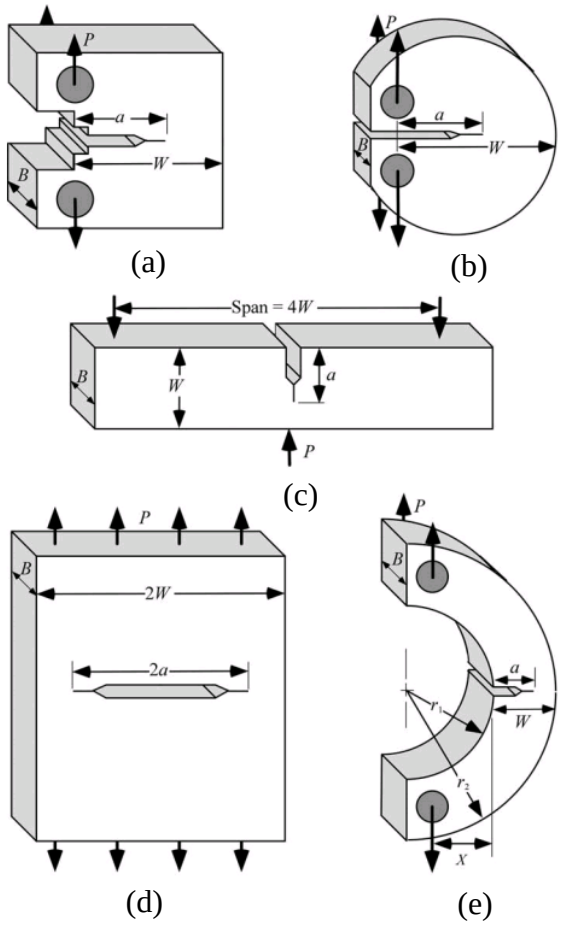

Figure 2-5: Typical fracture mechanics specimen geometries (a) compact tension C(T) specimen, (b) disk shaped compact specimen, (c) single-edge-notched bend SE(B) specimen, (d) middle tension (MT) specimen, and (e) arc-shaped specimen [54]

A vast majority of fracture mechanics tests are performed on C(T) or SE(B) geometries. Specimen size is also standardised and described in the ASTM standards and is generally scaled geometrically using the specific dimensions *B*, *W* and *a* where *B* is the thickness, *W* is the width and *a* is the crack length. In most cases, $W = 2B$ and $\frac{a}{W} = 0.5$ [59]. The specimen orientation is of particular interest and needs to be carefully considered. This is due to the fact that microstructure and therefore mechanical properties are often affected by the material

orientation [54]. This study focuses on C(T) specimen geometry which contains a through-thickness crack and is widely used for performing FCG tests on engineering materials.

2.3.3 Different modes of fracture

There are three different modes of fracture representing the way the force can be applied on the specimen to enable a crack to propagate. They are referred as Mode I, Mode II and Mode III [60] and are described in Figure 2-6. Mode I is the opening mode where the force is applied perpendicular to the crack plane. Mode II is the in-plane shearing mode, referring to the applied shear stress in the in-plane direction and normal to the leading edge of the crack. Mode III is the out-of-plane shearing mode describing the applied shear stress out of plane and parallel to the leading edge of the crack. For a 2 dimensional model, it is important to distinguish between plane stress and plane strain conditions. A material is under plane stress condition if the vector stress is negligible across one direction. The theory is discussed in greater detail in the literature [61].

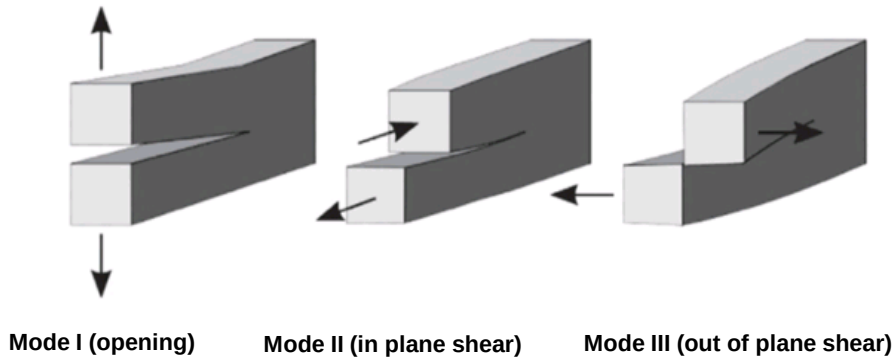

Figure 2-6: Fracture mechanics modes [60]

2.3.4 Linear Elastic Fracture Mechanics

The most important parameters in LEFM analysis are described in this section. The first parameter is the SIF, *K*, proposed by Irwin [62] in 1957. It describes the intensity of elastic crack-tip fields and for an infinite plate subjected to bi-axial stresses this parameter is defined as [54]:

$$K_I = \sigma\sqrt{\pi a} \qquad \text{Equation 2-7}$$

where K_I is the SIF for mode I, σ is the tensile stress applied on the plate and a is half of the entire crack length. Irwin [63] also proposed an energy approach equivalent to the Griffith

model [64]. It involves the energy release rate, *G*, which corresponds to the energy released during a crack increment. Under plane stress conditions, the energy release rate for a wide plate with a centre crack is given by [54]:

$$G = \frac{\pi\sigma^2 a}{E} \qquad \text{Equation 2-8}$$

where a is half of the entire crack length. The SIF and the energy release rate are correlated by the following equation [54]:

$$G = K_I^2/E' \qquad \text{Equation 2-9}$$

where $E' = E$ for plane stress conditions and $E' = E/(1 - v^2)$ for plane strain conditions.

Although LEFM is valid for the cases where the deformation ahead of the crack tip is dominantly elastic, this approach becomes invalid if the plastic zone size ahead of the crack tip, r_p, is significantly large. Some simple corrections are available when moderate yielding occurs but for more extensive yielding, non-linear material behaviour analysis needs to be taken into account. This can be achieved by implementing the elastic-plastic fracture mechanics (EPFM) rules. It is stated in [54] that the plastic zone size ahead of the crack tip must be $<< a$ for the LEFM to be still valid. All the techniques available for r_p calculation are listed in [65]. In order to characterise and estimate the plastic zone size ahead of the crack tip r_p, Irwin [66][55] developed the following equation under plane stress Mode I fracture mechanics loading conditions [59]:

$$r_p = \frac{1}{\pi}\left(\frac{K_I}{\sigma_y}\right)^2 \qquad \text{Equation 2-10}$$

where K_I is the SIF and σ_y is the 0.2% proof stress of the material, which is often taken as the yield stress. The general form of the plastic zone size equation which has expanded on Irwin's model is given as [54]:

$$r_p = \frac{1}{\beta\pi}\left(\frac{N-1}{N+1}\right)\left(\frac{K_I}{\sigma_y}\right)^2 \qquad \text{Equation 2-11}$$

where $\beta = 1$ for plane stress conditions and $\beta = 3$ for plane strain conditions whilst *N* is the Ramberg-Osgood material model constant.

The current study has been entirely undertaken under the LEFM approach and focuses on the fatigue testing of welded joints which is conducted at stress levels far below the yield stress

of the material. Welded joints are characterised by a heterogeneous microstructure and also contain complex residual stress profiles. It has also been demonstrated that most cracks within a welded joint initiate within the HAZ region [5].

2.3.5 Elastic-Plastic Fracture Mechanics

In the presence of large scale plasticity, LEFM cannot accurately characterise the fracture behaviour, and thus an alternative non-linear fracture mechanics approach is used [59]. The EPFM rules are based on the concept of J-integral, proposed by Rice in 1968 [57], to characterise the intensity of elastic-plastic crack-tip fields.

$$J = \int_{\Gamma} (W_d \, dy - T \frac{\partial u}{\partial x} ds) \qquad \text{Equation 2-12}$$

where Γ is a curve surrounding the notch tip, W_d is the strain energy density, T is the traction vector defined to the outward normal along Γ, dy is an infinitely small width of y and ds is an infinitely small width of s with s being the curvilinear abscissa.

Wells [67] suggested an alternative concept for characterisation of elastic-plastic fracture mechanics behaviour of materials in 1963 which is referred to as crack tip opening displacement (CTOD). The CTOD was the first parameter to determine fracture toughness in the elastic-plastic region. In a linear-elastic material deformation situation, $J = G$ [54].

2.4 Fatigue crack growth

2.4.1 Overview

Historically, August Wohler discovered that a single load far below the yield strength of the material would not cause any damage to the structure, however if the same load was applied repeatedly it could lead to fatal failure [68], which became known as fatigue failure. An example of fatigue failure is presented in Figure 2-7.

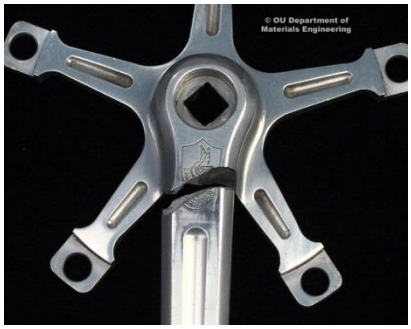

Figure 2-7: Bicycle crank failure (image courtesy of the Open University Department of Materials Engineering) [69]

One of the main applications of LEFM is to characterise the fatigue crack initiation and propagation under cyclic loading conditions by correlating the LEFM parameter, *K*, with the crack growth rate [54]. The fatigue crack growth rate in metals has been analysed by Paris [70][71][72][73] and the correlation with the LEFM parameter is described using the following equation:

$$da/dN = C(\Delta K)^m \qquad \text{Equation 2-13}$$

where *da/dN* is the fatigue crack growth per cycle (also known as FCG rate), *ΔK* is the SIF range, and *C* and *m* are material constants.

A typical fatigue crack growth curve is presented in Figure 2-8. As seen in this figure three main regions are generally observed in the FCG behaviour of a given material; threshold region where the crack starts to propagate, intermediate Paris region where there is a power-law correlation between the FCG rate and *ΔK* described by Equation 2-13, and acceleration region.

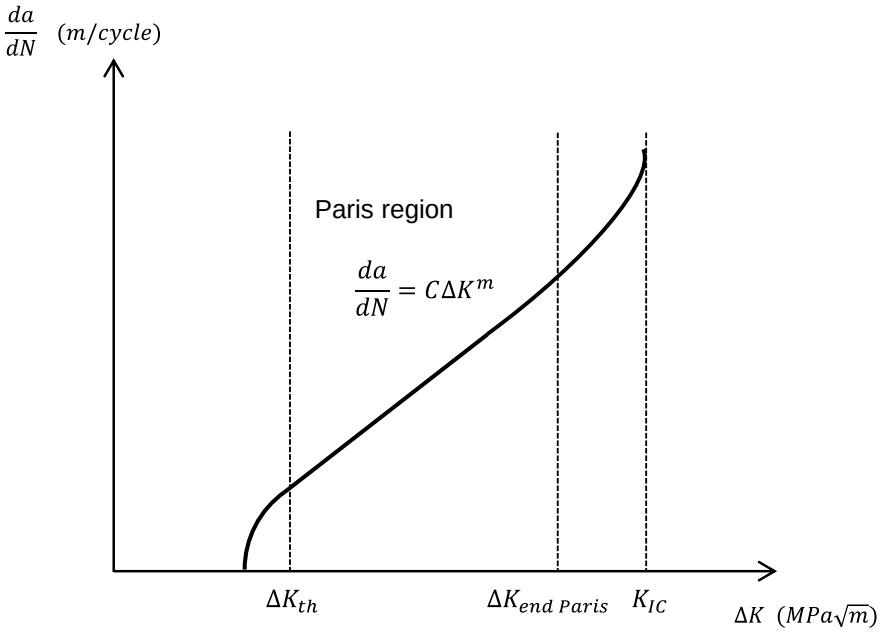

Figure 2-8: Typical fatigue crack growth curve

The SIF *K*, which depends on the stress distribution ahead of the crack tip, can be written as [68]:

$$K = YS\sqrt{\pi a} \qquad \text{Equation 2-14}$$

where the loading stress $S = \frac{P}{WB}$ for a C(T) specimen, a is the crack length, and Y is a dimensionless factor which depends on the cracked geometry. The [74] suggests that the SIF range for a C(T) specimen can be calculated using:

$$\Delta K = \frac{\Delta P}{B\sqrt{W}} \frac{(2+\alpha)}{(1-\alpha)^{\frac{3}{2}}} (0.886 + 4.64\alpha - 13.32\alpha^2 + 14.72\alpha^3 - 5.6\alpha^4) \qquad \text{Equation 2-15}$$

where ΔP is the load range, B is the specimen thickness, W is the width of the sample and $\alpha = a/W$. According to ASTM E647 standard this equations is valid for $a/W \geq 0.2$, however it has been shown in [5] that this equation encounters noticeable errors for $0.2 \leq a/W \leq 0.45$. An alternative equation that has been proposed in [5] for $0.2 \leq a/W \leq 0.7$ and has been used in this study is:

$$\Delta K = \left(\frac{\Delta P\sqrt{a}}{BW}\right)(-372.12\alpha^6 + 1628.60\alpha^5 - 2107.46\alpha^4 + 1304.65\alpha^3 - 391.20\alpha^2 + 54.81\alpha + 7.57) \qquad \text{Equation 2-16}$$

Fatigue occurs at low stress levels without any macro scale plastic deformation. The fatigue life of a structure under constant amplitude loading conditions occurs over different phases. The crack initiation stage, described by the stress concentration factor, is characterised by crack nucleation and micro crack growth. At this initiation stage, fatigue is a material surface damage phenomenon. This period is followed by the actual crack growth, described by the SIF and characterised by macro crack growth. The fatigue process ends at the final failure described by the fracture toughness of the material [68].

The elastic and plastic behaviour of a material depends on its crystal structure (i.e. Face Centered Cubic (FCC), Body Centered Cubic (BCC), or Hexagonal Close Packed (HCP) [68]). One of the microscopic characteristics of fatigue cracks in most of the materials is that they follow a transgranular path (i.e. propagating through the grains) and they do not follow the grain boundaries. At a macroscopic scale, the growth bands can be observed, where the growing direction is perpendicular to the principal stress direction, followed until the final failure stage occurs [68].

2.4.2 Fatigue parameters

In the following section, the main fatigue parameters for characterising the FCG behaviour of engineering materials have been described. The R-ratio is an important parameter as it has a significant effect on the crack growth rate. In a fatigue test the stress ratio is defined as [68]

$$R = \frac{\sigma_{min}}{\sigma_{max}} \qquad \text{Equation 2-17}$$

where σ_{min} and σ_{max} are the minimum and maximum stress levels applied in a fatigue cycle, respectively. It has been shown in [75][76] that for the same value of SIF range, the crack growth increases as the stress ratio increases and therefore the fatigue life is shorter. It has also been shown that the fatigue threshold decreases linearly when the stress ratio increases [77]. The Walker's model has been developed to account for the effect of stress ratio on the FCG behaviour of the material [76]. Indeed, the major limitation of the Paris law is its inability to account for the stress ratio. This drawback studied by Walker in 1970 lead to an improvement of the Paris model by including the effect of stress ratio. Walker proposed a new equation [78]

$$\frac{da}{dN} = C_W[\frac{\Delta K}{(1-R)^{1-\gamma_W}}]^{m_W} \qquad \text{Equation 2-18}$$

The mean stress is another parameter which has an effect on the fatigue life of the material. This has been studied in [79] and it has been concluded that an increase in mean stress reduces the life of the component. The main parameters of the load cycle are presented in Figure 2-9.

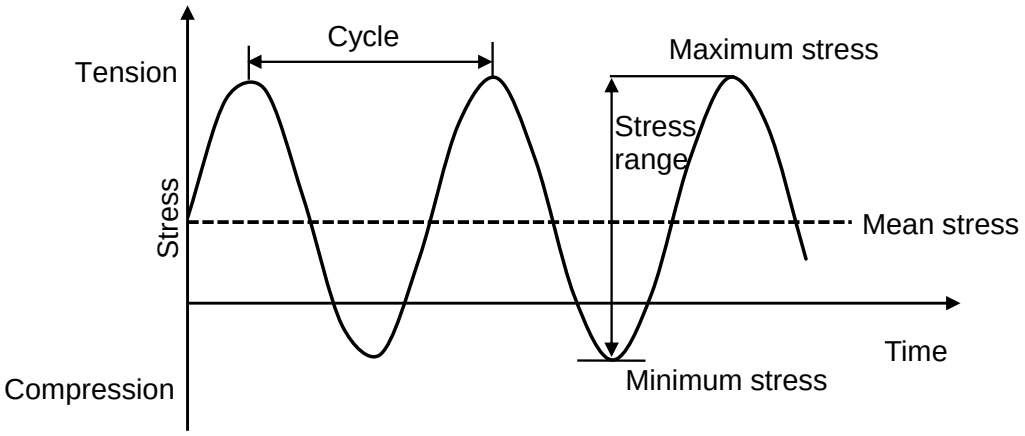

Figure 2-9: Characteristic parameters of load cycle in fatigue

At low ΔK values (generally below 10^{4} mm/cycle), crack growth rates increase with increasing thickness. At high ΔK values (generally above 10^{4} mm/cycle), the effect of thickness is less pronounced (except for negative stress ratio) [80]. Moreover, it is mentioned in [81] that in the threshold region of the FCG the SIF range to initiate the crack increases when the yield strength increases. It must be noted that the ΔK_{th} value is dependent on material properties, stress ratio, variable amplitude loading, residual stress profile, test environment, crack dimensions and specimen geometry [82].

One of the main fatigue crack growth criteria is that the crack follows the direction of the maximum stress, which needs to be taken into account in mixed mode conditions, and is sensitive to the grain size, as well as the microstructure. The Erdogan and Sih criterion is one of the most commonly used for in-plane mixed mode problems. According to this criterion, crack propagates from the crack tip radially at a direction which contains the maximum tangential stress. If this tangential stress exceeds a critical value or an equivalent stress intensity factor reaches the fracture toughness value of the material, crack propagation becomes unstable, and fracture occurs [83]. Another criterion developed for mixed mode-I/II problems is the Richard criterion. The equivalent SIF and crack deflection angle can be calculated. Pook also developed an in-plane mixed mode criterion and proposed

an equation from which the equivalent SIF can be obtained using mode-I and mode-II SIFs [83].

2.4.3 Crack closure

In 1970, Elber [84] discovered the phenomenon of crack closure. He observed and confirmed that a contact between the fracture surfaces could take place even during cyclic tensile loading. Crack closure is a phenomenon in fatigue loading, during which the crack remains in a closed position even though some external tensile force acts on the material until the applied force reaches a critical value. Crack closure can arise from many sources including plastic deformation or phase transformation during crack propagation. This effect would decrease the fatigue crack growth rate by reducing the effective SIF range [54]. When a specimen is cyclically loaded between K_{max} and K_{min}, the portion of the cycle below K_{op}, stress intensity at which the crack opens, does not contribute to crack propagation. Elber therefore defined an effective SIF range, ΔK_{eff}, as follows [84]

$$\Delta K_{eff} \equiv K_{max} - K_{op} \qquad \text{Equation 2-19}$$

Elber also suggested a modified Paris-Erdogan equation [84]:

$$\frac{da}{dN} = C\Delta K_{eff}^{m} \qquad \text{Equation 2-20}$$

Five mechanisms of fatigue crack closure have been identified in [85][86] as:

- Plasticity induced closure
- Roughness induced closure (under Mode II displacement)
- Oxide-induced closure (corrosion product)
- Closure induced by a viscous fluid
- Transformation induced closure

It has been demonstrated that crack closure depends on both the stress ratio R and the maximum SIF K_{max} [87]. The effect of crack closure on the fatigue behaviour of a steel material has been further studied in [88]. Crack closure is commonly measured using the compliance technique [85][86][89].

2.4.4 Fatigue threshold

The fatigue threshold, ΔK_{th}, is defined as the point below which a fatigue crack is not growing which has been observed in some materials such as mild steel, low strength alloy.

This phenomenon is also referred to as the fatigue limit of the material [58]. The fatigue threshold is a material property but also a function of loading variables such as R ratio [54]. It has been shown in [90] that the microstructure and the environment are the two main parameters which still have a significant influence on near-threshold fatigue crack growth even after crack closure correction. The growth behaviour of fatigue cracks near the threshold is also known to be dependent on the crack length [89]. The fatigue crack growth threshold is commonly measured using the ΔK_I-decreasing method as suggested in [91].

2.4.5 Experimental considerations

The C(T) specimen geometry is generally employed in FCG testing. M(T) and CCT (Centered Cracked Tension) specimens can also be used, however C(T) specimens are smaller, and therefore require less material, and a relatively low load is sufficient to apply a relatively high *K*-value. This can be convenient if the load capacity of the testing machine is limited [68]. During FCG experiments, two different ranges need to be considered. The high cycle range is characterised by low stresses and thus long fatigue life with a number of cycles greater than 50,000. The low stresses applied involve a small plastic zone size ahead of the crack tip and therefore the concept of LEFM is valid. The high cycle tests are known to be sensitive to the residual stress profile in the specimen. The low cycle range is characterised by high stresses, and thus short fatigue life, and therefore EPFM needs to be applied [58]. Low cycle tests include fatigue at stresses above the general yield point and involve less than 10,000 cycles to failure [92]. Residual stresses are known to have negligible impact on the low cycle fatigue tests. FCG tests are usually started with a single sharp notch [68] and specimen dimensions are given in the ASTM E647 [74]. Periodic observations of the crack tip location are made to record the crack growth which can be performed by using magnifying glass, travelling microscope and even cameras [68]. Fatigue crack growth can also be monitored using strain gauges. Back face strain measurements are studied and presented in [93][94][95] where this technique has been found to be particularly useful for FCG testing in seawater environment where direct access to the sample is impossible and optical crack growth monitoring techniques cannot be easily applied. The simplest representation of the results of such FCG tests is a calibration graph of the crack length versus the back face strain values.

As an inherent characteristic of structures, scatter is also part of the fatigue properties of the materials. It has been demonstrated in [68] that sources of scatter are expected to be different between the crack initiation period and the crack propagation section. This is due to the fact

that the crack initiation is dependent on the material surface whereas the crack propagation period depends on the material bulk properties. Various publications [96] have shown that the scatter of FCG of visible cracks is generally low. In order to minimise scatter, all the specimens should be manufactured in exactly the same way. Finally, the fracture surface should also be analysed in order to identify crack front shapes. Fatigue pre-cracking is also suggested in the ASTM E647 [74]. The importance of this step in the test procedure is to provide a sharpened crack tip in order to remove the machining effect. In this way, the effect of potential changing crack front shape is eliminated.

The criteria presented in the work [97] are based on the factors affecting the fatigue crack growth during testing, namely stress, crack-tip displacement, or energy dissipation. In the case of mixed-mode cracking, special attention should be paid to the energy approach (application of the J-integral and strain energy density), which seems to be very promising for elastoplastic materials. Under mixed-mode cracking, two things should be taken into account: the rate and direction of FCG.

2.4.6 Application to welded joints

Welding is a joining technology that helps to produce many engineering components and structures which cannot be fabricated by other manufacturing techniques. However, welding as a manufacturing procedure involves various problems. Different welding techniques are available, including arc welding, gas welding, electron beam welding, and laser welding [68].

The fracture properties of weldments are of particular interest due to their diverse applications. As mentioned in [54], the main property of welded joints is their heterogeneous microstructure and irregular shapes. Weldments also contain complex residual stress profiles. The residual stress distributions also make fatigue pre-cracking more difficult. The specimen design and manufacture needs to be carefully considered in order to achieve notch location and orientation in the correct region.

Welded joints are also known to have a number of weld defects, creating more challenges for mechanical testing and inspection. Scatter is expected in the fatigue properties of welded joints due to the variety of imperfections, and regions with higher stress concentration particularly around the weld toes. Some post-welding treatments can improve the fatigue strength of the component, such as grinding the weld toes, to remove stress risers, or post-weld heat treatments, to relax welding residual stresses [68]. When evaluating the fatigue life of welded components the mean stress needs to be carefully considered and included in the

analysis. As the yield strength varies locally in the WM, HAZ and BM, the FCG initiation may exhibit some variations in a welded joint [81]. In order to avoid fatigue failure in welded joints, it is recommended in [81] to use appropriate design codes and also to conduct periodic inspections.

2.5 Corrosion and corrosion-fatigue mechanisms

Offshore structures operate in an extreme corrosive environment, and therefore the risk of corrosion attached at the micro and macro level must be considered, particularly around the welded joints. The corrosion rate associated with welds is often higher for the WM than for the BM which is due to the microstructure effect and the residual stress [81]. A distinction must be made between corrosion without mechanical load and corrosion with mechanical load [34]. The details of various types of corrosion are described in [98]. Without mechanical loads, corrosion damage can appear in the form of general or uniform corrosion, crevice corrosion, pitting corrosion, deposition corrosion, selective corrosion (inter-/transgranular) or microbiologically influenced corrosion. With mechanical loads, corrosion can be stress corrosion cracking, corrosion-fatigue interaction, strain-induced corrosion, erosion corrosion, cavitation erosion or fretting corrosion. The damage resulting from corrosion can be prevented by coatings or cathodic protection, depending on the type of corrosion.

It has been demonstrated in [68] that when corrosion-fatigue interaction occurs in a welded geometry, salt water corrosion promotes the crack initiation and subsequent crack growth at very low stress amplitudes. Aggressive environments affect both the crack initiation stage as well as the crack growth stage. Having known that corrosion is a time dependent phenomenon, the operational frequency plays a significant role in the remaining life of welded structures subjected to corrosion-fatigue loading conditions [68]. Corrosion tests, developed over the years, combine atmospheric corrosion tests as well as immersion tests and electrochemical tests [81]. Immersion tests involve gaseous environment or liquid environment. The most well-known environment used in corrosion-fatigue test programs is salt water [68]. It has been shown in [99] that in a corrosive environment the large reduction of fatigue life of the material was obvious compared to the air condition. At the material surface, corrosion promotes crack nucleation to create the first micro cracks and subsequent FCG is assisted by corrosion. This process occurs at stress amplitudes far below the original fatigue limit [68].

As mentioned before, the load frequency significantly affects corrosion-fatigue tests as corrosion is a time dependent mechanism [68]. Corrosion-fatigue is a complex phenomenon and there are a large number of variables involved. In-situ observations are also compromised by the environment itself. The initial impact of the corrosive environment starts from the damage of the surface by dissolution of the material [68]. In an air environment, load frequency and wave shape do not have a significant influence on the fatigue behaviour of the material whereas in salt water, a strong frequency effect is expected under sinusoidal load cycles [100]. The trends observed by Gangloff [101] demonstrated a higher fatigue crack growth rate for the tests conducted in seawater for the same value of SIF range, compared to the air results. The salt water temperature also influences the FCG rate of the material, where it has been found that the corrosion mechanism is enhanced by an increased temperature [102].

In this study corrosion protection has not been considered and instead the seawater tests are performed in free-corrosion condition. This decision was made to provide a conservative estimate of the fatigue life of monopiles without considering the cathodic protection effects on the fatigue life of offshore structures.

2.6 Residual stresses and their influence on fatigue crack growth

Residual stresses play a major role in fatigue crack initiation and propagation behaviour of engineering materials [103]. These locked-in stresses are challenging to predict or measure and they are originally present in a stationary structure without being subjected to any external forces. Residual stresses can be introduced during fabrication or assembly or caused by heat and surface treatment [92]. The formation of residual stresses in engineering structures and their subsequent effects on the fatigue life of structures are described below.

2.6.1 Formation of residual stresses

Residual stresses are produced in metals by most manufacturing processes. Such processes induce plastic deformations through significant temperature gradients or mechanical forces, resulting in locked-in residual stresses [104]. In order to better understand and accurately assess the remaining lifetime of engineering structures, residual stresses need to be at the heart of the discussion. In this research project, a great level of attention is given to residual stresses originating from welding during the fabrication of offshore wind turbine monopiles. Welding is a very common manufacturing process that is used to join materials together to

form assemblies and systems. In many cases the welded joints are large, have reduced material properties (e.g., stress corrosion cracking resistance, fracture toughness), and contain defects [81]. The welded joints tend to be critical locations in terms of design and sustainment. For this reason, residual stress in welding is a primary concern and are the result of thermal expansion as materials expand or contract with temperature. The residual stress measurement techniques are described in the next section.

2.6.2 Residual stress effects on fatigue and effective stress intensity factor

It is well known that the residual stress effects would be predominantly demonstrated in the early fatigue life of the material. This is due to the fact that as the crack advances the RS begin to relax. Moreover, tensile RS will be detrimental, due to an increase in the mean stress, while compressive RS will have a positive effect on the fatigue life of the material as they will lead to crack closure. It has also been demonstrated that welding residual stresses are locally redistributed as a crack propagates and this may have an influence on the crack shape development and the crack path [105]. Further studies have shown that although some reduction and redistribution in RS will occur when laboratory scale specimens are extracted from the welded plates [106][107], the remaining RS field influences the FCG behaviour of the material, particularly in the near threshold region [108].

It has been demonstrated by many researchers that welding residual stresses notably influence the FCG behaviour of engineering materials. For example Lawrence et al. [17] have developed an analytical model to predict the influence of residual stress and stress ratio on the fatigue life of a welded component. The main drawback of their model is that it is limited to crack initiation, and cannot account for welding residual stress effects on crack propagation behaviour of the material [17]. The effects of compressive and tensile residual stresses on Mode I fatigue crack growth are discussed in [16] where residual stresses were introduced into the test specimens through shot peening. It has been demonstrated in references [16][18] that locked-in residual stresses alter the mean stress and also stress ratio under cyclic loading conditions and subsequently influence fatigue behaviour. Residual stresses particularly have more pronounced effects in the near threshold region during FCG process and as the crack advances residual stresses redistribute and eventually vanish towards the end of the fatigue test [16][17][18].

It has been demonstrated in the literature that the applied stress ratio ($R<0.67$) had little influence on the fatigue strength of as-welded joints containing high tensile residual stresses

[109]. If there is a pre-existing RS field behind the notch tip or if RS develop in service, subsequent service loads may alter the RS distribution before a crack begins to initiate [16]. The RS effect on fatigue of welded components is studied in [110] as a mean stress correlation and using the Palmgren-Miner rule of cumulative damage. Also, the local stress ratio R_{eff} will continually change as the crack propagates through the superimposed residual stress field for a constant R-ratio, and hence will cause a mean stress alteration at the crack tip.

In order to accurately predict the crack growth rate under LEFM conditions, it is required to calculate the effective SIF and therefore assess the RS effect on the fatigue life of components [111]. The weight function and associated superposition techniques are described by the RS effects considered in the FCG behaviour of the material [111]. The weight function method is commonly used for SIF calculations. The SIF can be obtained by integrating any stress field and the appropriate weight function, where the latter is related only geometrically and is simple to calculate [112]. Weight functions are first order tensors that depend only on the geometry of the cracked body and can be interpreted as the stress intensity resulting from a unit force applied to the crack face. This concept is not restricted to 2-Dimensional (2D) bodies, Mode I loading, or isotropic elastic materials [54] and Rice [113] showed that this concept can be extended to 3-Dimentional bodies (3D) as well. Various kinds of weight functions have been applied in the literature to determine the intensity of the crack tip elastic field for cracks introduced into the residual stress field [114].

2.7 Residual stress measurement techniques

2.7.1 Characterization techniques for polycrystalline materials

Evaluation of RS is of fundamental interest for the characterisation of the fatigue behaviour of engineering components and materials. RS measurement techniques can be destructive, semi-destructive and non-destructive. The most important ones are listed below:

- Ultrasonic (acoustic)
- Electromagnetic
- Neutron diffraction
- X-ray diffraction
- Chemical etchant
- Indentation

- Hole drilling

Most of these techniques have been reviewed in an EPRI report [104] and have been discussed in terms of reliability and cost. It was concluded in this report that hole drilling and X-ray diffraction were the most reliable and inexpensive techniques. It is however, worth noting that those two techniques, as mentioned above, are restricted to surface measurements. The techniques listed above are gathered in Figure 2-10, where the penetration depth is plotted against the spatial resolution.

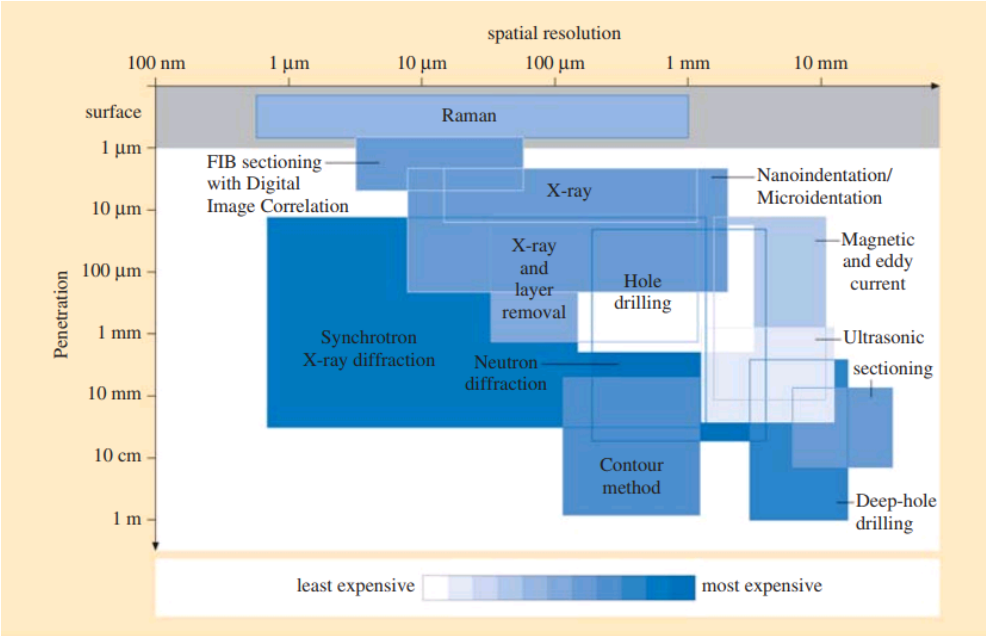

Figure 2-10: Penetration depth vs. spatial resolution for various residual stress measurement methods [115]

A vast majority of materials used for structural purposes and in engineering applications are polycrystalline metallic alloys. The global mechanical properties of these materials largely depend on their microstructure and they often exhibit anisotropic elastic and plastic properties, such as the Young's modulus which varies largely depending on the crystallographic orientation [116]. The current study focuses on neutron diffraction and neutron imaging non-destructive techniques as well as the destructive contour method as described in the following sections. Those techniques have been chosen as they provide a good ratio of penetration depth over spatial resolution giving therefore more accurate results and allowing measurements at the mid-thickness of the samples. The special advantage of the neutron diffraction technique is that it provides excellent penetration depth and a relatively high spatial resolution by providing non-destructively the three directions of strains required to calculate the residual stresses.

2.7.2 Principles of measuring residual stresses using neutron diffraction technique

The production of neutrons is a complex and expensive process. Two main methods are used to generate neutrons with the highest possible flux and the most suitable energy range for the intended applications: fission (in research reactors) and spallation (in accelerator driven spallation neutron sources) [117]. In a spallation source, protons dislodge one or two nucleons with high energy through direct impact. This energy is then released from the nucleus by evaporating up to 10 spallated neutrons [118]. Different experimental techniques using neutrons are being employed for materials science and engineering studies among which are neutron activation, based on the capture of neutrons for element analysis, and neutron imaging, related to capture and scattering of neutrons to provide information on the inner structure of a component [117]. The ND technique can be applied on components from 0.1m to 1.5m thick [119]. Such capabilities ensure accurate measurements without the need of sectioning or removing layers.

While X-rays and electrons interact with the electrons of an atom, neutrons interact with the nucleus and hence neutron radiation provides the ability to penetrate deeper into most structural materials. Neutrons have no charge, and their electric dipole moment is either zero or too small to be measured by the most sensitive of modern techniques. For these reasons, neutrons can penetrate matter far better than charged particles. Furthermore, neutrons interact with atoms via nuclear rather than electrical forces, and nuclear forces are very short range (of the order of a few femtometers). Thus, solid matter is not very dense because the size of a scattering centre (nucleus) is typically 100,000 times smaller than the distance between such centres. As a consequence, neutrons can travel large distances through most materials without being scattered or absorbed [120]. When scattering occurs from an ordered crystalline material, it produces coherent Bragg scattering and yields either the intensity of the various hkl reflections from a single crystal or the powder diffraction pattern [121].

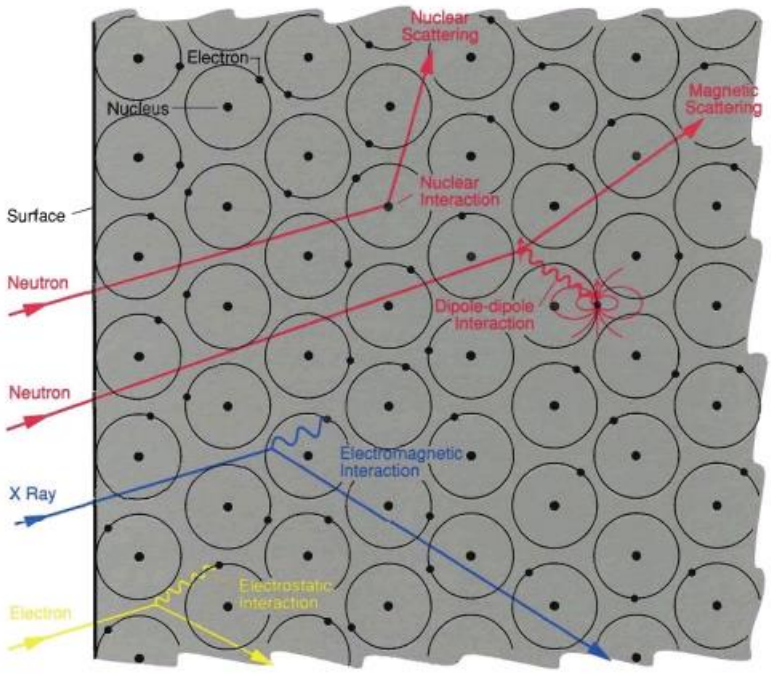

Figure 2-11: Scattering interactions of neutron, X-Ray and electron [120]

The high angle (i.e. high resolution) information means that the data can give very precise values for the atomic positions in the structure. The resolution can be improved by better defining the angular distribution of the beam. This is done with the help of collimators, which are arrays of absorbing neutron channels, which allow defining independently the divergence of the incoming and scattered beam. For a given divergence, the best resolution, which is the narrowest wavelength band, is obtained at 2θ = 180◦, in backscattering geometry [122].

The basic concepts of diffraction were formulated by Bragg in 1913 [123][124], describing the relationship between the wavelength of radiation, λ, the distance between the atomic lattice planes in a crystal, d_{hkl}, and the scattering angle, $2\theta_{hkl}$, where *hkl* are the Miller indices that specify the planes of the atomic lattice:

$$\lambda = 2d_{hkl} \sin \theta_{hkl} \qquad \text{Equation 2-21}$$

The parameters used in ND measurements using Bragg's law are illustrated in Figure 2-12, where the radiation interacts directly with the nucleus of the atom.

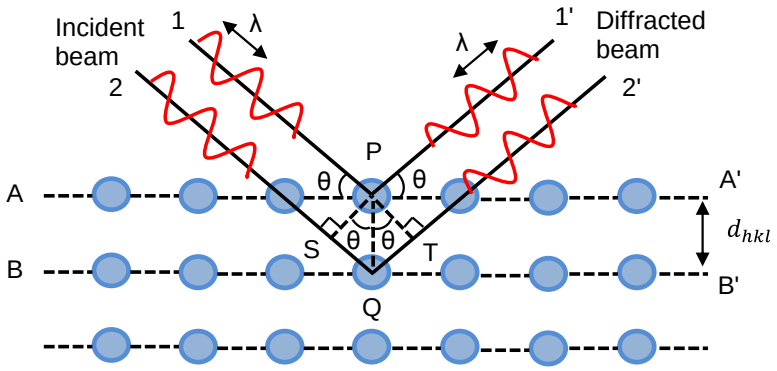

Figure 2-12: Radiation diffraction within a crystal structure

ND data analysis calculations are different depending on the neutron source. A reactor source uses a continuous monochromatic neutron beam and therefore λ is kept constant while θ_{hkl} is measured. A spallation source, such as the Rutherford Appleton Laboratory, is based on a pulsed polychromatic neutron beam where θ_{hkl} is a constant parameter while λ is measured and therefore d_{hkl} is calculated using Equation 2-21. Moreover, α-Fe materials, such as the S355 structural steel used in this study, have a BCC crystal structure, therefore the lattice parameters *a*, *b* and *c*, which are the physical dimensions of unit cells in a crystal lattice, in x, y and z directions respectively, are equal in ND data analysis. Thus after compiling the data, any of *a*, *b* or *c* values can be used to calculate d-spacing taking into account the corresponding error bars. The error bars plotted for the neutron measurements of stress represent the uncertainty of fitting a function to the peak shape and background of the diffracted data, and do not include other potential sources of error such as variations in the elastic modulus [125]. Plasticity induced errors, when the residual stresses approach yield, are also likely to affect the results [126]. Finally, determining accurate stress-free lattice parameters is crucial in neutron diffraction strain measurements as a small change can result in significant errors in the measured residual stress distribution [125].

The ISIS facility at the Rutherford Appleton Laboratory is a neutron source for time-of-flight (TOF) diffraction. ENGIN-X has been designed with the sole aim of making engineering strain measurements, essentially the accurate measurement of polycrystalline material lattice parameters, at a precisely determined location in an object. This approach has allowed considerable performance improvements to be made compared to previous instrumentation. Traditionally, neutron diffractometers have been built as "all-purpose" instruments, the ENGIN-X positioning table is capable of holding a sample weighing up to 1.5 tons and can move the sample in x, y, z, and θ axes [127]. The gauge volume has its most compact section

at a scattering angle of 90° with a tuneable resolution and interchangeable radial collimators [119]. The set-up of ND experiments for RS measurement is detailed in the ISO/TS 21432 [128] technical specification. Precision of the ND measurements is estimated using statistical analysis. The standard error for each component of the strain tensor is between $\pm(0.7\ to 1.4) \times 10^{-4}$ and, assuming that $E = 200\ GPa$ and $\nu = 0.3$, appropriate for ferritic materials, the precision of stress is then between $\pm\ (20\ to\ 40) MPa$ [119].

The calibration of the Engin-X instrument, prior to any actual measurements, is performed through vanadium, V, and ceria, CeO_2 scanning. Vanadium has practically no diffraction peaks and scatters isotropically. This is to ensure that the scattered intensity is identical on each neutron detector [119]. A reference sample is also measured to ensure accuracy of the results. The reference specimens contain near zero macroscopic stress. Ceria sample, CeO_2, is also measured as it is considered to be a good approximation to the instrument resolution [118]. Another factor to consider within the calibration stage of the experimental process is the selection of the gauge volume. The factors that must be considered when selecting an appropriate gauge volume are that, on the one hand, a large volume will maximise the data acquisition rate, but on the other, restricting gauge volume in certain directions will maximise spatial resolution [92]. Gauge volume is then set up through a slit system defining the size and shape of the incoming and diffracted beam [118].

Open Genie and General Structure Analysis System (GSAS) software are used for the data analysis of ND measurements. Neutron diffraction data analysis is based on Bragg Peak profile. Typical diffraction peaks are represented in a TOF diffraction spectrum, "Intensity vs Neutron Wavelength", at pulsed neutron sources. The data analysis is based on the Rietveld method [129] which averages the results over all the measured $\{hkl\}$. The Rietveld refinement technique for powder-diffraction data is in essence a multi-parameter curve fitting procedure [129]. This provides lattice parameters over the range of selected peaks.

As an industrial example of the application of the ND technique, a thick ferritic welded plate has been measured in [130] and the results have been discussed in terms of set-up tuning. The study also confirms that significant enhancement of the deep penetration capability of neutrons is available for the determination of residual stresses in an extra thick steel specimen.

2.7.3 Neutron imaging for strain analysis

2.7.3.1 Neutron imaging procedure

Neutron Imaging, NI, began with the photographic detection of neutrons in 1938 by Kallmann et al [131]. Neutron radiography has been used in a wide variety of applications ranging from inspection of aircraft engine turbine blades to the study of fluid flow in membrane fuel cells [132]. Only recently, NI evolved to more complicated contract mechanisms while many of the techniques are still under development. These include for example polarized neutron imaging [133], Bragg edge imaging [134], and neutron resonance absorption imaging [135].

The NI science can be divided into two sub-categories. The first one is radiography of the sample, giving a 2D representation, and the second one is the tomography technique, more complex process resulting in a 3D representation of the sample. Neutron imaging measurements are based on MicroChannel Plate (MCP) detector technology [136]. MCP detectors are high spatial and temporal resolution event counting devices consisting of multiple independently operating readout channels. They allow detection of multiple simultaneous events or detection of particles at high counting rates. More than 104 simultaneous events can be detected with a spatial resolution of approximately 55μm (pixel size). MCPs are of great interest in TOF applications with pulsed neutron sources where overlapping of signals and detection of multiple events arriving in bursts is a challenge. They are also capable of different modes of operation (high spatial resolution, high counting rate or event timing).

When a polychromatic beam passes through a sample, which may be characterised by various total macroscopic cross sections, the transmission of neutrons through matter follows the exponential Lambert's law [137]:

$$I(t) = I(0)e^{-\Sigma t} \qquad \text{Equation 2-22}$$

where Σ is the macroscopic cross section per unit volume and t is the total path length through the material.

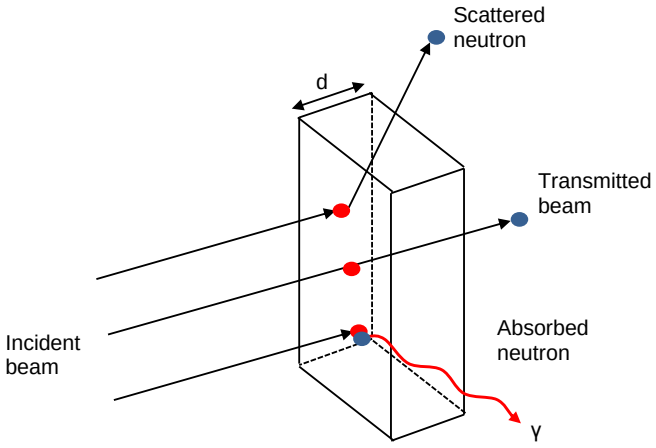

Figure 2-13: Neutron scattering principles

The neutron scattering principles are presented in Figure 2-13. When a polychromatic neutron beam passes through a crystalline material, neutrons of various energies are attenuated differently. As a result, the energy spectrum of the neutron beam changes with a sample in the beam. A careful analysis of the intensity ratio between the transmitted and incident beams can provide valuable information about the crystalline structure and microstructure of the sample [138]. Information related to the crystal structure of crystalline materials (strain, phase, texture) is traditionally obtained using (X-ray or neutron) diffractometers. In a diffractometer where a fixed wavelength is used, the diffraction angle is determined. If a wavelength spectrum is available (typically at neutron spallation sources), a wavelength-dependent intensity spectrum is recorded under some fixed angle to the direction of the incident neutron beam. The detected intensity maxima (so-called Bragg peaks) are accordingly plotted as a function of diffraction angle or wavelength. Due to the Bragg scattering effect, the same information can be obtained by recording the transmitted neutron beam through the sample. Some neutrons travel without interaction through the sample, some are absorbed, while those that are scattered out of the direction of the incident beam (which would be detected in a diffractometer), leave a characteristic pattern in the incident intensity spectrum, so-called Bragg edges. Hence, spatial information in two dimensions can be obtained if an imaging detector is used [139]. A review of the current engineering applications using NI is suggested in [140]. The authors also present the NI technique itself and a general experimental layout is shown on Figure 2-14.

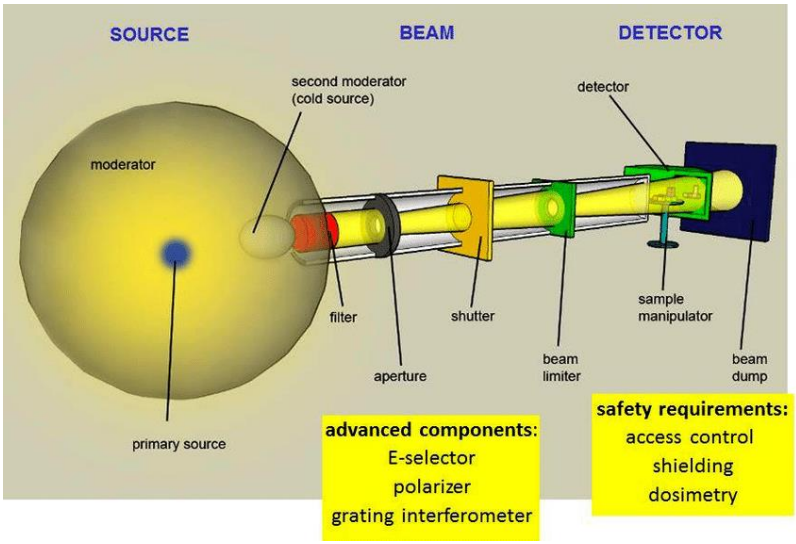

Figure 2-14: Schematic layout of a generic NI facility [140]

Neutron imaging data analysis is based on the Bragg Edge profile. It should also be noted that Bragg edge imaging is an energy selective method, and is sometimes referred to as energy-dispersive imaging or strain-radiography (when strains are being measured). In practice, there can often be a combination of edge shift and height change, averaged over the crystallites within the gauge volume, leading to significant broadening and distortion of the sharp Bragg Edges. Two samples of the same material can therefore have quite different transmission spectra [141].

The main components for a neutron imaging instruments are: the source, the collimation (or flight path) and the detector. The current state of neutron imaging detectors is presented in [142]. Performing Bragg edge transmission imaging with a detector positioned behind the sample, requires the possibility to record the transmitted neutron intensity as a function of wavelength [139]. Errors in NI measurements are mainly due to spatial and temporal variations in the incident beam intensity as well as some inhomogeneities in the scintillator and detector [139].

2.7.3.2 Residual stress analysis by Bragg Edge imaging

Neutron imaging measurements presented in the current study are performed on IMAT instrument at ISIS-STFC, Rutherford Appleton Laboratory. The IMAT instrument uses the MCP detector technology. Despite the major advancements for transmission at spallation sources, one major drawback so far is the lack of suitable detectors, which provide both spatial and time resolution [139]. This problem is being overcome by technologies under development such as the MCP detectors.

NI data processing and analysis is also another concern. The study performed in [143] provides evaluation tools for the analysis of NI data collected during the experiments. One of the most frequently used image processing tools for neutron imaging data is ImageJ. In terms of industrial purposes, NI is very popular and has many applications in diverse fields, such as biology, geology, archaeology, artworks, materials science and physics [139]. A review of the different industrial applications as well as new approaches for the utilisation of neutron beams for imaging purposes are presented in [140].

2.7.4 Contour method

The contour method is a mechanical technique for measuring RS in engineering structures. As a relatively recent development, first presented in the literature in 2000 [144][145], the method relies on carefully cutting the component in two, typically with wire electric discharge machining (EDM). Once cut, a surface profiling device with sufficient resolution is utilised to measure the surface deformation that results from stress relaxation.

The main advantage of the contour method is its simplicity and ability to produce a 2D map of RS acting normal to the cut surface. Moreover, the contour method is not affected by composition changes, large grain size, and crystallographic texture that can compromise other measurement diffraction techniques. However, it is very sensitive to the quality of sectioning and, in certain cases, errors associated with plasticity caused by stress redistribution ahead of the wire during the EDM cutting process [125].

2.8 Finite element analysis for effective stress intensity factor calculation

RS affects the SIF which can be accounted for using the weight function method or FEA simulations to evaluate the effective stress intensity factor. Previous numerical attempts have focused on balancing the initial stress artificially when introduced to FEA models [146][147][148]. Significant effort has been made by Busse [148] to develop a numerical model in order to calculate the effective stress intensity factor in the presence of residual stresses. Through the use of an ABAQUS subroutine combined with a Python code the effective stress intensity factor has been calculated on a laser peened CCT sample. Those FE models are based on the Virtual Crack Closure Technique (VCCT). The VCCT is an indirect method to calculate the SIF from FEA simulations and is based on the Irwin's energy

principle [68]. The VCCT relies on estimating the strain energy release rate, G, considering the nodal vertical displacement of the nodes involved in the crack propagation and the nodal reaction force of the new crack tip for a defined crack advance and for a fixed thickness. This method is implemented and verified in the current study.

There are few other numerical methods available for evaluating the SIF using FEA, such as the crack tip displacement extrapolation, the J-integral or the strain energy approach [114]. Another method, implemented for welded joints, uses the thermal expansion coefficient of the material in order to calculate the phase transformation, coupled with temperature calculation by means of the user subroutine program [149]. RS have also been predicted in girth welded pipes using an artificial neural network approach in [150].

The results presented in [151] indicate that the developed computational procedures are capable of accurately predicting dynamic crack propagation and arrest, based on the hypothesis that it exists a material property independent of the geometry. The results also demonstrate the importance of modelling the loading conditions and other boundary conditions highly accurately, in an elastodynamic crack propagation problem. A new theory is also proposed in [152] for predicting the crack-growth rate in cyclic loaded structures. The theory is an improvement over other theories because the effect of the stress ratio, R, and the crack instability at onset of fast fracture are taken into account. The theory showed excellent agreement with wide range of test data. Another numerical model is presented in [153] this paper in order to investigate the fracture of concrete by considering its microstructure. The matrix and inclusions in the numerically-generated concrete specimen are taken as brittle materials. Crack propagation is assumed to take place in the matrix and is controlled by the stress intensity factors defined in LEFM. This allows the investigation of the influence of the microstructure on the non-linear fracture behaviour of concrete. The stress intensity factors are calculated by the finite element method. Finally, fatigue crack growth simulations have been performed in [154] for functionally graded material, equivalent composite and aluminium alloy by Element Free Galerkin Method (EFGM) and extended finite element method (XFEM) under mixed mode cyclic loading. It was found that the spatial location of crack in a functionally graded material plays a major role in determining the fatigue life of component. The results also reveal that the fatigue life reduces considerably in case of mixed mode loading as compared to that of pure mode-I loading. The simplicity and effectiveness of the proposed criterion shows its potential to simulate realistic problems of fracture in functionally graded materials using EFGM.

2.9 Summary

The review of the literature presented in this chapter has demonstrated the importance of residual stresses in the accurate assessment of the FCG behaviour of engineering structures subjected to different loading conditions and operating in various environments. Special attention has been drawn on the offshore wind turbine monopile support structures. It has been shown that the main failure mechanism in offshore wind monopiles is corrosion-fatigue which may result in crack initiation and propagation within the HAZ of the circumferential welds in the presence of welding RS. It is therefore suggested to focus this study on the characterisation of welding residual stresses and investigate their subsequent effects on the crack propagation behaviour of the material to fill in the research gaps. The details of the test programme, including the specimen design and extraction will be presented in the next chapter, followed by RS measurements and FCG tests in air and in seawater.

3 Sample extraction and material characterisation

3.1 Specimen design and extraction

3.1.1 Material specifications and welding procedure

The material used in this study is EN-10225:09 S355 G10+M, which is widely used in the fabrication of offshore structures including offshore wind turbine monopiles as explained in the standard from Det Norske Veritas [13]. The multi-pass submerged arc welding (SAW) technique was used to fabricate a double V-grooved welded plate with the thickness of 90 mm. The solid wire electrode was EN ISO 14171-A (EN 756): S3Si and the chosen flux was EN ISO 14174: SA FB 1 55 AC H. The welding was conducted by EEW in Germany, who are one of the leading manufacturers of monopile foundations in Europe, and was carried out in accordance with DNV-OS-C401 recommendations. The material specifications provided by the manufacturer are set out in Appendix A as well as the chemical composition of the welded plate. The welding procedure specification is given in Appendix B. Welding was conducted parallel to the rolling direction using run off, thereafter cut, at each end of the plate as shown in Figure 3-1.

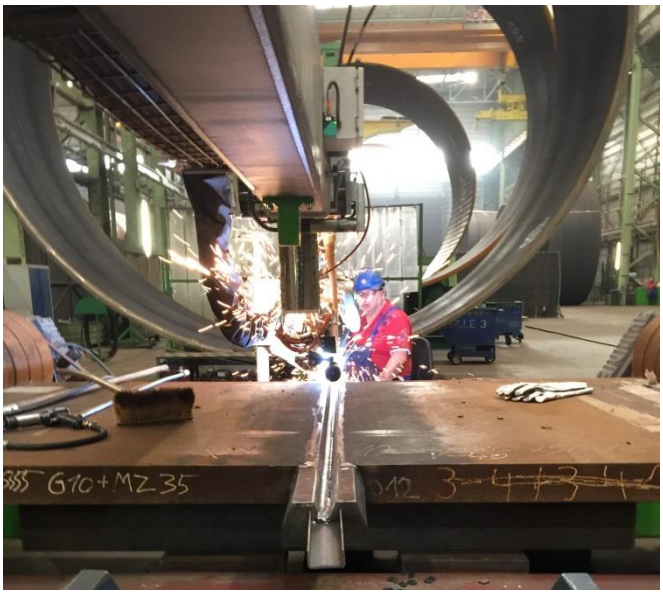

Figure 3-1: Multi-pass submerged arc welding conducted on S355 G10+M

The welding process first started with the edge preparation where two large hot rolled parent plates were placed next to each other and the first V-groove was machined. Then the tack welds were performed on the inside section first and then the outside with a preheat of 60 °C.

The weld run sequence started on the inside of the first milled groove and was gradually directed towards the external surface, using up to 3 electrode wires providing a heat input of up to 3.0 kJ/mm and an inter-pass temperature of not more than 250 °C. Gas burners were used for pre-heating the plates and the temperature was measured by thermo crayons. 18 weld beads were applied in total in the first V-groove. Once the first V-groove was welded, the plate was turned over and the second V-groove was machined. Welding on the second V-groove started with the same sequence running from the inside of the notch to the outside. 25 weld beads were applied in total in the second V-groove. The schematic welding sequence for the first and second V-groove is shown in Figure 3-2.

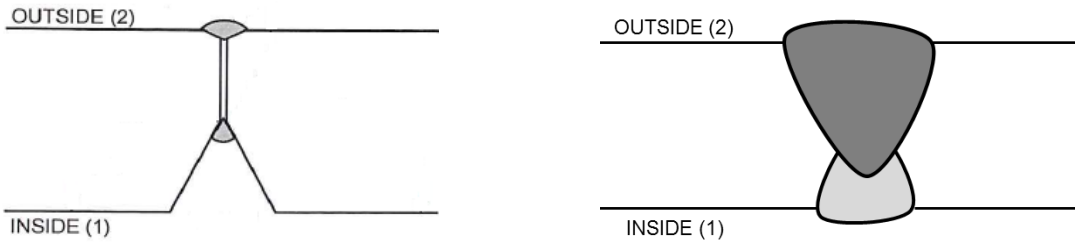

Figure 3-2: (a) Edge preparation of the welding sequence with inside/outside tack welds milled out (b) weld run sequence

The overall dimensions of the welded plate were 90 mm (in through thickness direction) × 800 mm (in longitudinal direction) × 1300 mm (in transverse direction). To facilitate transport of the welded plate, the width of the plate, the transverse dimension, after welding was reduced to 600 mm by flame cutting the BM plates at round 300 mm away from and at either side of the weld region. The length of the plate along the longitudinal direction was shortened by flame cutting to 600 mm. The section for contour method residual stress characterisation was measured 90 mm (thickness) × 600 mm (in longitudinal direction) × 600 mm (in transverse direction) as presented in Figure 3-3.

Figure 3-3: S355 large welded plate testing material as received

A smaller section with 90 mm (thickness) × 200 mm (in longitudinal direction) × 600 mm (in transverse direction) dimensions was prepared for the extraction of the C(T) specimens and also tensile specimens (which will be described in the following section) as presented in Figure 3-4.

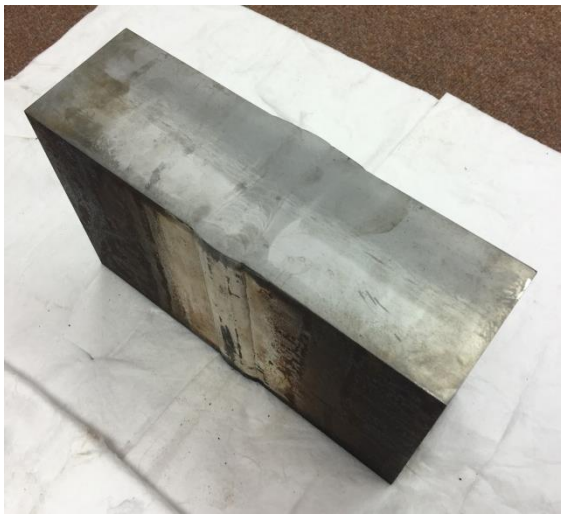

Figure 3-4: Smaller sectioned welded plate for the extraction of C(T) samples

It is worth noting that the welded plate sections were transported with a lot of care to minimise the vibration effects, environmental effects and temperature variation effects during transportation on the residual stress state. Moreover, the flame cut regions were selected to be sufficiently away from the weld region to minimise the effect of flame cutting on the residual stress profiles near the weld toes.

In order to be able to properly extract the lab test specimen, the large welded plate has been polished and etched using 10% Nital solution (Nitric acid in Methanol). This step helps to reveal the weld runs and the HAZ. A macrograph of the weld is shown in Figure 3-5, where the three regions of interest (BM, WM, HAZ) have been revealed and labelled.

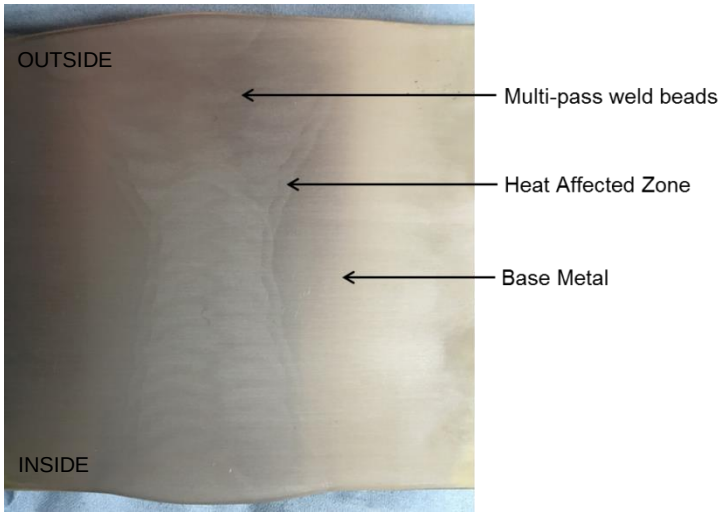

Figure 3-5: Weld macrograph after polishing and etching of the welded plate

It is worth noting that in the fabrication of monopiles, the weld toes can be ground flush or remain in the as-welded condition, as described in DNV standard recommendations [155]. In this study the welded plate was used in the as-welded condition with no post-weld heat treatment (PWHT), to replicate the common practice in the offshore wind industry.

3.1.2 Specimen preparation

As schematically shown in Figure 3-6, due to lateral wind and wave loads, crack initiation in monopiles may occur at the circumferential welds located at the outer surface and propagate in the through thickness direction.

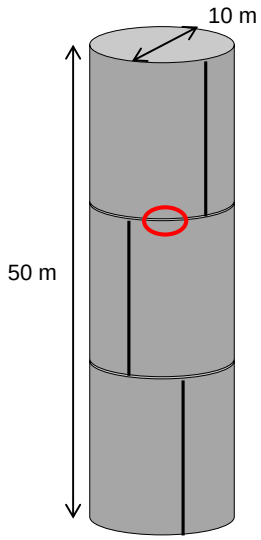

Figure 3-6: Schematic drawing of an offshore wind turbine monopile

To replicate the circumferential welds in monopiles, the welded plate mock-up in this study was fabricated to better understand the fatigue crack growth in the HAZ material. In order to extract fracture mechanics specimens for testing, first of all 11 slices were cut with 16 mm thickness from the welded plate, as seen in Figure 3-7, using the EDM technique.

Figure 3-7: An example of a welded slice for the extraction of C(T) specimens

As part of this project, the orientation effect has also been studied in order to identify the influence of the direction of the crack on the FCG behaviour of the material. A schematic representation of the two different orientations of the C(T) samples, here after denoted 0° and 180° specimens, extracted from a welded slice is shown in Figure 3-8.

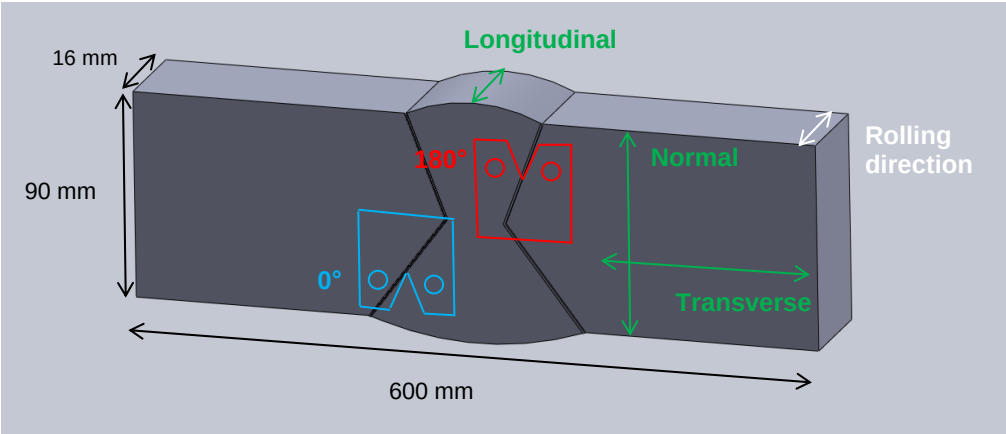

Figure 3-8: Schematic representation of a 16 mm thick welded slice and the location of C(T) specimens with different orientations extracted from the welded slice

As seen in Figure 3-7 and Figure 3-8, each of the extracted slices had the dimensions of 90 mm × 16 mm × 600 mm and were designed for the extraction of only one C(T) sample with the notch tip located in the HAZ region. EDM machining was used in extraction of C(T) specimens in order to minimise the machining effects at the outer surface and prevent manufacturing effects on the fatigue test results. C(T) specimens with the width of W = 50 mm and thickness of B = 16 mm were designed according to the ASTM E647 standard test method for measurement of fatigue crack growth rates [74]. The design of the test specimens was performed in CATIA V5 software. Technical drawings are presented in Appendix C. 11 slices were cut in total to extract 11 C(T) specimens with the crack tip located in the HAZ, as shown in Figure 3-9.

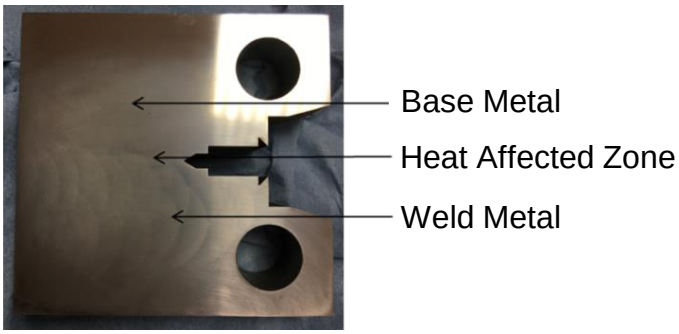

Figure 3-9: C(T) sample extracted from the welded plate after polishing and etching

In order to identify the exact location of the crack tip, the slices were initially ground, polished and etched to reveal the material microstructure. Grinding of the specimens was achieved using 120, 240 and 1200 wet sandpaper in ascending order mounted on a rotating wheel on a Metaserv grinding machine. Subsequent to grinding and polishing, the surface was etched using 10% Nital solution in order to be able to visualize the three different regions

of interest (BM, HAZ and WM). The sample specifications are presented in the following test matrix section. All the specimens had the loading axis parallel to the transverse direction, with respect to the welded plate, with the crack plane oriented along the through thickness direction. As seen in Figure 3-9, C(T) specimens were also ground, polished and etched post-manufacture to ensure that the crack tip is located at the pre-identified region within the HAZ and the crack path during fatigue tests is maintained within the HAZ region. It must be noted that no PWHT was performed on the extracted slices or C(T) specimens. Although it has been assumed that the level of remaining RS in C(T) specimens is relatively low, RS measurements have been conducted on C(T) specimens prior to and during testing, as described later in this project, to quantify the level of locked-in RS in the HAZ fracture mechanics specimens.

Compact tension C(T) specimens are typically used to characterise fracture properties and fatigue crack propagation behaviour of materials. C(T) specimens extracted from larger weldments are often assumed to be stress-free, hence the effect of any remnant residual stress on characterised fatigue or fracture behaviour is often mistakenly ignored. In order to investigate the level of remaining residual stresses in fracture mechanics specimens extracted from the large welded mock-up, a 20 mm thick slice was extracted from the 90 mm × 200 mm × 600 mm welded section, ground, polished and subsequently etched using 10% Nital solution in order to visualise the weld and HAZ zones. Previous studies [5] have shown that the crack initiation in monopiles are most likely to occur at the weld toe (in the as-welded condition) and in the HAZ region of the circumferential weld and propagates into the BM in through-thickness direction, due to lateral wind and wave loads, as schematically shown in Figure 3-10.

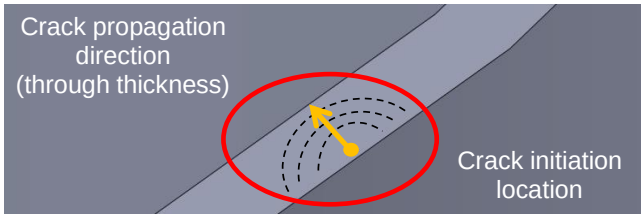

Figure 3-10: Representation of the crack initiation and propagation within a circumferential weld of a monopile

As discussed in [5] the fatigue crack initiation and propagation in the HAZ region as well as the residual stress profile need to be characterised. Therefore, a standard C(T) specimen with

the width of W = 50 mm, thickness of B = 16 mm and height of H = 60 mm [74] was extracted from the ground, polished and etched slice of the extracted 90 mm × 200 mm × 600 mm welded section with the initial crack tip located in the middle of the HAZ region similar to the procedure detailed in [5]. This sample, which was denoted as HAZ 0, was machined to initially perform non-destructive ND residual stress measurements followed by destructive contour method residual stress measurements. It must be noted that a thicker sample with B = 20 mm was initially extracted from the welded section from which a 4 mm thick slice was machined off for d_0 measurements in ND tests. The extracted C(T) specimen and its orientation with respect to the welded plate is shown in Figure 3-11.

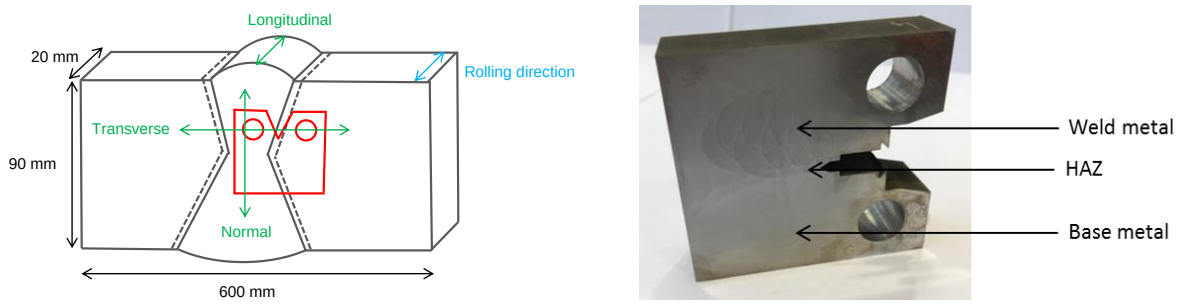

Figure 3-11: (a) C(T) specimen extraction location with respect to the welded mock-up (b) C(T) specimen extracted from the welded slice for ND and contour residual stress measurements

As illustrated in this figure, the loading condition for the extracted C(T) is parallel to the transverse welding direction to replicate the loading conditions in monopiles. This is consistent with the C(T) specimen orientations tested in [5]. The FCG rates for offshore wind turbine monopiles in air and in seawater for a structural steel grade, welded with similar procedure as this work, have been previously characterised in the SLIC project [5] on S355 G8+M structural steel where the remaining welding residual stresses in C(T) specimens were not measured and considered in the analysis. Hence the influence of residual stresses on fatigue crack growth behaviour of monopile weldments, particularly in the near threshold region, could not be investigated. The current study mainly focuses on characterising the transverse residual stress in the extracted C(T) specimen, which is parallel to the loading direction of the C(T) sample and perpendicular to the crack plane.

3.2 Test matrix

It was decided in this project to perform RS measurements using contour method, ND and NI techniques. The name and the orientation of each sample characterised using different RS measurement techniques are presented in Table 3-1.

Table 3-1: RS measurements test matrix

RS measurement technique / Specimen tested	Orientation	Contour method	Neutron diffraction	Neutron imaging
HAZ 0	0°	x	x	
HAZ 1	180°			x
HAZ 2	180°		x	x
HAZ 3	180°		x	
HAZ 4	0°		x	x
HAZ 7	0°		x	
HAZ 9	180°		x	

The extracted C(T) specimens were used to perform FCG tests in air and in seawater. The specimen orientation and dimensions including the initial crack tip before pre-cracking, a_i, initial crack tip after pre-cracking, a_0, final crack length at the end of the test, a_f, specimen width, W, and specimen thickness, B, are summarised in Table 3-2.

Table 3-2: FCG test matrix

Test ID	Environment	a_i (mm)	a_0 (mm)	a_f (mm)	W (mm)	B (mm)	Orientation (°)
HAZ 1	Air	17	21.2	35.1	50	16	180
HAZ 2	Air	17	21.0	34.6	50	16	180
HAZ 3	Air	17	20.8	35.6	50	16	180
HAZ 4	Air	17	21.3	35.2	50	16	0
HAZ 5	Air	17	20.9	35.0	50	16	0
HAZ 6	Air	17	21.1	35.8	50	16	0
HAZ 7	Seawater	17	20.4	29.0	50	16	0
HAZ 8	Seawater	17	20.3	33.3	50	16	0

HAZ 9	Seawater	17	20.4	27.6	50	16	180
HAZ 10	Seawater	17	20.3	29.4	50	16	180

3.3 Material characterisation

Material characterisation is a fundamental process in order to scientifically understand the behaviour of engineering materials. In order to characterise the material used in this study, tensile tests, hardness test, chemical composition analysis and EBSD measurements have been performed on the material, the results of which are presented below.

3.3.1 Tensile tests

Tensile tests were performed at Cranfield University in order to analyse the tensile behaviour of the material and more specifically of each of the three regions of interest (HAZ, BM and WM). Two cross-weld tensile specimens, with dog-bone geometries comprising of the BM, WM and HAZ material microstructures, with the cross sectional area of 8×8 mm^2 were extracted from the 90 mm × 200 mm × 600 mm welded section as shown in Figure 3-12.

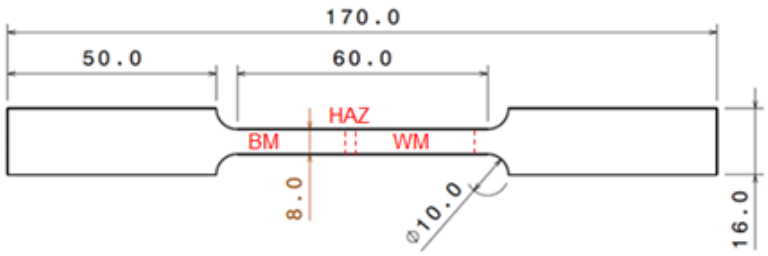

Figure 3-12: Tensile test specimen dimensions (all dimensions are in millimetres)

Tensile tests were performed at room temperature with the displacement rate of 1mm/min. The tensile force was continuously recorded during the test and the strain distributions were monitored using the digital image correlation (DIC) technique. The stress is calculated as the ratio of the load over the cross sectional area. A Dantec Q400 DIC system was used to record the strain within each of the three regions at the surface of the tensile specimen [5]. The average tensile curve obtained from these tests is shown in Figure 3-13, where the engineering stress is plotted against the engineering plastic strain.

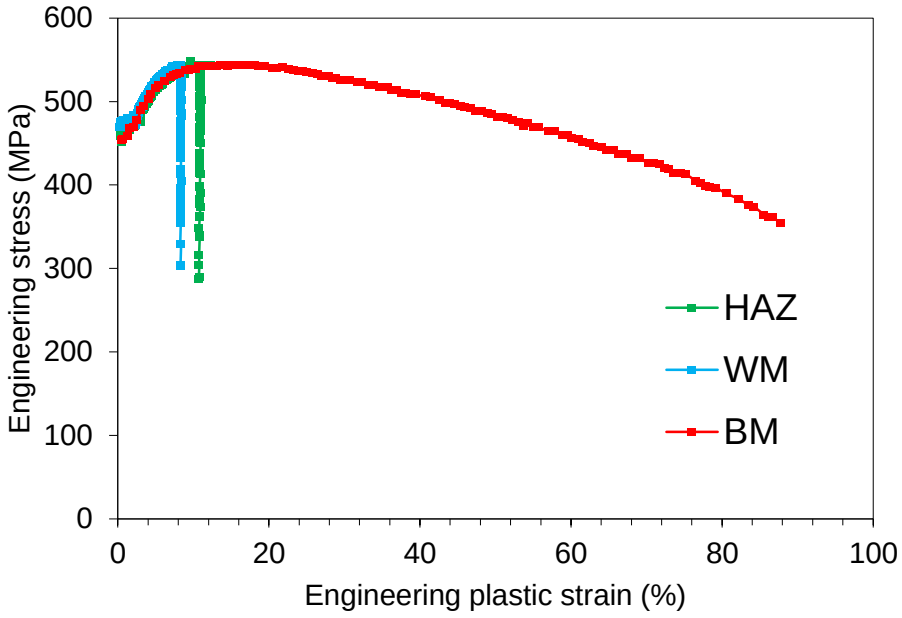

Figure 3-13: Cross-weld DIC tensile test results for the BM, HAZ and WM

Due to the resolution of the DIC technique, only plastic strains in the BM, HAZ and WM were measured using the DIC data. A separate test on a round bar geometry (see Appendix C) was performed in Rutherford Appleton Laboratory where the elastic properties were measured using an extensometer. The measured 0.2% proof stress, taken as yield stress σ_y, values obtained from tensile tests are 455 MPa for the BM, 469 MPa for the HAZ and 477 MPa for the WM. Moreover, the elastic Young's modulus measured from the tensile test on the round bar was found as E = 190 GPa with the Poisson's ratio of ν = 0.3 for all three material microstructures. The mechanical properties of the BM, HAZ and WM are summarised in Table 3-3.

Table 3-3: Mechanical properties of the BM, HAZ and WM

Material Microstructure	***E*** **(GPa)**	$\boldsymbol{\sigma_y}$ **(MPa)**	**UTS (MPa)**
BM	190	455	543
HAZ	190	469	543
WM	190	477	543

The tensile test results in Table 3-3 show that the current welded plate studied in this research is slightly overmatched, as the yield stress of the WM is above the one of the BM, and the mismatch ratio ($M = \sigma_{WM}/\sigma_{BM}$) is just above unity. The tensile properties of the S355 G10+M

material studied in this research project have also been compared with the S355 G8+M material used in the SLIC project and the results are shown in Table 3-4.

Table 3-4: Tensile properties of S355 G8+M [5] and S355 G10+M materials

Material Microstructure	**S355 G10+M**			**SLIC S355 G8+M**		
	E **(GPa)**	$\boldsymbol{\sigma_y}$ **(MPa)**	**UTS (MPa)**	***E*** **(GPa)**	$\boldsymbol{\sigma_y}$ **(MPa)**	**UTS (MPa)**
HAZ	190	469	543	190±56	448±47	585
BM	190	455	543	197±50	413±80	503
WM	190	477	543	207±30	477±43	549

It can be seen in Table 3-4 that the S355 G10+M used in this project displays a slightly higher yield stress in the BM and HAZ compared to the mean values obtained on S355 G8+M obtained from the SLIC project. The Young's modulus is also slightly different between S355 G10+M and S355 G8+M, possibly due to the inherent scatter in the data. These differences in mechanical properties might lead, to some extent, to different fatigue response of the materials as well as other factors, which will be discussed within the next chapters.

3.3.2 Ramberg-Osgood material model constants

The Ramberg-Osgood material model constants have been extracted from the tensile test results, based on the "True stress vs true strain" response of the HAZ region. These constants have been used, as detailed in the following chapters, to calculate the plastic zone size ahead of the crack tip and therefore confirm the use of the LEFM theory. The calculations are based on Equation 2-3, Equation 2-4, considering $E = 190\ GPa$ and $\sigma_{p0} = \sigma_{y,HAZ}$. By correlating them, α and ε_{p0} are calculated and kept constant. Thereafter, the value of the integer *N* is set and an iteration process is run to extract the value of *A*. The plasticity model can be used to find a value of *N* leading to the smallest error and the goal seek function in Excel is employed to run the iterations in order to get a value of the error as close as possible to zero. The graph of the comparison of both the Ramberg-Osgood material model and the tensile response of the HAZ are given in Figure 3-14 at the end of the iteration process. Table 3-5 also summarises the Ramberg-Osgood material parameters.

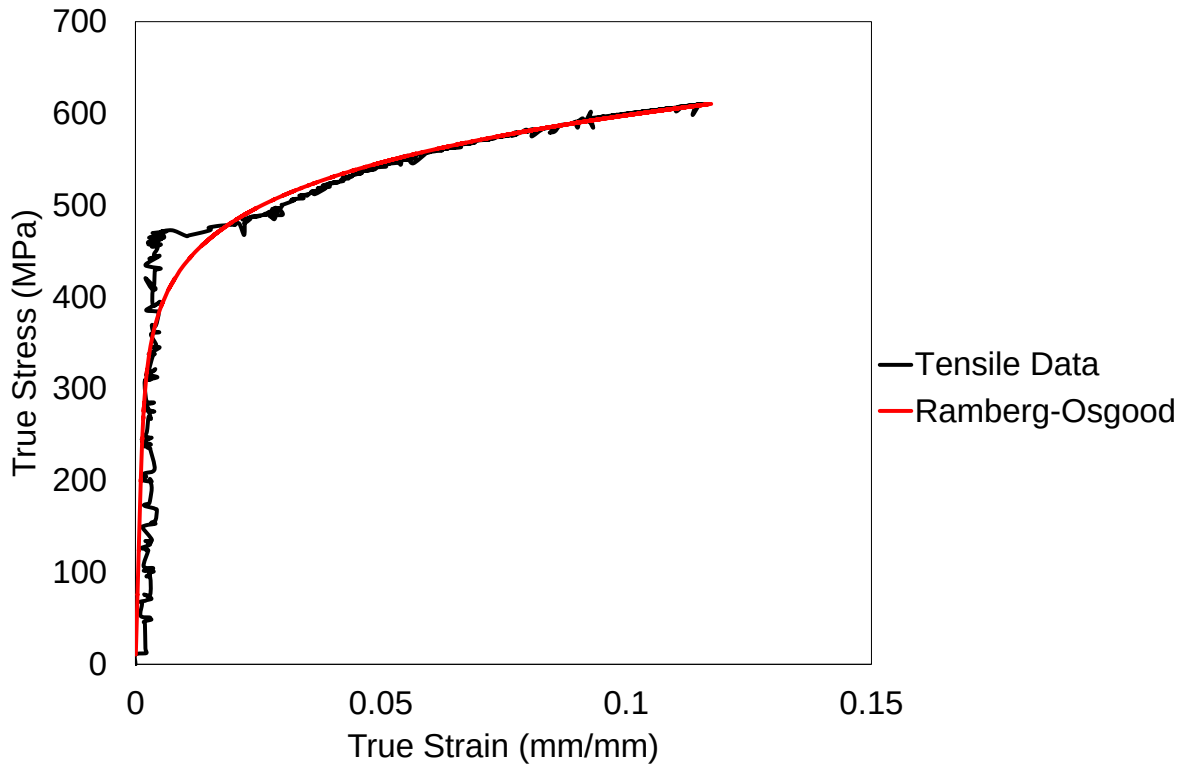

Figure 3-14: Ramberg-Osgood fit to the HAZ tensile data on S355 material

Table 3-5: Ramberg-Osgood material constants

Ramberg-Osgood material constants	***N***	A_p	α	ε_{p0}	σ_{p0} **(MPa)**
	8	5.92E-24	5.62	2.47E-03	469

3.3.3 Hardness tests

The hardness measurements were performed on a computer assisted INDENTEC Vickers micro hardness machine, as seen in Figure 3-15, with a diamond indenter and according to the ASTM E384 standard [156]. The measurements have been performed on a spare C(T) sample in order to avoid introducing potential uncertainties in future fracture mechanics tests arising from the surface indents, especially within the HAZ.

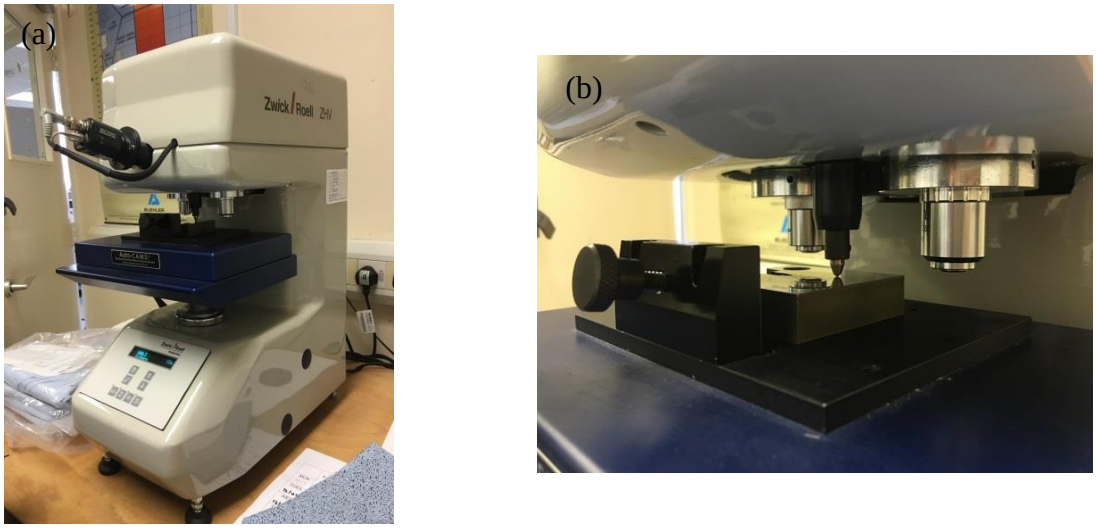

Figure 3-15: (a) INDENTEC Vickers micro hardness machine, (b) Micro hardness indentation on a C(T) specimen

A load of 300g was applied during hardness tests with a hold time of 15 seconds. Ten indentation lines were measured using the following procedure:

- One vertical line, close to the notch tip, of point spacing of 1 mm and 0.5 mm within the HAZ
- Nine horizontal lines of point spacing of 1 mm. The first line, was considered as the reference and was performed along the crack growth direction in the C(T) specimen. The other eight lines were placed at +5 mm, +10 mm, +15 mm, +20 mm, -5 mm, -10 mm, -15 mm and -20 mm with respect to the reference line.

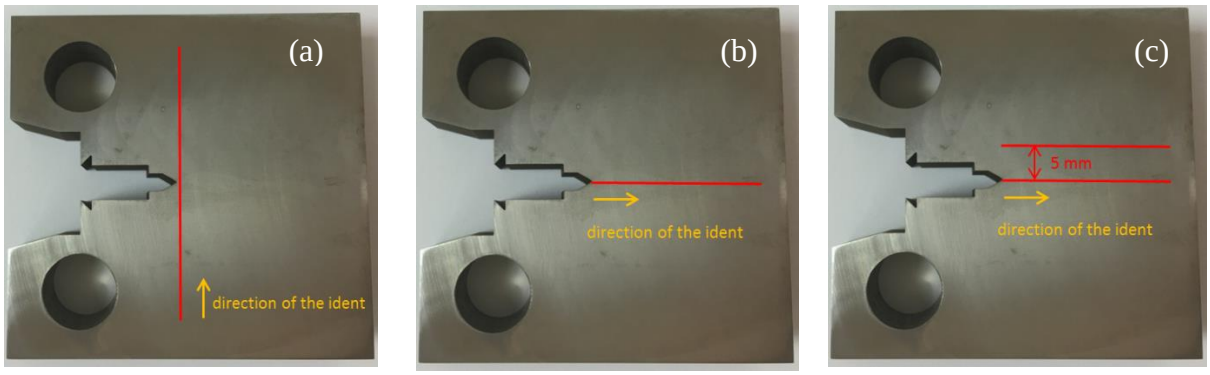

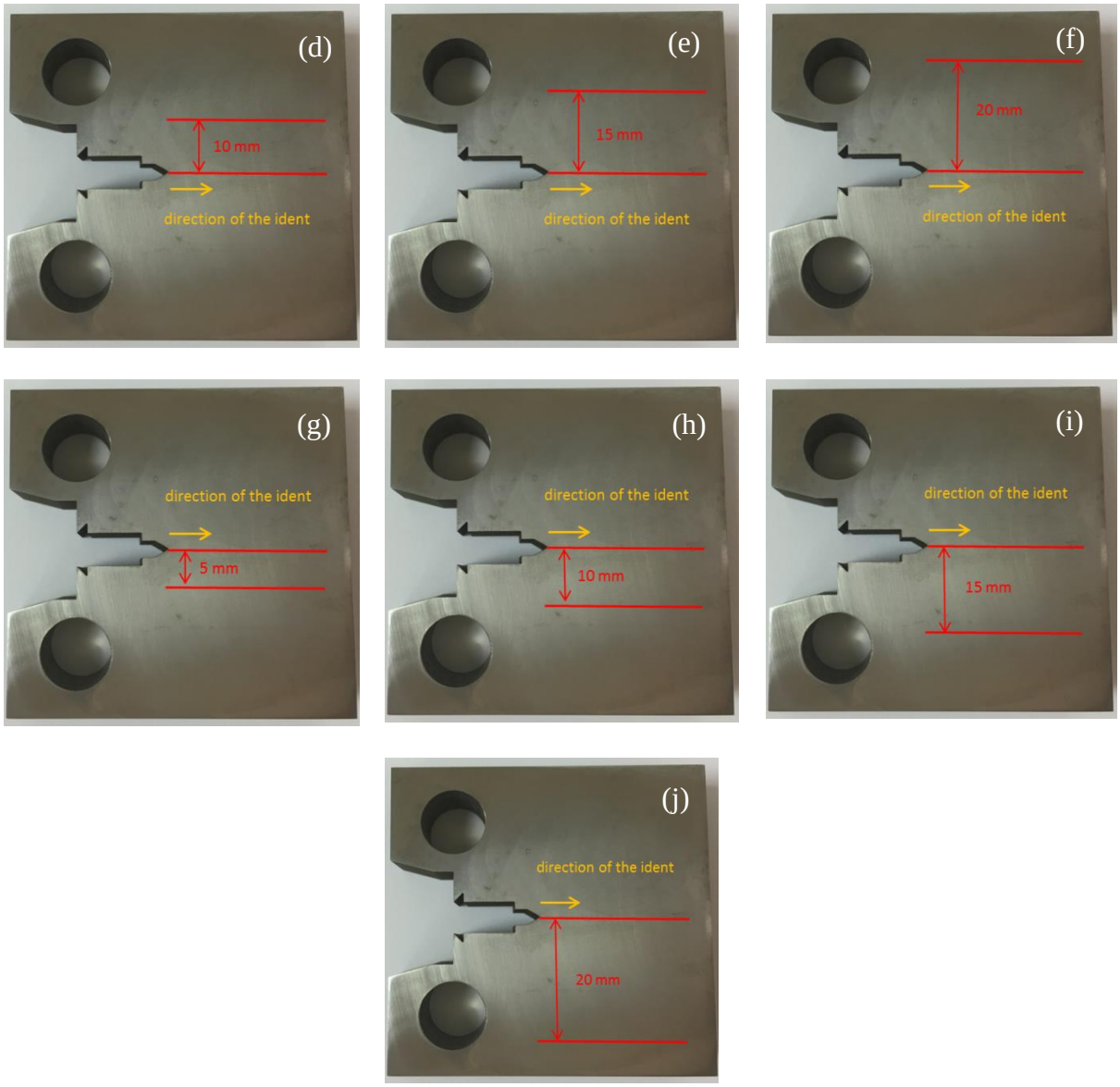

Figure 3-16: Indentation lines during Vickers hardness test: (a) Vertical indentation line, (b) Horizontal indentation line within the HAZ region, (c) Horizontal indentation line 5 mm above the HAZ line, (d) Horizontal indentation line 10 mm above the HAZ line, (e) Horizontal indentation line 15 mm above the HAZ line, (f) Horizontal indentation line 20 mm above the HAZ line, (g) Horizontal indentation line 5 mm below the HAZ line, (h) Horizontal indentation line 10 mm below the HAZ line, (i) Horizontal indentation line 15 mm below the HAZ line, (j) Horizontal indentation line 20 mm below the HAZ line

This procedure is demonstrated in Figure 3-16. Results of the hardness tests are presented in the following figures and are discussed in terms of comparison between the three regions of interest. It can be observed in Figure 3-17 that the hardness gradually increases from the BM to the HAZ and WM, considering that the reference point is the first indent within the BM at around 5 mm from the bottom edge of the C(T) specimen as seen in Figure 3-16(a). The observed trend in the hardness data is consistent with the yield stress values observed in

tensile tests. As seen in both hardness and tensile test results, the hardness value hence yield stress ($Hv \propto \sigma_y$) increases from BM to HAZ and from HAZ to WM.

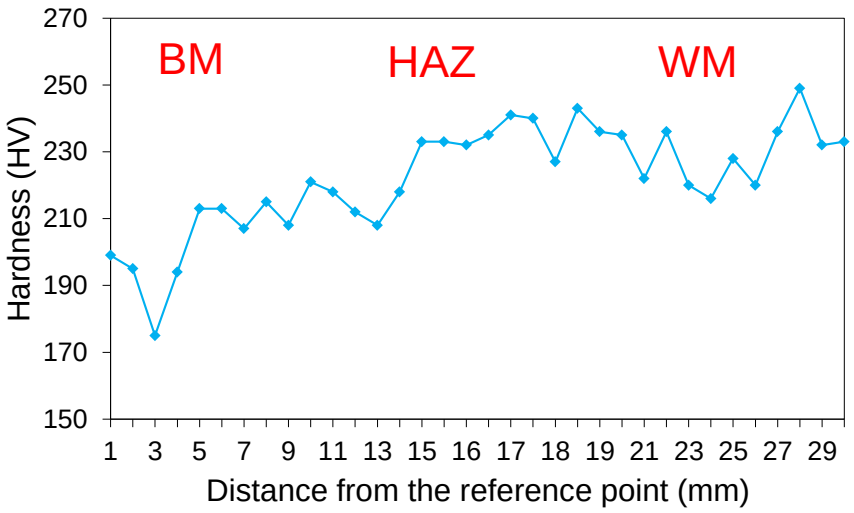

Figure 3-17: Hardness value along the vertical line case (a)

The hardness values obtained from the remaining eight measurement lines, shown and described in Figure 3-16, are presented in Figure 3-18. It can be seen in this figure that for each of the material microstructures, a level of scatter can be observed in the hardness values. The observed scatter can be associated with the microstructural effects on the hardness values, particularly in the HAZ and WM regions, where the variation in grain size can result in different hardness values.

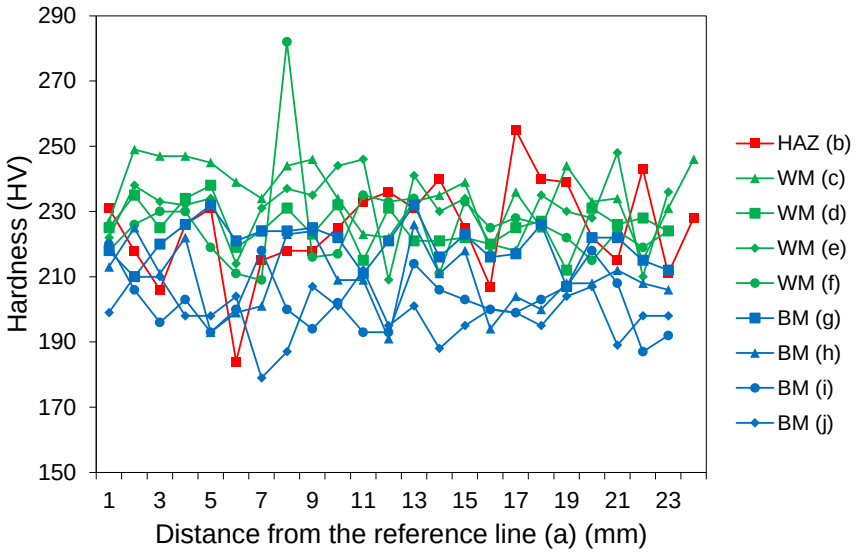

Figure 3-18: Hardness values for BM, HAZ and WM

The average hardness values from the eight horizontal measurement lines on the C(T) specimen have been presented for all three material microstructures in Figure 3-19. As seen in this figure, the observed trends show that the hardness values are, on average, lower in the BM than the WM and HAZ and higher in the WM than in the HAZ. The observed variation in the BM, HAZ and WM in horizontal lines is consistent with that of observed in the vertical measurement line shown in Figure 3-17.

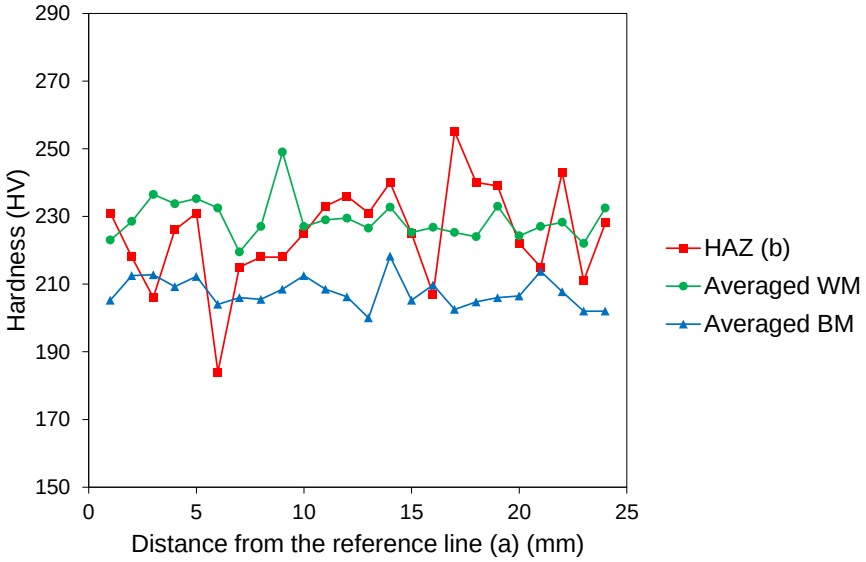

Figure 3-19: Average hardness values for the three material microstructures

Micro hardness measurements have also been performed on a spare welded slice under the same test conditions than for the C(T) sample and the results are presented in Figure 3-20.

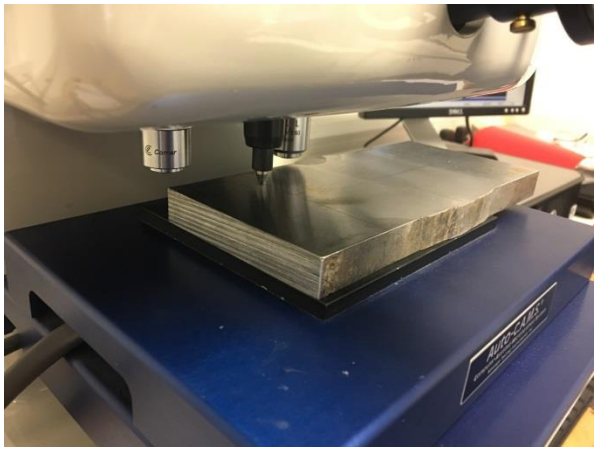

Figure 3-20: Hardness test on a welded slice

In order to facilitate the record of the hardness measurements, the plate was divided in four areas of 60 mm x 45 mm. Measurements have been performed every 5 mm vertically and each indentation line is horizontally spaced 5 mm from the previous one in the BM, 0.1 mm in the HAZ and 1 mm in the WM in order to measure as many representative points in each region of interest. A schematic of the hardness measurement plan on the welded slice is shown in Figure 3-21.

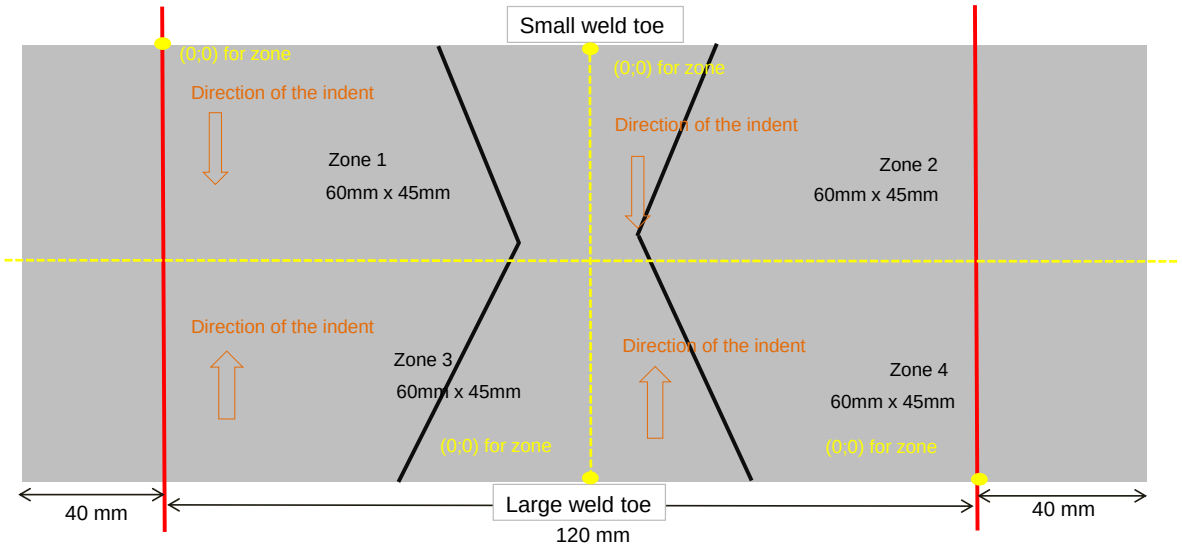

Figure 3-21: Hardness measurement process on the welded slice

The results from the hardness tests on the welded slice are shown as a contour map in Figure 3-22. It can be observed in this figure that the hardness values increase in the WM and HAZ regions compared to those of observed in the BM. This observation is consistent with the hardness test results obtained from the C(T) specimen as well as the observed trend in the yield stress obtained from the tensile tests.

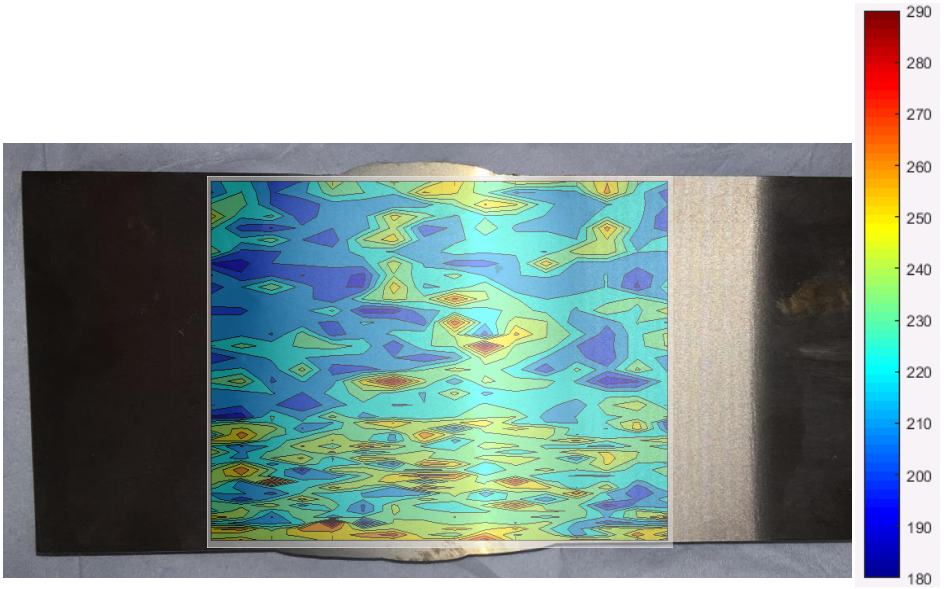

Figure 3-22: Contour map of the hardness values within the welded slice

3.3.4 Chemical composition analysis

Chemical composition analysis has been performed on one of the pre-cracked C(T) samples and the results are presented in this section. The analysis of the data has been performed using Aztec software and the results are presented in the form of a spectrum with peaks of different heights. Larger peaks show a larger concentration of a specific element while, on the opposite, smaller peaks represent elements that are not major components. Different locations have been examined for the chemical composition studies. The first section lies (i.e. Spectrum 1) within the HAZ region along the crack propagation direction as shown in Figure 3-23.

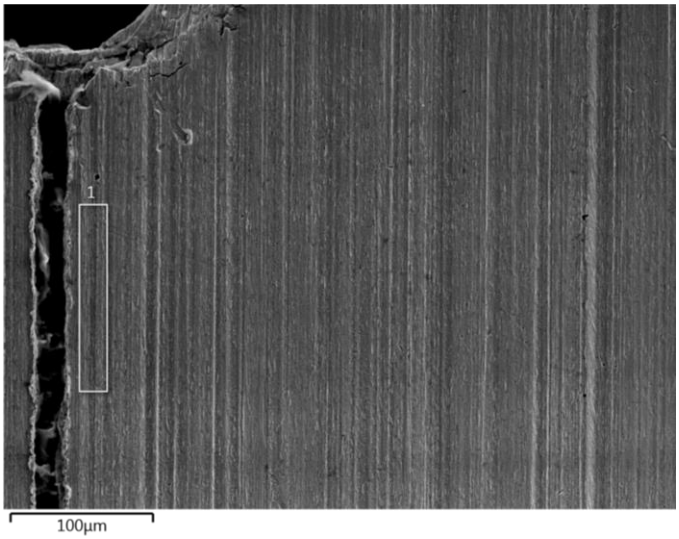

Figure 3-23: First measurement along the crack plane within the HAZ region

The spectrum of the results is represented in Figure 3-24 and Table 3-6. The elements present in the sample are reported in weight %. It can be noticed that a large majority of the S355 G10+M specimen is made of Fe and C.

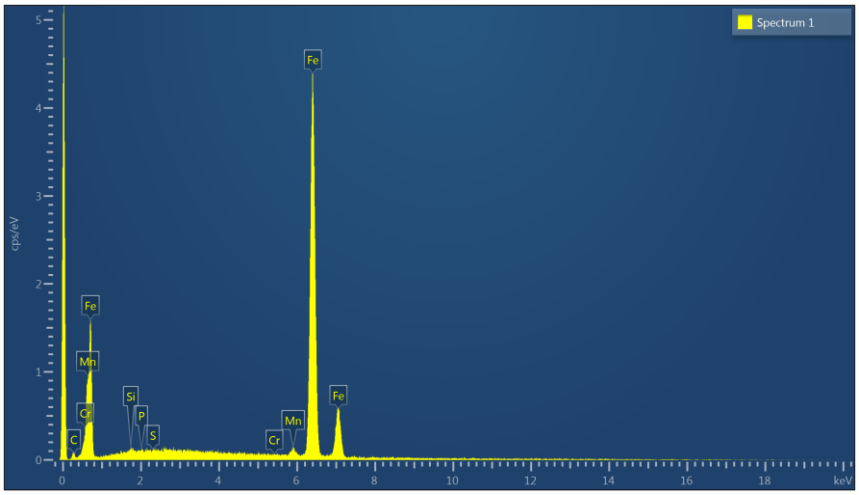

Figure 3-24: Element composition of the HAZ region

Table 3-6: Chemical composition analysis results within the HAZ region

Spectrum Label	**Spectrum 1 (weight %)**
C	3.90
Si	0.24
P	0.09

Cr	0.06
Mn	1.48
Fe	94.23
Total	100.00

A second area (i.e. Spectrum 5) has been scanned within the BM. The spectrum of the elements present in the BM region is shown in Figure 3-25. Similar to the chemical composition data analysis obtained from the HAZ region, the same main elements of Fe and C have been detected in the BM.

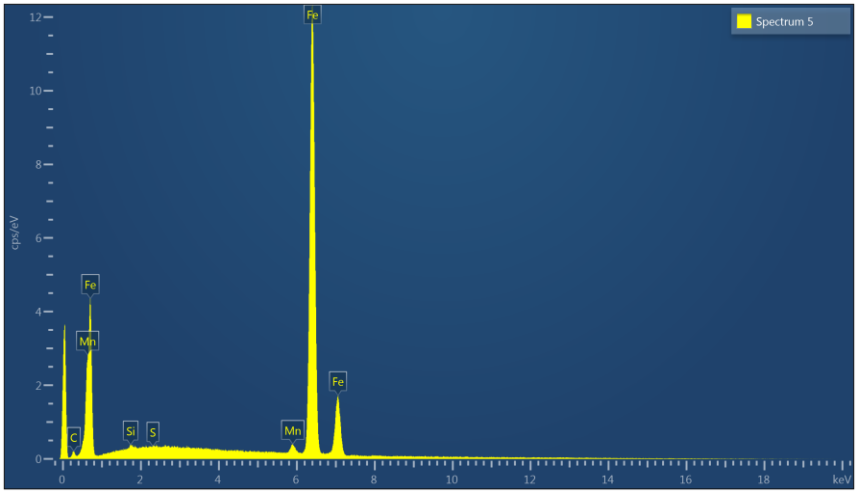

Figure 3-25: Spectrum of the elements present in the BM region

Finally, the WM region (Spectrum 6) has been scanned for the chemical composition analysis and the results are shown Figure 3-26. The same conclusion can be drawn since the elements present within the weld region are the same as the BM and HAZ region.

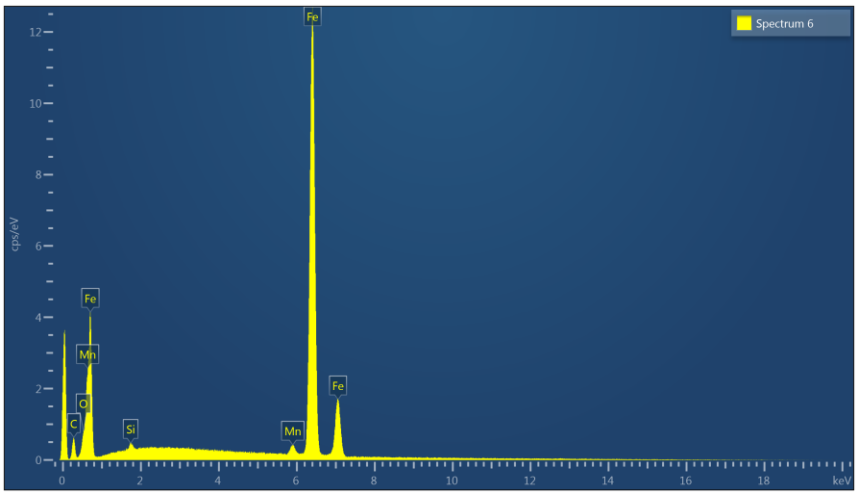

Figure 3-26: Spectrum of the elements present in the WM region

Final measurements were performed to obtain an element mapping of the HAZ area ahead of the crack tip, as seen in Figure 3-27. The coloured dots represent the element location within the scanned area. It appeared that the main elements present in the sample are uniformly spread with a slightly higher concentration of carbon along the crack boundary. However, the analysis has been currently limited by the scanning power of the machine and a deeper investigation should be performed in future work to precisely locate the elements within the grain and grain boundaries.

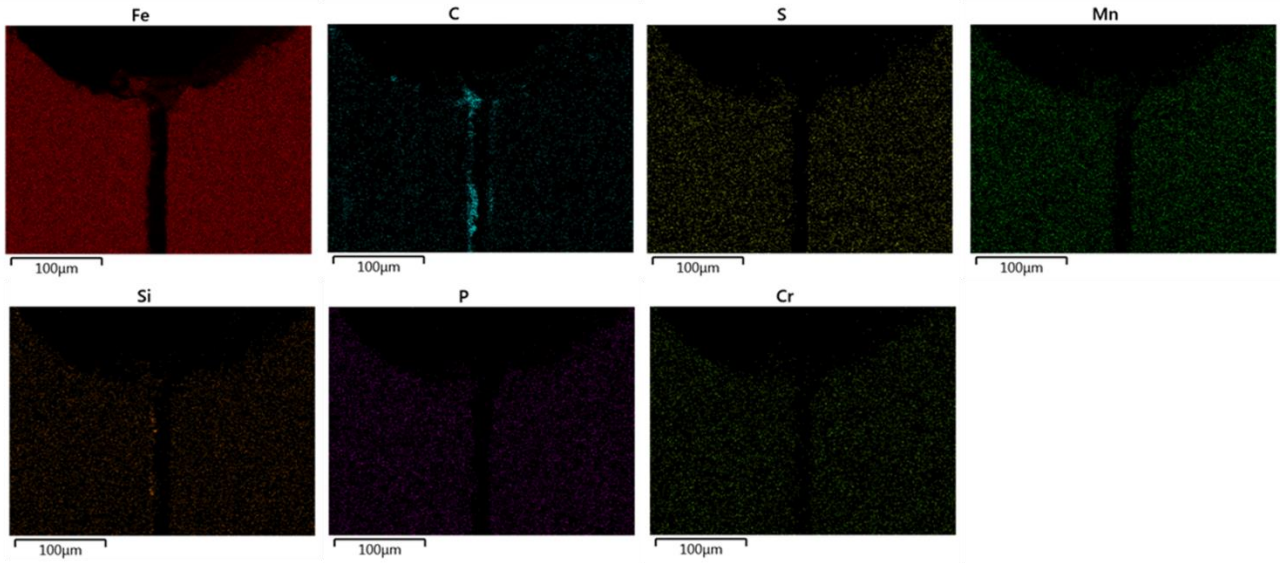

Figure 3-27: Element mapping ahead of the crack tip, within the HAZ region

The uniform values of the element composition analysis observed in the measurement results indicate that the elements were not diffused by the welding procedure. The Cr element

present allows corrosion resistance and Si and Mn offer good protection against S and P which have a tendency to weaken the grain boundaries. It can be noted that the carbon built up along the crack region is assumed to come from potential contamination. Indeed, the precracked region, on which SEM measurements have been done, was previously covered in oil in order to better see the notch tip as the oil would initiates bubbles. The contamination could also come from the EDM sample machining process which employs a cutting fluid that is sticking to the surface of the sample and might has been infiltrating as the crack propagates. Moreover, the results from chemical composition analysis are in good agreement with the tensile test results. Indeed, the overall mechanical responses of the HAZ, BM and WM are similar, with slight differences observed in the yield stress, which confirms that similar chemical compositions exist in all three material microstructures.

3.3.5 Phase analysis

Electron Back Scatter Diffraction (EBSD) measurements have been performed to initially investigate the presence of texture in the material in order to justify the Bragg Edge pattern obtained from the neutron imaging measurements as the data analysis process was under development. However, due to not enough samples tested and no conclusive results only the phase analysis is presented in this study.

EBSD analysis has been performed on small specimens extracted from a welded slice. Three small cubes have been extracted to analyse the WM/HAZ, HAZ/BM and BM regions as shown in Figure 3-28.

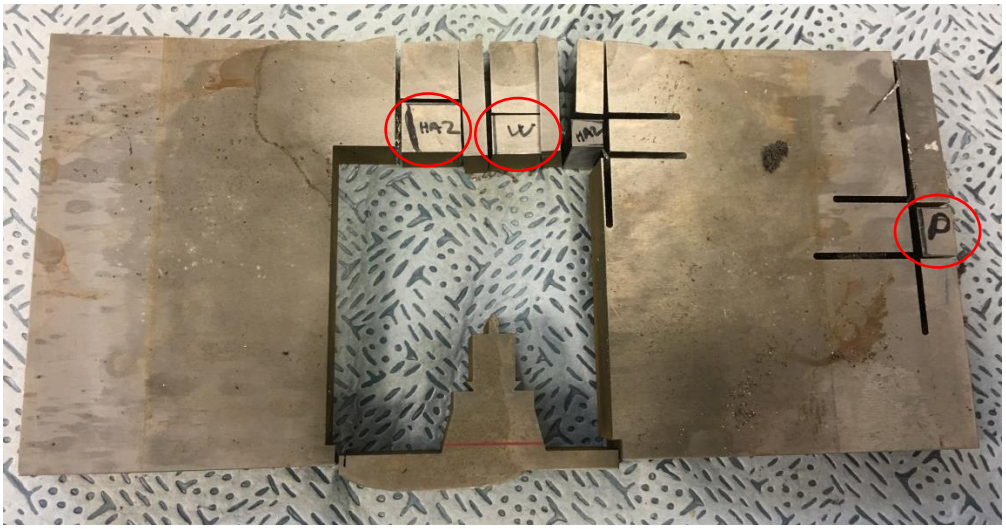

Figure 3-28: Specimen extraction location for the EBSD measurements

Each small cube is then inserted in an OPAL 410 instrument filled with a conductive resin, as seen in Figure 3-29, melted around the metal during the process to form the rounded specimens required for the EBSD measurements.

Figure 3-29: First stage of the sample preparation for EBSD measurements

The samples were polished with a SAPHIR 520 grinding machine with the polishing surface sprayed with diamond suspension of 9 micron and 3 micron. A load of 25 N was applied and a speed of 250 rounds per minute was used during this process. An example of the final surface finish after polishing is given in Figure 3-30.

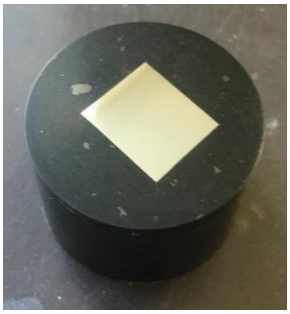

Figure 3-30: Final surface finish of the BM sample after polishing and before EBSD measurements

The results on the BM are presented in Figure 3-31 and the analyses results for the other regions (WM/HAZ and HAZ/BM) are included in Appendix D. The red dots in Figure 3-31 represent the iron BCC phase while the blue dots are the iron FCC. The results for the WM/HAZ and HAZ/BM presented in Appendix D display a similar phase map of the selected area. It can be observed that they all display the same pattern and it can be concluded that the material studied is a BCC iron as the processed image contains mainly red dots.

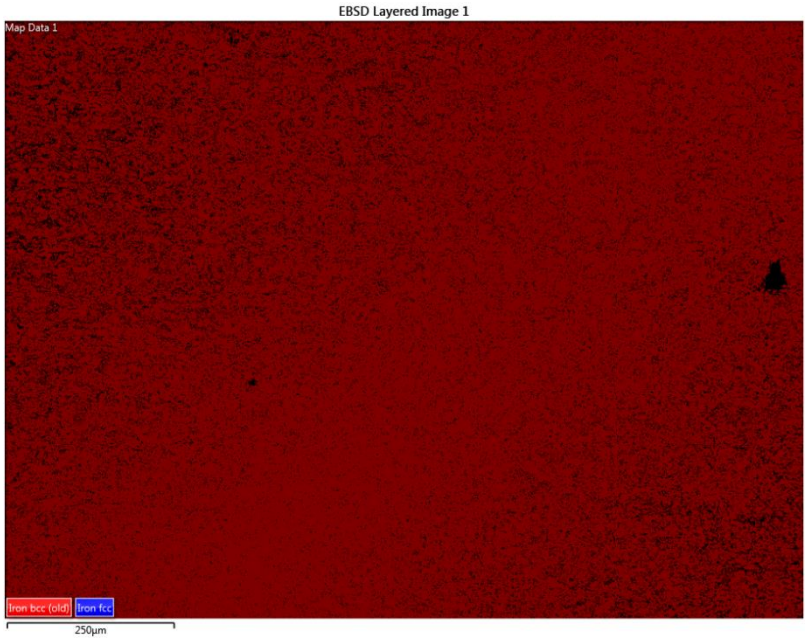

Figure 3-31: Phase analysis of the BM

3.4 Summary

To further understand and accurately interpret the future fatigue results, which will be presented in Chapters 5 and 7, the material supplied in this research was comprehensively characterised. Tensile and hardness tests as well as chemical composition and EBSD measurements have been performed and it can be concluded that the S355 G10+M structural steel material has a ferritic BCC structure with the hardness and yield stress values slightly higher in the WM, lower in the BM and mid-range values in the HAZ region. The Young's modulus as well as the Poisson's ratio will be used in the experimental and numerical sections to define the material tested. Moreover, the fatigue behaviour on the two different orientations will be justified by the microstructure effect.

4 Residual stress measurements

Residual stresses play a major role in the fatigue crack initiation and propagation behaviour of metallic materials [103] and are challenging to predict and measure since they are not immediately apparent. Originally present in a stationary structure without being subjected to external forces, residual stresses can be introduced during fabrication or assembly or caused by heat or surface treatment [92]. Residual stress measurements can be performed in a destructive, semi-destructive or non-destructive way. Neutron diffraction and neutron imaging techniques are the non-destructive measurement techniques which have been used in this study while the contour method is employed to destructively measure transverse residual stresses in fracture mechanics C(T) specimens which have been extracted for FCG tests in air and seawater. Moreover, the contour method is also used to measure a 2D map of residual stress distribution on a welded mock-up along the longitudinal direction. In the present study, the residual strains (and subsequently residual stresses) have been measured on six and three of the extracted C(T) samples using neutron diffraction and neutron imaging techniques on the Engin-X and IMAT instruments, respectively, at the Rutherford Appleton Laboratory (see Table 3-1). Neutron diffraction measurements provided the residual strains in all three directions whilst neutron imaging only gives the longitudinal residual strains in the chosen experimental conditions.

4.1 Neutron diffraction

The neutron diffraction measurements for this research project were performed at ISIS-STFC, a spallation neutron source presented in Figure 4-1, in the Rutherford Appleton Laboratory on Engin-X instrument. Further seen in Figure 4-1 is the location of the IMAT instrument at ISIS-STFC which has been used for neutron imaging analysis in this project.

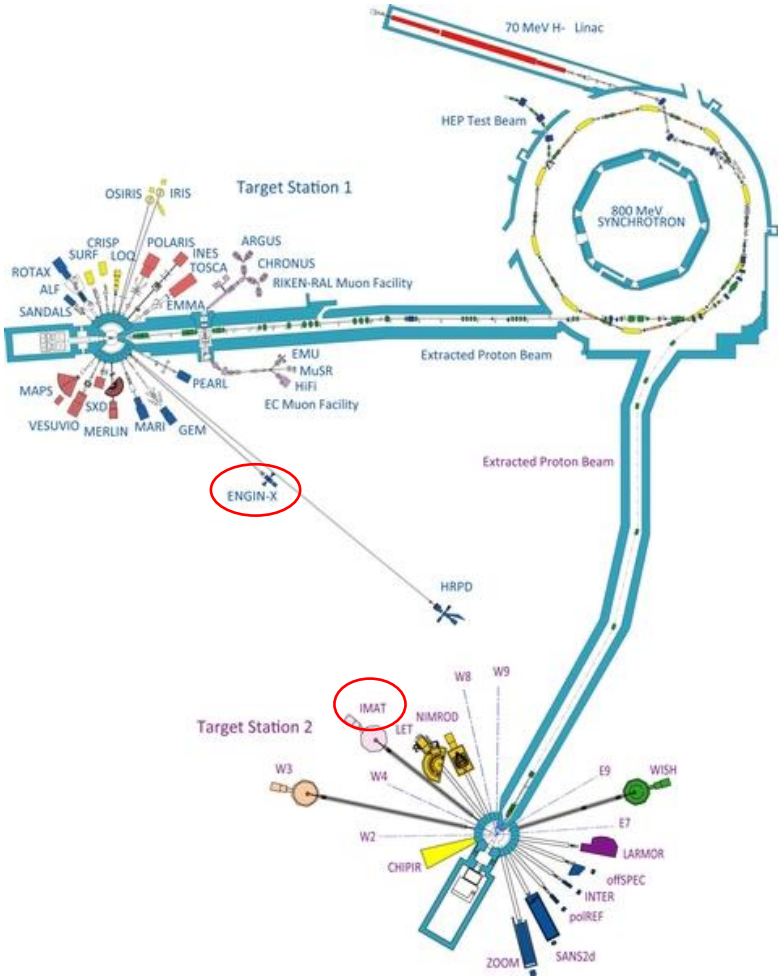

Figure 4-1: ISIS pulsed neutron source [157]

In this study, residual stresses in six of the extracted C(T) samples (HAZ 0, HAZ 2, HAZ 3, HAZ 4, HAZ 7 and HAZ 9) were measured non-destructively along three principal directions using the neutron diffraction technique. The direction of interest presented in this work corresponds to the transverse residual stresses, which is perpendicular to the direction of crack propagation and parallel to the loading direction in fracture mechanics tests on C(T) specimens. Longitudinal and normal RS have also been measured and the results are presented in Appendix E. Measurements were performed on C(T) specimens post-machining, prior to pre-fatigue cracking and also after few millimetres of crack growth for some of the samples.

4.1.1 Test set-up

The calibration of the Engin-X instrument is performed using vanadium at the beginning of each cycle, these measurements are dependent on the quality of the target, and ceria each time the collimators change. Residual stress measurements were performed using a gauge

volume of 2×2×2 mm^3 at the mid-thickness and mid-height of the C(T) specimens, along the crack propagation direction (i.e. specimen symmetry line). Moreover, d_0 measurements have been performed on 10 small cubes of 3×3×3 mm^3 extracted from the exact same region along the crack path in the main C(T) specimen using the EDM technique. The drawings for the extraction of the stress free cubes are presented in Appendix C.

At TOF instruments, pulsed neutrons are produced in time intervals and neutron speed is measured by timing their passage over a known distance. Moreover, the angle of scatter is fixed, since a single pulse contains a continuous spectrum of wavelength, and the TOF is proportional to the lattice spacing [158]. In crystalline materials, diffractometers measure the atomic interplanar spacing, where a specific volume is lit and the diffracted neutrons are recorded [159]. A schematic of the neutron diffraction measurement set-up on Engin-X is presented in Figure 4-2.

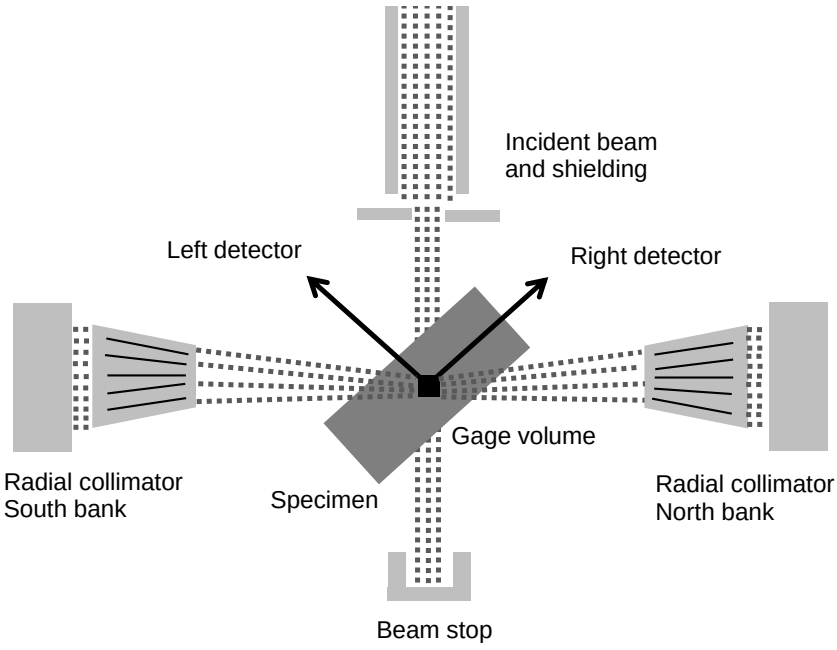

Figure 4-2: Schematic demonstration of neutron diffraction measurement set-up on Engin-X

By performing neutron diffraction tests on six of the C(T) specimens extracted from the welded plate, the lattice spacing, *d*, was initially measured along longitudinal, transverse and normal directions. Note that in neutron diffraction measurements on Engin-X, the lattice spacing at each point can be measured along two directions. Therefore, in the first set of measurements, the lattice spacing was measured along normal and longitudinal directions in the North bank and the South bank, respectively. After the sample rotation by 90°, the second set of measurements were conducted to measure lattice spacing along transverse and

longitudinal directions using the North and South banks, respectively. A picture of the setup is presented in Figure 4-3.

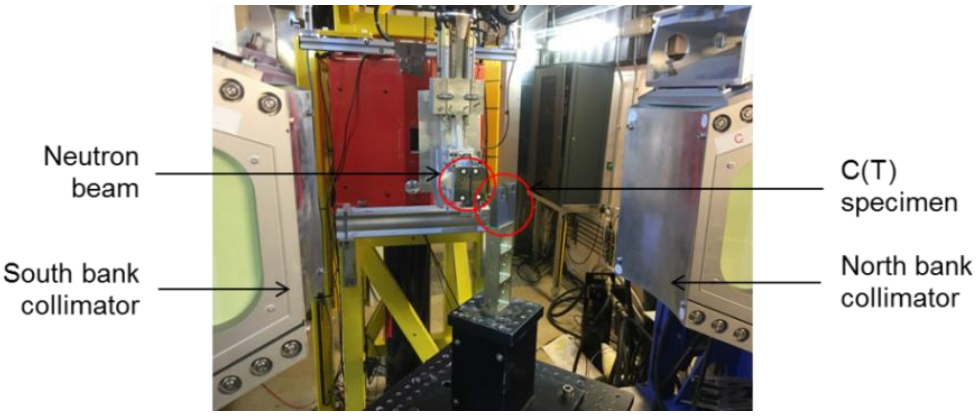

Figure 4-3: Neutron diffraction experimental set-up on Engin-X

4.1.2 Data analysis

The gathered *d*-spacing data from the ND experiments, which are calculated using the Bragg's law (see Equation 2-21), were analysed using General Structure Analysis System (GSAS) Open Genie software. The first five peaks have been selected (corresponding to 110, 200, 211, 220, 310 grain orientations) as the most dominant ones in BCC materials in "Neutron count vs. TOF" spectrum. HDF Explorer software was used to extract the *d*-spacing values from the Bragg peaks analysis. The analysis was performed by applying the Pawley fit [160], which is often used to analyse the neutron diffraction data for welded samples e.g. [22-24], to the obtained *d*-spacing data for different lattice planes and by employing elastic bulk properties of E = 190 GPa and ν = 0.3 in the analysis [164].

Subsequently, the residual strains can be calculated using:

$$\varepsilon_{hkl} = \frac{d_{hkl} - d_{0,hkl}}{d_{0,hkl}} \qquad \text{Equation 4-1}$$

where ε_{hkl} is the residual strain corresponding to the *hkl* plane, d_{hkl} is the lattice interplanar spacing of the crystal measured and $d_{0,hkl}$ is the lattice interplanar spacing of the strain-free sample.

The errors in the strain measurements are also calculated using:

$$\varepsilon_{err} = \sqrt{\frac{d_{err}^2}{d^2} + \frac{d_{0,err}^2}{d_0^2}} \qquad \text{Equation 4-2}$$

where ε_{err} is the error in the strain measurements, d_{err} is the error in the *d*-spacing measurements and $d_{0,err}$ is the error in the *d*-spacing measurements of the strain-free sample. Consequently, the residual stresses can be calculated using the equation below [165]:

$$\sigma_i = \frac{E_{hkl}}{1+\nu_{hkl}}\varepsilon_i + \frac{\nu_{hkl}E_{hkl}}{(1+\nu_{hkl})(1-2\nu_{hkl})}(\varepsilon_1+\varepsilon_2+\varepsilon_3) \qquad \text{Equation 4-3}$$

where σ_i is the residual stress corresponding to ε_i residual strain, E_{hkl} is the Young's modulus of the *hkl* plane, ν_{hkl} is the Poisson's ratio of the *hkl* plane, ε_1 is the residual strain in the first direction (e.g. longitudinal), ε_2 is the residual strain in the second direction (e.g. transverse) and ε_3 is the residual strain in the third direction (e.g. normal).

The error in the residual stress is calculated as per the following equation:

$$\sigma_{erri} = \sqrt{(\frac{E_{hkl}}{1+\nu_{hkl}}\varepsilon_{erri})^2 + (\frac{\nu_{hkl}E_{hkl}}{(1+\nu_{hkl})(1-2\nu_{hkl})})^2 \times (\varepsilon_{err1}^2 + \varepsilon_{err2}^2 + \varepsilon_{err3}^2)} \qquad \text{Equation 4-4}$$

where σ_{erri} is the error in the residual stress measurements, corresponding to the error in the residual strain measurements ε_{err} and ε_{err1} is the error in the strain measurement in the first direction (e.g. longitudinal), ε_{err2} is the error in the strain measurement in the second direction (e.g. transverse) and ε_{err3} is the error in the strain measurement in the third direction (e.g. normal).

As seen in Equation 4-1, an error in d_0 measurement will significantly affect the accuracy of residual strain and subsequently residual stress values obtained from neutron diffraction measurements. In order to minimise the error in d_0 measurements in this work, the strain-free measurements were performed on 10 small cubes of 3×3×3 mm^3 which were extracted from a nominally identical geometry, along the crack path. As explained before, a C(T) blank thicker than a standard one was initially extracted from the welded section. A 4 mm thick slice was machined off from the C(T) blank from which the individual strain-free cubes were extracted. These extracted cubes for strain-free measurements and their exact location with respect to the crack growth direction in C(T) specimen are shown in Figure 4-4.

(a) **(b)**

Figure 4-4: (a) Extraction location of the strain free samples for *d0* measurements (b) Strain free cube samples numbered from 1 to 10

The numbering of the cubes is to record the order of the extracted cubes with respect to the distance from the crack tip in the main C(T) sample. d_0 measurements were performed on individual cubes and their orientation specific values were recorded in North and South banks. The residual strains were calculated using Equation 4-1 and subsequently residual stresses were calculated in all three directions.

4.1.3 Results and discussion

The residual strain and residual stress measurements in all three directions from the HAZ 0 specimen, which was also tested using contour method, are presented against the distance from the crack tip in Figure 4-5 and Figure 4-6, respectively. It can be observed that the highest value of residual strain, and therefore residual stress, is obtained in the normal direction, followed by the longitudinal trend and finally the transverse results which are on average closer to zero.

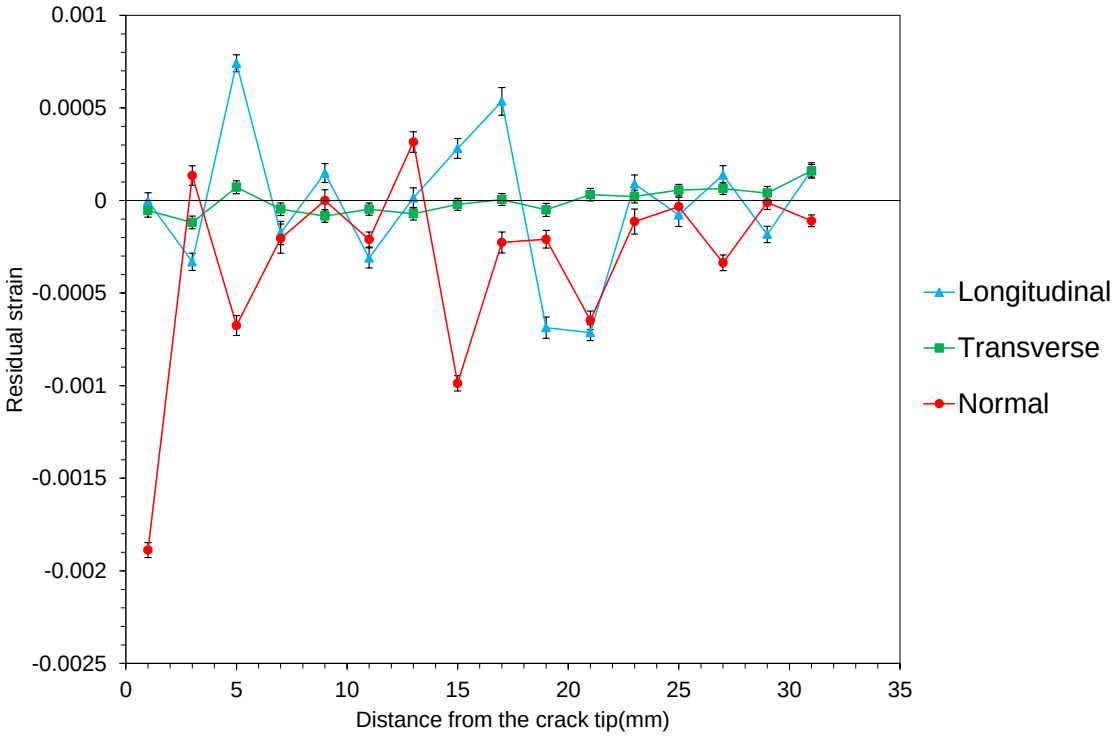

Figure 4-5: Residual strain measurements on HAZ 0 C(T) specimen using neutron diffraction technique

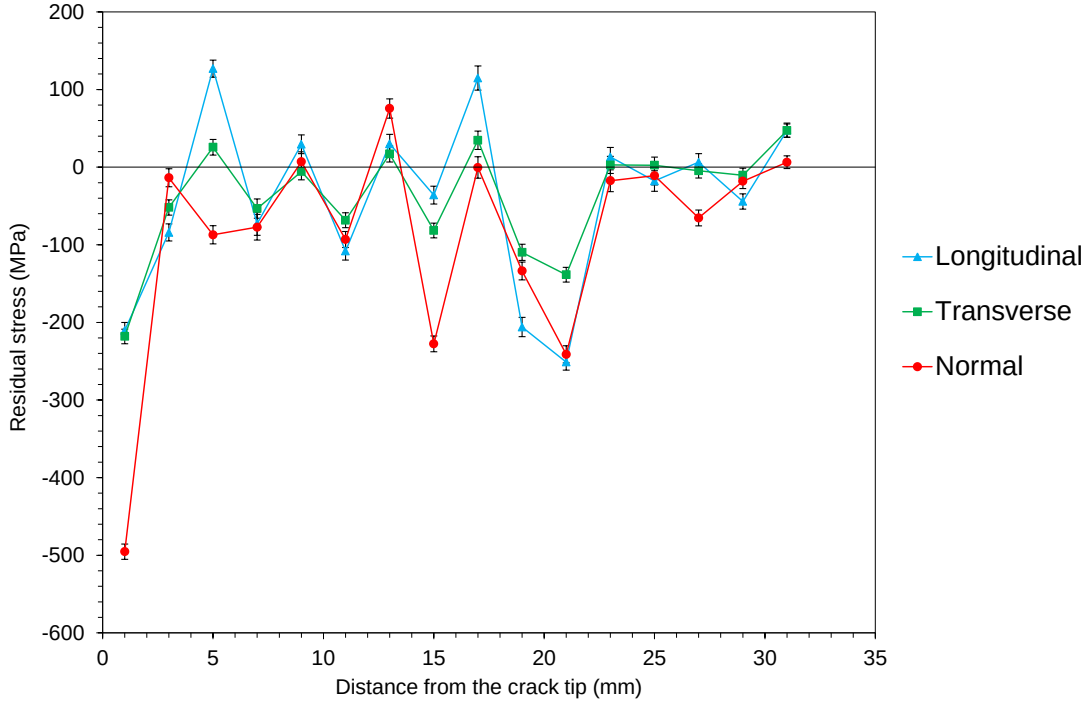

Figure 4-6: Residual stress measurements on HAZ 0 C(T) specimen using neutron diffraction

It is evident from Figure 4-6 that there is high level of compressive residual stress at the notch tip with the largest magnitude observed in the normal direction. Transverse residual

stress of around -200 MPa is measured at the notch tip, which is expected to influence the fatigue crack growth behaviour of the material, particularly at the early stages of the test. Ahead of the crack tip, along the expected crack propagation line at mid-thickness, there can be observed variation in the measured residual stress profiles. However, the trend of the transverse and normal residual stress profiles in particular, is overall in compression.

The residual stress measurements in the transverse direction, at mid-height and mid-thickness, from HAZ 2, HAZ 3 and HAZ 4 (samples that have then been tested in air) are presented against the distance from the crack tip in Figure 4-7. It is worth noting that HAZ 2 and HAZ 3 specimens had 180° orientation whereas HAZ 4 had 0° orientation (see Table 3-1). It can also be noticed that there is high level of compressive residual stresses on HAZ 3 and HAZ 4 while on HAZ 2 a combination of tensile and compressive can be observed. Such levels of transverse residual stresses are expected to influence the fatigue crack growth behaviour of the material, particularly at the early stages of the test.

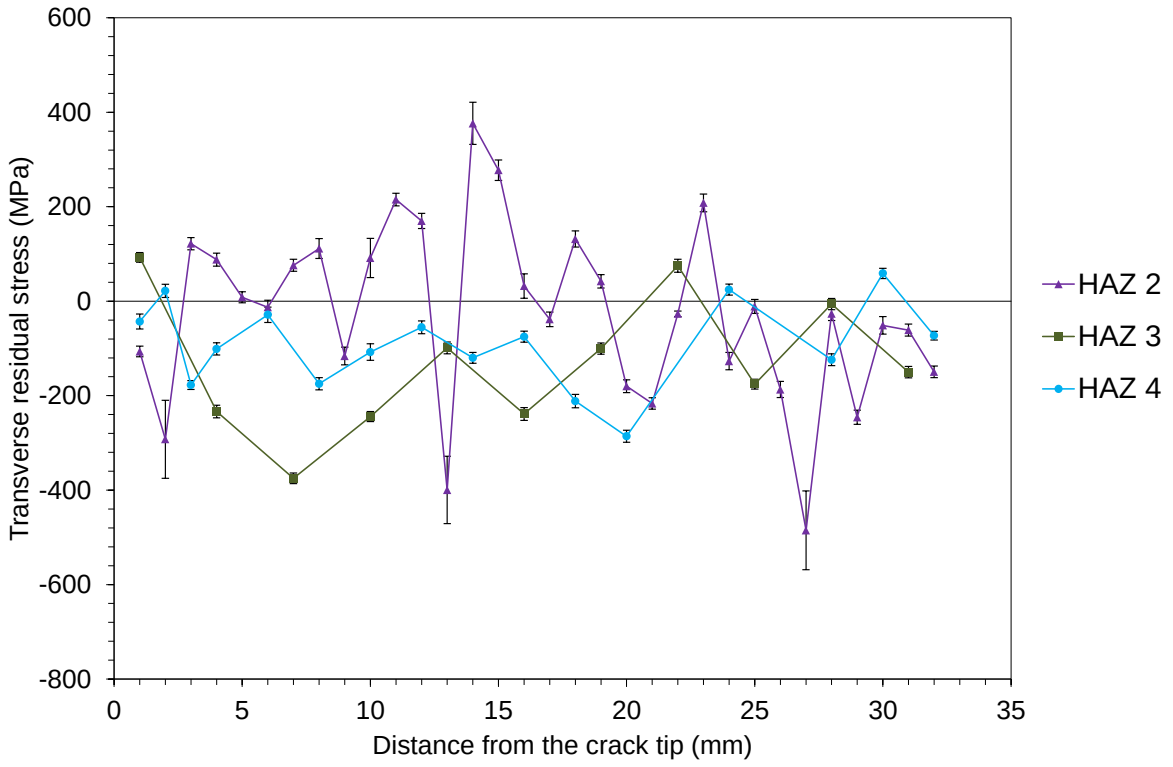

Figure 4-7: Transverse residual stresses on HAZ 2, HAZ 3 and HAZ 4 along the crack direction and before pre-cracking

The transverse residual stress measurement results from HAZ 7 and HAZ 9 C(T) specimens (samples that have then been tested in seawater) are presented in Figure 4-8. It is worth

noting that HAZ 7 had 0° orientation whereas HAZ 9 had 180° orientation (see Table 3-1). It can be observed, in the same way as for the previously presented results, RS in HAZ 7 and HAZ 9 are mainly compressive ahead of the crack tip and display a combination of tensile and compressive values towards the centre of the specimen. However, it can be expected that the first point measured on HAZ 9 representing a tensile value of RS at the crack tip will promote accelerated crack propagation, especially during pre-fatigue cracking. In contrast, the pre-cracking stage is expected to be performed on HAZ 7 under a higher number of cycles (i.e. longer time needed to propagate the crack).

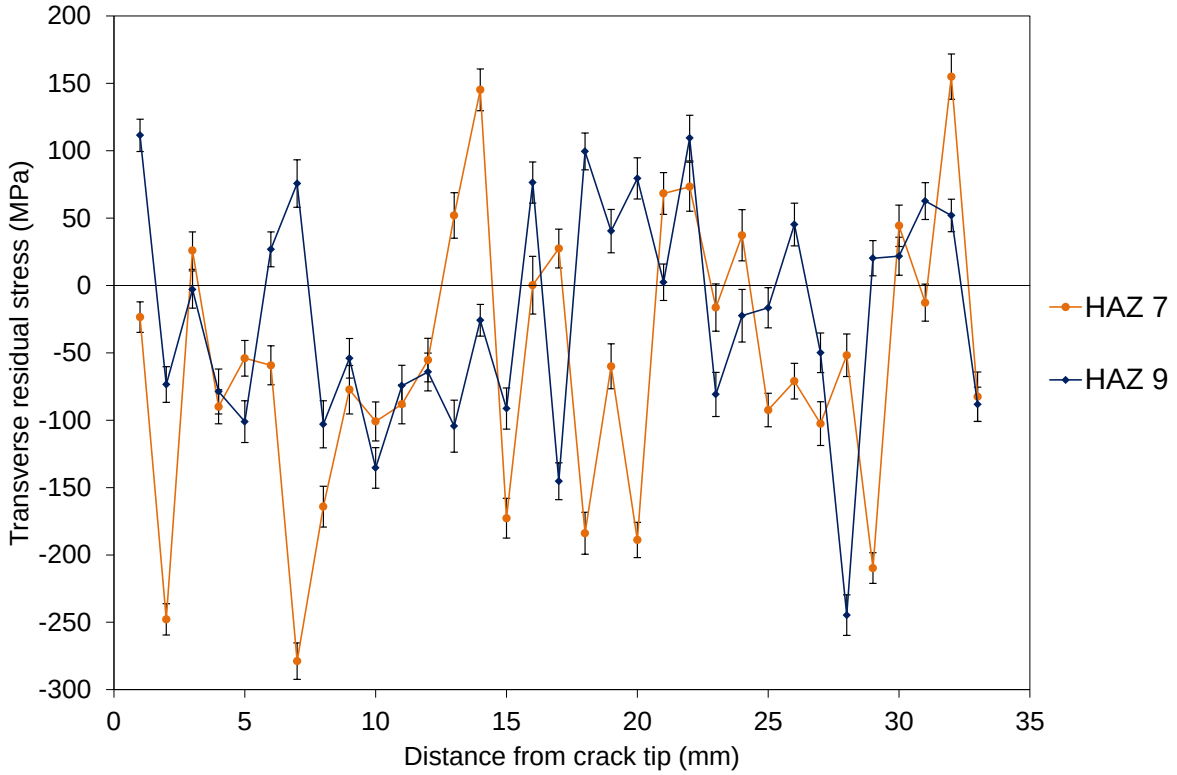

Figure 4-8: Transverse residual stresses on HAZ 7 and HAZ 9 along the crack direction and before pre-cracking

The whole set of measurements performed in this study using ND are gathered in Figure 4-9. The boundaries of the locked-in RS in transverse direction are given by HAZ 2, with a highest tensile value of 376 MPa measured and -485 MPa in compression. For the remaining C(T) specimens much lower peak values of tensile and compressive residual stresses have been measured using the ND technique. It can be seen in Figure 4-9 that the transverse residual stress values at the crack tip are generally between -100 and +100 MPa except HAZ 0 specimen which shows compressive transverse RS of -200 MPa at the crack tip.

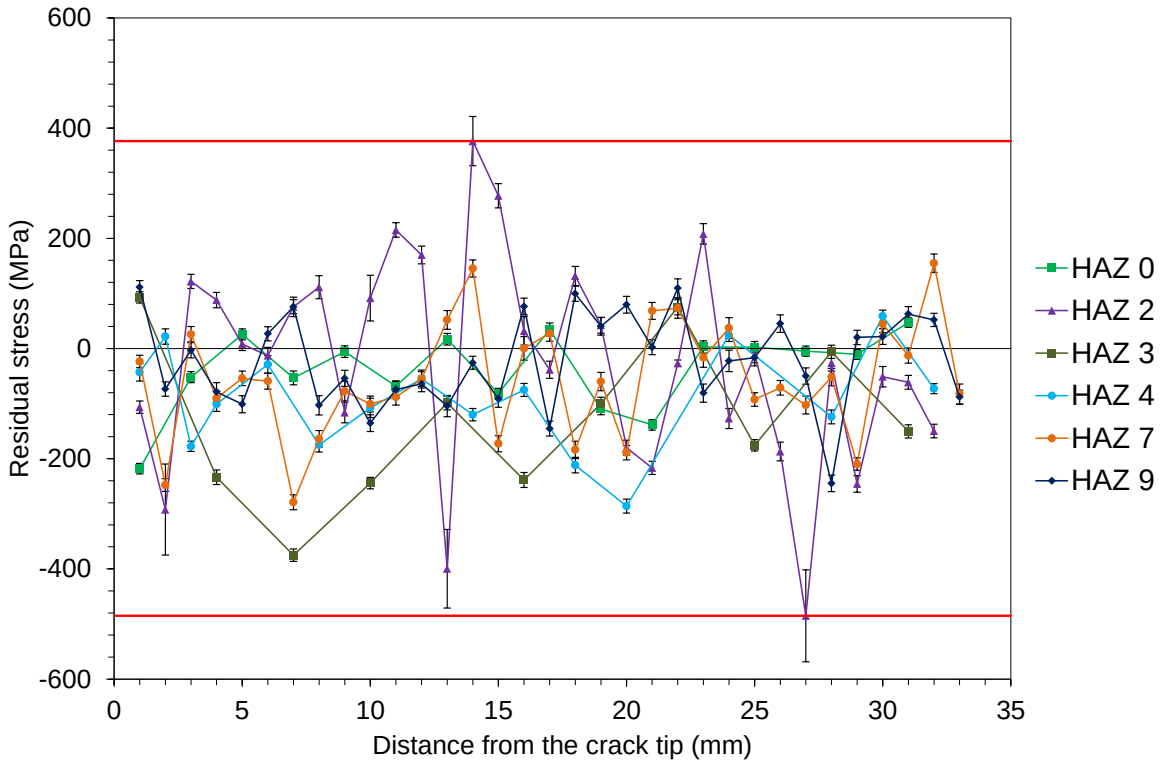

Figure 4-9: Transverse RS at mid-height and mid-thickness of all the HAZ samples measured on Engin-X

The locked-in welding residual stresses and their redistribution during FCG tests will change the *R*-ratio (stress ratio), the mean stress and effective stress intensity factor range, ΔK_{eff}. The effectiveness of mean stress conditions on the fatigue response of welded components is investigated in [166] where the presented results give an insight into the optimisation of the welding parameters in order to improve the fatigue life of welded components. The results obtained from this study have shown that in order to accurately characterise fatigue crack initiation and propagation behaviour in monopile welded structures, realistic values of residual stresses which are much greater than the remaining residual stresses in C(T) specimens must be considered in structural testing and analyses.

The ND measurements will be accounted for in interpretation of the FCG results in the following chapters and will be the foundation of the numerical work established in this project. For general reference and information, additional ND results are presented in Appendix E, longitudinal and normal directions are presented against the distance from the crack tip.

4.2 Neutron imaging

NI measurements have been performed on three C(T) specimens and at different stages of the FCG. A test matrix with the detail of the samples measured using the NI technique on IMAT instrument is recorded in Table 4-1. Measurements have been performed before pre-fatigue cracking (0 mm), after pre-cracking (4 mm), at 7 mm crack length and finally after 10 mm crack growth. The details of FCG in HAZ 1, HAZ 2 and HAZ 3 specimen will be presented in Chapter 5.

Table 4-1: HAZ samples tested on IMAT

	0 mm	**4 mm**	**7 mm**	**10 mm**
HAZ 1		x		
HAZ 2	x			
HAZ 4	x	x	x	x

It is worth noting that only longitudinal residual strains were studied in this section due to the unavailability of the data in transverse and normal directions. The measurements are compared with ND results and a sensitivity analysis was performed with respect to the strain free values to consider in the data analysis.

4.2.1 Test set-up

In this project, neutron imaging technique was used to produce radiographies of the samples where images were directly produced by transmitting a neutron beam through a specimen onto an MCP detector, the principle that is described by Tremsin et al. [136]. The calibration of the IMAT instrument follows the same process as ND measurements on Engin-X. In neuron transmission, the experimental set-up is such that the Bragg's angle is equal to 90° as shown in Figure 4-10. The C(T) samples were tested on IMAT and a sensitivity analysis has been performed with respect to the d_0 values chosen.

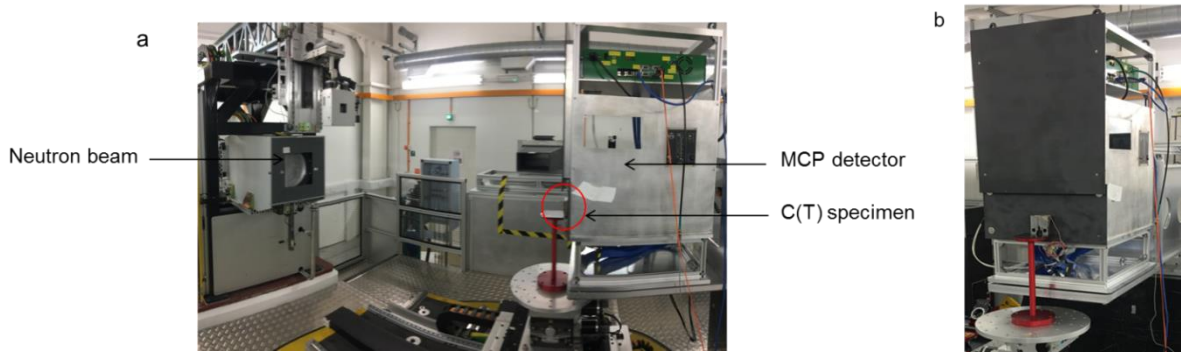

Figure 4-10: (a) Neutron imaging experimental set-up on IMAT; (b) C(T) specimen in front of the MCP detector

4.2.2 Data analysis

Bragg-edge transmission data analysis codes have been developed within different institutions. The Rietveld Imaging of Transmission Spectra (RITS) was developed by Hirotaka Sato at Hokkaido University in Japan. MCP Bragg Edge Release software and the software developed by Kenichi are also implemented in order to analyse NI data. However, due to confidentiality and difficulties in accessing software, the data analysis process presented in this work is based on a Python code kept confidential and developed at ISIS-STFC.

The code developed and used in this research project was based on the transmission Equation 2-22 presented in section 2.7.3.1 and has been executed through the command line. The raw data are corrected after uploading the open beam (measurements without any sample, the neutron beam directly hits the MCP detector) and sample beam measurements. An example of the radiography obtained with the neutron imaging technology is presented in Figure 4-11 where the weld beads and the HAZ region are clearly visible.

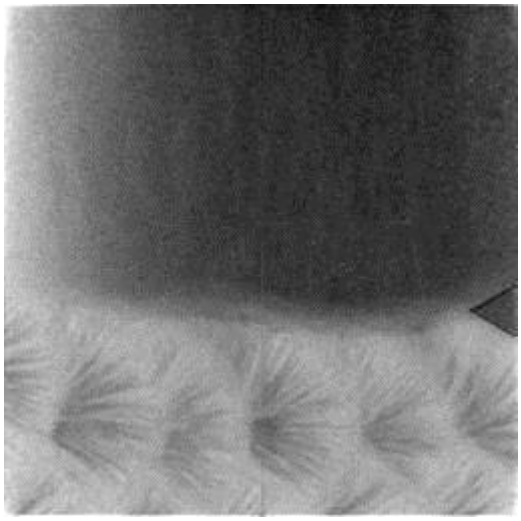

Figure 4-11: Raw image of a C(T) scanned on IMAT at the crack tip location

Based on a flight path of 56.4 m on IMAT and a selection of the area of interest, the transmission profile, expressed as "Neutron transmission vs Wavelength", can be plotted as shown in Figure 4-12. Each variation in transmission value represents a crystallographic plane orientation given by the Miller indices. The transmission spectrum of thermal neutrons through a polycrystalline sample displays sudden, well-defined increases in intensity as a function of neutron wavelength. These Bragg edges occur because for a given hkl reflection, the Bragg angle increases as the wavelength increases [167]. The region around the largest edge, corresponding to 110 orientation for BCC materials, is then selected and a fit curve is obtained as indicated in Figure 4-13. The parameters obtained from the Bragg edge fitting stage are then used in order to obtain a 2D strain mapping of the area of interest. An example of a map of the wavelength within the selected area obtained can be found in Figure 4-14.

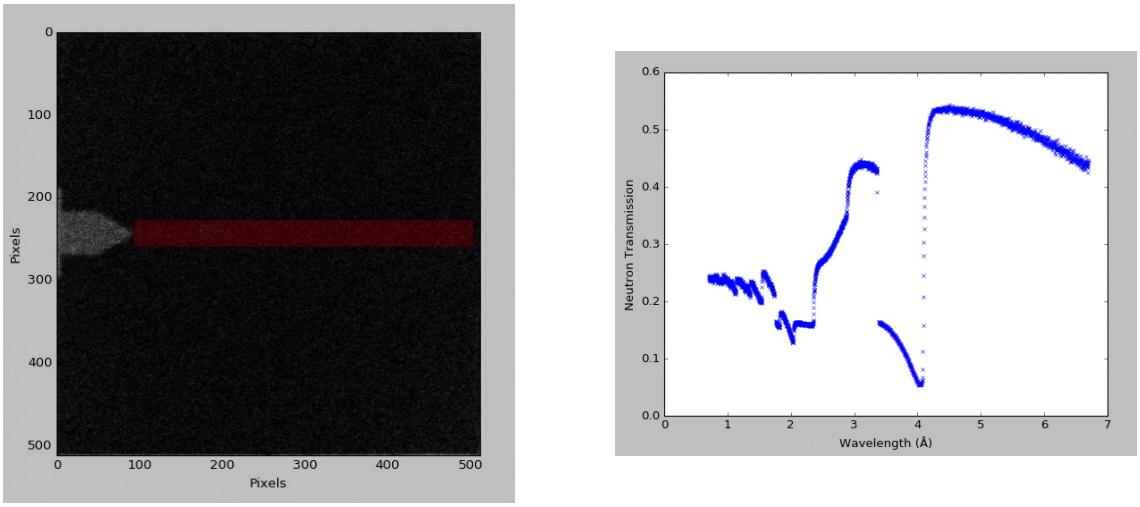

Figure 4-12: Transmission profile for the HAZ selected region

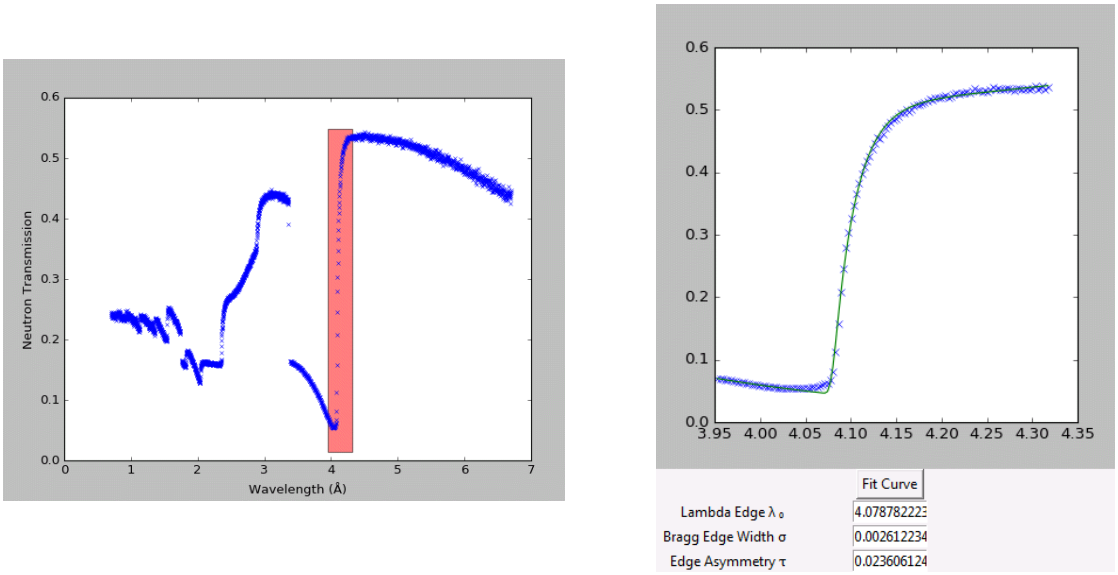

Figure 4-13: Bragg edge fitting stage

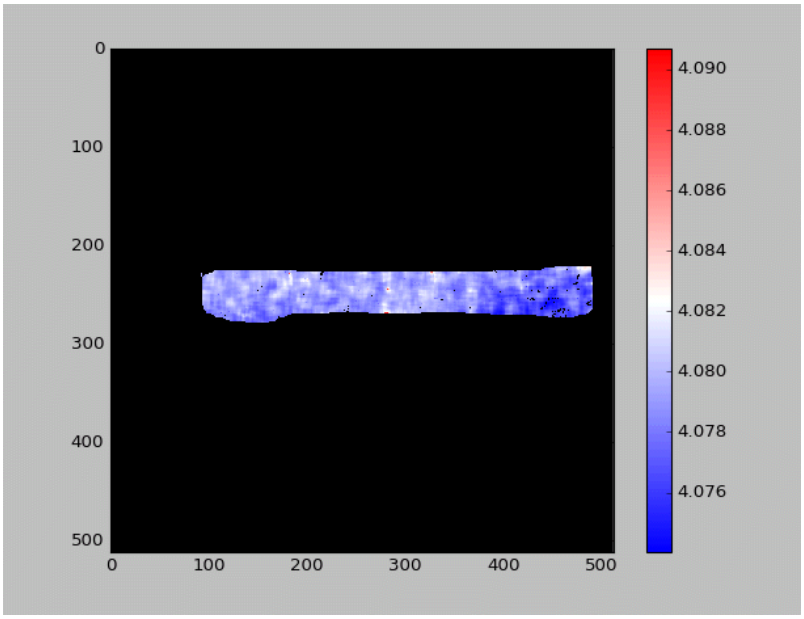

Figure 4-14: 2D map of the wavelength within the area of interest

The second stage of the NI data analysis is performed using the Fiji ImageJ software. A black and white image is exported from the previous stage so that ImageJ can process the pixel values as a grey scale. The same region is selected and a graph of the "Wavelength vs the distance from the crack tip in pixel" is obtained as shown in Figure 4-15. The distance in pixel is converted to distance in mm, knowing that 1 pixel is 55 µm. The imaging set-up is such that the incidence angle (between the beam line and the sample surface) is always 90°, therefore the sinus of 90 is equal to 1, hence, according to the Bragg's law, the *d*-spacing is obtained by dividing the wavelength by two. The strain is thereafter calculated in the same way as for ND data analysis.

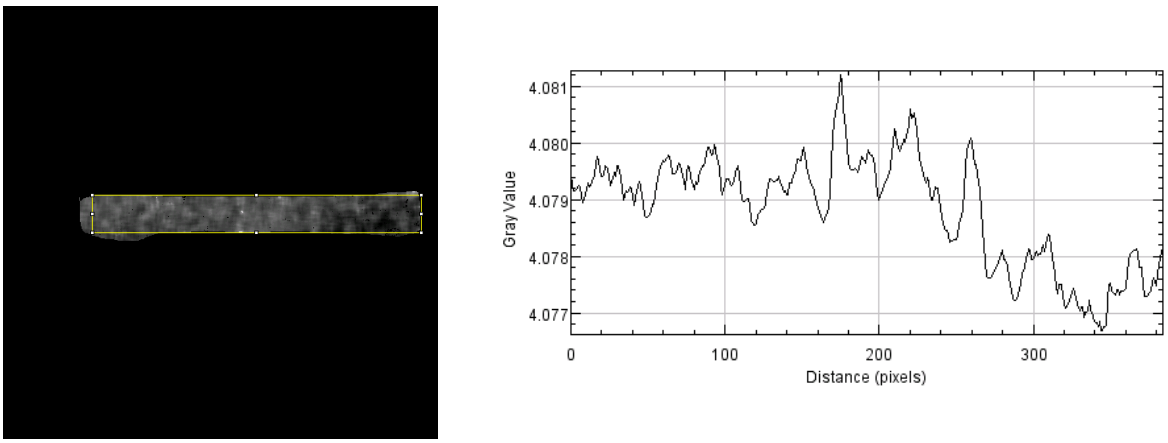

Figure 4-15: Wavelength profile within the selected region

4.2.3 Results and discussion

Neutron imaging technique was used to produce radiographies of the samples where images were directly produced by transmitting a neutron beam through a specimen onto an MCP detector, the principle that is described in [136]. The C(T) samples were tested on IMAT and a sensitivity analysis has been performed with respect to the d_0 values chosen. The following cases have been considered in the data analysis and the results compared:

- d_0 values taken from neutron diffraction measurements
- A single d_0 value taken as the average of the neutron imaging measurements within the HAZ region
- A single d_0 value taken from the strain balance through thickness in longitudinal direction
- A single d_0 value taken from the corner of the sample as described in Figure 4-16

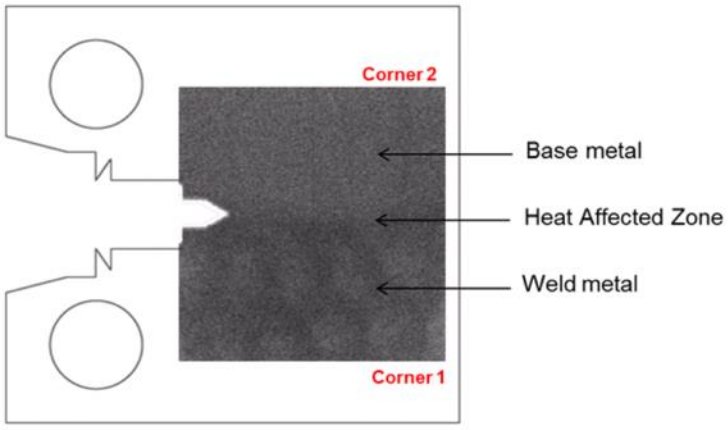

Figure 4-16: Neutron radiography of HAZ 2 and the d_0 location with respect to the BM, HAZ and WM

It is also worth noting that the corners taken for the d_0 measurements are not the actual corners of the sample and due to the size of the MCP detector only a portion of the sample can be imaged. Also, measurements of the small cubes used for the d_0 values of the neutron diffraction measurements could not be measured through neutron imaging due to their small size.

The residual strain measured using neutron diffraction and neutron imaging techniques in through thickness direction are presented and compared for HAZ 2 specimen in Figure 4-17. Indeed, neutron imaging is a volumetric measurement applied on a plane to measure residual

strains in a direction normal to the plane orientation, while neutron diffraction provides residual strains along two directions (i.e. strains in all three directions can be generated by rotating the sample) at a specific point. It can be seen in this figure that the neutron imaging residual strain results, analysed using different d_0 assumptions, follow the same trend. Moreover, the location of the corner for the d_0 value seems to influence the analysis. Corner 1 (see Figure 4-16) may include non-strain free conditions as it is located within the WM while d_0 values taken from corner 2 (Figure 4-16) provide similar values as the other cases studied as it is located within the BM. Finally seen in this figure is that the residual strain (hence residual stress) trends lie on top of each other when d_0 is taken as the average of the neutron imaging data in the HAZ region and in the case where d_0 value comes from the strain balance of the same region in through thickness direction. The results obtained from these two cases agree well with the analysis based on d_0 value at corner 2 and all of these results are in good agreement with ND residual strain measurements on the C(T) specimens.

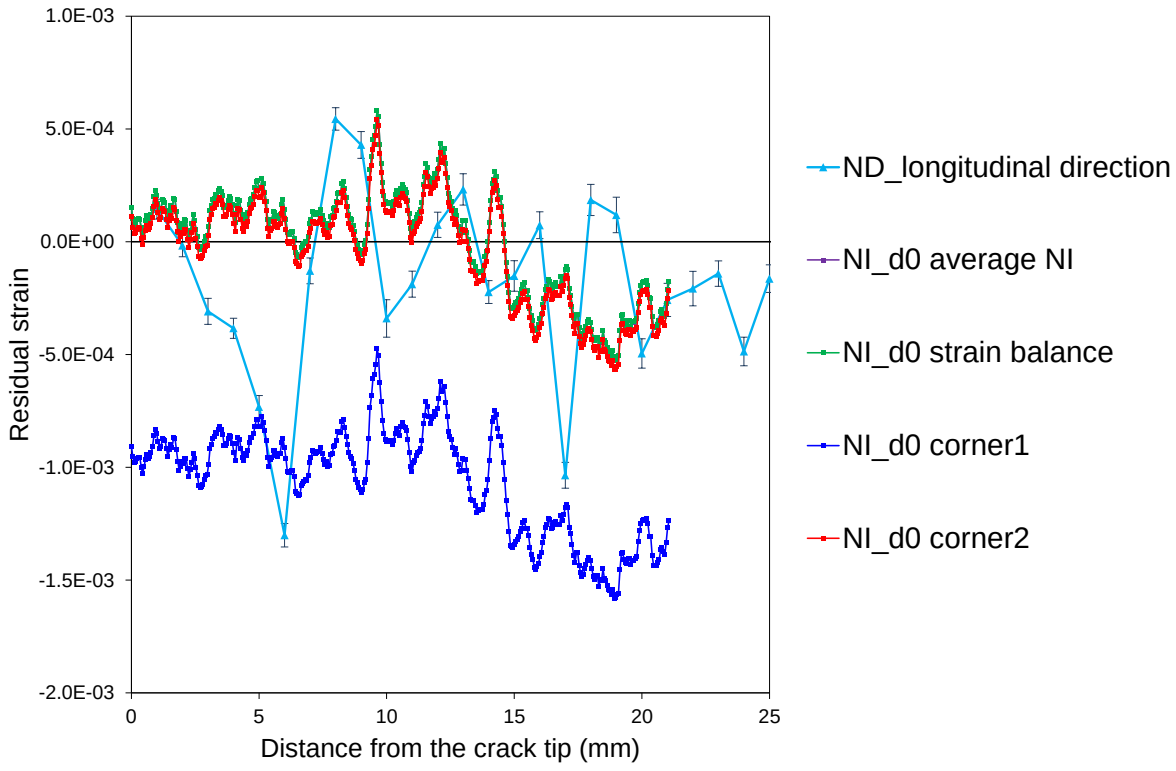

Figure 4-17: Longitudinal residual strains within HAZ 2 using ND and NI techniques with different d_0 assumptions

The NI data analysis on HAZ 2 specimen study has shown that d_0 value for residual strain calculation can be taken as the average of the d values measured but it can also be taken from the strain balance as both curves overlap. In order to avoid potential uncertainties and for the

purpose of repeatability of the data analysis process, d_0 was subsequently taken as the average of the d values measured in NI. The residual strains measured in longitudinal direction on HAZ 1 and HAZ 4 are presented in Figure 4-18 and Figure 4-19, respectively. Neutron imaging and neutron diffraction results are compared for HAZ 4 only as no neutron diffraction data was available for HAZ 1.

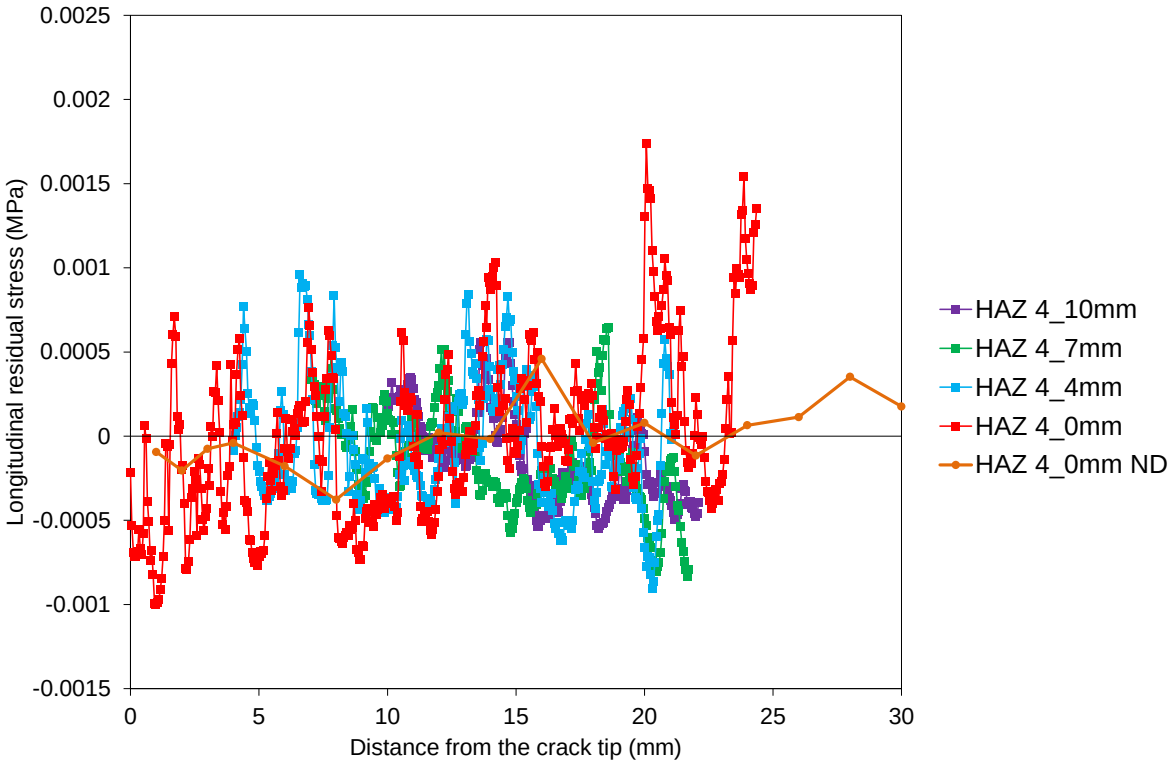

Figure 4-18: Longitudinal residual strain variations against crack length on HAZ 4

Neutron diffraction results were only available for HAZ 4 and with no crack. It can be observed that the neutron imaging results fit along the neutron diffraction curve. It can be also seen that as the crack propagates, residual strains redistribute and tend towards zero. However, at 10 mm crack growth, the remaining residual strains may still have an effect on the fatigue crack growth of the material as they are not completely vanished. The results obtained from neutron imaging and presented in Figure 4-19 provide a justification to the FCG behaviours observed on the exact same samples and will be discussed over the next chapters where HAZ 1 and HAZ 4 are tested in air.

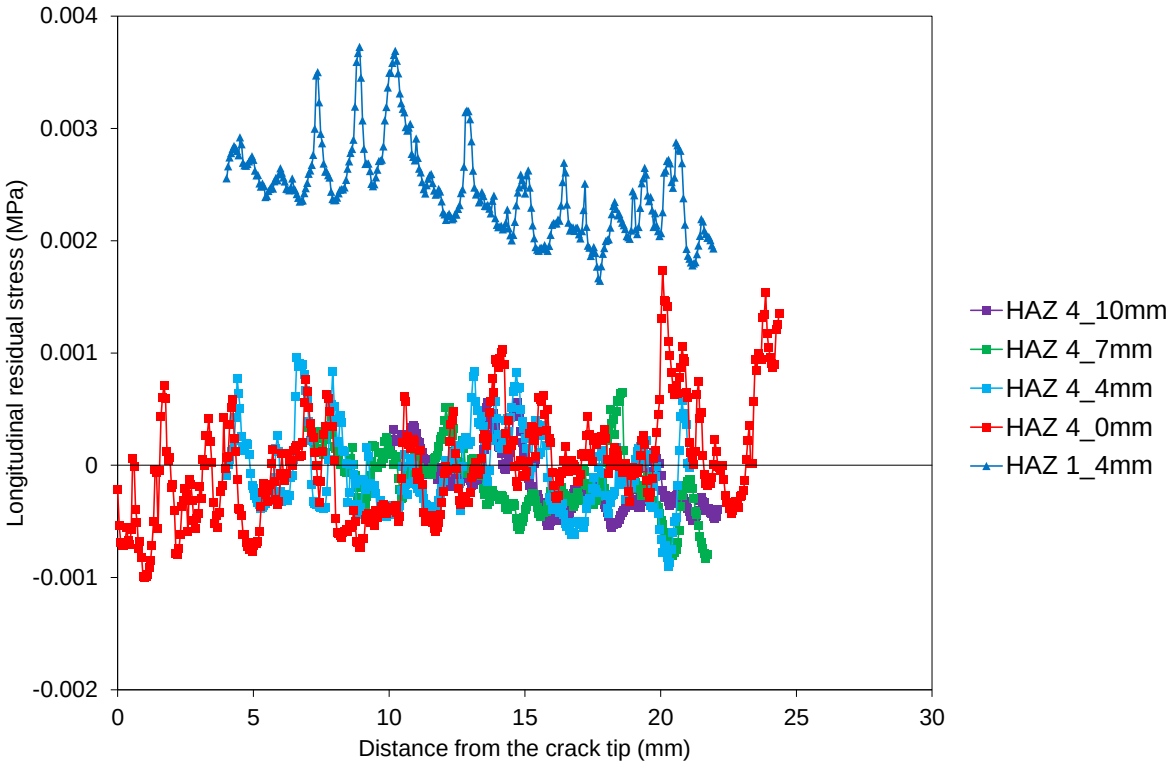

Figure 4-19: Longitudinal residual strain on HAZ 1 and HAZ 4 from neutron imaging measurements

4.3 Contour method

The contour method of residual stress measurement involves carefully cutting the specimen of interest using wire EDM, measuring the out of plane deformation profile of the newly created cut faces, averaging the measured deformation profiles from the two cut parts, filtering out experimental noise, applying the reverse of the averaged smoothed profile as nodal displacement boundary conditions in an FEA model of the cut part and finally performing an elastic stress analysis [168]. The back calculated stresses on the cut surface obtained from the FEA modelling step is a true representation of the residual stress component acting normal to the cut plane that was present in the sample prior to performing the cut.

4.3.1 Measurements on a C(T) specimen

The contour method residual stress measurement was performed on HAZ 0 C(T) specimen, after non-destructive neutron diffraction measurements, over the plane of expected fatigue crack growth; that is a longitudinal cut plane to measure transverse stresses (see Figure 4-20).

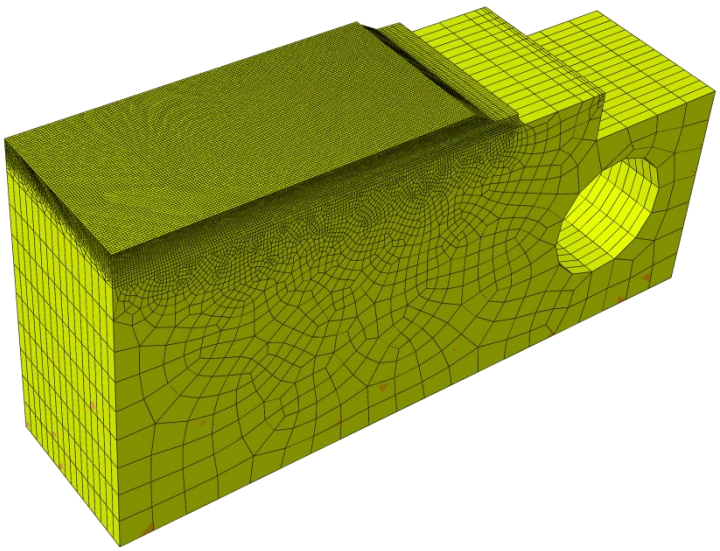

Figure 4-20: Illustration of the mesh of the FE model used in the contour method residual stress determination of the C(T) specimen

An Agie Charmilles Cut 1000 EDM machine with a 50 μm diameter brass wire was used to perform the contour cut. Prior to the cut, a layer of sacrificial material was attached to the top and bottom surfaces using electrically conductive glue to mitigate the wire entry and exit cutting artefacts [169]. The sample was securely clamped to the EDM stage (see Figure 4-21), which was then filled with deionised water and left to reach thermal equilibrium before starting the cut. The cut surfaces were cleaned using acetone, isopropanol, and a soft brush and placed in the lab to reach thermal equilibrium with the ambient air. A Zeiss Eclipse coordinate measuring machine, fitted with a Micro-Epsilon laser probe and a 2 mm diameter ruby-tipped Renishaw PH10M touch trigger probe was used for surface deformation measurements. The surface profile of both cut surfaces was measured using the laser probe with an in-plane point spacing of 25 μm adopted. In addition, the perimeters of the two cut parts were measured with the touch-probe and later used for precisely aligning the measurements of the two cut parts before averaging the profiles and for creating an accurate FEA model geometry.

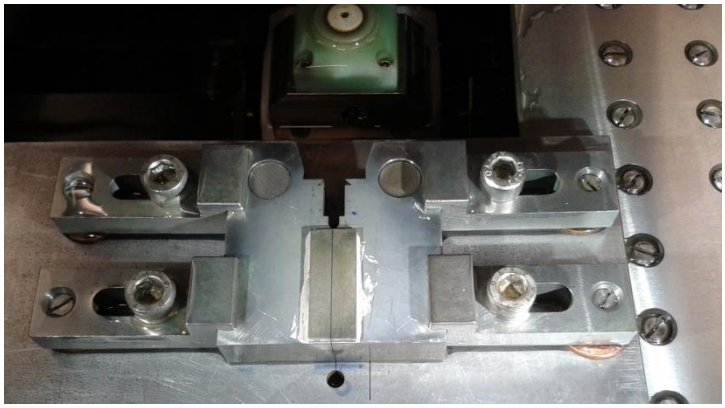

Figure 4-21: Clamping arrangement for the EDM cutting step of the contour method on the C(T) sample. The photo also shows the sacrificial layer on the top surface

To calculate the displacement profile, the data sets for opposing cut surfaces were aligned using the measured perimeters and then interpolated onto a common grid before averaging to remove errors due to shear stress and possible anti-symmetric cutting artefacts [168]. Due to the uncertainty in the coordinate measuring machine measurements and the roughness of the EDM cut surfaces, noise in the displacement profile is unavoidable and it would be further amplified in the stress calculation. Therefore, the profile was smoothed using a median filter. The smoothing level was modulated by varying the 'mask size' between 0.275 and 2.025 mm in steps of 0.25 mm and the optimum smoothing level within this range was given by a mask size of 1.525 mm. For this mask size, the overall fitting error, estimated using the approach in [170], was just over 7 MPa.

To calculate the stresses, an FEA model was created in ABAQUS with the geometry of one of the cut halves (see Figure 4-20). The model was meshed using linear hexahedral elements with reduced integration (C3D8R). The mesh at the cut surface was biased from 0.25 mm near the surface of interest up to 3 mm on the opposite face. The model was assigned uniform isotropic elastic properties, with a Young's modulus of 190 GPa and Poisson's ratio of 0.3. The smoothed displacement profile, with a reverse sign, was applied as surface boundary condition on the surface nodes of the FEA model of the cut parts and an elastic stress analysis was performed. The 2D map of transverse residual stress obtained from the contour method, shown in Figure 4-22, provides a rich set of information about the distribution of residual stress over the expected plane of crack growth in the C(T) specimen.

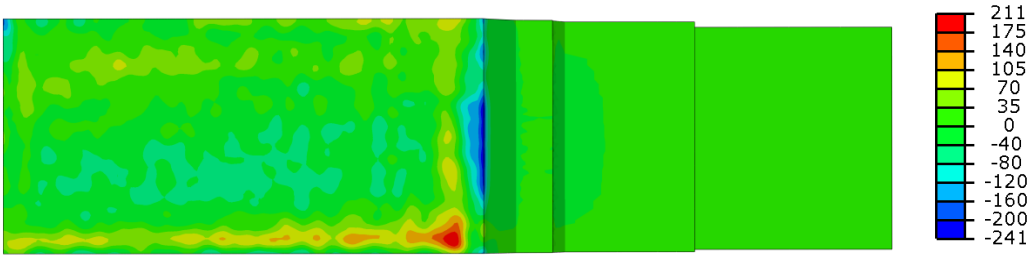

Figure 4-22: Contour residual stress measurement results along transverse direction of the weld on the C(T) specimen. The stress scale is in MPa

The contour map showed the presence of high compressive residual stress at the central region through the thickness of the sample near the crack tip with much lower level of compressive stresses further ahead of the notch. An important observation from the 2D cross-sectional map of transverse residual stress is the variation of transverse residual stress through the thickness of the sample.

The transverse residual stresses measured using the contour method and neutron diffraction for a line profile at mid-thickness of the C(T) sample are compared in Figure 4-23. Similar to neutron diffraction measurements, the contour method showed the presence of high level of compressive transverse residual stress of around -200 MPa at the crack tip. It is worth noting that neutron diffraction gives averaged stresses over the measured gauge volume (in this case 2mm x 2mm x 2mm). Therefore, in order to compare the results on a fair basis, an additional line profile for the contour method is provided where the contour stresses are averaged over the neutron diffraction gauge area. Both the local contour stress line profile and the contour stress line profile averaged over neutron diffraction gauge volume confirmed that transverse residual stresses ahead of the crack tip are predominantly in compression and the level of stress is less than -50 MPa further ahead of the crack tip.

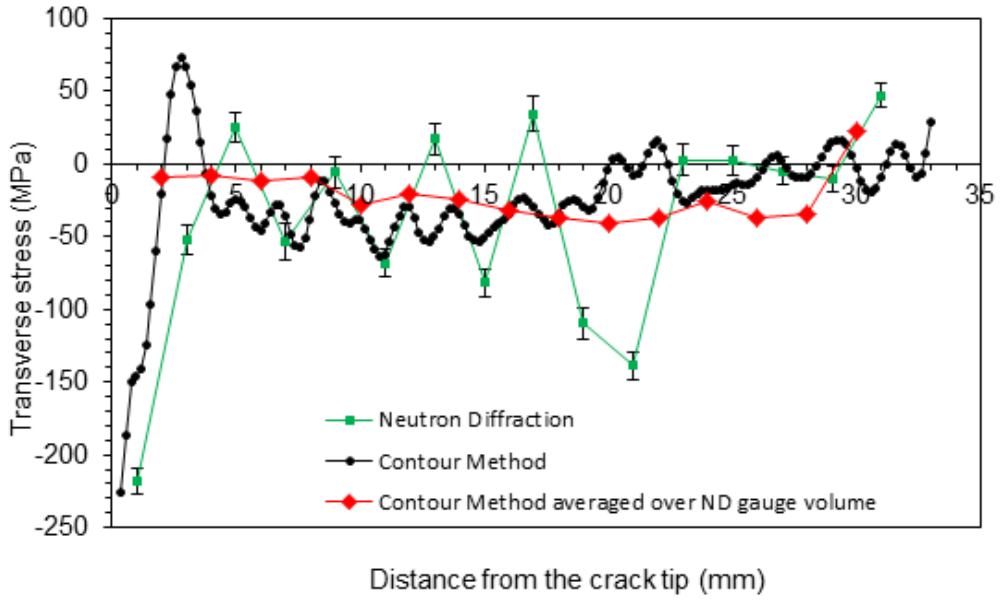

Figure 4-23: Comparison of transverse residual stress measurements on the C(T) specimen using neutron diffraction and the contour method

The study carried out on C(T) specimens extracted from a welded plate has shown a non-uniform distribution of transverse residual stresses on the crack plane (i.e. compressive at the mid-thickness and tensile at the outer surfaces as observed on the contour measurement results). The varying through-thickness residual stress distribution profile subsequently influences the crack propagation rate profile leading to uncertainties in crack growth monitoring in fracture mechanics specimens. This indicates that the crack length measured on the outer surface may differ to the crack length at the mid-thickness, depending on the residual stress distribution profile. As the crack propagates, residual stresses redistribute and are likely to slowly vanish. However, the presence of residual stress significantly influences the effective threshold stress intensity factor range, $\Delta K_{eff,th}$, and hence the crack initiation and early crack propagation. Therefore, more pronounced effects from residual stresses are expected on the fatigue crack initiation and early stage fatigue crack propagation.

4.3.2 Measurements on a welded mock-up

For the large welded mock-up the contour method was conducted on a transverse plane at mid-length to map 2D distribution of longitudinal stresses. An Agie Charmilles FI 440 ccS EDM machine was used to perform the cut using a 250 µm diameter brass wire. The sample was firmly clamped to the EDM stage, which was then filled with deionised water and left to reach thermal equilibrium before starting the cut. To mitigate plasticity and the so-called

bulge error [27–29], the main cut through the weld was performed between two pilot holes and the remaining ligaments were cut afterwards.

The cut surfaces were cleaned and then measured with the same measurement equipment described earlier. In addition, the perimeters of the two cut parts were measured with the touch-probe. The standard data analysis approach as explained earlier was performed on the measured surface deformations. Figure 4-24 shows the averaged displacement profile prior to smoothing.

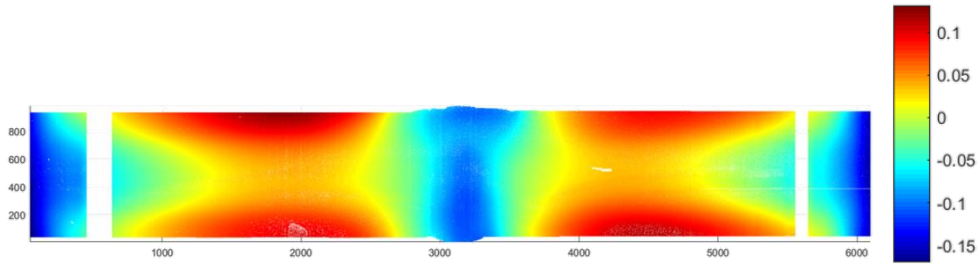

Figure 4-24: Map of the averaged surface deformation of the cut surfaces for the contour method. Deformation unit is in millimetres

The smoothing level was modulated by varying the ‘mask size’ of a median filter between 3.1 and 10.1 mm in steps of 1 mm and the optimum smoothing level within this range was given by a 6.1 mm mask size. For this mask size, the overall fitting error, estimated using the approach in [170], was less than 5 MPa.

The FEA model to back calculate the stresses, see Figure 4-25, was meshed using linear hexahedral elements with reduced integration (C3D8R). The mesh on the cut surface was biased from 1 mm near the weld up to 3.5 mm away from the weld. A bias was also applied in the extrusion direction, moving away from the cut face, from 0.5 up to 50 mm. The model was assigned uniform isotropic elastic properties, with a Young’s modulus of 190 GPa and Poisson’s ratio of 0.3. The smoothed displacement profile, with a reverse sign, was applied as boundary condition on the surface nodes of the simulated cut parts.

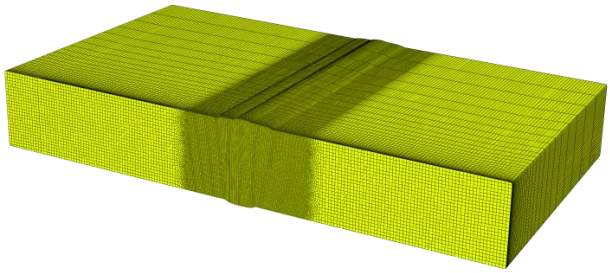

Figure 4-25: Illustration of the mesh of the FE model used in the contour method residual stress determination of the welded mock-up

The resulting 2D map of the stress component normal to the cut surface represents the initial residual stress distribution acting longitudinally to the weld (Figure 4-26). It can be seen in Figure 4-26 that there are two distinct regions of tensile stress within the weld, which correlate to the double-groove welding sequence. Compressive stresses are observed on the top and bottom faces of the plate away from the weld, while high tensile stresses are present towards the ends of the cross-section (extreme left and right-hand-sides). The compressive stresses, observed at top and bottom faces, are believed to have been introduced as a result of the rolling process that the plates were subjected to before welding. In addition, these compressive stresses may have been intensified to balance the tensile stresses introduced due to the welding process elsewhere within the cross-section. The tensile residual stresses towards the ends of the plate are believed to be the result of the flame cutting operation that was performed to extract the 600 mm x 600 mm sample out of the larger (2600 mm × 800 mm) welded mock-up. Note that these near surface tensile residual stresses at two ends of the plate are sufficiently away from the weld region with insignificant penetration depth, confirming that the flame cuts had negligible effects on the residual stress profiles near the weld toes. Due to the presence of pilot holes, no deformation data was recorded adjacent to the pilot holes.

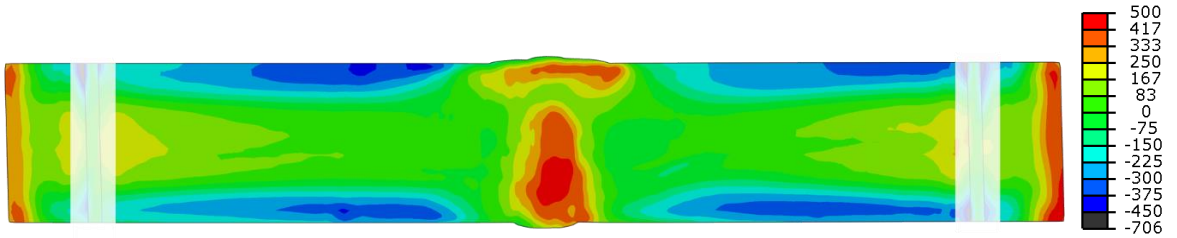

Figure 4-26: Longitudinal residual stress measurement obtained from the contour method. The stress unit is in MPa

A comparison of the residual stresses in longitudinal direction between the C(T) specimen, measured using neutron diffraction technique, and the large welded mock-up, measured using

the contour method, is given in Figure 4-27. In order to accurately compare both measurements, the results from the welded plate have been taken within the region exactly where the C(T) sample was extracted from. As seen in Figure 4-27, the longitudinal residual stresses measured on the C(T) sample are significantly lower than those in the welded plate as they tend to vanish and redistribute during the specimen extraction process. The residual stress reduction due to sample extraction has also been noted and discussed by other researchers in [28-29]. The results from the literature and the current study demonstrate that although specimen extraction reduces the residual stress levels, a substantial amount of residual stresses still remain in the extracted samples which can play a significant role in laboratory scale FCG tests on C(T) fracture mechanics specimens. This observation confirms the ND and NI measurement results which showed significant remaining residual stresses in C(T) specimens even after 100 mm of crack growth. Therefore, these stresses need to be measured and considered in the FCG data analysis.

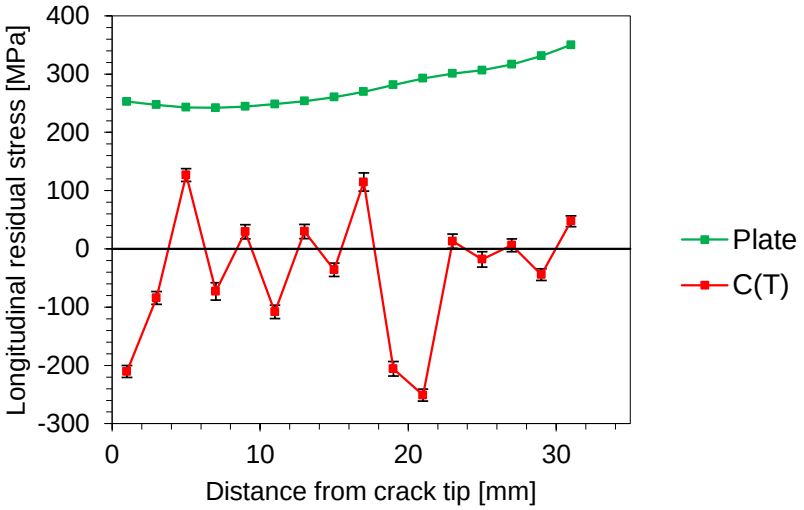

Figure 4-27: Comparison of longitudinal residual stresses in the C(T) specimen measured using neutron diffraction technique and in the welded plate measured using the contour method

A comparison of the measurements results obtained within the welded plate and the C(T) sample shows that the longitudinal residual stress in the welded plate (300 MPa on average) is significantly greater than the longitudinal residual stress in the C(T) sample (in the order of -50MPa). Although the normal and transverse components of the residual stresses on the welded mock-up are not available and will be measured in future work, a similar scaling factor might be expected in residual stress measurements in the transverse direction between

the welded mock-up and the C(T) sample. This implies that the transverse residual stresses at circumferential welds in monopiles can be very large and close to the yield stress of the material which subsequently results in accelerated crack initiation and propagation under corrosion-fatigue loading conditions. According to [176] and based on the measurements performed, it appeared that the maximum and minimum residual stress levels that can occur after welding may be up to the yield strength of the material. The worst case scenario would present tensile residual stress with a magnitude of about the yield stress of the material which would inevitably lead to crack initiation and propagation and therefore fatal fracture.

4.4 Summary

In this chapter, the locked-in RS have been measured on six C(T) specimens using ND technique. It has been found that the transverse residual stresses are, on average, between 100 MPa and -100 MPa at the crack tip while the overall peak values are collected between 376 MPa and -485 MPa. NI technique has also been used in order to assess longitudinal residual strains and a process has been developed for the data analysis on IMAT. This study has also shown that neutron diffraction and neutron imaging measurement results on C(T) specimens are in good agreement when a suitable d_0 is employed in NI analysis. Moreover, the NI results have shown that significant RS stress levels exist in C(T) specimens even after 10 mm of crack propagation. Finally, the contour residual stress measurement results have been found in good agreement with ND measurements on a C(T) specimen and the residual stress levels measured using contour method in a welded mock-up have been found to be much higher than the C(T) specimen.

5 Fatigue crack growth tests in air

In this chapter FCG tests have been performed in an air environment on six C(T) samples with two different orientations, as explained in Chapter 3. The characterisation of the RS, especially in transverse direction, has been used to provide a justification of the trends observed in this chapter. The air tests have also been employed to provide a calibration, in terms of crack growth monitoring, for the tests in seawater which are presented in Chapter 7.

5.1 Sample preparation and test set-up

FCG tests were performed under Mode I fracture mechanics loading conditions on a standard 100 kN servo-hydraulic fatigue testing Instron machine. The drawings of the pins and shackles are presented in Appendix F. The recommendations in ASTM E647 standard were followed during the test set-up, main phase of fatigue testing and data analysis [74]. All the tests were performed in air with the load ratio of $R = 0.1$. The tests were conducted at room temperature under load control mode, and both the load and position limits were set in order to ensure that the sample was not overloaded, hence avoiding unexpected plasticity at the crack tip. Sinusoidal cyclic waves form using constant amplitude loading with the frequency of 5 Hz was used for fatigue testing on all six C(T) specimens. Previous studies have shown that, in an air environment, the frequency has negligible effects on the FCG behaviour of steel materials [5].

The initial crack length, a_i, in C(T) samples, which is reported as the distance between the centre of the pin hole and the machined V-notch in the samples, was 17 mm (see Table 3-2). All six samples were initially pre-fatigue cracked by approximately 4 mm from the initial V-notch tip using the K-decreasing procedure as suggested in [177]. Particular attention has been given during this process to ensure that the K_{max} value at the end of the pre-cracking stage did not exceed the initial K_{max} value at the beginning of the main FCG test. This extra care during the specimen pre-cracking helps to ensure that there is limited plasticity ahead of the crack tip after pre-cracking and before the start of the main FCG test. The values of plastic zone size ahead of the crack tip at the beginning of the main FCG test (i.e. at a_0) are calculated using Equation 2-11. The crack length was measured, every 5000 cycles, using two cameras positioned in front of both sides of the sample. Individual measurements were conducted on each side and the average value was used as the effective crack length, a. Back Face Strain (BFS) measurements have also been performed in order to obtain a calibration

curve for the tests in seawater the results of which are presented in Chapter 7. It is worth noting that following instructions provided in ASTM E647, it was ensured that the difference between the crack lengths at the outer surfaces never exceeded 1 mm at any stage of testing, including pre-cracking and the main fatigue testing phase. The experimental set-up, as well as an example of optical crack growth monitoring on C(T) specimens is presented in Figure 5-1.

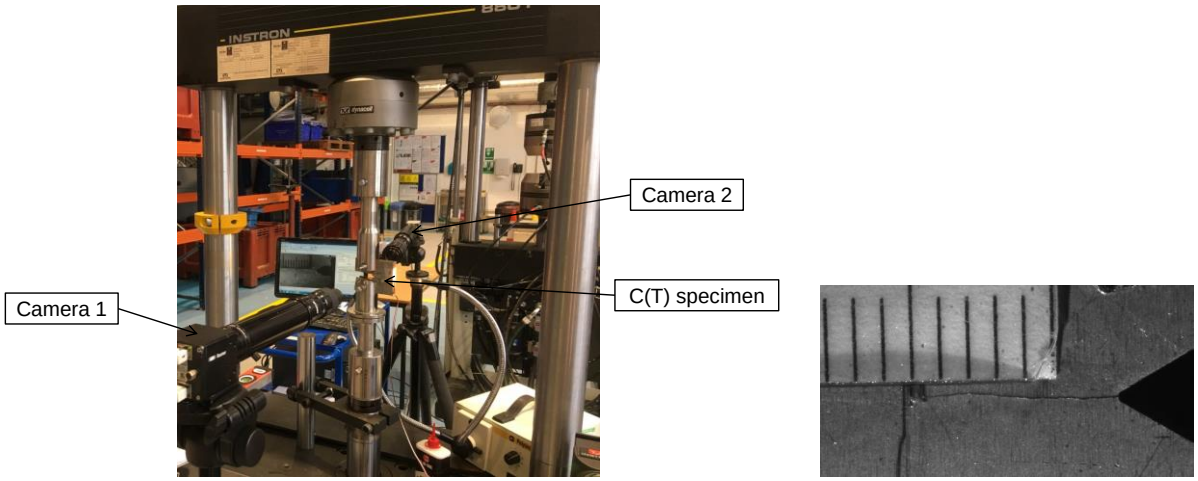

Figure 5-1: (a) Fatigue crack growth test set-up, (b) Crack growth monitoring on a C(T) specimen

After pre-fatigue cracking, the main fatigue crack growth testing was conducted on C(T) specimens by applying sinusoidal fatigue waveforms using the loading conditions summarised in Table 5-1. As seen in this table the maximum and minimum applied loads in all six tests were P_{max} = 10 kN and P_{min} = 1 kN respectively. Also included in this table are the plastic zone size, r_p, values at the beginning of the main FCG test. The calculations have been performed under plane strain conditions and using the following equation:

$$r_p = \frac{1}{\beta_1 \pi}\left(\frac{N-1}{N+1}\right)\left(\frac{K_{max}}{\sigma_y}\right)^2 \qquad \text{Equation 5-1}$$

Where $\beta_1 = 3$ under plane strain conditions, N is the Ramberg-Osgood plastic stress exponent calculated in Chapter 3, K_{max} is the maximum stress intensity factor ahead of the crack tip at the beginning of the FCG test and σ_y is the yield stress of the HAZ material.

The results have shown that the plastic zone size after pre-fatigue cracking is negligible in all six specimens, therefore plasticity does not have any influence on the subsequent FCG behaviour of the material examined in these tests.

Table 5-1: C(T) specimen dimensions and loading conditions for air tests

	HAZ 1	**HAZ 2**	**HAZ 3**	**HAZ 4**	**HAZ 5**	**HAZ 6**
a_0 **(mm)**	21.2	21.0	20.8	21.3	20.9	21.1
a_f **(mm)**	35.1	34.6	35.6	35.2	35.0	35.8
W **(mm)**	50	50	50	50	50	50
B **(mm)**	16	16	16	16	16	16
P_{max} **(kN)**	10	10	10	10	10	10
P_{min} **(kN)**	1	1	1	1	1	1
f **(Hz)**	5	5	5	5	5	5
r_p **(mm)**	0.17	0.17	0.18	0.17	0.17	0.17

5.2 Data analysis

The instantaneous crack length, *a*, and fatigue cycle number, *N*, were captured during the fatigue tests. The fatigue crack growth rate, *da*/*dN*, was calculated using a combination of the seven-point incremental polynomial method for most of the obtained data points and the secant method for the first and last three points where enough data points were not available to use the incremental polynomial technique. The SIF range, ΔK, which is suggested for C(T) specimen geometry in ASTM E647, is presented in Equation 2-15 [74]. As mentioned before, due to the validity limitation of Equation 2-15 for relatively short cracks, a new shape function solution for C(T) specimen geometry presented in [5] and shown in Equation 2-16 is used to analyse the obtained test data from this study. Note also that as discussed in [5], the ΔK values calculated using Equation 2-15 are more accurate for a wider range of normalised crack lengths (i.e. $0.2 \leq a/W \leq 0.7$).

5.3 Results and discussion

The results of the FCG tests in air performed in this research project have been presented and discussed in terms of "crack length vs. number of cycles" and "crack growth rate vs. stress intensity factor range". A particular emphasis on the Paris region has been made on the "da/dN vs ΔK" graphs. Note that the results "crack length vs BFS" will be presented and used in Chapter 7 for calibration of the FCG results in seawater.

5.3.1 *"a vs N" results*

The raw data from FCG tests are first presented in the form of "a vs N" curves as seen in Figure 5-2. It can be observed that FCG is propagating faster on samples extracted from 0° orientation compared to samples extracted from 180° orientation. This is evident from steeper slopes observed in 180° oriented samples at the beginning of the tests. This figure shows that the orientation of the crack propagation has an important influence on the fatigue life of the material. This is thought to be mainly due to material microstructure effects on the observed FCG behaviour in the welded plate. Also seen in Figure 5-2 is that for a given specimen orientation, while the samples were tested under the same loading conditions, different fatigue lives were observed in various specimens. This is thought to be due the inherent scatter in the FCG data as well as different RS profiles in each test specimen. For instance, the crack is propagating faster on HAZ 3 than it is on HAZ 2. This is due to the fact that RS are compressive ahead of the crack tip on HAZ 2, while HAZ 3 contains tensile locked-in RS. The compressive RS ahead of the crack tip are therefore slowing down the crack propagation.

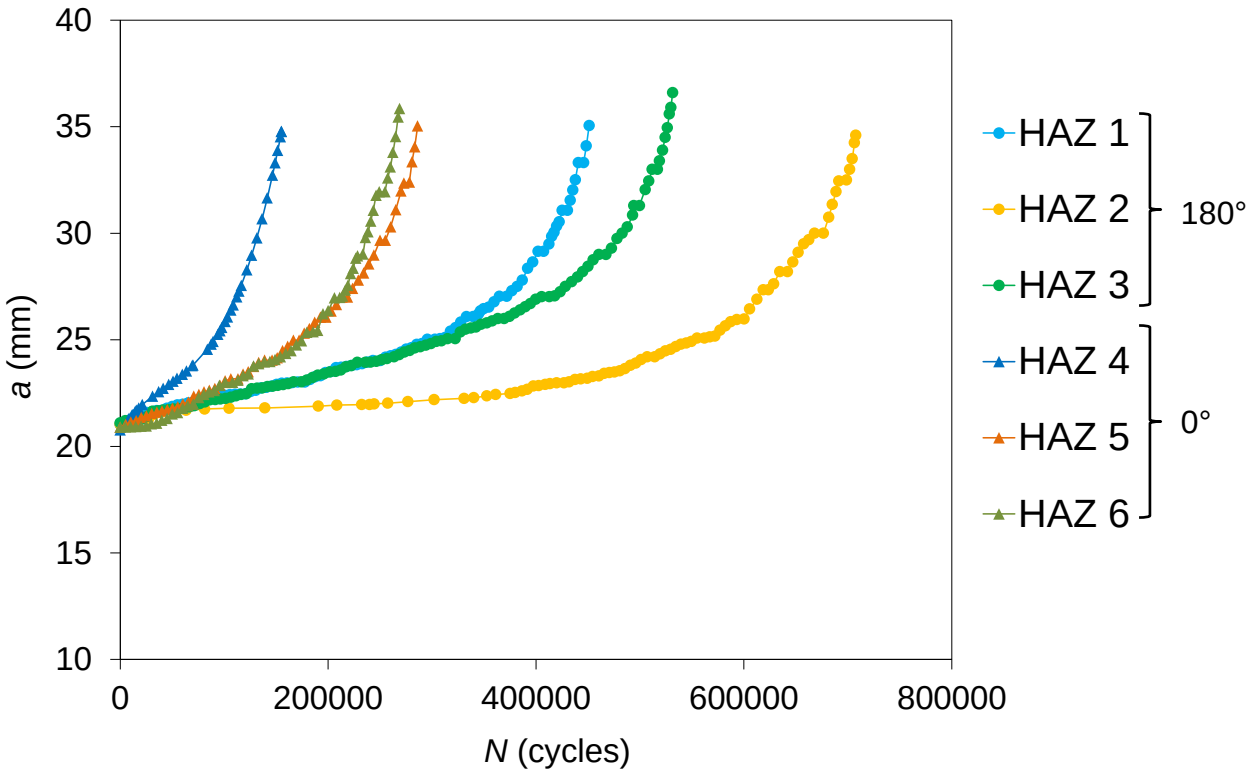

Figure 5-2: Crack length vs. number of cycles for the FCG tests in air

5.3.2 *"da/dN vs ΔK" results*

The fatigue crack growth rate, da/dN, for each of the tests conducted on the HAZ specimens is correlated with the SIF range, ΔK, and the results are presented in Figure 5-3. The analysis

mainly focuses on the Paris region of the fatigue crack growth curves. It is also worth noting that it has been assumed that the crack closure effect was negligible as the crack was continuously propagating indicating that in C(T) specimens the compressive RS was not high enough to lead to crack closure but it is expected to be higher in actual monopile. As explained in [178] [179] the welding residual stresses redistribute in fracture mechanics tests and may finally vanish as the crack propagates; however, residual stress effects and the subsequent redistribution have not been considered in the experimental data analysis presented in Figure 5-3. As seen in Figure 5-3, the fatigue crack growth trends from all the first three tests on HAZ 1, HAZ 2 and HAZ 3 specimens with 180° orientation fall on top of each other over the entire ΔK experimental range, indicating a good repeatability across the tests. However, the results from the last three HAZs extracted from 0° orientation display a more sparse distribution. Also included in this figure are the lines of best fit made to the experimental data on the HAZ specimens with 180° and 0° orientations, within the Paris region, to identify the power law constants. The Paris law constants obtained from this fit for the 180° orientation are C = 1.85×10-15, m = 5.10 with R2 = 0.97 and C = 1.58×10-13, m = 3.96 with R2 = 0.71 for the 0° orientation. The high value of R2 from the 180° specimens implies that the line of best fit describes the experimental data trend accurately and that little variation is observed in the FCG behaviour of the HAZ 1, HAZ 2 and HAZ 3 specimens. On the other hand, the lower value of R2 from the 0° samples suggests a less accurate fit due to the fact that the results are more scattered than the 180° specimens. Finally seen in Figure 5-3 is that for a given value of ΔK, the FCG rate is on average approximately 100% higher in the 0° specimens compared to the 180° samples. The difference between FCG behaviour at different specimen orientations might be associated with the change in material microstructure and also the residual stress profile from one crack plane orientation to another. Indeed, the study presented in [180] found that microstructure has a strong effect on the FCG behaviour of steels in the Paris region, both in air and seawater. The effect of microstructure and fatigue testing parameters on fatigue behaviour, mechanisms of fatigue crack initiation and propagation along with the evolution of microstructure during cycling loading were also analysed in [181]. It has been found in [182] that microstructure of quenched and partitioned steels plays a key role in their fatigue behaviour. Microstructural analysis of new bainitic steel subject to heat treatment was performed and directly compared with those achieved from the microstructure of R-260 pearlitic rail steel. The obtained test results demonstrated that the two microstructures exhibit different cyclic stress responses, hence the importance of the effect of microstructure.

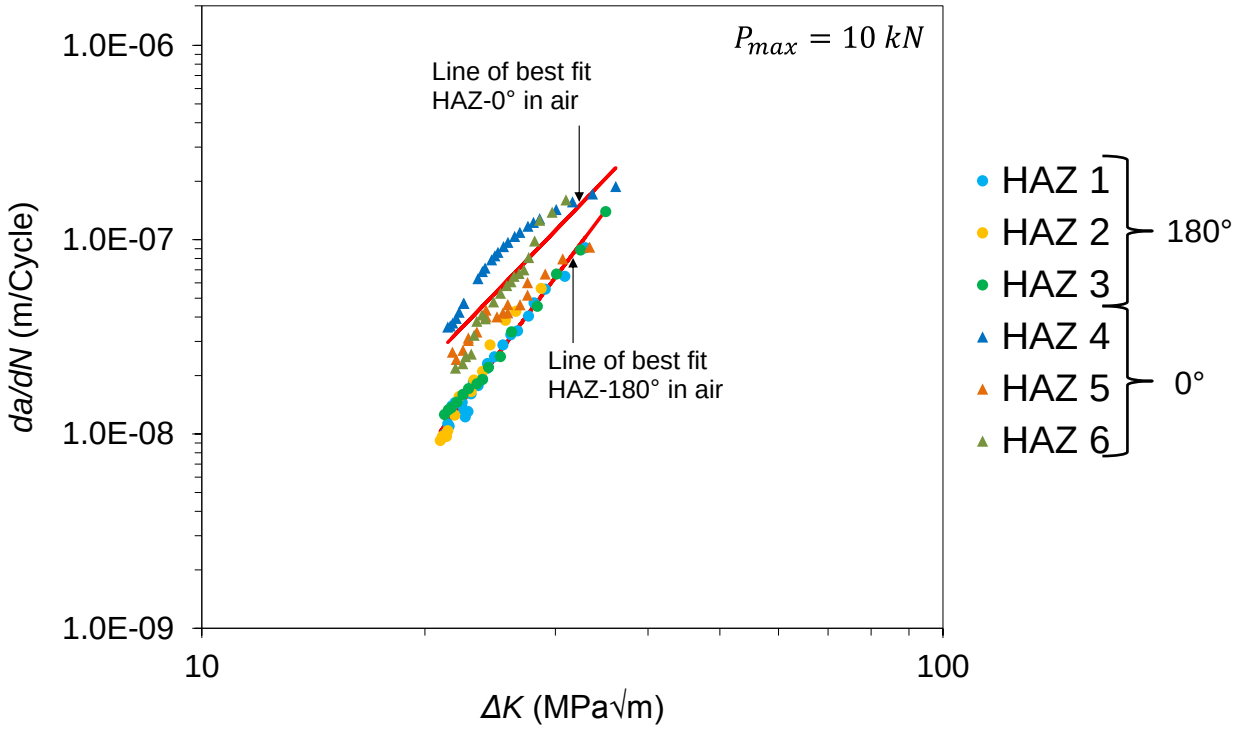

Figure 5-3: Fatigue crack growth behaviour of the six HAZ tested samples in an air environment

The fatigue crack growth data on S355 G10+M structural steel from the HAZ C(T) specimens from this study are compared with the fatigue test data in air available in the literature on other grades of steel that are used in offshore structures as well as the proposed trends in BS7910 standard [27]. Additional information about the materials used in this section for comparison purposes can be found in Table 5-2 where the welding processes of the plates and the specimen geometries and thicknesses are summarised. As seen in Table 5-2 the data collated from the literature are on different ranges of medium to high strength structural steels tested on various specimen geometries, load levels and specimen thicknesses. The specimen thickness effects on the FCG rate of metallic structures have been investigated in [183] [184] and it has been shown that the FCG rate increases by increasing the specimen thickness, due to the higher constraint level in thicker specimens. It must also be noted that the BS7910 curves presented in this study for comparison purposes are based on the mean curves proposed in BS7910 for the welded joints in air [27].

All the HAZ materials presented in this section are summarised in Table 5-2 with the S355 G10+M structural steel corresponding to the material employed in the current study. The HAZ materials used for comparison are S355 G8+M [5], S355 NL [185], 420 MPa structural

steel [186], 4140 vacuum-degassed high tensile steel [187], S355 J2+N steel [24], S355 EMZ high strength [188], SE702 steel [189], C-Mn structural steel [190], C-Mn-V steel [191] and 50D steel [192]. Also included in this table are the BM yield stress σ_y and UTS. As seen in Table 5-2 the majority of the HAZ test data from the literature were gathered from C(T) specimens, whereas Single Edge Notched specimen in Bending, SE(B), was employed in two of the previous studies. Also seen in this table is that the specimen thickness ranges from 8 mm to 50 mm for various materials used for comparison in this study.

The FCG rate data from the present study on HAZ material are plotted against the SIF range and compared with the literature data and BS7910 curves in Figure 5-4. As seen in this figure, the majority of the FCG curves obtained from the tests on different steels fall close to each other with the test results presented by Bertini [190] and Albuquerque et al. [185] on C-Mn structural and S355 NL steels, respectively, falling significantly below the main population of fatigue data on other steels. This might be associated with relatively low load levels, in association with the given specimen thickness, employed in these two studies. Also the fact that the C-Mn structural steel specimens tested by Bertini [190] were subjected to PWHT may have had an impact on the fatigue crack growth behaviour of the material by relaxing possible tensile (i.e. damaging) residual stresses in those specimens.

The comparison of FCG trends from a wide range of steels in Figure 5-4 demonstrates that some variation can be observed in the fatigue crack growth behaviour of different steels tested under various loading conditions and on different specimen geometries. It can be observed in this figure that for a given value of ΔK the FCG rate for various materials considered in this study varies by a factor of approximately three above and below the trend obtained from the tests on S355 G10+M HAZ specimens. Also included in Figure 5-4 are the proposed trends for welded joints from BS7910 based on the simplified law and 2-stage law. The comparison in this figure shows that for the range of materials considered, the majority of data points fall upon or below the simplified law proposed by BS7910. These results show that although BS7910 2-stage law provides a conservative prediction of the fatigue crack growth behaviour for the materials considered in this study, the recommended trend is not overly conservative and the upper bound fatigue data points fall only slightly below the 2-stage BS7910 curve. The Paris law constant for each of the HAZ materials considered in this study and presented in Figure 5-4 are summarised in Table 5-3. It can be seen in Figure 5-4 and Table 5-3 that although the Paris law coefficient, *C*, and Paris law constant, *m*, show

some variation for the range of materials considered in this study, the average slope from the experimental data is similar to the simplified law proposed in BS7910.

Table 5-2: Specimen specifications and welding process for each HAZ material presented

	σ_y (MPa)	UTS (MPa)	Specimen geometry	Specimen thickness (mm)	Welding process
S355 G10+M	455	544	C(T)	16	SAW tandem twin, multi-pass double V-groove hot rolled
S355 G8+M [5]	413	503	C(T)	16	Multi pass butt-weld double V-groove
S355 NL [185]	345	550	C(T)	32	Butt weld double V-groove
420 MPa structural steel [186]	450	549	SEN(B)	50	SAW
4140 vacuum-degassed high tensile steel [187]	338	577	C(T)	8	SAW U-groove
S355 J2+N steel [24]	363	535	C(T)	16	WA-Twin/Tandem-twin
S355 EMZ high strength [188]	355	540	C(T)	15	SAW T-joint
SE702 steel [189]	780 For 160 mm thick	850 For 160 mm thick	C(T)	16	SAW K-welded joint
C-Mn structural steel [190]	490	510	C(T)	12	GMAW with PWHT
C-Mn-V steel [191]	360	524	C(T)	25	SAW
50D steel [192]	386	536	SE(B)	15	Single V-groove

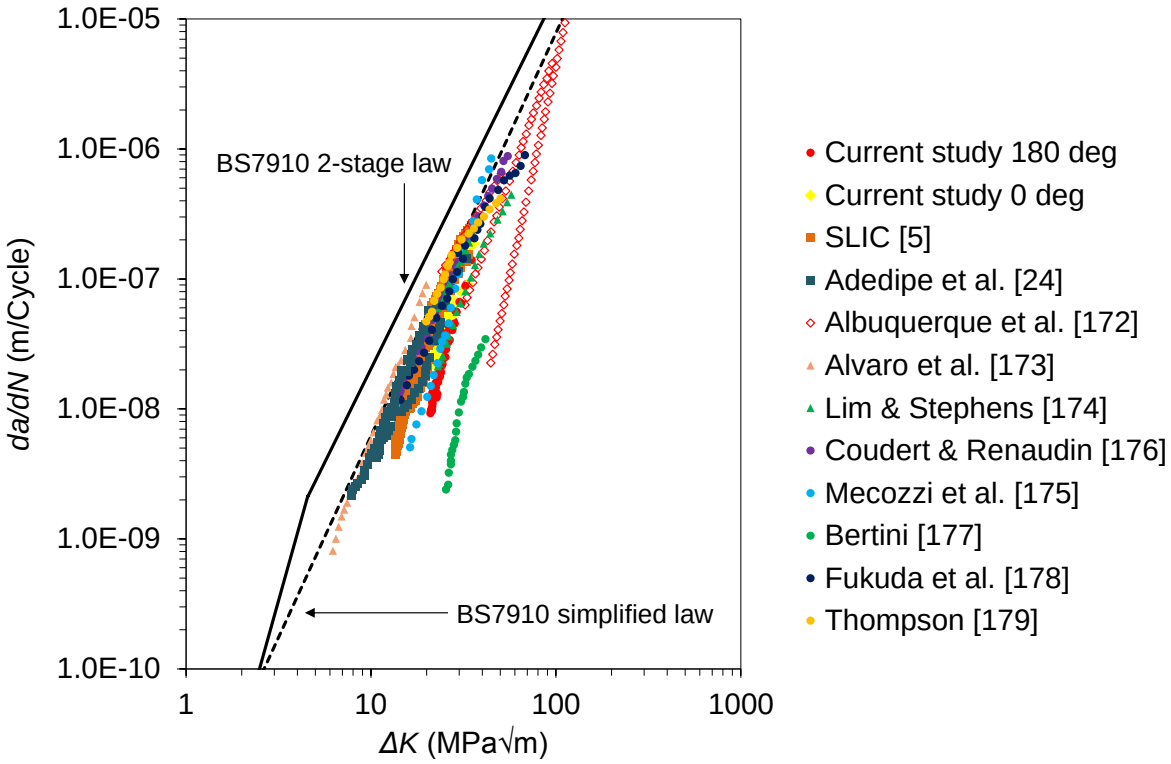

Figure 5-4: Fatigue crack growth data on HAZ material in air compared with the literature data and BS7910 curves

Table 5-3: Simplified Paris law constants for da/dN in m/Cycle and ΔK in MPa$\sqrt{m}$ for the HAZ material from different studies

Material	***C***	***m***
S355 G10+M 180°	1.85×10^{-15}	5.10
S355 G10+M 0°	1.58×10^{-13}	3.96
S355 G8+M [5]	8.63×10^{-14}	4.26
S355 NL [185]	1.15×10^{-12}	3.19
420 MPa structural steel [186]	6.76×10^{-13}	3.94
4140 vacuum-degassed high tensile steel [187]	3.68×10^{-12}	2.95
S355 J2+N [24]	5.66×10^{-12}	2.88
S355 EMZ high strength steel [188]	3.16×10^{-15}	5.10
SE702 steel [189]	3.15×10^{-12}	3.14
C-Mn structural steel [190]	5.19×10^{-17}	5.54
C-Mn-V steel [191]	3.55×10^{-12}	3.04
50D steel [192]	5.04×10^{-11}	2.35

5.3.3 Post-mortem analysis

Fractography analysis has been performed on all the tested samples in order to confirm the crack growth monitoring technique and therefore the FCG results. In order to carry out macro analysis of the fracture surfaces, the specimens were fully immersed in liquid nitrogen with a temperature of approximately - 196°C until disappearance of the bubbles in the liquid. They were then broken into two halves by pulling them while mounted on the Instron machine. The specimens were then dried with a hair dryer.

It is known that the residual stress profiles have a stronger effect at the early stages of the fatigue crack growth test on the crack shape compared to later stages. The less effect from residual stresses at the later stages is due to the fact that the residual stresses are redistributing to eventually be at a minimal level as the crack propagates [178]. There is therefore a competitive effect between the triaxiality and residual stresses present in the sample which can be observed during the post mortem analysis after the samples are split-open using liquid nitrogen, as shown on Figure 5-5. Beach markings have been performed during the FCG test in order to highlight this effect, as presented on Figure 5-6. Beach marks (also known as clamshell marks, tide marks, or arrest marks) are typically found on service fractures where the part is loaded randomly, intermittently, or with periodic variations in mean stress or alternating stress. Many fatigue fractures produced under conditions of uninterrupted crack growth and without load variations do not exhibit beach marks. Beach marks of different depths are due to crack growth rate variation following random cycling amplitude. Beach marking has been performed on four of the C(T) samples tested in air following the process described in [81].

Figure 5-5: Sample separation using tension and liquid nitrogen

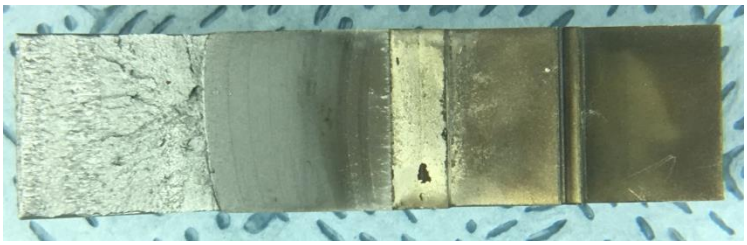

Figure 5-6: Crack surface analysis after separation showing fatigue striations

Comparisons between the effective crack length measurements in through thickness direction and the values measured using the optical technique at the outer surface has been performed using ImageJ software. A ruler has been used on the pictures to set the scale, as seen on Figure 5-7. The area of interest is then measured and by dividing this value by the thickness of the sample, 16 mm, the effective crack length at the end of the test is obtained. The crack extension, Δa, values are calculated as the difference between the final, a_f, and initial, a_i, crack length (before pre-fatigue cracking) and the results are compiled in Table 5-4. It can be noticed that the crack extension measurements from fractography are always found to be slightly smaller than those measured using optical cameras on the two opposite outer surfaces of the specimens. This difference in the crack extension can be explained by the crack tunnelling effect. The same fractography analysis has then been applied on the available C(T) samples with beach marks in order to check the crack length measured during crack propagation.

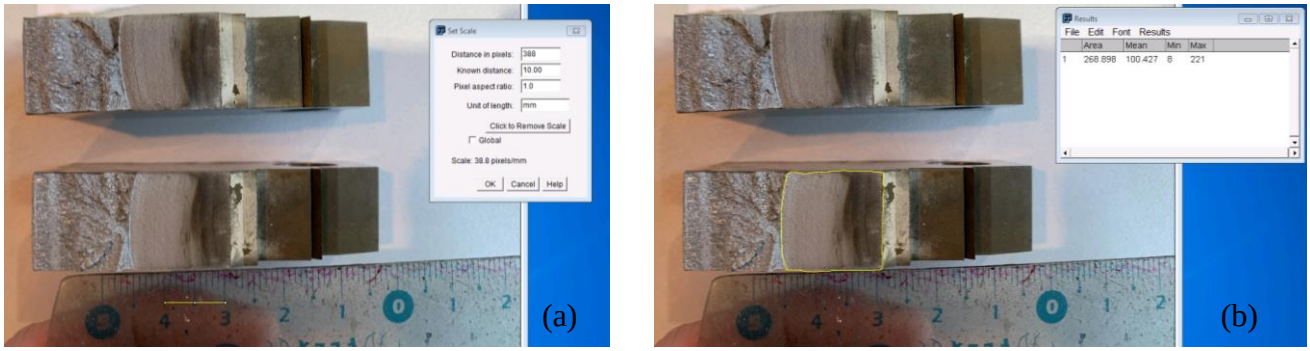

Figure 5-7: Numerical crack growth measurement on HAZ 2 using ImageJ (a) scaling (b) fracture area measurement

Table 5-4: Comparison of the final crack extension from fractography to optical measurements for air tests

	Optical measurement Δa (mm)	**ImageJ calculation Δa (mm)**
HAZ 1	18.1	16.3
HAZ 2	17.6	16.1
HAZ 3	18.6	17.0
HAZ 4	18.2	16.7
HAZ 5	18.0	16.3
HAZ 6	18.9	17.4

5.4 Summary

FCG tests have been performed in air environment on six C(T) samples. Sample preparation and test set-up have been described as well as the data analysis process. “a vs N” results have been presented and the difference in the results can be explained by the RS effect, especially at the early stage of the fatigue tests, as well as the orientation of the specimen. The material behaviour has also been examined through “da/dN vs ΔK” graphs and the results have been compared with the literature data as well as the BS7910 recommended trends. It has been found that the BS7910 curves suggest conservative predictions and that some variation can be observed in the fatigue crack growth behaviour of different steels tested under various loading conditions and on different specimen geometries. Finally post-mortem analysis has been performed in order to confirm the FCG results, especially the reliability of the crack length measurements obtained from the optical technique applied at the outer surfaces of the C(T) specimens.

6 Residual stress effects on near threshold fatigue crack growth behaviour

In order to accurately characterise the effect of residual stresses on the fatigue crack growth behaviour of HAZ samples tested in air with measured residual stress profiles, finite element analyses have been performed to numerically calculate the effective SIF, ΔK_{eff}, at different stages of the tests.

6.1 Finite element model set-up

ABAQUS CAE was employed to design the 2D model and to perform the FEA. Only half of the specimen was designed applying the Y-symmetry boundary condition to the crack line, in order to minimise the total number of elements and, therefore, the computational time. The material, with the elastic properties summarised in Table 6-1, was defined and assigned to the specimen.

Table 6-1: Specimen dimensions, properties and fatigue test parameters

W (mm)	B (mm)	a_0 (mm)	a_f (mm)	f (Hz)	R	P_{max} (kN)	v	E (GPa)
50	16	17	35	5	0.1	10	0.3	190

Moreover, another material property was specified with a Young's modulus of 100,000 GPa and the same Poisson's ratio. This extremely rigid material property was assigned to the section corresponding to the pin hole in order to avoid possible deformations due to the application of the load on this section. Plane strain conditions were applied to the 2D model as the specimen is a thick component with a real thickness of 16 mm. The first model created for the introduction of residual stresses only used boundary conditions and no external load was applied. A finer mesh was considered along the crack line in order to obtain more accurate results, as seen in Figure 6-1. The mesh consists of 4-node bilinear elements with reduced integration. Each small rectangle corresponds to 1 mm over which the mesh seeds were divided every 0.25 mm.

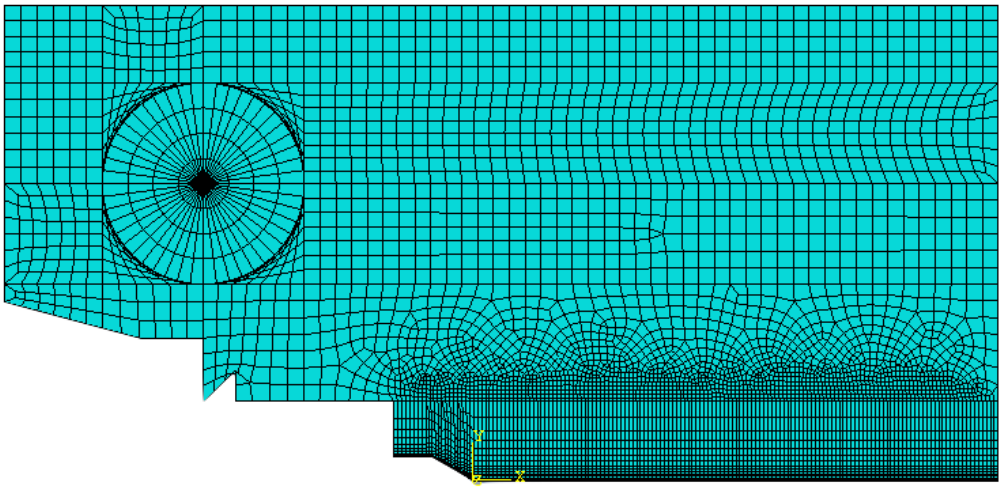

Figure 6-1: Mesh design for the C(T) specimen symmetric model

For the purpose of model validation, a mesh sensitivity analysis was performed in order to individuate the optimal mesh to achieve reliable results. The details of the mesh sensitivity analysis are not presented here for brevity, though the optimum element size along the crack path was found to be 0.25 mm.

6.2 Iteration process for RS introduction

The RS profile introduced in the FEA model is based on the residual stress measurements previously presented in Figure 4-7 from the neutron diffraction tests. Three models have been created for the three different HAZ samples considered with known RS profiles (i.e. HAZ 2, HAZ 3 and HAZ 4). As ABAQUS automatically applies a force balance after defining the initial boundary conditions, the first step in the numerical analysis was to find the correct RS input values to introduce in the FEA model. To do so, an iterative process was implemented using a Python code and the user subroutine SIGINI, which is used to define all active initial stress components at material points. A diagram of the numerical iterative process is presented in Figure 6-2, where k is the iteration number.

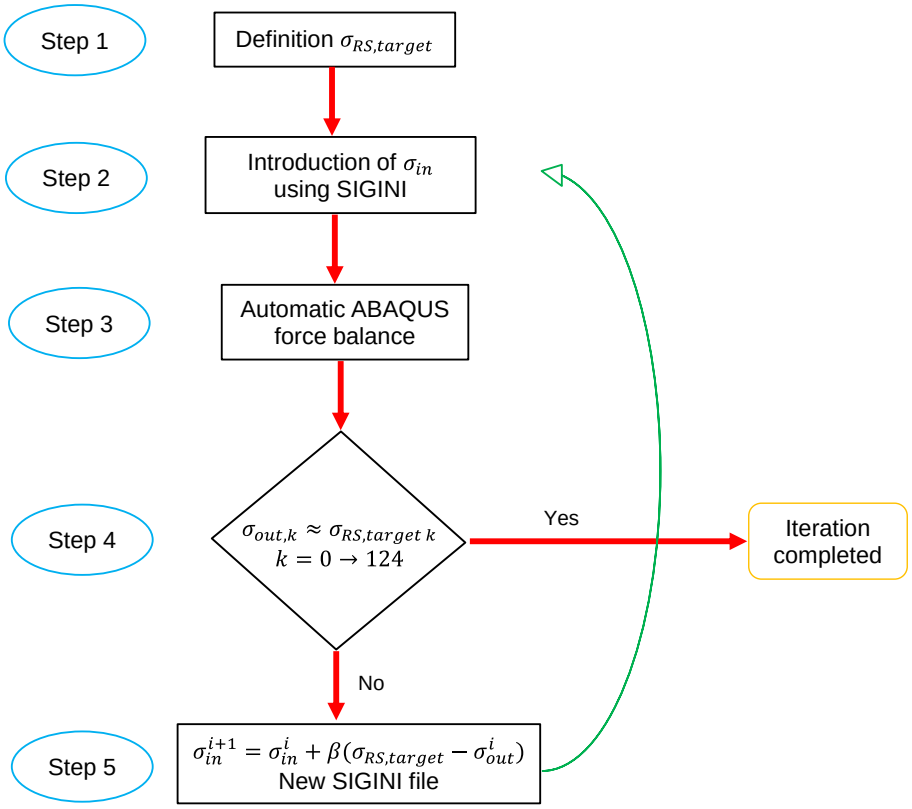

Figure 6-2: Diagram of the iterative procedure for RS introduction

The general purpose of this procedure is to define an initial stress field at known distances from the crack tip where residual stresses were previously measured using neutron diffraction tests. The results at the end of the iterations are presented in Figure 6-3 for HAZ 2, HAZ 3 and HAZ 4, with the RS target corresponding to the RS measured from neutron diffraction.

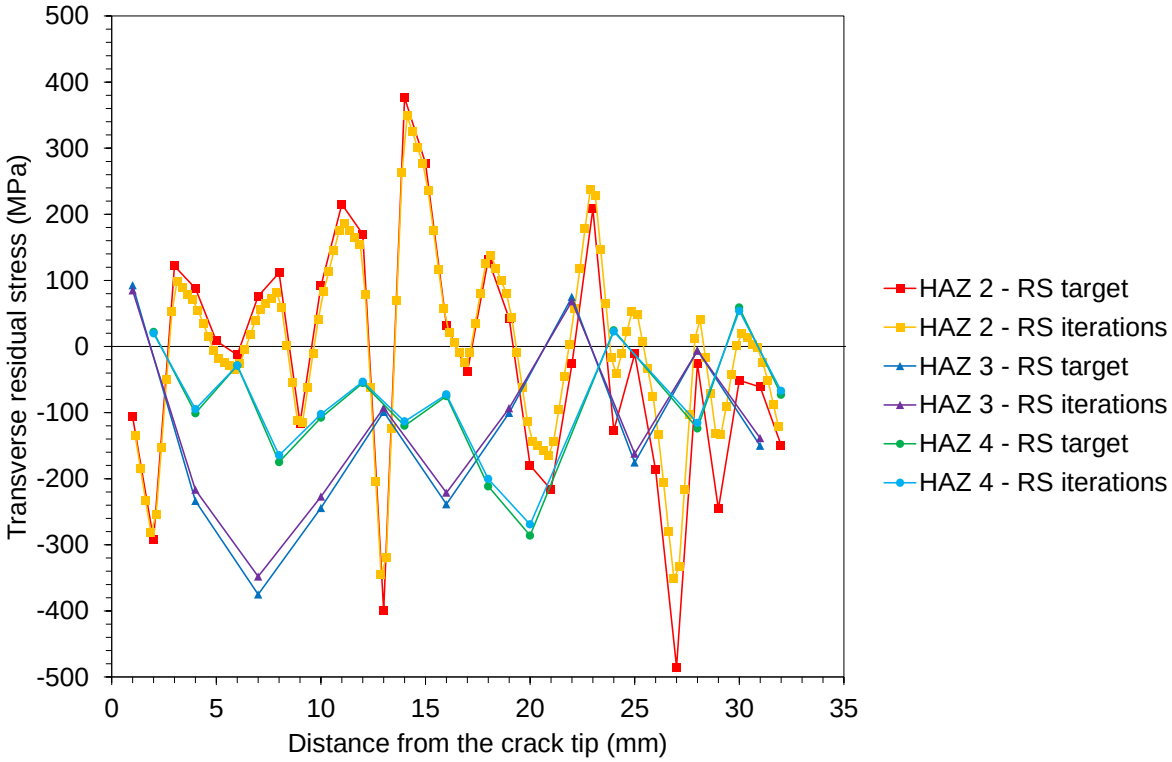

Figure 6-3: RS target and RS at the end of the iteration process on the three HAZ considered

It can be seen in Figure 6-3 that for HAZ 2 more data points were considered for the iteration process since finer neutron diffraction residual stress measurements were performed on this sample. A linear interpolation between the available data points was applied in all simulations where the target RS value at a given node was not available from the neutron diffraction measurements. It was found that the error between the target and the iteration curves are minor, as can be seen from the results on HAZ 3 and HAZ 4, where fewer data points from the neutron diffraction measurements were available due to coarser neutron diffraction measurements.

An example of the RS redistribution after the force balance achieved by iterations on HAZ 2 can be seen in Figure 6-4. Although the stress components were introduced only into the crack line, the software ABAQUS redistributes the RS within the whole specimen during the simulation. Bearing in mind that this stress distribution should be mirrored with respect to the symmetry axis, the RS distribution influences the elements along the whole crack line.

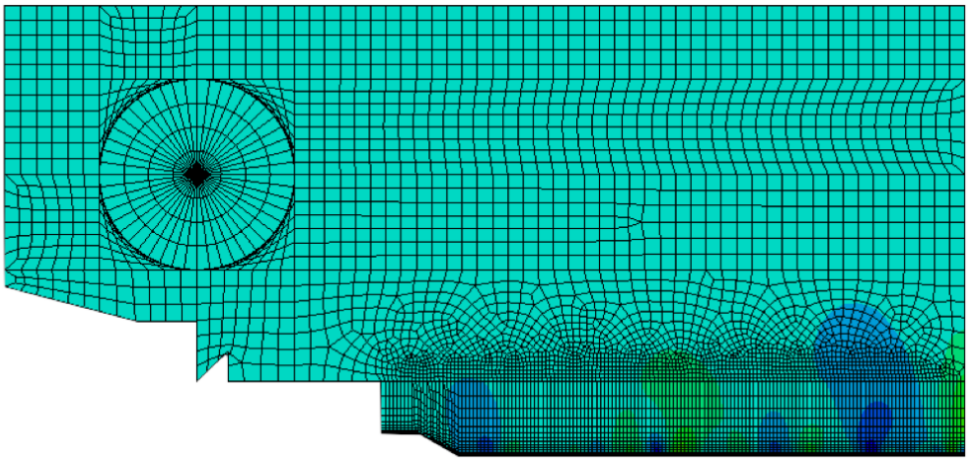

Figure 6-4: RS distribution at the end of the iteration process on HAZ 2

6.3 Fatigue test results in the presence of RS

Once the target RS values are obtained by iterating the input values in the SIGINI file, the FEA model accurately represents the real specimen condition by taking into consideration the initial RS profile. The next phase consists of replicating, using ABAQUS, the real test executed in the laboratory on the HAZ samples. The first significant modification of the FEA model is to simulate the crack propagation. In ABAQUS, it is possible to create a crack initiation, selecting manually the crack front and specifying the direction of the crack extension; however, this process is valid only for quasi-static cracks. Since the purpose of this work is to reproduce a fatigue test condition, a dynamic crack propagation approach was necessary; however, it was found unnecessary to simulate crack propagation for examination of the RS effects on the fatigue crack growth trend as a part of this study. Subsequently, according to the ASTM standards [74], which states that the fatigue test needs at least 18 mm of crack propagation, a further 18 steps were created. The aim at this step was to represent the crack propagation by debonding the nodes from the boundary conditions (Y-symmetry) at every 1 mm at each step. Therefore, at every step the nodes are released, hence the crack advances by 1 mm until the last 18^{th} millimetre. An example of the procedure is shown in Figure 6-5.

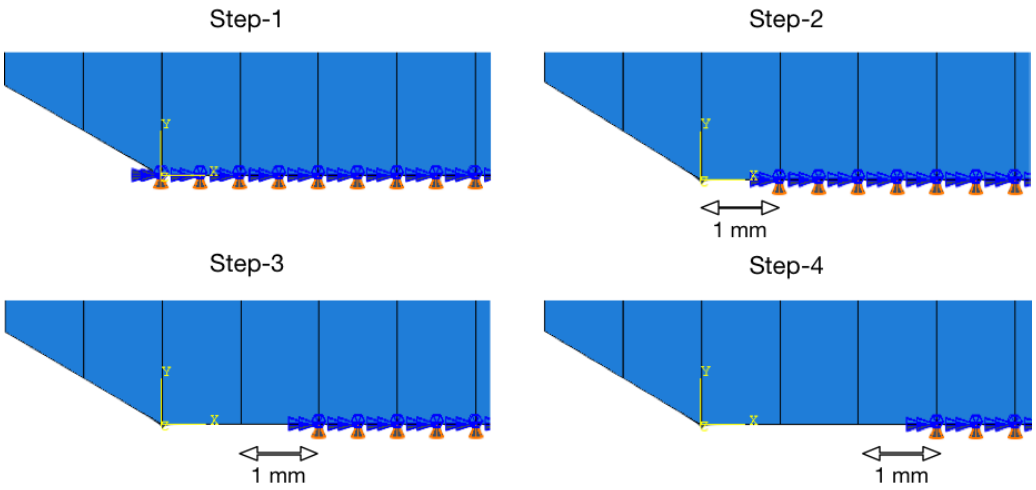

Figure 6-5: Example of crack propagation unbinding nodes from Boundary Conditions (BC) every 1 mm

The second modification concerns the application of external loads. As summarised in Table 6-1, the fatigue test was performed with an R ratio of 0.1, a maximum load P_{max} of 10 kN and consequently a minimum load P_{min} of 1 kN. In ABAQUS, these factors are represented with two different FEA models, both derived from the FEA model used for the iteration with the first adjustment made. For both models, a load was created as a concentrated tensile force and was applied to the centre of the pin hole along the direction perpendicular to the crack plane with a magnitude of 10,000 N for the P_{max} model and 1,000 N for the P_{min} one. Both loads were set-up with a tabular amplitude required to simulate the periodical and sinusoidal fatigue test. The results from both simulations were required in order to obtain reliable outcomes to compare with the experimental data, and to calculate maximum and minimum SIFs in the presence of residual stresses, $K_{max,RS}$ and $K_{min,RS}$, and subsequently calculate the effective SIF range, ΔK_{eff}, in the presence of residual stresses. Both models were run with these modifications after introducing the initial residual stress profile in the model.

The loading effect in the presence of RS has been shown for HAZ 4 in Figure 6-6 as an example. The state of RS can be seen in this figure, at the end of the iterations, under 1 kN and under 10 kN. The residual stress profile has been found to slightly and more severely shift up by applying the minimum and maximum applied load, respectively. It can be seen in Figure 6-6 that under small loading conditions, the state of RS before any crack growth is very similar to the one without any external load applied. Moreover, under 10 kN, the state of

RS is higher, especially near the crack tip. These observations demonstrate numerically the loading effect in the presence of RS using ABAQUS.

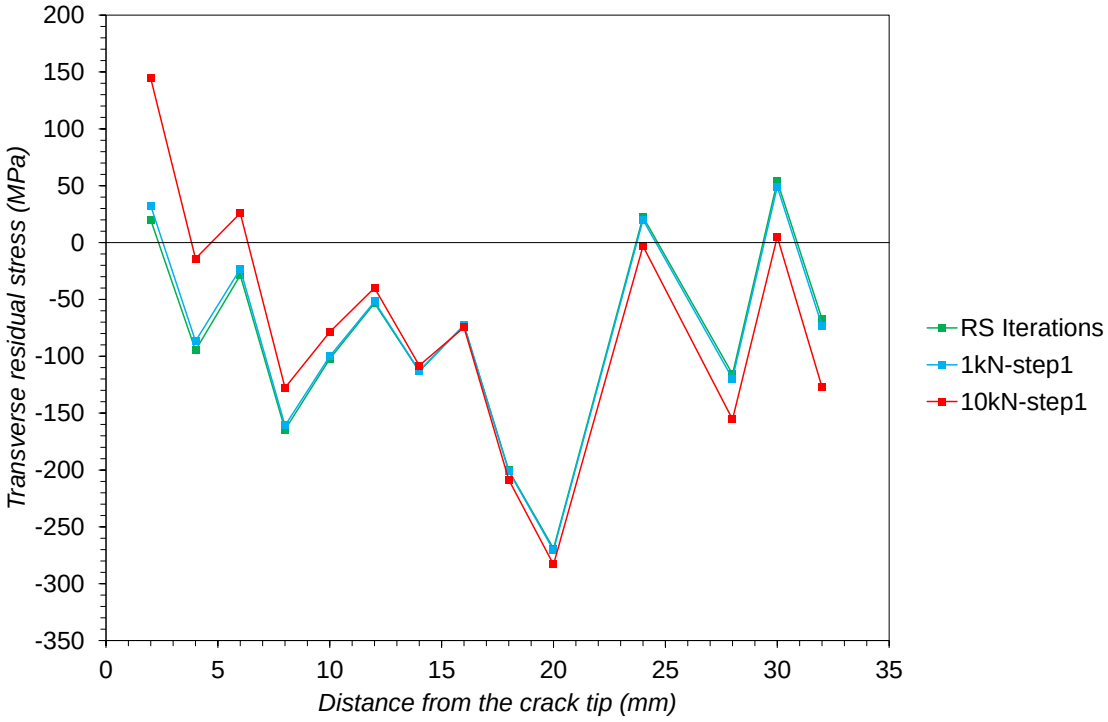

Figure 6-6: Residual stress state at the end of the iterations and under loading on HAZ 4

6.4 Stress intensity factor calculation

Several methods exist to calculate the SIF from ABAQUS simulations following a direct or indirect approach. One of the indirect methods is the Virtual Crack Closure Technique (VCCT) which was chosen for the SIF computation in this work. This approach is well known in the literature [193], especially to calculate the SIF through FEA simulations [146][147][148]. It is based on the Irwin's energy principle [68], and it relates to the SIF and the strain energy release rate, G, using Equation 2-9. The VCCT relies on the estimation of G, considering the nodal vertical displacement of the nodes involved in the crack propagation and the nodal reaction force of the new crack tip for a defined crack advance and for a fixed thickness. The parameters involved are shown in Figure 6-7.

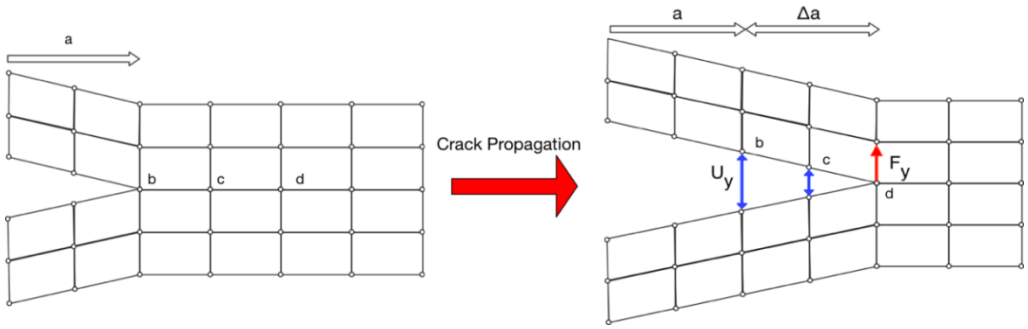

Figure 6-7: Parameters involved in the VCCT to calculate G from ABAQUS results

For a crack propagation Δa, the nodal vertical displacements of the two nodes involved in the crack opening, are taken into consideration. The nodal reaction force is evaluated from the new crack tip after the crack advance. All these parameters can be extracted from an ABAQUS simulation post-processing the outcomes. The strain energy release rate is then calculated using the following equation:

$$G = -\frac{1}{2t\Delta a}[F_{y,d}U_{y,b} + F_{y,d}U_{y,c}] \qquad \text{Equation 6-1}$$

where t is the sample thickness, Δa is the crack extension, $F_{y,d}$ is the force in y direction applied on node d, $U_{y,b}$ is the displacement along y direction on node b, $U_{y,c}$ is the displacement along y direction on node c. The calculation of G, and consequently K, was performed at each step of the FCG simulation. This procedure has been performed at each step in order to obtain different K values as a function of the distance from the crack tip, for both models under P_{max} and P_{min} respectively. The SIF range ΔK_{eff} is then calculated at every step following the equation below.

$$\Delta K_{eff} = K_{max,RS} - K_{min,RS} \qquad \text{Equation 6-2}$$

where $K_{max,RS}$ is the SIF calculated from the model under P_{max} of 10 kN in the presence of RS and $K_{min,RS}$ is the one from the model under P_{min} of 1 kN. In order to confirm the results obtained, the accuracy of the VCCT technique has been verified by comparing the results with the contour integral method performed by ABAQUS and it has been shown that after a few contours the SIF values tend to converge.

Finally, it is worth noting that the redistribution of the RS during crack growth is unachievable by ABAQUS. Indeed, the process employed here is similar to the weight function approach [194] where the initial residual stress profile is taken into consideration without accounting for subsequent RS redistribution. Prediction and validation of residual

stress redistribution is beyond the scope of this study and is a subject for further investigations in the future.

6.5 Numerical analysis of ΔK_{eff}

The results from the calculations previously described are compared with the experimental data for HAZ 2, HAZ 3 and HAZ 4. In the following figures, ΔK_{eff} (i.e. deltaK$_{eff}$) is the effective SIF range calculated from the numerical analysis accounting for the RS and ΔK_{app} (i.e. deltaK$_{app}$) is the experimental SIF range taking into account only the global load applied during the actual experiments.

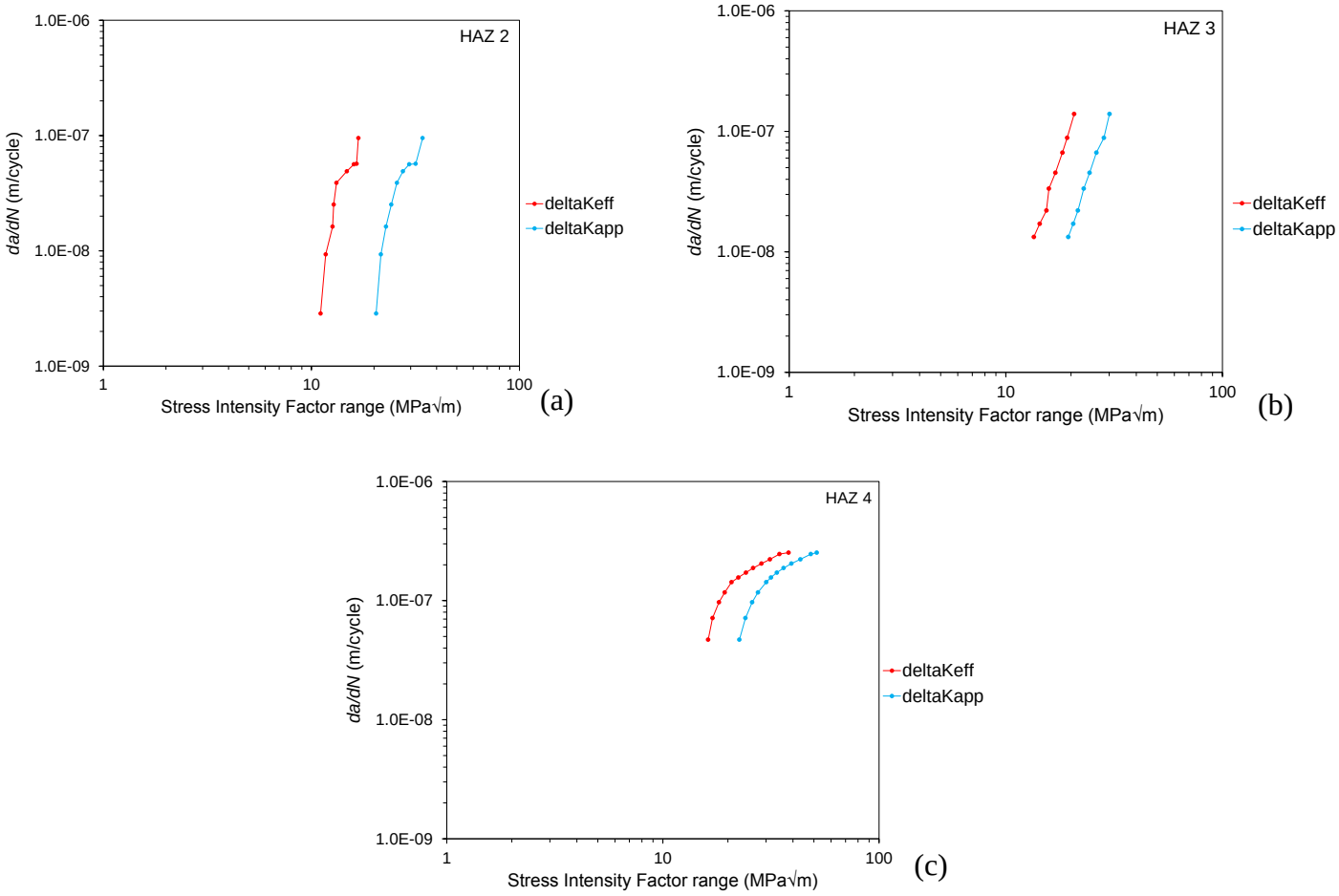

Figure 6-8: Numerical and experimental FCG trends for (a) HAZ 2 (b) HAZ 3 and (c) HAZ 4

It is important to note that the *da/dN* values for both curves represented in each graph have been taken from the experimental data available for the corresponding crack growth. It can be seen in Figure 6-8 that the presence of RS tends to influence the FCG behaviour of the material in an air environment. In all three cases, the effective FCG behaviour presented lower SIF range values of up to 10 MPa√m for a given value of *da/dN*. Similar effect has

been observed by other researchers and reported in the literature [195][196]. It would also be expected to see the curve from ΔK_{eff} overlap with the curve from ΔK_{app} in the Paris region, as the RS tend to redistribute and eventually vanish as the crack propagates [178][179]. The shift in effective SIF in HAZ 3 and HAZ 4, where the RSs were predominantly compressive, is less than 10 $MPa\sqrt{m}$ and similar in both samples. Finally, a greater shift in effective SIF in HAZ 2, where the RS in near crack tip region was close to zero on average and more balanced in the through thickness direction, can be observed.

6.6 Results and discussion

The final study of the numerical analysis part of the project was to look at the RS redistribution during crack growth using the SIGINI approach in ABAQUS software. Numerical predictions are presented after unloading of the sample in order to examine the remaining RS state, and the results are presented in Figure 6-9 for HAZ 4.

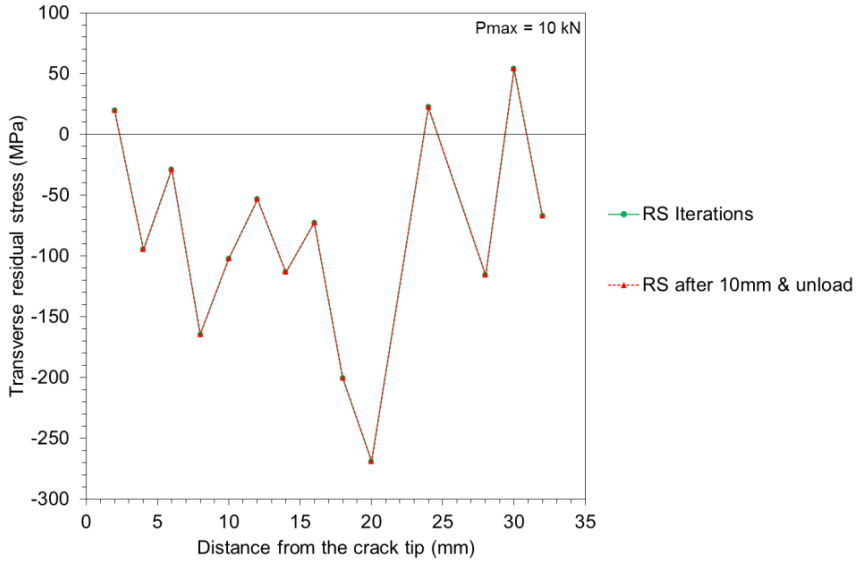

Figure 6-9: Numerical transverse RS profile on HAZ 4

It can be observed from the numerical results that the SIGINI approach implemented in this study does not allow for RS redistribution. Indeed, the RS state at the end of the iteration process previously described is the same as after 10 mm crack growth and unloading. Regardless of the new crack tip location, analyses show that after unloading the residual stress state is the same as the initial residual stresses, obtained at the end of the equilibrium.

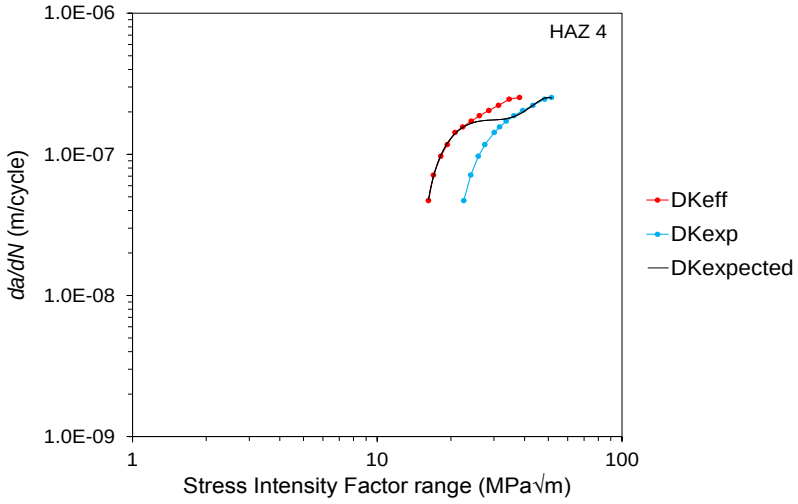

Figure 6-10: da/dN vs ΔK for HAZ 4

Another proof that the SIGINI approach does not account for RS redistribution is presented in Figure 6-10. If the redistribution was performed a different FCG trend would have been observed. As shown in Figure 6-10 the results from ΔK_{eff} would converge towards ΔK_{app} showing that the RS are redistributing and slowly vanishing. It can be concluded that when SIGINI approach is implemented in simulations ABAQUS assumes constant RS profile throughout the test similar to the weight function approach.

6.7 Summary

This work provided significant and useful outcomes in terms of numerical analysis: at first, it has demonstrated the efficiency of the method proposed for the introduction of RS into the FEA model representing the specimen tested in the laboratory. Moreover, the results provided by the FEA simulations have revealed to be reliable and in agreement with the theoretical and experimental expectations of the previous studies, in addition to the fact that some new aspects have been examined for the first time. However, it has also been demonstrated that the SIGINI approach implemented does not account for RS redistribution.

7 Fatigue crack growth tests in seawater

Corrosion-fatigue is a complex cumulative damaging phenomenon occurring on structures subjected to cyclic loading in a corrosive environment, such as seawater. In this research project FCG in seawater will be investigated in a free-corrosion environment. Moreover, calculations and analyses are performed under the LEFM hypothesis, considering a small plastic zone size ahead of the crack tip. Tests are performed under free-corrosion condition, with no cathodic protection to account for the worst case scenario in structural integrity assessment of monopiles.

7.1 Sample preparation and test set-up

Fracture mechanics tests are performed in seawater environment on four C(T) specimens with the crack tip located in the heat affected zone, denoted HAZ 7, HAZ 8, HAZ 9 and HAZ 10. In these tests, the crack growth in the main corrosion-fatigue tests is monitored using back face strain measurements. In order for the tests to be performed in a seawater environment, the back face of the samples where the strain gauge is attached must be protected against water. To do so, polysulfide coating is applied for waterproof protection of the strain gauge. Thereafter, samples are soaked in seawater for approximately 48 hours prior to testing (after pre-cracking) in order to replicate real life conditions where corrosion pits would induce corrosion-fatigue interaction mechanism. The sample preparation is presented in Figure 7-1. The micro-strain results obtained from the strain gauge records are converted into millimetres of crack length using the results obtained from the calibration tests which were previously conducted in air and their results were presented in Chapter 5.

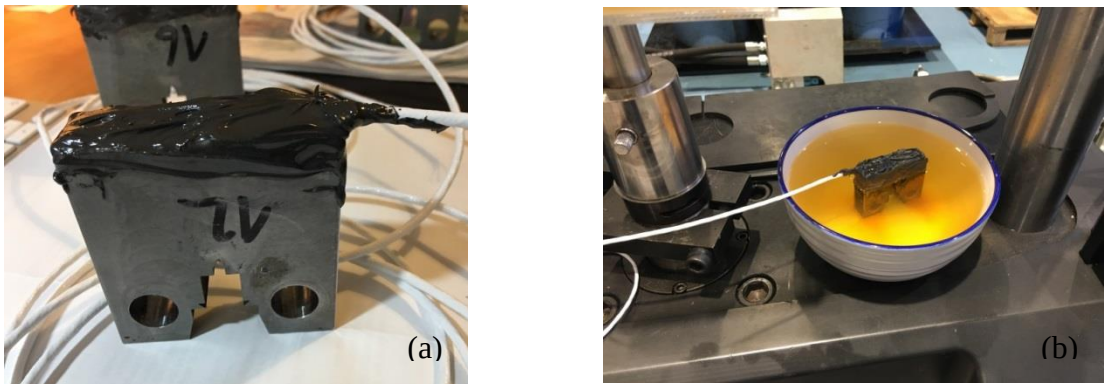

Figure 7-1: (a) C(T) sample after strain gauging, (b) Specimen soaked in seawater prior to testing

Corrosion-fatigue crack growth tests were performed under Mode I fracture mechanics loading conditions on a standard 100 kN servo-hydraulic fatigue testing Instron machine. The tests were performed in seawater with the load ratio of $R = 0.1$. The tests were conducted under load control mode and both the load and position limits were set in order to ensure that the sample is not overloaded, hence avoiding unexpected plasticity at the crack tip. Sinusoidal cyclic wave form using constant amplitude loading with the frequency of 0.3 Hz was used for corrosion-fatigue testing on the C(T) specimens. Consistency with the literature and for data comparison purposes, 70 L of substitute ocean seawater, using deionised water, was used and prepared in accordance with ASTM D1141-98 [197]. The composition of the artificial seawater prepared in the laboratory is given in Table 7-1.

Table 7-1: Chemical composition of artificial seawater [197]

Chemical compound	Concentration (g/L)
$NaCl$	24.53
$MgCl_2$	5.20
Na_2SO_4	4.09
$CaCl_2$	1.16
KCl	0.695
$NaHCO_3$	0.201
KBr	0.101
H_3BO_3	0.027
$SrCl_2$	0.025
NaF	0.003

The initial crack length in C(T) samples, which is reported as the distance between the centre of the pin hole and the machined V-notch in the samples, was a_i = 17 mm. All four samples to be tested in seawater were initially pre-cracked by approximately 4 mm from the initial V-notch tip using the K-decreasing procedure as suggested in [177]. Similar to the FCG tests in air, particular attention has been given during this process to ensure that the K_{max} value at the end of the pre-cracking stage did not exceed the initial K_{max} value at the beginning of the main corrosion-fatigue test. The crack length was measured using the back face strain measurements. The experimental set-up is presented in Figure 7-2 where it can be seen that the specimen was fully immersed in seawater at all times during the test.

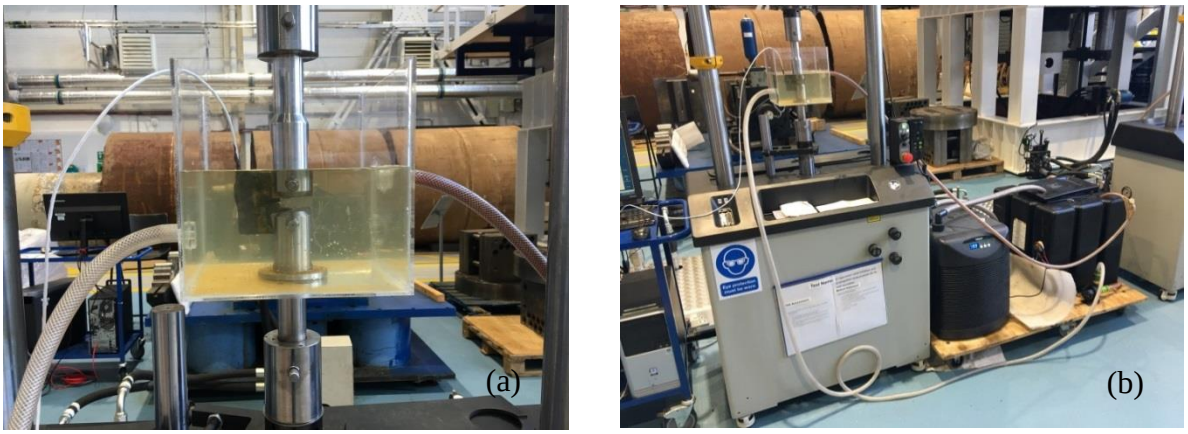

Figure 7-2: (a) Pertex corrosion chamber, (b) Corrosion-fatigue crack growth test set-up

The seawater was circulated through a Pertex chamber using pumps as shown in Figure 7-2 at a continuous rate of 4L/min. During the test, the temperature of the seawater in the chamber was controlled using Hailea refrigeration unit, Figure 7-2, and varied between 7.5 °C to 8.2 °C to replicate the operational conditions in the North Sea. The pH level at the beginning of the experiment was 8.1, which decreased with time until a level of pH 7.7 where the seawater was subsequently replaced. In total, 70 L of seawater was used for each experimental run where the specimen was completely immersed in the seawater throughout the test period. The loading conditions, specimen dimensions as well as initial and final crack lengths in HAZ 7, HAZ 8, HAZ 9 and HAZ 10 specimens are summarised in Table 7-2.

Table 7-2: C(T) specimen dimensions and loading conditions for corrosion-fatigue tests

	HAZ 7	**HAZ 8**	**HAZ 9**	**HAZ 10**
a_0 **(mm)**	20.4	20.3	20.4	20.3
a_f **(mm)**	29.0	33.3	27.6	29.4
W **(mm)**	50	50	50	50
B **(mm)**	16	16	16	16
P_{max} **(kN)**	10	10	10	10
P_{min} **(kN)**	1	1	1	1
f **(Hz)**	0.3	0.3	0.3	0.3
r_p **(mm)**	0.17	0.17	0.18	0.17

7.2 Data analysis

The data for the FCG tests performed in seawater environment have been analysed using the same equations as for the tests in air. However, the crack length in seawater tests was recorded with BFS gauges due to the environmental conditions and limited access to the test specimens immersed in seawater. BFS measurements and number of cycles have been recorded every five minutes. The maximum and minimum applied loads in all four tests on HAZ 7, HAZ 8, HAZ 9 and HAZ 10 specimen tests were P_{max} = 10 kN and P_{min} = 1 kN respectively. Using the calibration curves generated by performing tests on nominally identical specimens in air, the instantaneous values of crack length were estimated using the collected BFS data post-testing. The fatigue crack growth rate, da/dN, was calculated using a combination of the seven-point incremental polynomial method for most of the obtained data points and the secant method for the first and last three points where enough data points were not available to use the incremental polynomial technique. As explained earlier in Chapter 5 new shape function solution for C(T) specimen geometry presented in [8] were used to analyse the obtained corrosion-fatigue test data from this study. Note that as discussed in [8], the ΔK values calculated using Equation 2-16 are more accurate for a wider range of normalised crack lengths $0.2 \leq a/W \leq 0.7$ and therefore this equation was used to analyse the data obtained from corrosion-fatigue tests.

The results from these corrosion-fatigue tests have been compared with the fatigue trends for welded joints in free-corrosion recommended in BS7910 standard to examine the suitability of the existing trends for fatigue life prediction of offshore wind monopile foundations. All the tests were performed in seawater and the obtained results are compared with the literature data as well as the BM of the same structural steel and also the recommended BS7910 trends using the 2-stage law and simplified law.

7.3 Results and discussion

The results of the FCG tests in seawater performed in this research project have been presented and discussed in terms of “crack length vs. number of cycles” and “crack growth rate vs. stress intensity factor range”. The crack length measurements have been obtained using a calibration curve from the test in air based on BFS measurements. The tests have also been performed assuming uniform corrosion conditions.

7.3.1 "a vs. BFS" results

In order to accurately estimate the instantaneous crack length during seawater tests, BFS technique was employed to measure the bending strain at the back face of the C(T) specimen. The basis of this crack growth monitoring approach is as the crack advances, the bending strain at the back of the specimen increases. Therefore, by developing an empirical calibration curve the instantaneous crack lengths can be estimated using the BFS data. The BFS vs. crack length trends from the tests performed in air (see Chapter 5) have been found to overlap, therefore only the empirical correlation for HAZ 3 specimen has been shown in Figure 7-3 and used to estimate the crack lengths from BFS data in seawater tests.

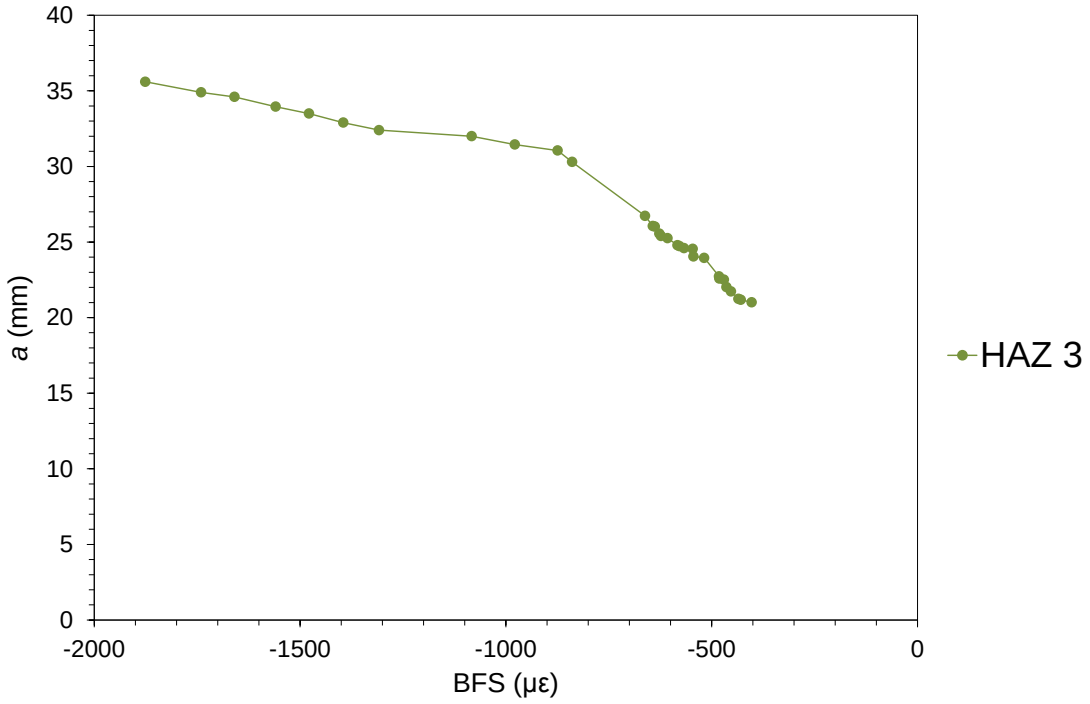

Figure 7-3: a vs BFS results for the tests in seawater

7.3.2 "a vs. N" results

After estimating the instantaneous crack lengths using the BFS data and calibration curve shown in Figure 7-3, the crack length values were plotted against the number of cycles and the results shown in Figure 7-4, for all the tests in seawater. It can be observed that a lower number of cycles (approximately three to four times lower) was required to grow the same crack length on 0° orientation samples compared to 180°. The difference between the crack growth rate in specimens with different orientations can be associated with the microstructure effects in the weld section. This observation agrees well with the tests in air, where the crack propagated faster in 0° orientation specimens. Similarly, the gradient in the crack length for a

given number of cycles was greater on HAZ 7 and HAZ 8 samples compared to HAZ 9 and HAZ 10.

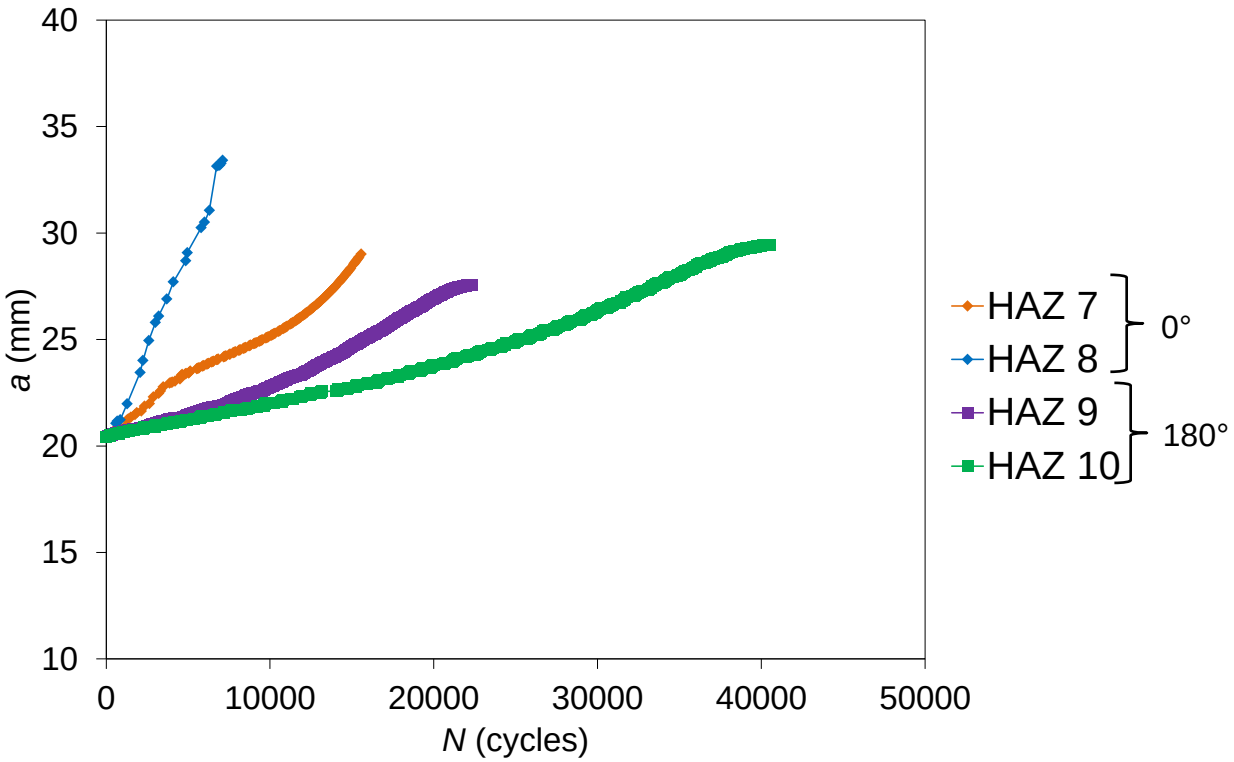

Figure 7-4: a vs N results for the tests in seawater

The raw data from corrosion-fatigue tests are compared with the air tests in Figure 7-5. It can be seen in this figure that in seawater environment, a lower number of cycles with reduced frequency are required to obtain a given value of crack extension compared to the air environment.

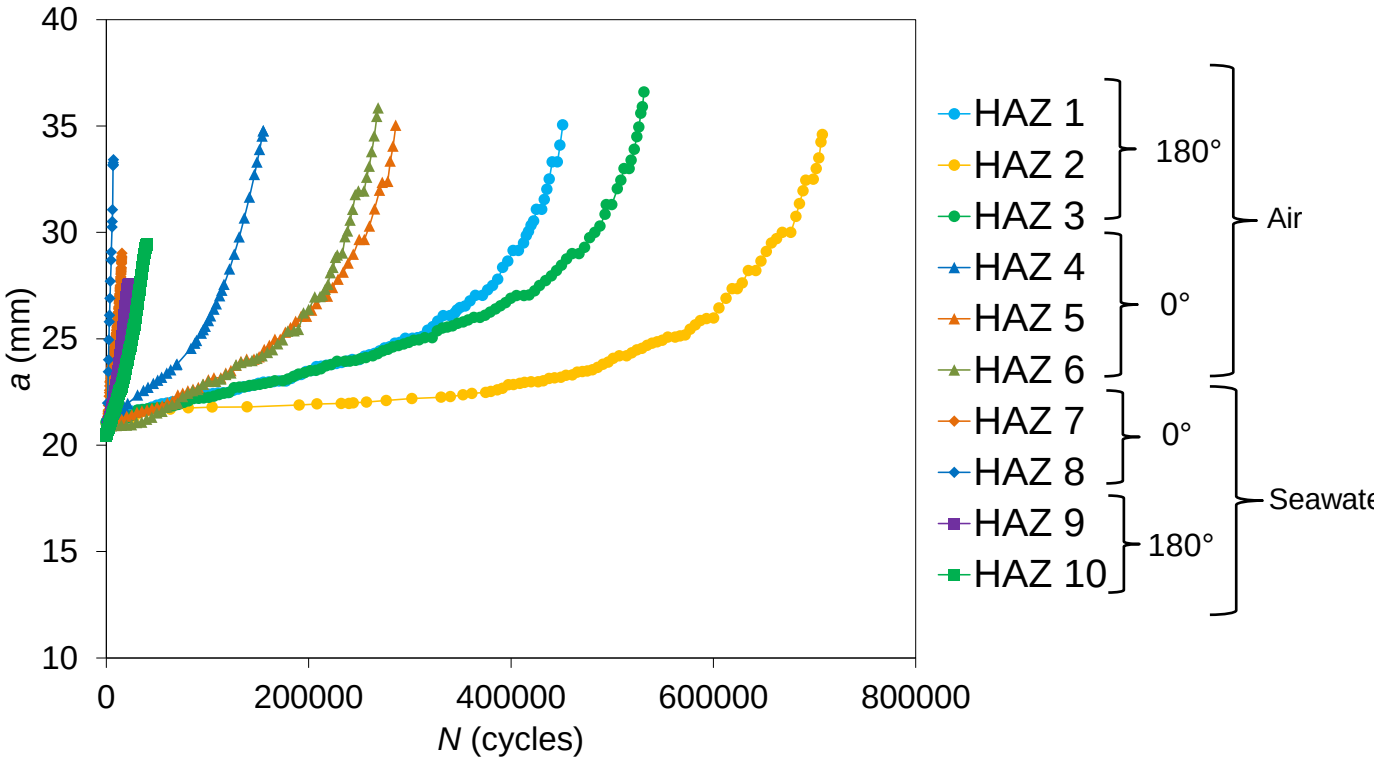

Figure 7-5: Comparison of the results for the tests in air and in seawater

7.3.3 "da/dN vs ΔK" results

Similar to the tests in air, the FCG rates for the four samples tested in seawater are correlated with ΔK and the results are shown in Figure 7-6. The line of best fit for the two orientations considered, 0° and 180°, have also been plotted to identify the power law constants. The Paris law constants obtained from this fit for the 180° orientation are $C = 2.0\times10^{-10}$, $m = 2.01$ with $R^2 = 0.96$ and $C = 6.0\times10^{-10}$, $m = 1.83$ with $R^2 = 0.80$ for the 0° orientation. A similar observation regarding the distribution of the results can be made on the seawater test as for the test in air. Indeed, the data points are slightly sparser for the 0° orientation samples. It can also be seen in Figure 7-6 that for a given value of ΔK, the FCG rate in seawater tests is on average 50% greater in 0° specimens compared to the 180° samples.

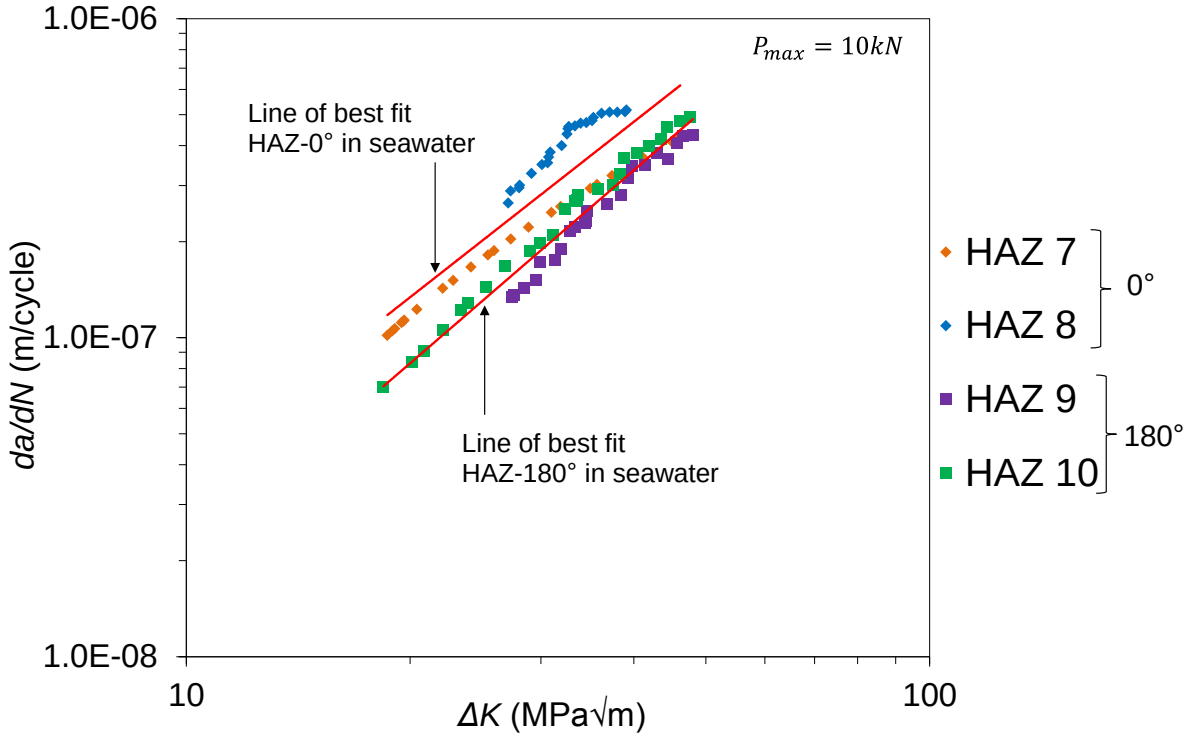

Figure 7-6: Corrosion-fatigue crack growth rates and the lines of best fit for the tests in seawater

The FCG data from the seawater tests on both specimen orientations are compared with the air tests in Figure 7-7. As seen in this figure, in both test environments the FCG trend for 0° orientations fall above the 180° orientation, however this shift is greater in the air tests (i.e. around 100% higher) compared to the seawater tests (i.e. 50% higher). Also seen in this figure is that for the air tests, the observed slope in the FCG data is steeper than the seawater tests, though the seawater data generally lies above the air test data. Finally, it can be seen in Figure 7-7 that the increased FCG rate in seawater tests compared to air tests is more pronounced in the lower ΔK region, although this difference reduces in the high ΔK region where the results from the test in both environments begins to converge.

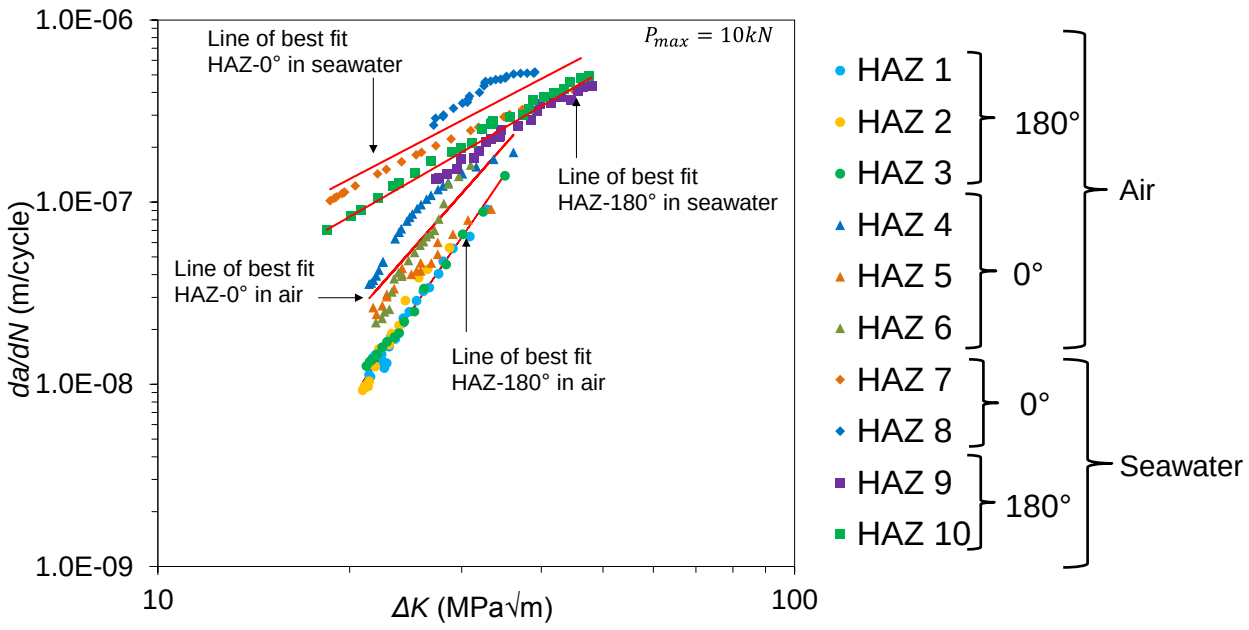

Figure 7-7: FCG rates comparison for the tests in air and in seawater

The corrosion-fatigue crack growth data on S355 G10+M structural steel from HAZ 7, HAZ 8, HAZ 9 and HAZ 10 C(T) specimens in this study are compared with the corrosion-fatigue test data on the BM and the results are shown in Figure 7-8. Also included in this figure are the seawater HAZ data available from the SLIC project (on S355 G8+M) as well as similar steels and the proposed trends in BS7910 standard [27]. It can be seen in this figure that the corrosion-fatigue data from the HAZ specimens with 180° orientation in the high ΔK region fall on top of the S355 G10+M BM corrosion-fatigue results obtained from the tests under the same loading conditions (P_{max} = 10 kN). It has also been noted that the SLIC corrosion-fatigue data fall in between the upper bound and lower bound trends obtained from 0° and 180° specimen orientations examined in this study.

The corrosion-fatigue HAZ data taken from the literature on similar steels and presented in Figure 7-8 are S355 G8+M [5], S355 J2+N [198], C-MN-V steel [191], 50D steel [199], API X70 steel [200], RQ Tuf501 steel [201]. It can be observed in Figure 7-8 that the corrosion-fatigue HAZ data from other steels generally falls upon or above the upper bound trend obtained from the current study on HAZ specimens with 0° orientation. Also seen in this figure is that for the dominant majority of the data points obtained from HAZ materials across a wide range of steels, the simplified law recommended in BS7910 provides a good fit to the upper bound data cloud. Finally seen in Figure 7-8 is that all data points from

corrosion-fatigue tests on various BM and HAZ materials fall below the 2-stage law recommended for welded joints in free-corrosion in BS7910.

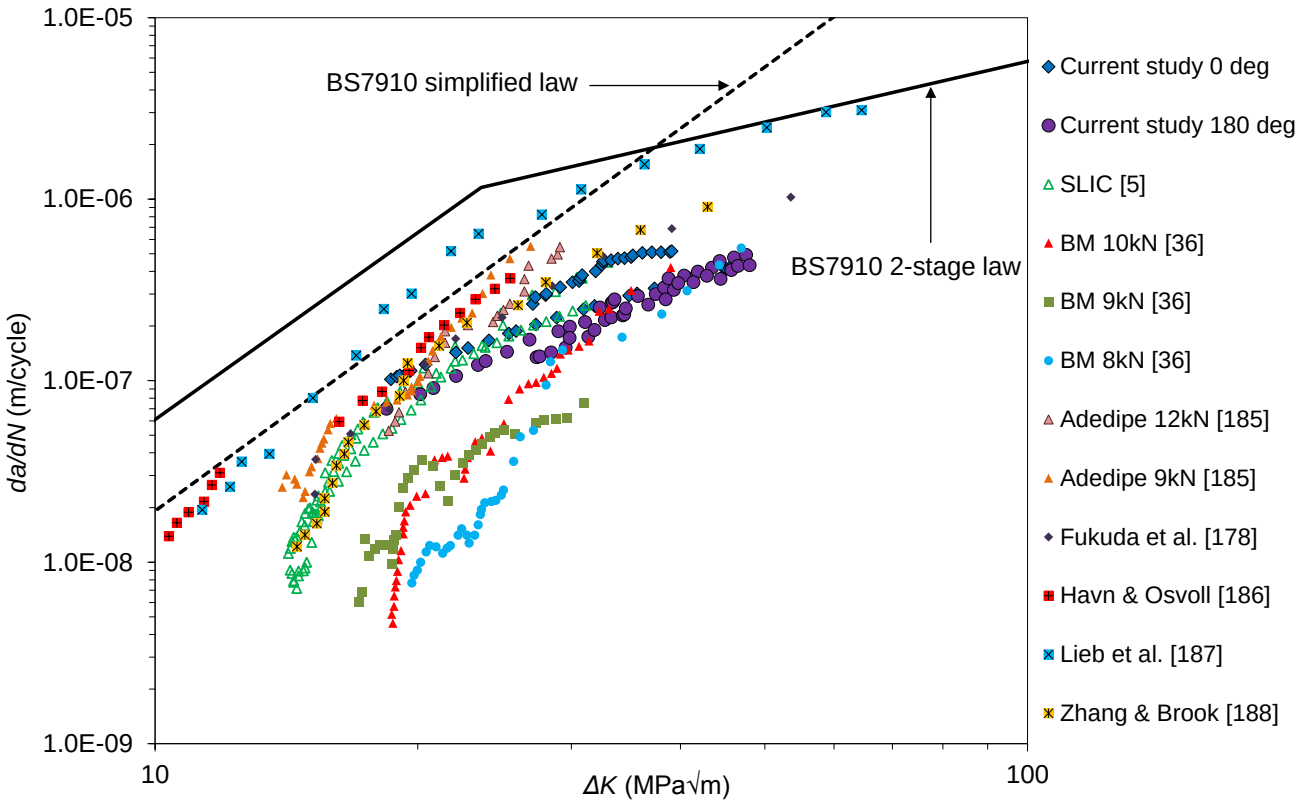

Figure 7-8: Comparison of the FCG data in seawater environment compared with the literature data and BS7910 recommended trends

7.3.4 Post-mortem analysis

The same procedure as for the tests in air was conducted for fractography analysis of the samples tested in seawater. An example of the broken open corrosion-fatigue test specimen is presented in Figure 7-9 where the scale for converting pixels to mm can also be observed. The crack extension at the end of the test on all four samples has been measured on the fracture surface and the results are compared with the estimated crack extension values in Table 7-3. The crack extension, Δa, values in Table 7-3 are calculated as the difference between the final, a_f, and initial, a_i, crack length (before pre-fatigue cracking). As seen in this table, the maximum difference between the estimated and measured crack extensions in all four specimens is 1.5 mm indicating that relatively accurate estimations of the instantaneous crack lengths can be made by using the BFS crack growth monitoring technique for corrosion-fatigue tests.

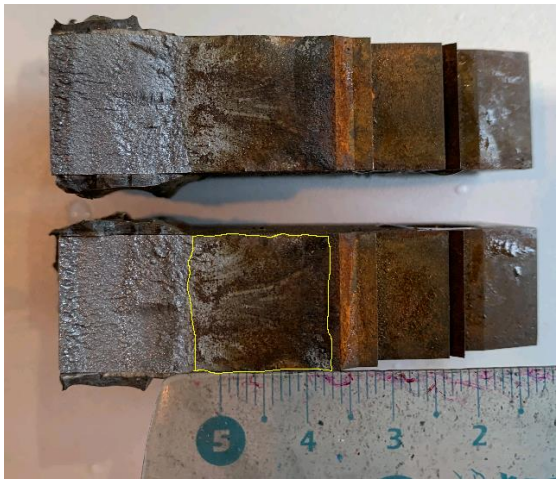

Figure 7-9: Fractography analysis on HAZ 7 after break-open

Table 7-3: Comparison of the final crack extension from fractography to optical measurements for seawater tests

	Optical measurement Δa (mm)	**ImageJ calculation Δa (mm)**
HAZ 7	16.3	15.2
HAZ 8	18.0	16.8
HAZ 9	16.0	14.9
HAZ 10	17.5	16.0

7.4 Summary

Corrosion fatigue tests have been performed on HAZ C(T) specimens with different orientations. The corrosion-fatigue crack growth results obtained from this study have been compared with the recommended BS7910 trends as well as the experimental data on similar steels. It has been shown in this study that the recommended BS7910 curves provide a good fit to the upper bound scatter of the corrosion-fatigue test data obtained from this study and across a wider range of steels. Moreover, it has been seen that similar to the air tests, the specimens with 0° orientation show higher FCG rates compared to 180° orientation samples in seawater tests.

8 Conclusions and future work

8.1 Conclusions

This study presented residual stress characterisation in structural steel offshore wind monopile weldments using neutron diffraction, neutron imaging and the contour method. The residual stress measurements, presented in Chapter 4, revealed a significant redistribution and reduction in the level of residual stresses by extracting laboratory samples from large scale welded structures. The remnant residual stresses in the standard laboratory samples are significant enough to have impacts on fatigue crack initiation, in particular, and crack propagation of subsequent fatigue tests on fracture mechanics C(T) specimens. The contour method measurements on the large welded mock-up showed significantly large level of tensile residual stress in the welded structure in the as-welded condition. This close to yield magnitude of tensile residual stress, if not reliably treated or accounted for in structural integrity assessments, could inevitably lead to accelerated fatigue crack initiation and propagation and unexpected catastrophic failure of monopile structures.

The experimental results from fatigue crack growth tests in air, in Chapter 5, have shown that the specimen orientation, with respect to the weld geometry, plays a significant role in fatigue crack growth behaviour of the material and for a given value of ΔK the specimens with 0° orientation show on average around twice the fatigue crack growth rates compared to the specimens with 180° orientation. Neutron diffraction measurements have been performed on six of the extracted HAZ specimens and the results have shown RS values of approximately +100 MPa and -100 MPa at the crack tip with peak residual stress values of between +380 MPa and -490 MPa along the transverse direction.

This study also showed a comparison of the neutron diffraction and neutron imaging measurements on a C(T) sample extracted from offshore wind monopile weldments. Moreover, a sensitivity analysis has been conducted in neutron imaging data analysis and the results have shown that: 1- The location of the corner in the neutron imaging radiography for the single d_0 value influences the residual strain results, 2- In cases where d_0 value corresponds to the average of the neutron imaging results and d_0 value is taken as the strain balance in through thickness direction, the analysed trends were similar and in good agreement with the residual strain results obtained from neutron diffraction measurements.

The present research project focused on a better understanding of the fatigue crack growth behaviour of S355 structural steel in the presence of RS. The experimental FCG results have been compared with the literature data. It has been shown in this study that the recommended BS7910 curves provide a conservative estimate of the fatigue crack growth behaviour in air and in seawater (under free corrosion condition) for the HAZ material using the corresponding 2-stage law and simplified law, respectively. Moreover, the results have shown that within the inherent experimental scatter the specimen orientation within the welded plate also has an effect on the FCG behaviour.

In order to examine the influence of residual stresses on near threshold fatigue crack growth behaviour of the material, a numerical model, presented in Chapter 6, has been constructed in ABAQUS where residual stresses are introduced into the model through an iterative process using the SIGINI subroutine and a Python code. The effective SIF was evaluated by applying the VCCT approach at each simulated stage of the crack propagation. The numerical results obtained from the characterised HAZ specimens with measured residual stress profiles have shown that for a given value of *da/dN* the effective stress intensity factor range in the near threshold region is up to 10 MPa√m lower compared to the applied stress intensity factor range. The shift of the analysed fatigue crack growth trend in the presence of residual stresses to lower values of ΔK is thought to be due to dominantly compressive residual stress profiles in the HAZ specimens examined using numerical simulations. Finally, it is expected that the curve from ΔK_{eff} overlaps with the curve from ΔK_{app} in the Paris region, if the redistribution of the residual stresses was modelled in numerical simulations.

This study demonstrates both the importance and necessity of the complete comprehension of the RS influence on the FCG behaviour in welded components and structures such as offshore wind turbine monopile foundations in order to obtain a more reliable and accurate service life prediction. This research project also examined the influence of remaining residual stresses in the C(T) HAZ specimens on the fatigue crack growth behaviour of offshore structural steel materials, particularly in the near threshold region.

The scientific contributions of this study are summarised below:

- A framework applicable to large scale structures was developed on C(T) specimens.
- Residual stress measurements on monopile welds have been presented for the first time.

- Original contour results from a large welded plate extracted from a monopile support structure have been introduced.
- A range of RS values has been provided for C(T) specimens from ND measurements.
- The size effect has been demonstrated by showing a significantly greater RS profile within the welded plate compared to the C(T) specimen.
- The effect of specimen orientation, with respect to the rolling direction, on fatigue behaviour has been studied. The difference in the results could be due to the microstructure as well as the slicing process, which could be further studied.
- The difference in the fatigue life of S355 steel in air and in seawater environments has been presented to show how much faster the tests were in seawater compared to air in mid-range ΔK.

8.2 Future work

As a future work it is suggested to perform larger scale component testing, taking into account the effect of RS, as it has been shown that the amount of locked-in RS is scale dependent. Further experimental studies should include variable amplitude loading as it is expected that the loads on the actual monopile structure are not applied with a constant amplitude in real life conditions. Scatter of the data in the FCG results should be further analysed as well. Having known that the amount of compressive RS could be potentially much higher in the actual monopile/larger scale structures, the crack closure effect should also be considered and studied further in future work. With respect to the RS measurements, ND could be performed after bending and rolling of the welded plate as the mechanical process might change the RS profile (redistribute, amplify or mitigate them). In order to fully understand the corrosion effect on the RS profile, ND could also be completed after few millimetres of crack growth in seawater environment. Finally, it is suggested to compare analytically calculated SIF values with FEA results, considering the applied load only, without RS. This would help to calibrate the FEA model for subsequent calculations of SIF values taking into account RS. Moreover, the FEA analysis could be performed on a 3D model in future work in order to consider the through thickness RS distribution. Similar analysis could also be done for the tests in seawater, as the effective stress intensity factor has only been calculated for the tests in air. The effect of corrosion pitting on RS redistribution in offshore wind turbine monopile foundations can be studied in future work as well. Last but

not least, the effect of microstructure could also be studied in order to justify the FCG trends, especially the difference observed between the 0° and 180° orientations.

9 References

[1] P. A. Owusu and S. Asumadu-Sarkodie, “A review of renewable energy sources, sustainability issues and climate change mitigation,” *Cicil Environ. Eng.*, vol. 3, 2016.

[2] P. H. Jensen, T. Chaviaropolos, and A. Natarajan, “LCOE reduction for the next generation offshore wind turbines,” 2017.

[3] G. Smart, “Offshore Wind Cost Reduction Recent and future trends in the UK and Europe,” 2016.

[4] Energy UK, “Offshore Wind Market Development and Cost Reduction Background,” 2018.

[5] A. Mehmanparast, F. Brennan, and I. Tavares, “Fatigue crack growth rates for offshore wind monopile weldments in air and seawater: SLIC inter-laboratory test results,” *Mater. Des.*, vol. 114, pp. 494–504, 2017.

[6] J. F. Manwell, J. G. McGowan, and A. L. Rogers, *Wind energy explained: theory, design and application*. 2009.

[7] R. Scharff and M. Siems, “Monopile foundations for offshore wind turbines - solutions for greater water depths,” 2013.

[8] W. Musial, S. Butterfield, and B. Ram, “Energy from Offshore Wind,” in *Offshore Technology Conference*, 2006, pp. 1–11.

[9] J. Velarde, “Design of Monopile Foundations to Support the DTU 10 MW Offshore Wind Turbine,” 2016.

[10] J. van der Tempel, N. F. B. Diepeveen, C. S. D.J., and W. E. de Vries, “Design of support structures for offshore wind turbines,” in *WIT Transactions on State of the Art in Science and Engineering*, vol. 44, 2010, pp. 1–25.

[11] L. Arany, S. Bhattacharya, J. Macdonald, and S. J. Hogan, “Design of monopiles for offshore wind turbines in 10 steps,” *Soil Dyn. Earthq. Eng.*, vol. 92, pp. 126–152, 2016.

[12] A. Jacob, J. Oliveira, A. Mehmanparast, F. Hosseinzadeh, J. Kelleher, and F. Berto, “Residual Stress Measurements in Offshore Wind Monopile Weldments using Neutron Diffraction Technique and Contour Method,” *Theor. Appl. Fract. Mech.*, Jun. 2018.

[13] Det Norske Veritas AS, “Offshore Standard DNV-OS-B101: Metallic Materials,” 2009.

[14] J. Peeringa and G. Bedon, “Fully integrated load analysis included in the structural reliability assessment of a monopile supported offshore wind turbine,” in *Energy Procedia*, 2017, vol. 137, pp. 255–260.

[15] J. Velarde and E. E. Bachynski, “Design and fatigue analysis of monopile foundations to support the DTU 10 MW offshore wind turbine,” in *Energy Procedia*, 2017, vol. 137, pp. 3–13.

[16] D. V. Nelson, “Effects of Residual Stress on Fatigue Crack Propagation,” in *Residual Stress Effects in Fatigue, ASTM STP 776, American Society for Testing and Materials*, 1982, pp. 172–194.

[17] F. V. Lawrence, J. D. Burk, and J.-Y. Yung, “Influence of Residual Stress on the Predicted Fatigue Life of Weldments,” *Residual Stress Eff. Fatigue, ASTM STP 776, Am. Soc. Test. Mater.*, pp. 33–43, 1982.

[18] J. Baumgartner, “Enhancement of the fatigue strength assessment of welded components by consideration of mean and residual stresses in the crack initiation and propagation phases,” *Weld. World*, vol. 60, no. 3, pp. 547–558, 2016.

[19] F. A. Kandil, J. D. Lord, A. T. Fry, and P. V Grant, “A Review of Residual Stress Measurement Methods -A Guide to Technique Selection,” 2001.

[20] C. O. Ruud, “A review of selected non-destructive methods for residual stress measurement,” *NDT Int.*, vol. 15, no. 1, pp. 15–23, 1982.

[21] X. Lu, “Influence of Residual Stress on Fatigue Failure of Welded Joints,” NC State University, 2003.

[22] P.-Y. Cheng, “Influence of Residual Stress and Heat Affected Zone on Fatigue Failure of Welded Piping Joints,” NC STate University, 2009.

[23] J. Krebs and M. Kassner, “Influence of Welding Residual Stresses on Fatigue Design of Welded Joints and Components,” *Weld. World*, vol. 51, no. 7/8, pp. 54–68, 2007.

[24] O. Adedipe, F. Brennan, A. Mehmanparast, A. Kolios, and I. Tavares, “Corrosion fatigue crack growth mechanisms in offshore monopile steel weldments,” *Fatigue Fract. Eng. Mater. Struct.*, vol. 40, no. 11, pp. 1868–1881, 2017.

[25] A. Mehmanparast, O. Adedipe, F. Brennan, and A. Chahardehi, “Welding sequence effects on residual stress distribution in offshore wind monopile structures,” *Frat. ed Integrità Strutt.*, vol. 35, pp. 125–131, 2016.

[26] B. Jonsson, G. Dobmann, A. F. Hobbacher, M. Kassner, and G. Marquis, *IIW Guidelines on Weld Quality in Relationship to Fatigue Strength*. Cham: Springer International Publishing, 2016.

[27] The British Standards Institution, “BSI Standards Publication Guide to methods for assessing the acceptability of flaws in metallic structures,” 2015.

[28] Wind Europe, “Offshore Wind in Europe Key trends and statistics in 2018,” 2019.

[29] Department for Business Energy & Industrial Strategy, “UK Energy in Brief 2018,” 2018.

[30] S. Malhotra, “Selection, Design and Construction of Offshore Wind Turbine Foundations,” 2011.

[31] J. van der Tempel, N. Diepeveen, D. Cerda Salzmann, and W. de Vries, “Design of support structures for offshore wind turbines,” in *Wind power generation and wind turbine design*, 2010.

[32] Dillinger Hutte GTS, “Solutions in Steel for Offshore Wind Energy Installations,” 2018.

[33] G. Masi, F. Matteucci, and J. Tacq, “State of the Art Study on Materials and Solutions against Corrosion in Offshore Structures,” 2018.

[34] A. Momber, “Corrosion and corrosion protection of support structures for offshore wind energy devices (OWEA),” *Mater. Corosion*, vol. 62, no. 5, pp. 391–404, 2011.

[35] DNVGL Offshore standard, *DNVGL-OS-B101 Metallic materials*. 2015.

[36] V. Igwemezie, A. Mehmanparast, and A. Kolios, “Materials selection for XL wind turbine support structures: A corrosion-fatigue perspective,” *Mar. Struct.*, vol. 61, no. June 2018, pp. 381–397, 2018.

[37] I. P. Ward, “Natural frequency analysis of offshore wind turbine monopiles,” in *Proceedings of the Institution of Civil Engineers - Engineering and Computational Mechanics*, 2016, vol. 169, no. 4, pp. 196–208.

[38] J. W. Gaythwaite, *Design of Marine Facilities for the Berthing, Mooring, and Repair*

of Vessels. 1990.

[39] D. Amar Bouzid, S. Bhattacharya, and L. Otsmane, "Assessment of natural frequency of installed offshore wind turbines using nonlinear finite element model considering soil-monopile interaction," *J. Rock Mech. Geotech. Eng.*, vol. 10, no. 2, pp. 333–346, Apr. 2018.

[40] ASM International, "Introduction to Tensile Testing," in *Tensile Testing*, Second Edi., 2004.

[41] R. Hooke, "Lecture de Potentia Resitutiva, or of spring, explaining the power of springing bodies to which are added some collections," *L. Martin*, p. 56, 1678.

[42] J. Rychlewski, "On Hooke's law," *J. Appl. Math. Mech.*, vol. 48, no. 3, pp. 303–314, Jan. 1984.

[43] W. Ramberg and W. R. Osgood, "Description of stress-strain curves by three parameters," 1943.

[44] A. Mehmanparast, "The Influence of Inelastic Damage on Creep, Fatigue and Fracture Toughness," Imperial College London, 2012.

[45] S. Ebnesajjad, "Surface and Material Characterization Techniques," in *Surface Treatment of Materials for Adhesive Bonding*, Second Edi., 2014, pp. 39–75.

[46] J. Bergström, "Experimental Characterization Techniques," in *Mechanics of Solid Polymers*, William Andrew Publishing, 2015, pp. 19–114.

[47] J. F. Luo *et al.*, "EBSD measurements of elastic strain fields in a GaN/sapphire structure," *Microelectron. Reliab.*, no. 46, pp. 178–182, 2006.

[48] Y. Bergstrom and H. Hallen, "Hall-Petch relationships of iron and steel," *Met. Sci.*, vol. 17, no. 7, pp. 341–347, 1983.

[49] S. H. Whang, "Nanostructured Metals and Alloys - Processing, Microstrucre, Mechanical Properties and Applications," in *Metals and Surface Engineering*, Woodhead Publishing, 2011, pp. xxi–xxxv.

[50] M. O. Lai and K. B. Lim, "On the prediction of tensile properties from hardness tests," *Mater. Sci.*, vol. 26, pp. 2031–2036, 1991.

[51] V. John, "Hardness and its Measurement," in *Testing of Materials*, London: Macmillan Education UK, 1992, pp. 5–20.

[52] ASTM International, *ASTM E384-17 Standard Test Method for Microindentation Hardness of Materials*. 2017.

[53] D. Kopeliovich, "Hardness test methods," *Substances and Technologies*, 2014. .

[54] T. L. Anderson, "Fracture Mechanics Fundamentals and Applications," *Angew. Chemie Int. Ed.*, 2001.

[55] G. R. Irwin, "Plastic zone near a crack and fracture toughness.," in *Proceedings of the 7th Sagamore Ordonance Maerials Conference*, 1960, pp. 463–478.

[56] A. A. Wells, "Unstable Crack Propagation in metals, Cleavage and Fast Fracture," in *The Crack Propagation Symposium, Cranfield*, 1961, vol. 1.

[57] J. R. Rice, "A Path Independent Integral and the Approximate Analysis of Strain Concentration by Notches and Cracks," *J. Appl. Mech.*, vol. 35, pp. 379–386, 1968.

[58] P. J. G. Schreurs, "Fracture Mechanics," 2012.

[59] X.-K. Zhu and J. A. Joyce, "Review of Fracture Toughness (G, K, J, CTOD, CTOA) testing and standardization," *Eng. Fract. Mech.*, vol. 85, pp. 1–46, 2012.

[60] D. Roylance, "Introduction to Fracture Mechanics," Cambridge, 2001.

[61] J. R. Barber, "Plane Strain and Plane Stress," in *Elasticity. Solid Mechanics and Its Applications, vol 12.*, 1992, pp. 31–37.

[62] G. R. Irwin, "Analysis of Stresses and Strains Near the End of a Crack Traversing a Plate," in *Applied Mechanics Division Summer Conference, ASME*, 1957.

[63] G. R. Irwin, "Onset of Fast Crack Propagation in High Strength Steel and Aluminum Alloys," in *Sagamore Research Conference Proceedings*, 1956, pp. 289–305.

[64] A. A. Griffith, "The Phenomena of Rupture and Flow in Solids," *Philos. Trans. R. Soc. A Math. Phys. Eng. Sci.*, 1921.

[65] A. Uguz and J. W. Martin, "Plastic zone size measurement techniques for metallic materials," *Mater. Charact.*, 2002.

[66] G. R. Irwin, J. A. Kies, and H. L. Smith, "Fracture strengths relative to onset and arrest of crack propagation," in *Proc Am Soc Test Mater*, 1958, vol. 58, pp. 640–660.

[67] A. A. Wells, "Application of Fracture Mechanics at and Beyong General Yielding," *Br. Weld. J.*, 1963.

[68] J. Schijve, *Fatigue of structures and materials*. 2009.

[69] The Open University, "Component Failure Museum," 2017. [Online]. Available: http://technology.open.ac.uk/materials/mem/mem_ccf4.htm. [Accessed: 21-Jul-2019].

[70] P. C. Paris and F. Erdogan, "A Critical Analysis of Crack Propagation Laws," *ASME*, pp. 528–533, 1963.

[71] P. C. Paris, "A Note on the Variables Effecting the Rate Crack Growth Due to Cyclic Loading," *Boeing Company, Doc. No. D-17867, Add. N*, 1957.

[72] P. C. Paris, "Crack Propagation Caused by Fluctuating Loads," *ASME Pap. No. 62*, 1962.

[73] P. C. Paris, M. P. Gomez, and W. E. Anderson, "A Rational Analytic Theory of Fatigue," *Trend Eng.*, vol. 13, no. 1, p. 9, 1961.

[74] ASTM Standard E647 − 13a, "Standard Test Method for Measurement of Fatigue Crack Growth Rates," *Am. Soc. Test. Mater.*, 2014.

[75] A. H. Noroozi, G. Glinka, and S. Lambert, "A study of the stress ratio effects on fatigue crack growth using the unified two-parameter fatigue crack growth driving force," *Int. J. Fatigue*, vol. 29, no. 9–11, pp. 1616–1633, Sep. 2007.

[76] X. Huang and T. Moan, "Improved modeling of the effect of R-ratio on crack growth rate," *Int. J. Fatigue*, vol. 29, no. 4, pp. 591–602, Apr. 2007.

[77] O. Vosikovsky, "The effect of stress ratio on fatigue crack growth rates in steels," *Eng. Fract. Mech.*, vol. 11, no. 3, pp. 595–602, Jan. 1979.

[78] S. M. Beden, S. Abdullah, and A. K. Ariffin, "Review of Fatigue Crack Propagation Models for Metallic Components," *Eur. J. Sci. Res.*, vol. 28, no. 3, pp. 364–397, 2009.

[79] S. V. Kumbhar and R. M. Tayade, "A Case Study on Effect of Mean Stress on Fatigue Life," *Int. J. Eng. Dev. Res.*, vol. 2, no. 1, pp. 304–308, 2014.

[80] J. Woodtli, W. Muster, and J. C. Radon, "Residual stress effects in fatigue crack growth," *Eng. Fract. Mech.*, vol. 24, no. 3, pp. 399–412, Jan. 1986.

[81] J. C. Lippold, *Welding Metallurgy and Weldability*. 2015.

[82] U. Zerbst, M. Vormwald, R. Pippan, H.-P. Gänser, C. Sarrazin-Baudoux, and M. Madia, "About the fatigue crack propagation threshold of metals as a design criterion –

A review," *Eng. Fract. Mech.*, vol. 153, pp. 190–243, Mar. 2016.

[83] O. Demir, A. O. Ayhan, S. Iric, and H. Lekesiz, "Evaluation of mixed-mode-I/II criteria for fatigue crack propagation using experiments and modeling," *Chinese J. Aeronaut.*, vol. 31, no. 7, pp. 1525–1534, 2018.

[84] W. Elber, "Fatigue crack closure under cyclic tension," *Eng. Fract. Mech.*, vol. 2, pp. 37–45, 1970.

[85] S. Suresh and R. O. Ritchie, "Propagation of short fatigue cracks," *Int. Metall. Rev.*, vol. 29, pp. 445–476, 1984.

[86] R. M. J. Kemp, "Fatigue Crack Closure - A review," 1990.

[87] T. T. Shih and R. P. Wei, "A study of crack closure in fatigue," *Eng. Fract. Mech.*, vol. 6, no. 1, pp. 19–32, Mar. 1974.

[88] J. A. F. O. Correia, A. M. P. De Jesus, P. M. G. P. Moreira, and P. J. S. Tavares, "Crack Closure Effects on Fatigue Crack Propagation Rates: Application of a Proposed Theoretical Model," *Adv. Mater. Sci. Eng.*, pp. 1–11, Mar. 2016.

[89] K. Tanaka, Y. Nakai, and M. Yamashita, "Fatigue growth threshold of small cracks," *Int. J. Fract.*, vol. 17, no. 5, 1981.

[90] J. Petit, G. Henaff, and C. Sarrazin-Baudoux, "Mechanisms and Modeling of Near-Threshold Fatigue Crack Propagation," *Fatigue Crack Growth Threshold. Endur. Limits, Des. ASTM STP 1372*, pp. 3–30, 2000.

[91] R. Lindstrom, P. Lidar, and B. Rosborg, "Fatigue Crack Growth Thresholds Measurements in Structural Materials," *Fatigue Crack Growth Threshold. Endur. Limits, Des. ASTM STP 1372*, pp. 400–410, 2000.

[92] M. T. Hutchings, P. J. Withers, T. M. Holden, and T. Lorentzen, *Introduction to the characterization of residual stress by neutron diffraction*. Taylor & Francis, 2005.

[93] A. Graner Solana, A. D. Crocombe, and I. A. Ashcroft, "Fatigue life and backface strain predictions in adhesively bonded joints," *Int. J. Adhes. Adhes.*, vol. 30, no. 1, pp. 36–42, 2010.

[94] V. Shenoy, I. A. Ashcroft, G. W. Critchlow, A. D. Crocombe, and M. M. Abdel Wahab, "An investigation into the crack initiation and propagation behaviour of bonded single-lap joints using backface strain," *Int. J. Adhes. Adhes.*, vol. 29, no. 4,

pp. 361–371, 2009.

[95] A. D. Crocombe, C. Y. Ong, C. M. Chan, M. M. A. Wahab, and I. A. Ashcroft, “Investigating Fatigue Damage Evolution In Adhesively Bonded Structures Using Backface Strain Measurement,” *J. Adhes.*, vol. 78, no. 9, pp. 745–776, 2002.

[96] D. A. Virkler, B. M. Hillberry, and P. K. Goel, “The Statistical Nature of Fatigue Crack Propagation,” *J. Eng. Mater. Technol.*, vol. 101, pp. 148–153, 1979.

[97] D. Rozumek and E. Macha, “A Survey of Failure Criteria and Parameters in Mixed-Mode Fatigue Crack Growth,” *Mater. Sci.*, vol. 45, no. 2, pp. 190–210, 2009.

[98] *DIN EN ISO 8044 Corrosion of metals and alloys - Basic concepts*. 2015.

[99] H. J. Gough and D. G. Sopwith, “Some Comparative Corrosion Fatigue Tests Employing Two Types of Stressing Action,” *J. Iron Steel Inst.*, vol. 127, pp. 301–332, 1933.

[100] J. M. Barsom, “Effect of Cyclic Stress Form on Corrosion Fatigue Crack Propagation Below KIscc in a High Yield Strength Steel,” in *Corrosion Fatigue: Chemistry, Mechanics and Microstructure*, 1972, vol. NACE-2, Na, pp. 424–436.

[101] R. P. Gangloff, “Corrosion Fatigue Crack Propagation in Metals,” 1990.

[102] P. J. E. Forsyth, *The Physical Basis of Metal Fatigue*. 1969.

[103] G. Pouget and A. P. Reynolds, “Residual stress and microstructure effects on fatigue crack growth in AA2050 friction stir welds,” *Int. J. Fatigue*, vol. 30, no. 3, pp. 463–472, 2008.

[104] C. O. Ruud, “Nondestructive and Semidestructive Methods for Residual Stress Measurement,” in *Residual Stress Effects in Fatigue, ASTM STP 776, American Society for Testing and Materials*, 1982, pp. 3–5.

[105] D. Radaj, C. M. Sonsino, W. Fricke, D. Radaj, C. M. Sonsino, and W. Fricke, “Crack propagation approach for seam-welded joints,” *Fatigue Assess. Welded Joints by Local Approaches*, pp. 233–295, Jan. 2006.

[106] G. Pouget and A. P. Reynolds, “Residual stress and microstructure effects on fatigue crack growth in AA2050 friction stir welds,” *Int. J. Fatigue*, vol. 30, no. 3, pp. 463–472, Mar. 2008.

[107] S. J. Lewis, S. Hossain, D. J. Smith, C. E. Truman, and M. Hofmann, “Determination

of Remnant Residual Stresses in Fracture Toughness Specimens Extracted From Large Components," *Strain*, vol. 47, pp. e333–e343, Jun. 2011.

[108] R. John, K. . Jata, and K. Sadananda, "Residual stress effects on near-threshold fatigue crack growth in friction stir welds in aerospace alloys," *Int. J. Fatigue*, vol. 25, no. 9–11, pp. 939–948, Sep. 2003.

[109] S. J. Maddox, "Influence of Tensile Residual Stresses on the Fatigue Behavior of Welded Joints in Steel," *Residual Stress Eff. Fatigue, ASTM STP 776, Am. Soc. Test. Mater.*, pp. 63–96, 1982.

[110] F. Lawrence, J. Burk, and J.-Y. Yung, "Influence of Residual Stress on the Predicted Fatigue Life of Weldments," in *Residual Stress Effects in Fatigue*, 2009.

[111] A. P. Parker, "Stress Intensity Factors, Crack Profiles, and Fatigue Crack Growth Rates in Residual Stress Fields," in *Residual Stress Effects in Fatigue, ASTM STP 776, American Society for Testing and Materials*, 1982, pp. 13–31.

[112] B. Qiang, Y. Li, C. Yao, and X. Wang, "Through-thickness welding residual stress and its effect on stress intensity factors for semi-elliptical surface cracks in a butt-welded steel plate," *Eng. Fract. Mech.*, vol. 193, no. February, pp. 17–31, 2018.

[113] J. R. Rice, "Some remarks on elastic crack-tip stress fields," *Int. J. Solids Struct.*, vol. 8, no. 6, pp. 751–758, Jun. 1972.

[114] R. Bao, X. Zhang, and N. A. Yahaya, "Evaluating stress intensity factors due to weld residual stresses by the weight function and finite element methods," *Eng. Fract. Mech.*, vol. 77, no. 13, pp. 2550–2566, 2010.

[115] G. S. Schajer, *Practical Residual Stress Measurement Methods*. United Kingdom: John Wiley & Sons Ltd, 2013.

[116] R. Woracek, "Energy selective neutron imaging for the characterization of polycrystalline materials," 2015.

[117] G. Burca, "Combined Neutron Imaging and Diffraction: Instrumentation and Experimentation," Open University, 2012.

[118] W. Reimers, A. R. Pyzalla, A. Schreyer, and H. Clemens, *Neutrons and Synchrotron Radiation in Engineering Materials Science*. 2017.

[119] G. S. Schajer, *Practical Residual Stress Measurement Methods*. 2013.

[120] R. Pynn, *Neutron Scattering - A Primer*. Los Alamos Science 19, 1990.

[121] G. J. Long, "Neutron Diffraction," in *Comprehensive Coordination Chemistry II*, 2003, pp. 83–90.

[122] H. Schober, "Neutron Scattering Instrumentation," in *Neutron Scattering Applications and Techniques*, 2009, pp. 37–104.

[123] W. H. Bragg and W. L. Bragg, "The reflection of X-rays by crystals," in *Proceeding of the Royal Society of London. Series A 88*, 1913, pp. 428–438.

[124] W. L. Bragg, "The Structure of Some Crystals as Indicated by Their Diffraction of X-rays," in *Proceedings of the Royal Society of London. Series A 89*, 1913, pp. 248–277.

[125] J. Mathew, R. J. Moat, S. Paddea, J. A. Francis, M. E. Fitzpatrick, and P. J. Bouchard, "Through-Thickness Residual Stress Profiles in Austenitic Stainless Steel Welds: A Combined Experimental and Prediction Study," *Metall. Mater. Trans. A*, vol. 48.

[126] M. C. Smith, O. Muránsky, Q. Xiong, P. J. Bouchard, J. Mathew, and C. Austin, "Validated prediction of weld residual stresses in austenitic steel pipe girth welds before and after thermal ageing, part 1: Mock-up manufacture, residual stress measurements, and materials characterisation," *Int. J. Press. Vessel. Pip.*, vol. 172, pp. 233–250, May 2019.

[127] M. Daymond and L. Edwards, "ENGIN-X: A Fully Refined Diffractometer Designed Specifically for Measurement of Stress," *Neutron News Sci. Rev.*, 2010.

[128] ISO, "Non-destructive Testing-standard Test Method for Determining Residual Stresses by Neutron Diffraction. Technical Specification ISO/TS 21432," 2005.

[129] H. M. Rietveld, "A profile refinement method for nuclear and magnetic structures," *J. Appl. Crystallogr.*, vol. 2, no. 2, pp. 65–71, Jun. 1969.

[130] W. Woo, V. T. Em, B. S. Seong, P. Mikula, and G. B. An, "Residual stress determination in a thick ferritic steel weld plate using neutron diffraction," *J. Mater. Sci.*, vol. 47, pp. 5617–5623, 2012.

[131] H. Kallmann and E. Kuhn, "Photographic Detection of Slowly Moving Neutrons. United States Patent 2,186,757," 1940.

[132] A. K. Heller and J. S. Brenizer, "Neutron Radiography," in *Neutron Imaging and Applicaitons*, 2009, pp. 67–80.

[133] N. Kardjilov *et al.*, “Three-dimensional imaging of magnetic fields with polarized neutrons,” *Nat. Phys.*, vol. 4, pp. 399–403, 2008.

[134] J. R. Santisteban *et al.*, “Strain imaging by Bragg edge neutron transmission,” *Nucl. Instruments Methods Phys. Res. Sect. A Accel. Spectrometers, Detect. Assoc. Equip.*, vol. 481, pp. 765–768, 2002.

[135] A. S. Tremsin *et al.*, “High resolution neutron resonance absorption imaging at a pulsed neutron beamline,” *IEEE Trans. Nucl. Sci.*, vol. 59, pp. 3272–3277, 2012.

[136] A. S. Tremsin, J. V. Vallerga, J. B. McPhate, and O. H. W. Siegmund, “Optimization of high count rate event counting detector with Microchannel Plates and quad Timepix readout,” *Nucl. Instruments Methods Phys. Res. Sect. A Accel. Spectrometers, Detect. Assoc. Equip.*, vol. 787, pp. 20–25, 2015.

[137] W. Treimer, “Neutron Tomography,” in *Neutron Imaging and Applications*, 2009, pp. 81–108.

[138] W. Kockelmann, G. Frei, E. Lehmann, P. Vontobel, and J. R. Santisteban, “Energy-selective neutron transmission imaging at a pulsed source,” *Nucl. Instruments Methods Phys. Res. A 578*, pp. 421–434, 2007.

[139] R. Woracek, “Energy selective neutron imaging for the characterization of polycrystalline materials,” University of Tennessee, Knoxville, 2015.

[140] E. Lehmann, D. Mannes, A. Kaestner, and C. Grunzweig, “Recent Applications of Neutron Imaging Methods,” in *8th International Topical Meeting on Neutron Radiography*, 2017, pp. 5–12.

[141] D. Penumadu, “Material Science and Engineering with Neutron Imaging,” in *Neutron Imaging and Applications*, 2009.

[142] L. Crow, “Neutron Detectors for Imaging,” in *Neutron Imaging and Applications*, 2009, pp. 47–63.

[143] A. P. Kaestner and M. Schulz, “Processing Neutron Imaging Data - Quo Vadis?,” in *10 World Conference on Neutron Radiography*, 2014, pp. 336–342.

[144] M. B. Prime and A. R. Gonzales, “The Contour Method: Simple 2-D Mapping of Residual Stresses,” in *Sixth International Conference on Residual StressesSixth International Conference on Residual Stresses, July 10-12*, 2000.

[145] M. B. Prime, “Cross-Sectional Mapping of Residual Stresses by Measuring the Surface Contour After a Cut,” *J. Eng. Mater. Technol.*, 2002.

[146] A. Leski, “Implementation of the virtual crack closure technique in engineering FE calculations,” *Finite Elem. Anal. Des.*, vol. 43, no. 3, pp. 261–268, 2007.

[147] E. F. Rybicki and M. F. Kanninen, “A finite element calculation of stress intensity factors by a modified crack closure integral,” *Eng. Fract. Mech.*, vol. 9, no. 4, pp. 931–938, 1977.

[148] D. Busse, “Extending fatigue life of aircraft fuselage structures usin laser-peening,” Cranfield University, 2017.

[149] X. Wang, F. Li, Q. Yang, and A. He, “FEM analysis for residual stress prediction in hot rolled steel strip during the run-out table cooling,” *Appl. Math. Model.*, vol. 37, no. 1–2, pp. 586–609, Jan. 2013.

[150] J. Mathew, R. J. Moat, S. Paddea, M. E. Fitzpatrick, and P. J. Bouchard, “Prediction of residual stresses in girth welded pipes using an artificial neural network approach,” *Int. J. Press. Vessel. Pip.*, vol. 150, pp. 89–95, Feb. 2017.

[151] T. Nishioka and S. N. Atluri, “Numerical analysis of dynamic crack propagation: generation and prediction studies,” *Eng. Fract. Mech.*, vol. 16, no. 3, pp. 303–332, 1982.

[152] R. G. Forman, V. E. Kearney, and R. M. Engle, “Numerical Analysis of Crack Propagation in Cyclic-Loaded Structures,” *J. Basic Eng.*, pp. 459–463, 1967.

[153] J. Wang, P. Navi, and C. Huet, “Numerical analysis of crack propagation in tension specimens of concrete considered as a 2D multicracked granular composite,” *Mater. Struct.*, vol. 30, pp. 11–21, 1997.

[154] M. Pant, K. Sharma, and S. Bhattacharya, “Application of EFGM and XFEM for Fatigue Crack Growth Analysis of Functionally Graded Materials,” in *11th International Symposium on Plasticity and Impact Mechanics*, 2017, pp. 1231–1238.

[155] Det Norske Veritas AS, “Fatigue Design of Offshore Steel Structures,” 2005.

[156] ASTM International, “ASTM E384: Standard Test Method for Knoop and Vickers Hardness of Materials,” 2012.

[157] UK Research and Innovation, “Science & Technology Facilities Council.” .

[158] IAEA International Atomic Energy Agency, “Measurement of residual stress in materials using neutrons,” in *Proceedings of a technical meeting* , 2003.

[159] R. Woracek, “Energy selective neutron imaging for the characterization of polycrystalline materials,” University of Tennessee, 2015.

[160] G. S. Pawley, “Unit-cell refinement from powder diffraction scans,” *J. Appl. Crystallogr.*, vol. 14, no. 6, pp. 357–361, 1981.

[161] S. Pratihar, M. Turski, L. Edwards, and P. J. Bouchard, “Neutron diffraction residual stress measurements in a 316L stainless steel bead-on-plate weld specimen,” *Int. J. Press. Vessel. Pip.*, vol. 86, pp. 13–19.

[162] M. E. Kartal, C. D. M. Liljedahl, S. Gungor, L. Edwards, and M. E. Fitzpatrick, “Determination of the profile of the complete residual stress tensor in a VPPA weld using the multi-axial contour method,” *Acta Mater.*, vol. 56, no. 16, pp. 4417–4428, 2008.

[163] J. R. Santisteban, M. R. Daymond, J. A. James, and L. Edwards, “ENGIN-X: A third-generation neutron strain scanner,” *J. Appl. Crystallogr.*, vol. 39, no. 6, pp. 812–825, 2006.

[164] M. T. Hutchings, Withers.P.J, T. M. Holden, and T. Lorentzen, *Introduction to characterization of residual stress by neutron diffraction*, vol. 8. 2005.

[165] A. Mehmanparast, C. M. Davies, and K. M. Nikbin, “Quantification and Prediction of Residual Stresses in Creep Crack Growth Specimens,” *Mater. Sci. Forum*, vol. 777, pp. 25–30, 2014.

[166] M. Leitner, “Influence of effective stress ratio on the fatigue strength of welded and HFMI-treated high-strength steel joints,” *Int. J. Fatigue*, vol. 102, pp. 158–170, 2017.

[167] J. R. Santisteban *et al.*, “Strain imaging by Bragg edge neutron transmission,” *Nucl. Instruments Methods Phys. Res. Sect. A Accel. Spectrometers, Detect. Assoc. Equip.*, vol. 481, no. 1–3, pp. 765–768, Apr. 2002.

[168] M. B. Prime, “Cross-Sectional Mapping of Residual Stresses by Measuring the Surface Contour After a Cut,” *J. Eng. Mater. Technol.*, vol. 123, no. 2, p. 162, 2001.

[169] F. Hosseinzadeh, P. Ledgard, and P. J. Bouchard, “Controlling the Cut in Contour Residual Stress Measurements of Electron Beam Welded Ti-6Al-4V Alloy Plates,”

Exp. Mech., vol. 53, no. 5, pp. 829–839, 2013.

[170] M. B. Prime, R. J. Sebring, J. M. Edwards, D. J. Hughes, and P. J. Webster, "Laser surface-contouring and spline data-smoothing for residual stress measurement," *Exp. Mech.*, vol. 44, no. 2, pp. 176–184, 2004.

[171] F. Hosseinzadeh, Y. Traore, P. J. Bouchard, and O. Muránsky, "Mitigating cutting-induced plasticity in the contour method, part 1: Experimental," *Int. J. Solids Struct.*, vol. 94–95, pp. 247–253, 2016.

[172] O. Muránsky, C. J. Hamelin, F. Hosseinzadeh, and M. B. Prime, "Mitigating cutting-induced plasticity in the contour method. Part 2: Numerical analysis," *Int. J. Solids Struct.*, vol. 94–95, pp. 254–262, 2016.

[173] M. B. Prime and A. L. Kastengren, *The Contour Method Cutting Assumption: Error Minimization and Correction*. Experimental and Applied Mechanics, Volume 6, 2010.

[174] C. D. M. Liljedahl, O. Zanellato, M. E. Fitzpatrick, J. Lin, and L. Edwards, "The effect of weld residual stresses and their re-distribution with crack growth during fatigue under constant amplitude loading," *Int. J. Fatigue*, vol. 32, no. 4, pp. 735–743, 2010.

[175] K. A. Venkata, C. E. Truman, D. J. Smith, and R. C. Wimpory, "Relaxation of residual stresses when extracting a specimen from a dissimilar metal electron beam welded plate," in *7th International Conference on Creep, Fatigue and Creep-Fatigue Interaction*, 2016, vol. 7, pp. 19–22.

[176] Y.-H. Zhang, S. Smith, W. Liwu, and C. Johnston, "Residual stress measurements and modelling," *Fatigue Fract. Eng. Mater. Struct.*, no. 40, pp. 1868–1881, 2017.

[177] British Standard Institution, "BS ISO 12108:2012, Metallic materials - Fatigue testing - Fatigue crack growth method," London, 2012.

[178] Y. C. Lam and K. S. Lian, "The effect of residual stresses and its redistribution on fatigue crack growth," *Theor. Appl. Fract. Mech.*, vol. 12, pp. 59–66, 1989.

[179] M. R. James, "The relaxation of residual stresses during fatigue," in *Residual stress and stress relaxation*, 1982, pp. 297–298.

[180] V. Igwemezie, P. Dirisu, and A. Mehmanparast, "Critical assessment of the fatigue crack growth rate sensitivity to material microstructure in ferrite-pearlite steels in air and marine environment," *Mater. Sci. Eng. A*, vol. 754, no. March, pp. 750–765, 2019.

[181] I. de Diego-Calderón *et al.*, “Effect of microstructure on fatigue behavior of advanced high strength steels produced by quenching and partitioning and the role of retained austenite,” *Mater. Sci. Eng. A*, vol. 641, pp. 215–224, Aug. 2015.

[182] B. Adamczyk-Cieślak, M. Koralnik, R. Kuziak, T. Brynk, T. Zygmunt, and J. Mizera, “Low-cycle fatigue behaviour and microstructural evolution of pearlitic and bainitic steels,” *Mater. Sci. Eng.*, vol. 747, pp. 144–153, Feb. 2019.

[183] H.-B. Park and B.-W. Lee, “Effect of specimen thickness on fatigue crack growth rate,” *Nucl. Eng. Des.*, vol. 197, no. 1–2, pp. 197–203, 2000.

[184] J. D. M. Costa and J. A. M. Ferreira, “Effect of stress ratio and specimen thickness on fatigue crack growth of CK45 steel,” *Theor. Appl. Fract. Mech.*, vol. 30, no. 1, pp. 65–73, 1998.

[185] C. M. C. Albuquerque, R. M. C. Miranda, V. Richter-Trummer, M. A. V. de Figueiredo, R. Calçada, and P. M. S. T. de Castro, “Fatigue crack propagation behaviour in thick steel weldments,” *Int. J. Struct. Integr.*, vol. 3, no. 2, pp. 184–203, 2012.

[186] A. Alvaro, O. M. Akselsen, X. Ren, and A. Kane, “Fatigue Properties of a 420 MPa Structural Steel at Low Temperature,” in *Proceedings of the Twenty-sixth International Ocean and Polar Engineering Conference*, 2016, pp. 331–337.

[187] R. I. Stephens and J. K. Lim, “Fatigue Crack Growth and Retardation in the Welded HAZ of 4140 Steel,” *Weld. Res. Suppl.*, pp. 294–304, 1990.

[188] E. Mecozzi *et al.*, *Fatigue behaviour of high-strength steel-welded joints in offshore and marine systems (FATHOMS)*. 2010.

[189] E. Coudert and C. Renaudin, “Variable amplitude corrosion fatigue behaviour and hydrogen embrittlement of high strength steels for offshore applications,” *Int. Offshore Polar Eng. Conf.*, vol. IV, pp. 116–122, 1998.

[190] L. Bertini, “Influence of seawater and residual stresses on fatigue crack growth in C - M n steel weld joints,” *Theor. Appl. Fract. Mech.*, vol. 16, pp. 135–144, 1991.

[191] T. Fukuda, T. Iwadate, and M. Shimazaki, “Consideration on the scatter of COD and fatigue crack propagation characteristics of heavy section C-Mn-V forged steel for offshore structure,” *Offshore Technol. Conf.*, pp. 109–112, 1982.

[192] J. W. C. Thompson, “Phenomenological investigation of the influence of cathodic protection on corrosion fatigue crack propagation behaviour , in a BS 4360 50D type structural steel and associated weldment micro-structures, in a marine environment,” 1984.

[193] R. Krueger, “Virtual crack closure technique: History, approach, and applications,” *Appl. Mech. Rev.*, 2004.

[194] W. Zhao, X. R. Wu, and M. G. Yan, “Weight function method for three dimensional crack problems—II. Application to surface cracks at a hole in finite thickness plates under stress gradients,” *Eng. Fract. Mech.*, vol. 34, no. 3, pp. 609–624, Jan. 1989.

[195] J. Schijve, *Fatigue of structures and materials*. 2009.

[196] W. Elber, “The significance of fatigue crack closure,” 1971.

[197] American Society For Testing and Materials - ASTM D1141, “Standard Practice for the Preparation of Substitute Ocean Water,” *ASTM Int.*, 2013.

[198] O. Adedipe, “Integrity of offshore structures,” 2015.

[199] T. Havn and H. Osvoll, “Corrosion fatigue of steel in seawater,” in *NACE International Corrosion Conference*, 2002, pp. 1–11.

[200] K. Lieb, R. Horstman, B. Power, R. Meltzer, M. Vieth, and O. Vosikovsky, “Effects of Stress Ratio on Fatigue Crack Growth Rates in X70 Pipeline Steel in Air and Saltwater,” *J. Test. Eval.*, vol. 8, no. 2, pp. 68–73, 1980.

[201] W. Zhang and R. Brook, “The effect of loading sequence on fatigue crack growth of an offshore structural steel,” in *International Offshore and Polar Engineering Conference*, 1993, pp. 98–103.

10 Appendices

Appendix A	Material specifications
Appendix B	Welding procedure and specification
Appendix C	Specimen technical drawings
Appendix D	EBSD measurement results
Appendix E	Neutron diffraction measurements
Appendix F	Pins and shackles drawings for the 100 kN Instron machine
Appendix G	List of publications

Appendix A: Material specifications

In this appendix, material specifications are presented. The material certification obtained from EEW is shown in Figure 10-1.

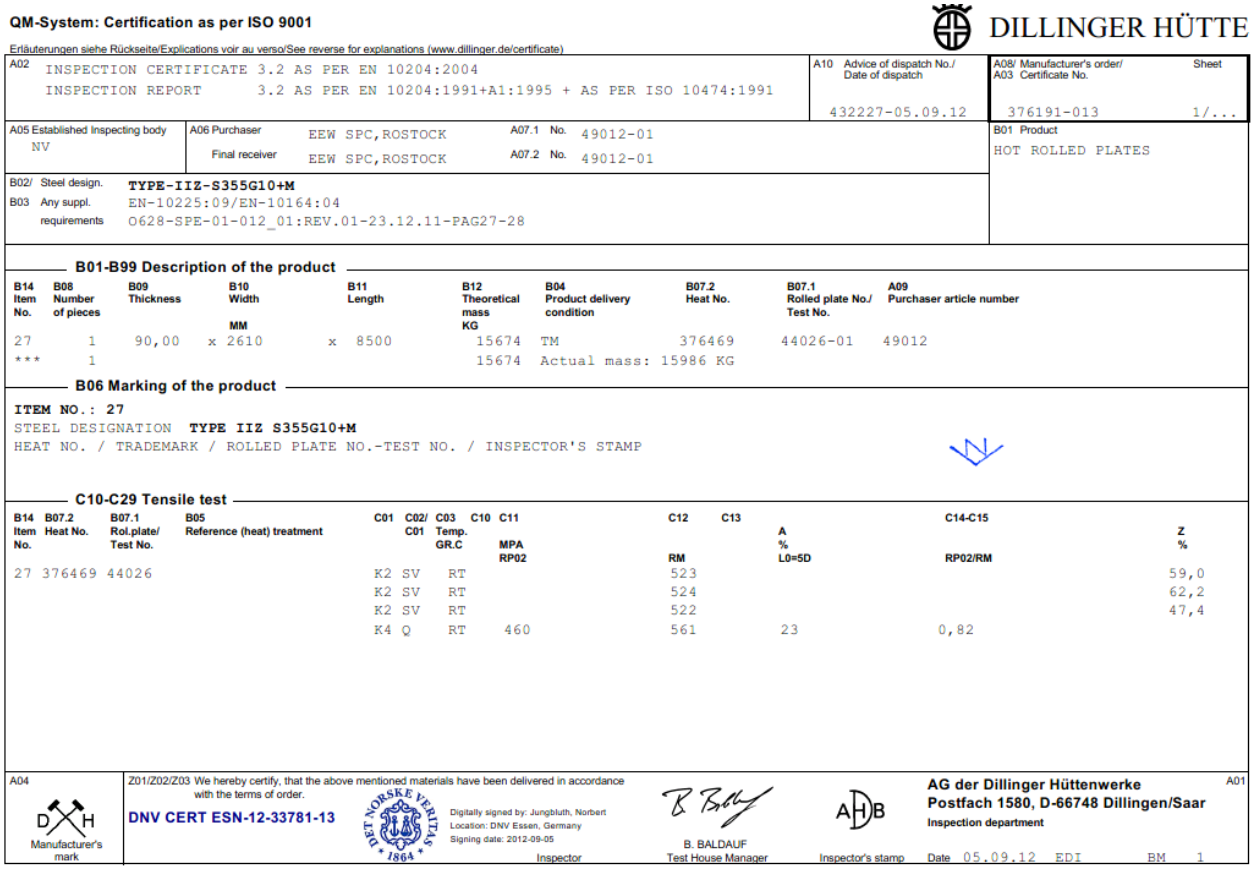

QM-System: Certification as per ISO 9001

DILLINGER HÜTTE

Erläuterungen siehe Rückseite/Explications voir au verso/See reverse for explanations (www.dillinger.de/certificate)

A02 INSPECTION CERTIFICATE 3.2 AS PER EN 10204:2004
INSPECTION REPORT 3.2 AS PER EN 10204:1991+A1:1995 + AS PER ISO 10474:1991

A10 Advice of dispatch No./ Date of dispatch: 432227-05.09.12

A08/ A03 Manufacturer's order/ Certificate No.: 376191-013 Sheet: 1/...

A05 Established Inspecting body: NV

A06 Purchaser: EEW SPC,ROSTOCK A07.1 No. 49012-01

Final receiver: EEW SPC,ROSTOCK A07.2 No. 49012-01

B01 Product: HOT ROLLED PLATES

B02/ Steel design. TYPE-IIZ-S355G10+M

B03 Any suppl. requirements: EN-10225:09/EN-10164:04
O628-SPE-01-012_01:REV.01-23.12.11-PAG27-28

B01-B99 Description of the product

B14 Item No.	B08 Number of pieces	B09 Thickness	B10 Width MM	B11 Length	B12 Theoretical mass KG	B04 Product delivery condition	B07.2 Heat No.	B07.1 Rolled plate No./ Test No.	A09 Purchaser article number
27	1	90,00	x 2610	x 8500	15674	TM	376469	44026-01	49012
***	1				15674	Actual mass: 15986 KG			

B06 Marking of the product

ITEM NO.: 27
STEEL DESIGNATION TYPE IIZ S355G10+M
HEAT NO. / TRADEMARK / ROLLED PLATE NO.-TEST NO. / INSPECTOR'S STAMP

C10-C29 Tensile test

B14 Item No.	B07.2 Heat No.	B07.1 Rol.plate/ Test No.	B05 Reference (heat) treatment	C01	C02/ C01	C03 Temp. GR.C	C10	C11 MPA RP02	C12 RM	C13	A % L0=5D	C14-C15 RP02/RM	Z %
27	376469	44026		K2	SV	RT			523				59,0
				K2	SV	RT			524				62,2
				K2	SV	RT			522				47,4
				K4	Q	RT		460	561		23	0,82	

A04 D H Manufacturer's mark

Z01/Z02/Z03 We hereby certify, that the above mentioned materials have been delivered in accordance with the terms of order.

DNV CERT ESN-12-33781-13

DET NORSKE VERITAS 1864

Digitally signed by: Jungbluth, Norbert
Location: DNV Essen, Germany
Signing date: 2012-09-05

Inspector

B. BALDAUF
Test House Manager

A H B Inspector's stamp

A01 AG der Dillinger Hüttenwerke
Postfach 1580, D-66748 Dillingen/Saar
Inspection department

Date 05.09.12 EDI BM 1

Figure 10-1: Test material certificate

The chemical composition provided by the steel manufacturer is also presented in Figure 10-2.

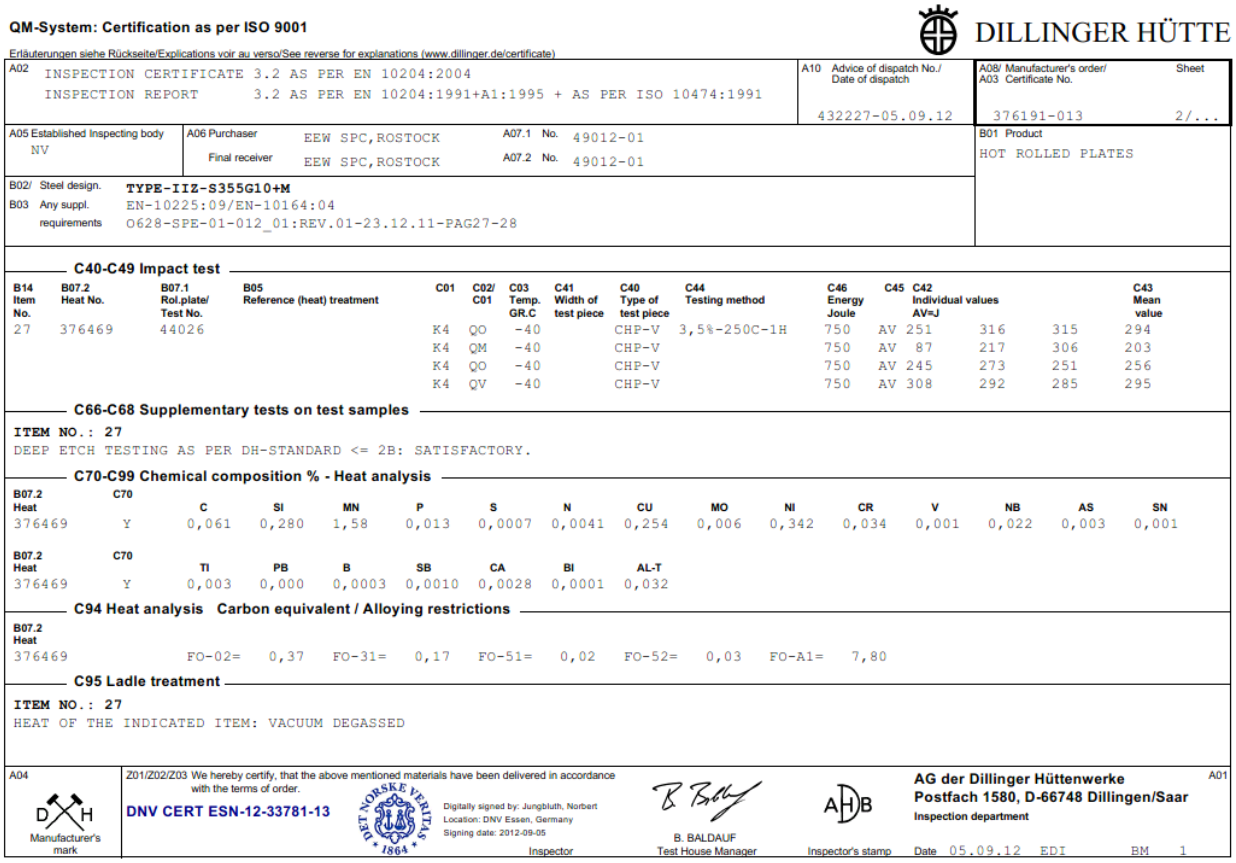

QM-System: Certification as per ISO 9001

DILLINGER HÜTTE

Erläuterungen siehe Rückseite/Explications voir au verso/See reverse for explanations (www.dillinger.de/certificate)

A02 INSPECTION CERTIFICATE 3.2 AS PER EN 10204:2004
INSPECTION REPORT 3.2 AS PER EN 10204:1991+A1:1995 + AS PER ISO 10474:1991

A10 Advice of dispatch No./ Date of dispatch: 432227-05.09.12

A08/ A03 Manufacturer's order/ Certificate No.: 376191-013 Sheet: 2/...

A05 Established Inspecting body: NV

A06 Purchaser: EEW SPC,ROSTOCK A07.1 No. 49012-01

Final receiver: EEW SPC,ROSTOCK A07.2 No. 49012-01

B01 Product: HOT ROLLED PLATES

B02/ Steel design. **TYPE-IIZ-S355G10+M**

B03 Any suppl. requirements: EN-10225:09/EN-10164:04 O628-SPE-01-012_01:REV.01-23.12.11-PAG27-28

C40-C49 Impact test

B14 Item No.	B07.2 Heat No.	B07.1 Rol.plate/ Test No.	B05 Reference (heat) treatment	C01	C02/ C01	C03 Temp. GR.C	C41 Width of test piece	C40 Type of test piece	C44 Testing method	C46 Energy Joule	C45	C42 Individual values AV=J			C43 Mean value
27	376469	44026		K4	QO	-40		CHP-V	3,5%-250C-1H	750	AV	251	316	315	294
				K4	QM	-40		CHP-V		750	AV	87	217	306	203
				K4	QO	-40		CHP-V		750	AV	245	273	251	256
				K4	QV	-40		CHP-V		750	AV	308	292	285	295

C66-C68 Supplementary tests on test samples

ITEM NO.: 27

DEEP ETCH TESTING AS PER DH-STANDARD <= 2B: SATISFACTORY.

C70-C99 Chemical composition % - Heat analysis

B07.2 Heat	C70	C	SI	MN	P	S	N	CU	MO	NI	CR	V	NB	AS	SN
376469	Y	0,061	0,280	1,58	0,013	0,0007	0,0041	0,254	0,006	0,342	0,034	0,001	0,022	0,003	0,001

B07.2 Heat	C70	TI	PB	B	SB	CA	BI	AL-T
376469	Y	0,003	0,000	0,0003	0,0010	0,0028	0,0001	0,032

C94 Heat analysis Carbon equivalent / Alloying restrictions

B07.2 Heat											
376469	FO-02=	0,37	FO-31=	0,17	FO-51=	0,02	FO-52=	0,03	FO-A1=	7,80	

C95 Ladle treatment

ITEM NO.: 27

HEAT OF THE INDICATED ITEM: VACUUM DEGASSED

A04 D H Manufacturer's mark

Z01/Z02/Z03 We hereby certify, that the above mentioned materials have been delivered in accordance with the terms of order.

DNV CERT ESN-12-33781-13

DET NORSKE VERITAS 1864

Digitally signed by: Jungbluth, Norbert
Location: DNV Essen, Germany
Signing date: 2012-09-05

Inspector

B. BALDAUF
Test House Manager

AHB Inspector's stamp

AG der Dillinger Hüttenwerke
Postfach 1580, D-66748 Dillingen/Saar
Inspection department

A01

Date 05.09.12 EDI BM 1

Figure 10-2: Chemical composition of the welded plate

Appendix B: Welding procedure and specification

The welding procedure and specification provided by the manufacturer are presented in this appendix.

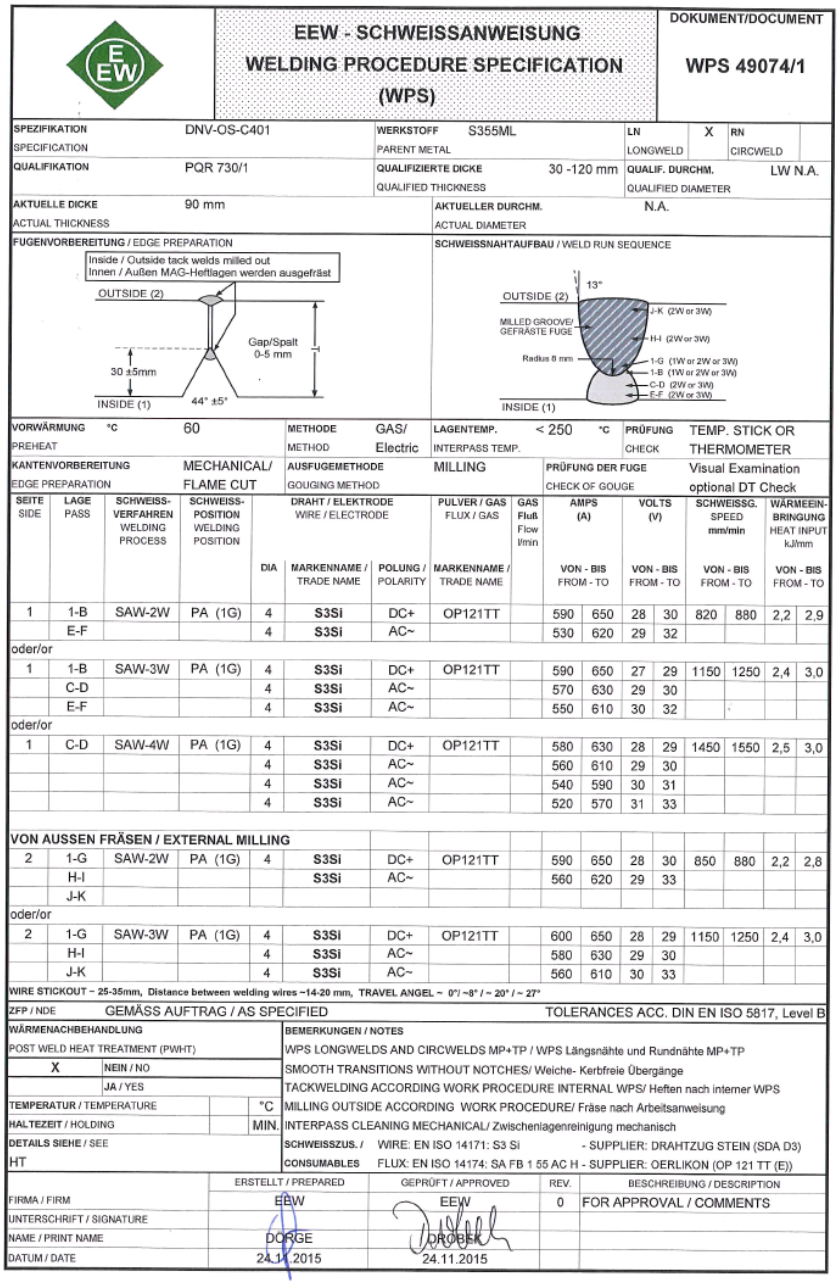

EEW - SCHWEISSANWEISUNG
WELDING PROCEDURE SPECIFICATION (WPS)

DOKUMENT/DOCUMENT: WPS 49074/1

SPEZIFIKATION / SPECIFICATION	DNV-OS-C401	WERKSTOFF / PARENT METAL	S355ML	LN / LONGWELD	X
QUALIFIKATION	PQR 730/1	QUALIFIZIERTE DICKE / QUALIFIED THICKNESS	30 -120 mm	QUALIF. DURCHM. / QUALIFIED DIAMETER	LW N.A.
AKTUELLE DICKE / ACTUAL THICKNESS	90 mm	AKTUELLER DURCHM. / ACTUAL DIAMETER	N.A.		

FUGENVORBEREITUNG / EDGE PREPARATION

SCHWEISSNAHTAUFBAU / WELD RUN SEQUENCE

VORWÄRMUNG / PREHEAT °C	60	METHODE / METHOD	GAS/ Electric	LAGENTEMP. / INTERPASS TEMP. °C	< 250
PRÜFUNG / CHECK	TEMP. STICK OR THERMOMETER	KANTENVORBEREITUNG / EDGE PREPARATION	MECHANICAL/ FLAME CUT	AUSFUGEMETHODE / GOUGING METHOD	MILLING
PRÜFUNG DER FUGE / CHECK OF GOUGE	Visual Examination optional DT Check				

SEITE / SIDE	LAGE / PASS	SCHWEISS-VERFAHREN / WELDING PROCESS	SCHWEISS-POSITION / WELDING POSITION	DRAHT / ELEKTRODE / WIRE / ELECTRODE DIA	MARKENNAME / TRADE NAME	POLUNG / POLARITY	PULVER / GAS FLUX / GAS	GAS Fluß Flow l/min	AMPS (A) VON - BIS / FROM - TO		VOLTS (V) VON - BIS / FROM - TO		SCHWEISSG. SPEED mm/min VON - BIS / FROM - TO		WÄRMEEIN-BRINGUNG / HEAT INPUT kJ/mm VON - BIS / FROM - TO	
1	1-B	SAW-2W	PA (1G)	4	S3Si	DC+	OP121TT		590	650	28	30	820	880	2,2	2,9
	E-F			4	S3Si	AC~			530	620	29	32				
oder/or																
1	1-B	SAW-3W	PA (1G)	4	S3Si	DC+	OP121TT		590	650	27	29	1150	1250	2,4	3,0
	C-D			4	S3Si	AC~			570	630	29	30				
	E-F			4	S3Si	AC~			550	610	30	32				
oder/or																
1	C-D	SAW-4W	PA (1G)	4	S3Si	DC+	OP121TT		580	630	28	29	1450	1550	2,5	3,0
				4	S3Si	AC~			560	610	29	30				
				4	S3Si	AC~			540	590	30	31				
				4	S3Si	AC~			520	570	31	33				
VON AUSSEN FRÄSEN / EXTERNAL MILLING																
2	1-G	SAW-2W	PA (1G)	4	S3Si	DC+	OP121TT		590	650	28	30	850	880	2,2	2,8
	H-I				S3Si	AC~			560	620	29	33				
	J-K															
oder/or																
2	1-G	SAW-3W	PA (1G)	4	S3Si	DC+	OP121TT		600	650	28	29	1150	1250	2,4	3,0
	H-I			4	S3Si	AC~			580	630	29	30				
	J-K			4	S3Si	AC~			560	610	30	33				

WIRE STICKOUT ~ 25-35mm, Distance between welding wires ~14-20 mm, TRAVEL ANGEL ~ 0°/ ~8° / ~ 20° / ~ 27°

ZFP / NDE: GEMÄSS AUFTRAG / AS SPECIFIED — TOLERANCES ACC. DIN EN ISO 5817, Level B

WÄRMENACHBEHANDLUNG / POST WELD HEAT TREATMENT (PWHT)	BEMERKUNGEN / NOTES
X NEIN / NO	WPS LONGWELDS AND CIRCWELDS MP+TP / WPS Längsnähte und Rundnähte MP+TP
JA / YES	SMOOTH TRANSITIONS WITHOUT NOTCHES/ Weiche- Kerbfreie Übergänge
TEMPERATUR / TEMPERATURE °C	TACKWELDING ACCORDING WORK PROCEDURE INTERNAL WPS/ Heften nach interner WPS
HALTEZEIT / HOLDING MIN.	MILLING OUTSIDE ACCORDING WORK PROCEDURE/ Fräse nach Arbeitsanweisung
DETAILS SIEHE / SEE HT	INTERPASS CLEANING MECHANICAL/ Zwischenlagenreinigung mechanisch
	SCHWEISSZUS. / CONSUMABLES WIRE: EN ISO 14171: S3 Si - SUPPLIER: DRAHTZUG STEIN (SDA D3)
	FLUX: EN ISO 14174: SA FB 1 55 AC H - SUPPLIER: OERLIKON (OP 121 TT (E))

	ERSTELLT / PREPARED	GEPRÜFT / APPROVED	REV.	BESCHREIBUNG / DESCRIPTION
FIRMA / FIRM	EEW	EEW	0	FOR APPROVAL / COMMENTS
UNTERSCHRIFT / SIGNATURE				
NAME / PRINT NAME	DORGE	DROBEK		
DATUM / DATE	24.11.2015	24.11.2015		

Figure 10-3: Welding procedure specification

Appendix C: Specimen technical drawings

Technical drawings of the tested samples are presented in this Appendix.

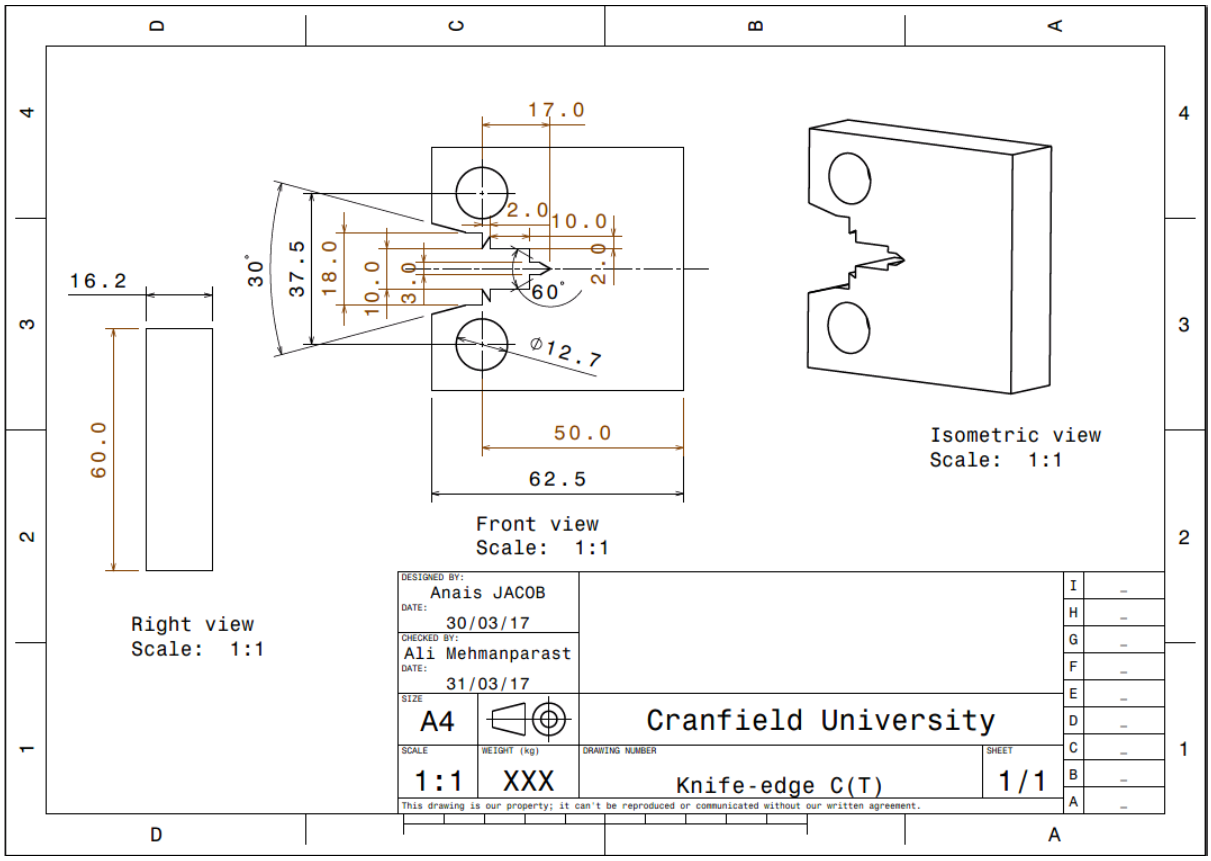

Figure 10-4: Technical drawing of the knife-edge C(T) sample tested

Tensile test specimen drawings are given below, in Figure 10-5 and Figure 10-6.

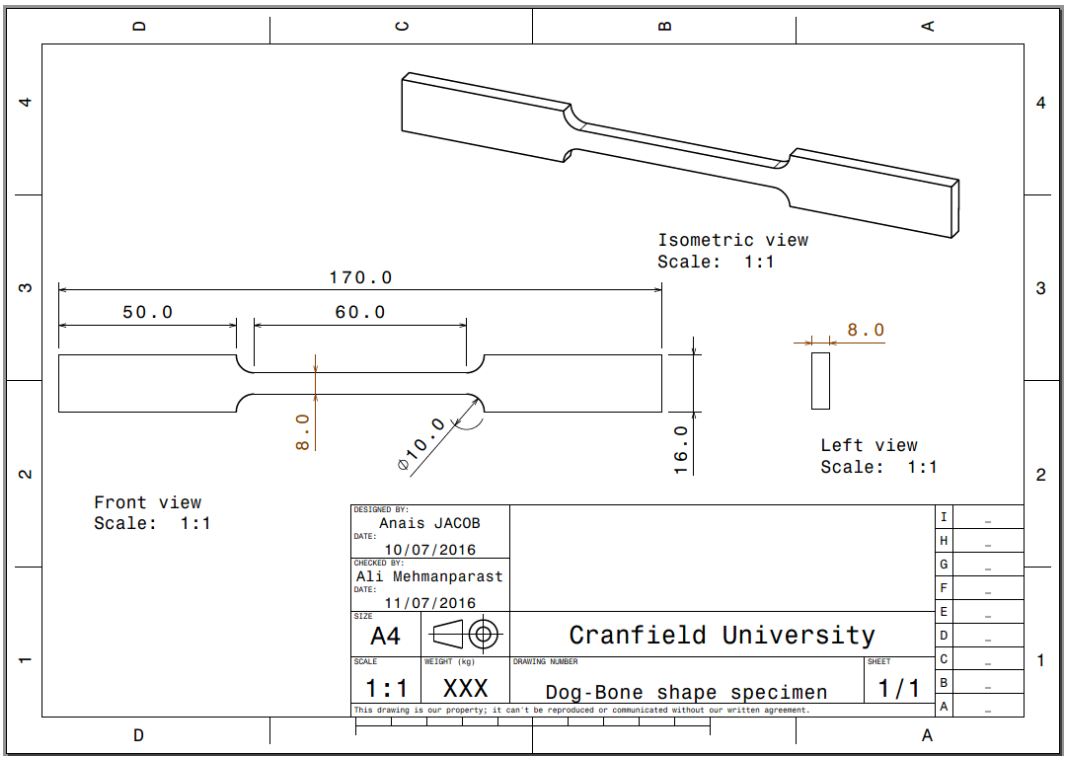

Figure 10-5: Technical drawing of the dog-bone shape tensile test specimen

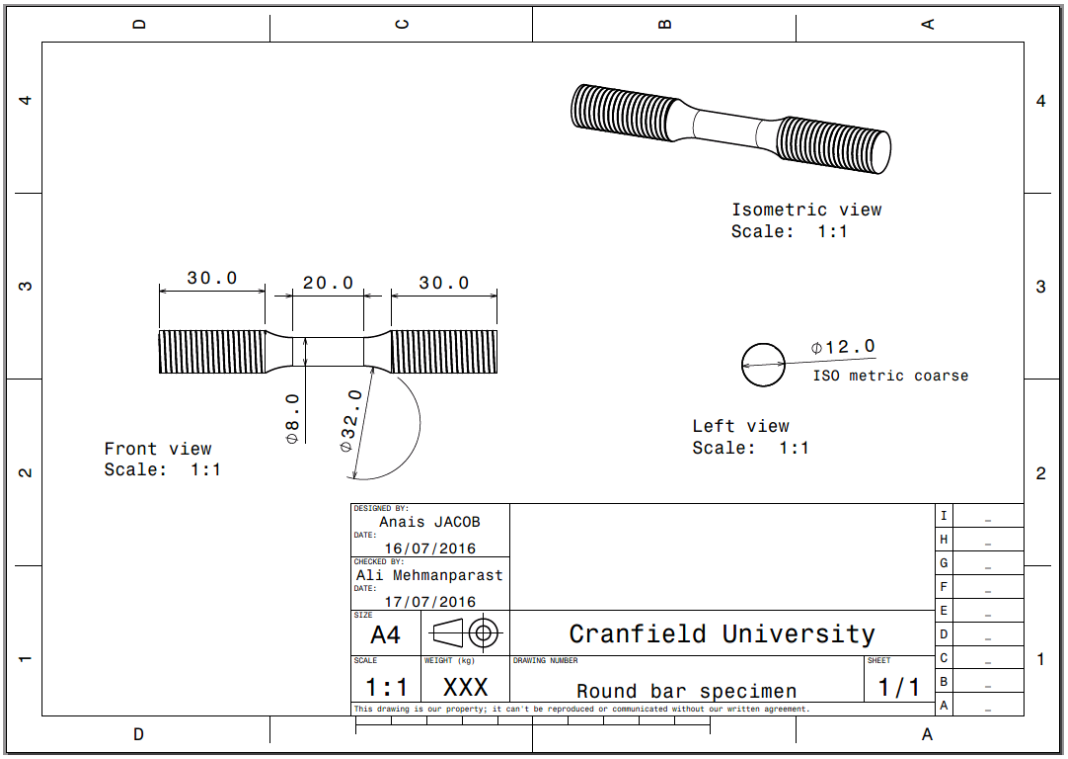

Figure 10-6: Technical drawing of the round bar tensile test specimen

The two different stages of the extraction of the stress free cubes, used in the data analysis of ND results, are also detailed below.

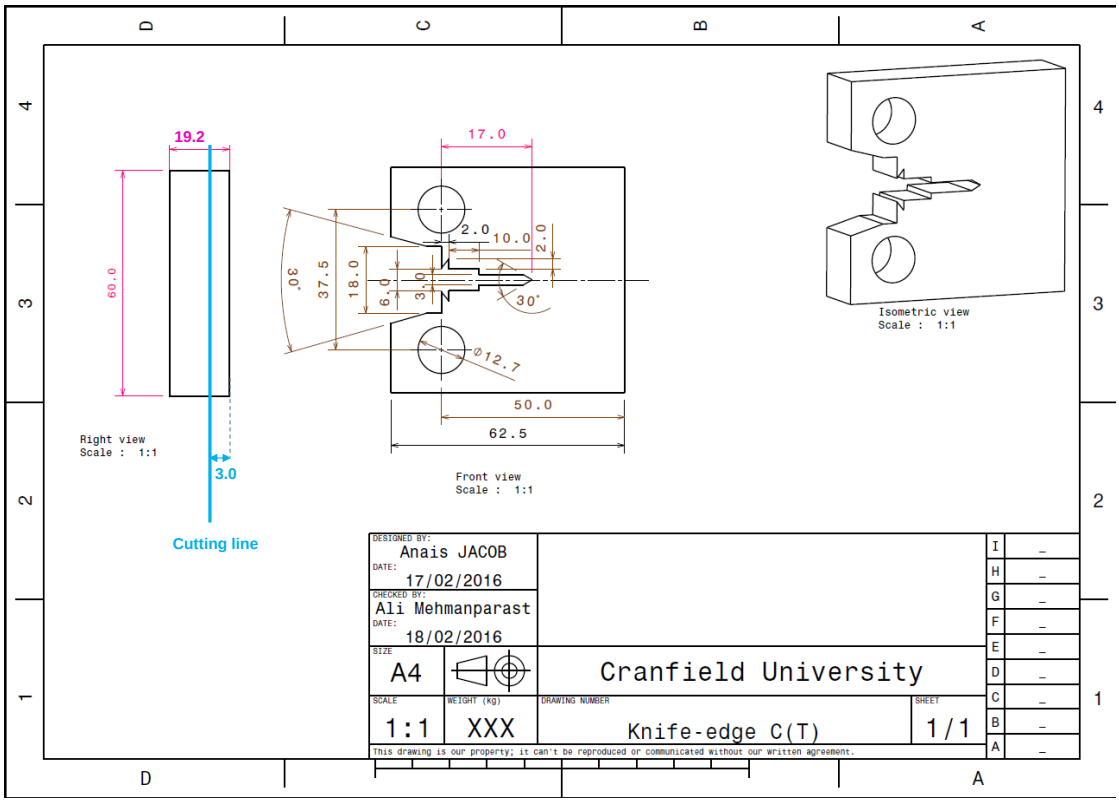

Figure 10-7: First stage of the stress free cubes for ND data analysis

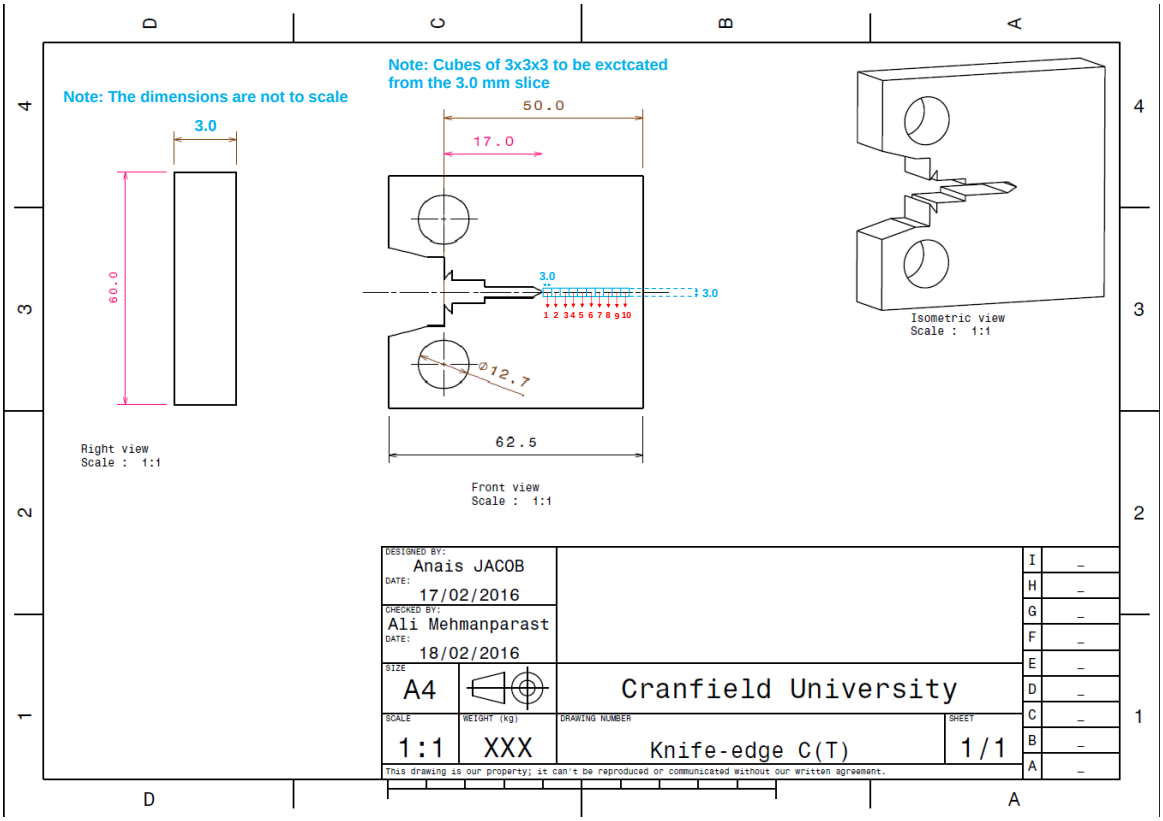

Figure 10-8: Second stage of the stress free cubes for ND data analysis

Appendix D: EBSD measurement results

The phase analysis results of the WM/HAZ and HAZ/BM regions are presented below.

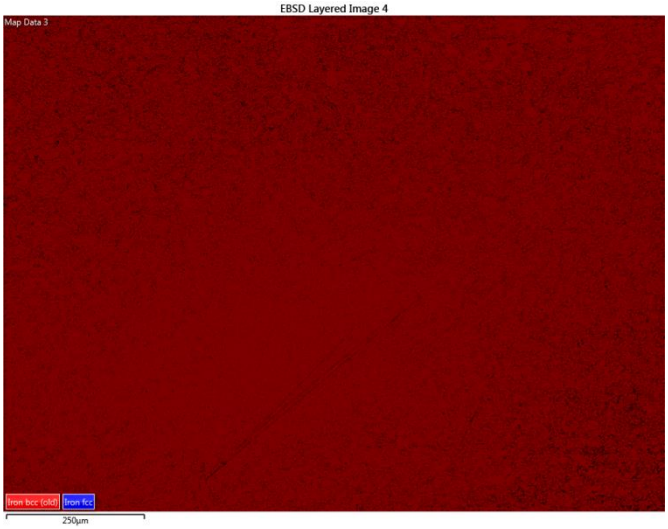

Figure 10-9: WM/HAZ phase analysis

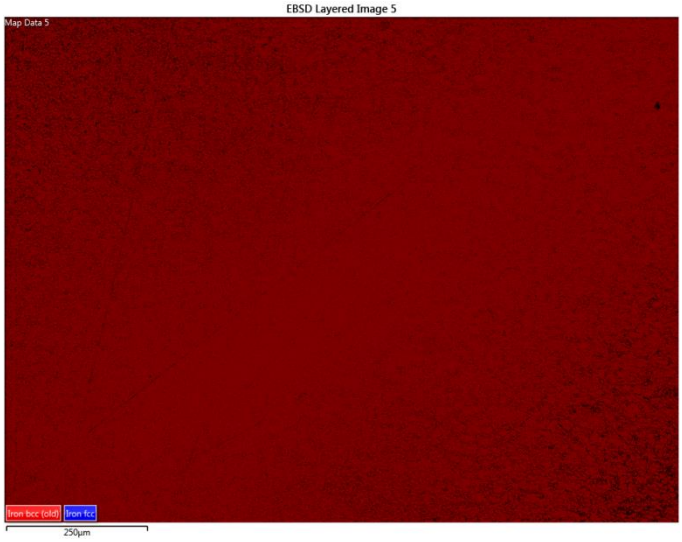

Figure 10-10: HAZ/BM phase analysis

Appendix E: Neutron diffraction measurements

The ND results are presented below or the RS measure in normal and longitudinal directions.

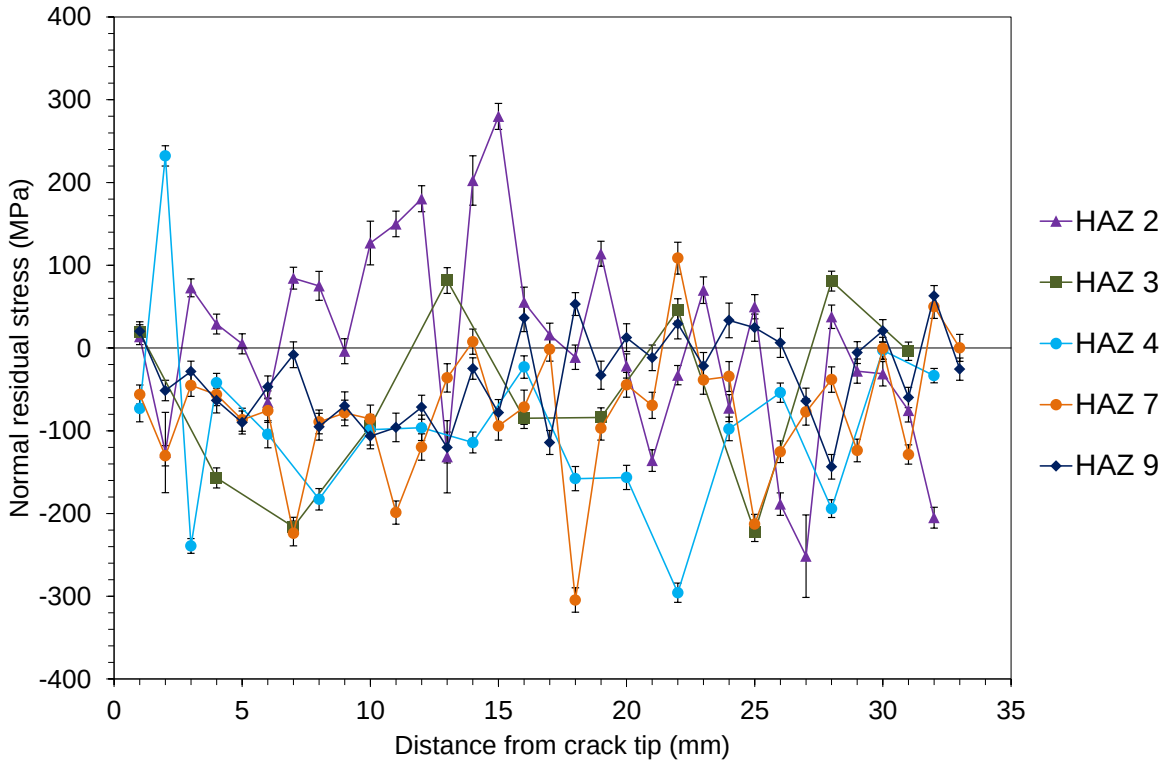

Figure 10-11: Normal RS at mid-height and mid-thickness of all the HAZ samples measured on Engin-X

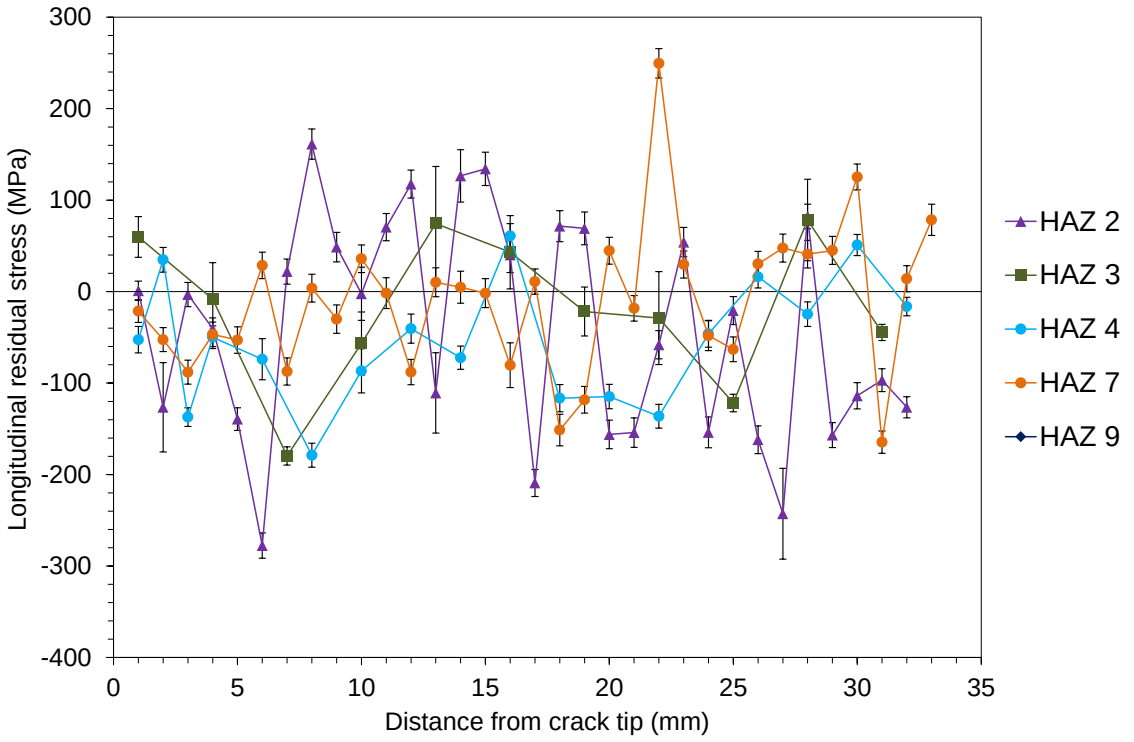

Figure 10-12: Longitudinal RS at mid-height and mid-thickness of all the HAZ samples measured on Engin-X

Appendix F: Pins and shackles drawings for the 100 kN Instron machine

Pins and shackles have been designed and manufactured according to the following drawings and have been used on the 100 kN INSTRON machine.

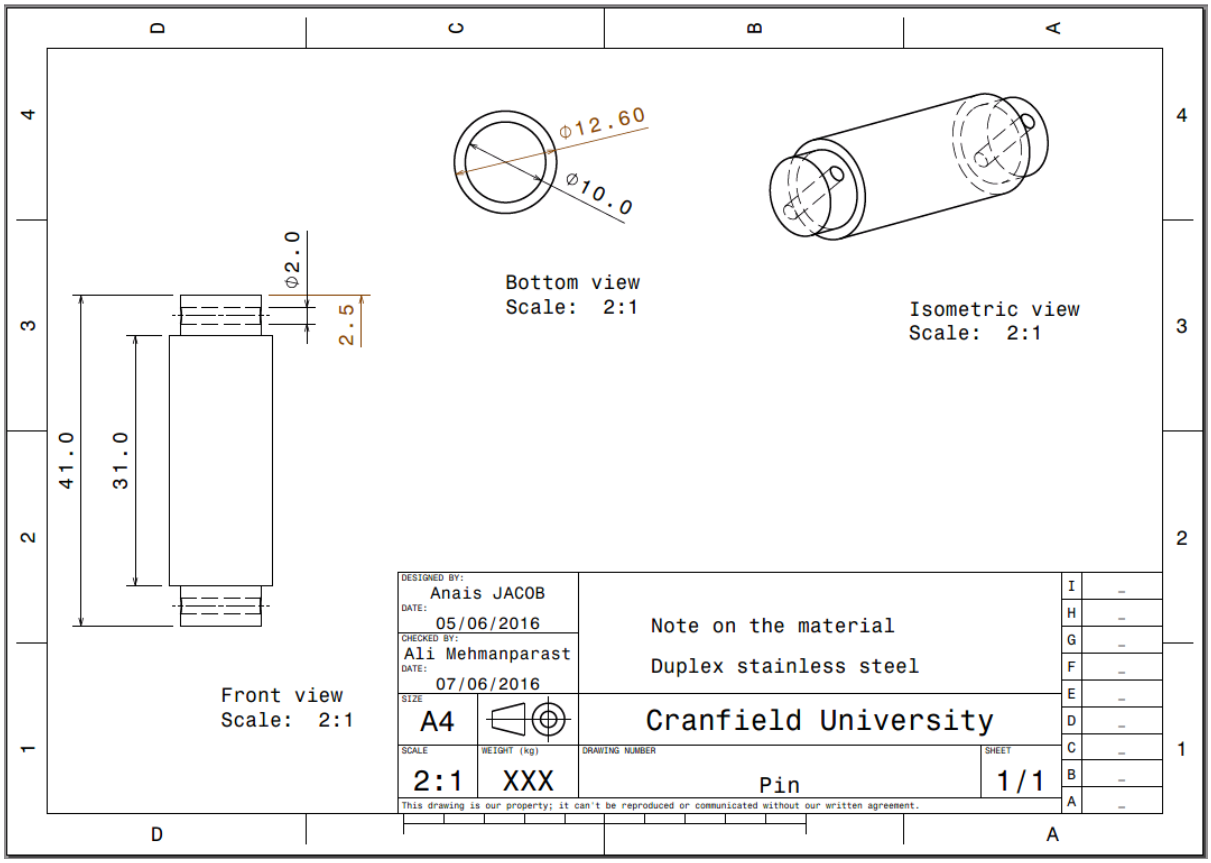

Figure 10-13: Technical drawing of the pins manufactured for the FCG tests

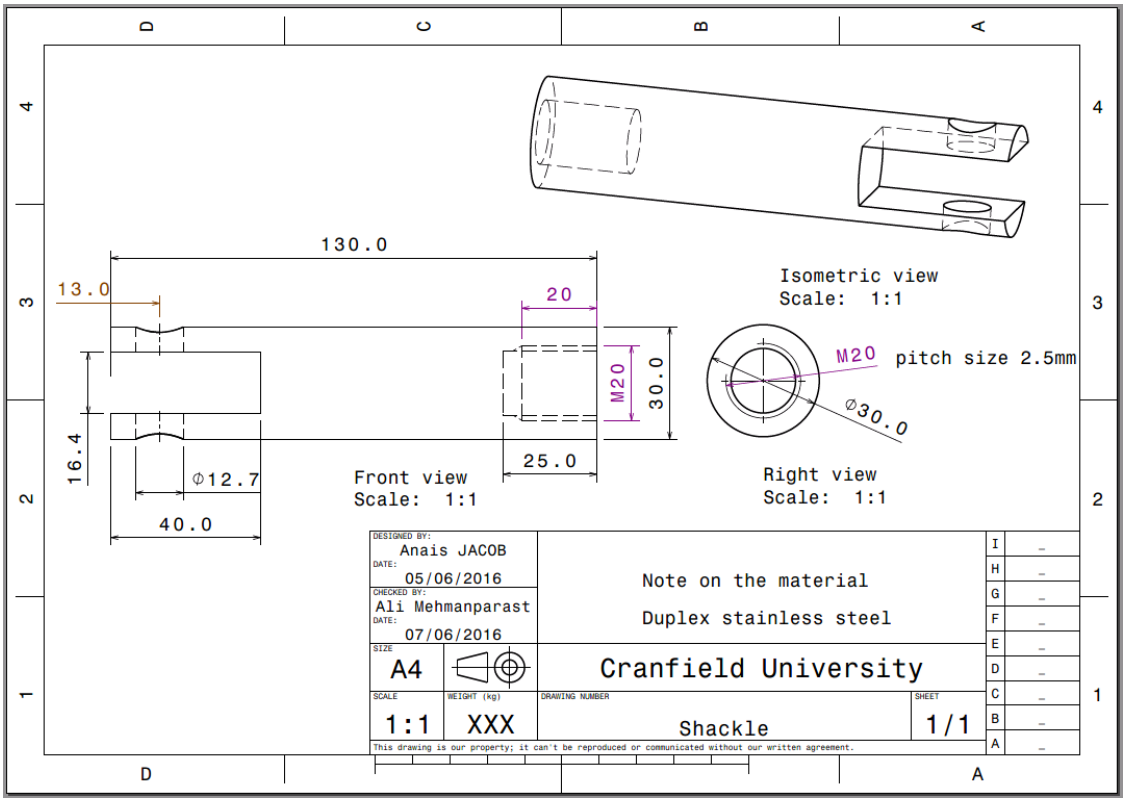

Figure 10-14: Technical drawing of the shackles manufactured for the FCG tests

Appendix G: List of publications

Journal papers

1- Jacob, A. and Mehmanparast, A., 2016. Sensitivity analysis of material microstructure effects on predicted crack paths using finite element simulations. *Journal of Multiscale Modelling*, 7(02), p.1650003.
2- Jacob, A., Oliveira, J., Mehmanparast, A., Hosseinzadeh, F., Kelleher, J. and Berto, F., 2018. Residual stress measurements in offshore wind monopile weldments using neutron diffraction technique and contour method. *Theoretical and Applied Fracture Mechanics*, *96*, pp.418-427.
3- Jacob, A., Mehmanparast, A., D'Urzo, R. and Kelleher, J., 2019. Experimental and Numerical Investigation of Residual Stress Effects on Fatigue Crack Growth Behaviour of S355 Steel Weldments. *International Journal of Fatigue*, p.105196.

Conference papers:

1- Jacob, A., Mehmanparast, A., Kelleher, J. and Burca, G., 2018. Neutron diffraction and neutron imaging residual strain measurements on offshore wind monopile weldments. *Procedia Structural Integrity*, *13*, pp.517-522.
2- Jacob, A., de Oliveira, J.A., Mehmanparast, A., Hosseinzadeh, F. and Berto, F., 2018, June. Should Residual Stresses Be Taken Into Account in Structural Integrity Assessment of Offshore Monopiles?. In *ASME 2018 37th International Conference on Ocean, Offshore and Arctic Engineering* (pp. V003T02A051-V003T02A051). American Society of Mechanical Engineers.

Conference presentations:

1- The 5th International Conference on Crack Path (CP 2015), Ferrara, Italy, September 2015
2- Engineering Neutron User Meeting, Abingdon, UK, January 2017
3- 14th International Conference on Fracture, Rhodes, Greece, June 2017
4- 3rd REMS Annual Conference, Cranfield, UK, September 2017
5- European Academy of Wind Energy 2017, 13th PhD Seminar, September 2017
6- 22nd European Conference on Fracture, Belgrade, Serbia, August 2018